University of Warsaw
Faculty of Physics

Doctoral Thesis

The low-energy models of Mott insulators with a finite spin-orbit coupling

Niskoenergetyczne modele dla izolatorów Motta ze skończonym sprzężeniem spin-orbita

---

Dorota Gotfryd

Advisor:
Dr hab. Krzysztof Wohlfeld

A dissertation in fulfillment of the requirements for the degree of Doctor of Philosophy

Warsaw, September 2020

Acknowledgements

Doctoral studies span over several years, during which we mature as scientists and human beings. I would like to aknowledge people who inspired me during that journey and shared with me its ups and downs:

Firstly, I would like to thank dr hab. Krzysztof Wohlfeld, my doctoral thesis advisor, for the enthusiastic approach to problems, large amount of creativity in solving them, and huge help in submitting the thesis in the pandemic times. I would also like to thank my former advisors prof. Tomasz Dietl and prof. Krzysztof Byczuk, for kindly taking care of the formal side of the studies. I am deeply grateful for the close collaboration with prof. Andrzej M. Oleś, my master's thesis supervisor, i.a. for many inspiring discussions, wise advice and introduction to the exciting scientific topics and opportunities, e.g., Kitaev physics.

Sencondly, I would like to express my deep gratitude to dr Jiří Chaloupka, for having the patience to teach me efficient programming, strong support in fighting the CMFT bias as well as many inspiring discussions about physics. I would also like to thank Juraj Rusnačko, his PhD student, for the extensive technical help at the beginning of my PhD journey and very useful programming tips.

Thirdly, I would like to thank dr hab. Przemysław Piekarz and his group from the Institute of Nuclear Physics of Polish Academy of Sciences in Kraków, for the warm welcome in an *ab-initio*-methods project and a lot of understanding to my thesis writing, as well as the officemates and colleagues from the Institute of Theoretical Physics of the University of Warsaw and colleagues from the Department of Quantum Many-Body Theory at Jagiellonian Unversity in Kraków, for the friendly and creative atmosphere.

Throughout all these years I experienced a lot of support from my family and friends. I would especially like to thank my sister, Małgosia, and my parents, for being always on my side and for inspiring me to create my own opportunities, and my friends Banhi, Katja, Natalia, Kasia and Diana, for keeping their fingers crossed.

To the students doubting in their self-improvement ...

Abstract

This dissertation deals with the low-energy physics of the Mott-insulating systems with a finite spin-orbit coupling. In general, for the Mott-insulating materials one sees a finite charge gap in experiments, while the conventional density functional theory predicts them to be metals. If the materials in question belong to the class of the $3d$ transition metal compounds, the on-site Coulomb repulsion U is large enough to open the charge gap. In contrast, for some of the $4d$ and $5d$ transition metal compounds the realistic U value is too weak to open the gap and simulating the insulating behaviour is possible only after taking into account the on-site spin-orbit coupling, significant for these materials.

Recently it has been shown that the low energy models for two materials belonging to the latter class—Na_2IrO_3 and α-$RuCl_3$, contain the celebrated Kitaev term, whose ground state is exactly solvable Kitaev spin liquid—a highly quantum entangled state. This drove immense interest to the field due to the topologically protected excitations possible for the gapped versions of the state, giving hope for the stable qubits. Despite the materials turning out to be magnetically ordered instead, the hope for realising Kitaev physics is not completely gone, and the continuous effort to estimate the "distance" of the above materials coupling parameters to the Kitaev spin liquid regions on the phase diagrams of the so-called Kitaev-like models is starting to bring fruits.

In this dissertation we consider the physics of the Mott insulators with a large spin-orbit coupling in two contexts:

Firstly, we consider which ground state properties of the Kitaev-like models can be measured experimentally and whether they can help with localizing Na_2IrO_3 and α-$RuCl_3$ in the parameter space of the models. To this end we calculate the dependence of the ordered moment on the parameters of the Kitaev-like models, and compare it to the experimentally obtained magnetic moment of Na_2IrO_3 and α-$RuCl_3$. We thoroughly discuss the relevance of our predictions in narrowing down the range of Hamiltonian parameters for the materials in question and suggest further steps how to improve the computations.

Secondly, we explore how one can induce quantum entanglement (which is one of the defining features of the Kitaev spin liquid) by finite spin-orbit coupling. Thus, we investigate the spin-orbital entanglement evolution with increasing spin-orbit coupling on the example of the minimal 1D model for a Mott insulator with a finite spin-orbit interaction, consisting of the $SU(2) \otimes SU(2)$ symmetric (Kugel-Khomskii) term and the on-site spin-orbit coupling term of the Ising type. In particular, we examine the relation between the quantum entanglement in the effective degrees of freedom enforced by the large spin-orbit coupling and the spin-orbital entanglement in the full spin-orbital model. As a result, we find that even the classical spin-orbit coupling can both enhance and suppress the spin-orbital entanglement and we discuss the universality of this result.

Streszczenie

Niniejsza dysertacja dotyczy niskoenergetycznych modeli dla izolatorów Motta ze skończonym sprzężeniem spin-orbita. Ogólnie rzecz ujmując, w eksperymentach na izolatorach Motta pokazuje się przerwa izolująca, pomimo że standardowa teoria funkcjonału gęstości przypisuje im właściwości metaliczne. W szczególności, dla tego typu izolatorów należących do klasy związków metali przejściowych z czwartego okresu układu okresowego oddziaływanie kulombowskie na węźle (U) jest wystarczająco duże aby otworzyć przerwę izolującą. Tymczasem, dla niektórych związków metali przejściowych z piątego i szóstego okresu realistyczne wartości U są zbyt małe aby otworzyć przerwę. Odtworzenie właściwości izolujących jest możliwe jedynie po uwzględnieniu znacznych wartości sprzężenia spin-orbita na węźle, charakteryzujących takie materiały.

W przeciągu ostatnich kilkunastu lat pokazano, że niskoenergetyczne modele dla dwóch materiałów z tej kategorii—Na_2IrO_3 oraz α-$RuCl_3$ zawierają tzw. człon Kitajewa, którego stan podstawowy można uzyskać analitycznie. Jest to tzw. ciecz spinowa Kitajewa, silnie kwantowo splątany stan, którego wersja z przerwą topologiczną pozwala na uzyskanie wzbudzeń "chronionych topologicznie". Ten ostatni fakt spowodował silne zainteresowanie fizyką powyższych materiałów ze względu na możliwość wykorzystania takich wzbudzeń w charakterze stabilnych kubitów. Pomimo że ostatecznie wspomniane materiały okazały się być uporządkowane magnetycznie, wciąż tli się nadzieja na zrealizowanie fizyki Kitajewa w granicy silnego sprzężenia spin-orbita. Coraz to nowe grupy badawcze podejmują się ustalenia "odległości" pomiędzy parametrami Hamiltonianu oszacowanymi dla ww. materiałów oraz obszarami cieczy spinowej Kitajewa zidentyfikowanymi na diagramie fazowym dla tzw. uogólnionych modeli Kitajewa, co zaczyna przynosić pierwsze rezultaty.

W ramach niniejszej dysertacji rozważamy fizykę izolatorów Motta w granicy silnego sprzężenia spin-orbita w dwóch aspektach:

Po pierwsze, zastanawiamy się które z własności stanu podstawowego uogólnionych modeli Kitajewa mogą być zweryfikowane eksperymentalnie oraz które z nich mogą ułatwić określenie pozycji Na_2IrO_3 i α-$RuCl_3$ w przestrzeni parametrów dla tychże modeli. W tym celu prezentujemy obliczenia zależności uporządkowanego momentu magnetycznego od parametrów Hamiltonianu i zestawiamy je z uzyskanymi eksperymentalnie wielkościami związanymi z momentem magnetycznym dla Na_2IrO_3 i α-$RuCl_3$. Zamieszczamy również gruntowną dyskusję adekwatności uzyskanych przewidywań w zawężaniu obszaru parametrów efektywnego Hamiltonianu dla powyższych materiałów oraz proponujemy kroki mające na celu uzyskanie lepszych wyników.

Po drugie, badamy do jakiego stopnia splątanie kwantowe, będące jedną z definiujących cech cieczy spinowej typu Kitajewa, może zostać spowodowane skończonym oddziaływaniem spin-orbita. W tym celu śledzimy ewolucję tzw. splątania spinowo-orbitalnego wraz z rosnącym sprzężeniem spin-orbita na przykładzie minimalnego jednowymiarowego modelu dla izolatora Motta ze skończonym sprzężeniem spin-orbita, składającego się ze spinowo-orbitalnego oddziaływania nadwymiany (typu Kugela-Khomskiego) z członu Kugela-Khomskiego o symetrii $SU(2) \otimes SU(2)$ oraz sprzężenia spin-orbita (na węźle) typu Isinga. W szczególności, badamy związek pomiędzy splątaniem kwantowym dotyczącym efektywnych stopni swobody narzuconych przez sprzężenie spin-orbita a splątaniem spinowo-orbitalnym w ramach pełnego modelu spinowo-orbitalnego. W rezultacie okazuje się, że nawet klasyczne splątanie spin-orbita jest w stanie wzmóc bądź wyciszyć splątanie spinowo-orbitalne. Zamieszczamy również dyskusję ogólności powyższego rezultatu.

Authorship of original figures

Below we specify the authorship of the original figures (produced by the author of this dissertation (D.G.) and/or her collaborators).

1. Schematic figures by D.G.:
   2.7, 2.9, 2.16, 2.17, 2.19, 3.1, 3.22, 4.1, 4.2, 5.1, 5.9, A.1, A.3

2. Figure and data by D.G.:
   3.3, 3.8, 3.11, 3.13, 3.14, 3.16, 3.17, 3.24, 3.27, 5.2, 5.3, 5.5, 5.7, 5.10, 5.11, A.2, B.2, B.3, B.5, B.6, B.7, B.8

3. Figure (and data) by Jiří Chaloupka:
   3.2, 3.10, A.4

4. Figure by Jiří Chaloupka, data by D.G.:
   3.4

5. Figure and ED data by Jiří Chaloupka, CMFT data by D.G.:
   3.5, 3.6

6. Figure, ED and classical energy data by Jiří Chaloupka, CMFT data by D.G., SOPT data by Juraj Rusnačko, LSWT data by George Jackeli and Krzysztof Wohlfeld:
   3.7

7. Figure by Jiří Chaloupka, ED data by Juraj Rusnačko, CMFT data by D.G.:
   3.9

8. Figure by D.G., ED data by Jiří Chaloupka and Juraj Rusnačko, CMFT data by D.G.:
   3.15, 3.18, 3.19, 3.25

9. Panels (a)-(b) by D.G., panel (c) by Jiří Chaloupka:
   3.12

10. Figure and data by Juraj Rusnačko and Jiří Chaloupka:
    3.20, 3.21, 3.23

11. Figure and data in panels (a)-(e) by D.G., data in panels (e)-(f) by Jiří Chaloupka:
    5.4, 5.6

12. Figure by D.G., data for L = 4, 8, 12 sites by D.G. and Jiří Chaloupka, data for L = 16, 20 by Jiří Chaloupka. The fits were produced independently by both coauthors:
    5.8

13. Figure by DG, data by D.G. and Jiří Chaloupka:
    B.4

14. Figure by D.G., data by Jiří Chaloupka:
    B.1

List of Abbreviations

AF	antiferromagnet, antiferromagnetic
AF $\otimes$ **FO**	antiferromagnet(ic) $\otimes$ ferro-orbital
AF KSL	antiferromagnetic Kitaev spin liquid
BZ	Brillouin zone
CF	crystal field
CMFT	self-consistent cluster mean-field theory
DFT	density-functional theory
ED	exact diagonalization
FM	ferromagnet, ferromagnetic
FM $\otimes$ **AO**	ferromagnet(ic) $\otimes$ alternating-orbital
FM $\otimes$ **FO**	ferromagnet(ic) $\otimes$ ferro-orbital
FM KSL	ferromagnetic Kitaev spin liquid
IES	intermediate entangled state
IKc	Ising-Kitaev-compass
INS	inelastic neutron scattering
KH	Kitaev-Heisenberg
KSL	Kitaev spin liquid
LDA	local-density approximation
LHB	lower Hubbard band
LRO	long-range order
LSWT	linear spin-wave theory
MF PBC	mean-field periodic boundary conditions
ND	neutron diffraction
NN	nearest-neighbor, nearest neighbors
PBC	periodic boundary conditions
QMC	quantum Monte Carlo
REXS	resonant elastic X-ray scattering
RIXS	resonant inelastic X-ray scattering
RVB	resonating valence bond
SOC	on-site spin-orbit coupling
SOPT	second-order perturbation theory
SSB	spontaneous symmetry breaking
TMO	transition-metal oxide
UHB	upper Hubbard band

Contents

Chapter 1

Preface

When insulating behaviour of a material can be reproduced only after incorporating the Coulomb repulsion U between electrons, the material is called a Mott insulator [1, 2]. The simplest model simulating opening of the charge gap is the half-filled single-band Hubbard model. Despite its simplicity, solving the Hubbard model in general case is far from trivial. Only once the Coulomb repulsion dominates over the hopping of electrons and for commensurate fillings (the Mott insulating limit) the low-energy sector of this model can be described by the effective Heisenberg model, i.e. solely utilizing spin degrees of freedom [1]. Because the latter model has a smaller Hilbert space, it is easier to solve numerically. In fact, the Heisenberg model reproduces the low-energy physics of the undoped copper oxides (e.g. La_2CuO_4) [2].

However, for some transition-metal compounds this model is still too simple, because of the high crystal symmetry leading to partial occupancy of the atomic-like orbitals. The problem is solved by taking into account the orbital degeneracy, resulting in a multi-band Hubbard model. Similarly to the previous case, in the Mott-insulating limit one obtains the effective models—a class of the so-called Kugel-Khomskii models, involving this time spin *and* orbital degrees of freedom [3]. Because of the increase in the size of Hilbert space for these models (as compared to spin-only Heisenberg model) they are quite challenging numerically, often requiring ingenious numerical approaches.

In recent years some of the late transition-metal compounds, i.e. with partially filled $4d$ or $5d$ orbitals, for which also the substantial on-site spin-orbit coupling of relativistic origin has to be taken into account to reproduce the Mott-insulating behaviour, stirred enormous interest. The reason was that for the quasi-2D honeycomb materials, e.g. Na_2IrO_3 and α-$RuCl_3$ [4, 5, 6] the effective model in the large spin-orbit coupling limit contains the so-called Kitaev term [7], whose ground state is the celebrated Kitaev spin liquid, of a potential use for quantum computing. Extensive experimental and theoretical effort revealed that while the above materials possess long-range magnetic order below the Néel temperature, their higher energy sector still retains features of strong bond-directional frustration, characteristic for Kitaev physics. Hence, the materials seemed not extremely far from the Kitaev spin-liquid state and researchers started efforts to drive these and other materials of this kind into the Kitaev spin-liquid state. This self-consistent experimental and theoretical effort lead to the derivation of the gradually more precise effective models for the materials—the so-called Kitaev-like models [8, 9, 10].

Aim and contents of the thesis

In this thesis we focus on two aspects of the of the low-energy physics of the Mott insulators with a non-negligible spin-orbit coupling: (1) What are the ground state properties of the Kitaev–like models that can be measured experimentally and compared against the existing experiments on the materials proposed to host Kitaev physics? (2) How the quantum entanglement in the degrees of freedom enforced by the large on-site spin-orbit coupling is related to the spin-orbital entanglement, and how the ground state evolves from the negligible to large spin-orbit coupling limit? In this dissertation we attempt to partially answer the above questions. To this end we firstly examine the properties of the magnetic ordered moment in the ground state of a number

of Kitaev-like models. Secondly, we evolve the simplest possible, though nontrivial, spin-orbital model from the negligible to the large spin-orbit coupling limit. More precisely, the results of the two projects, which form the basis of this dissertation, can be summarised as follows:

- **Obtaining the properties of the magnetic ordered moment for the Kitaev-like models on the honeycomb lattice**
  This work was performed using the self-consistent cluster mean-field theory (CMFT) approach for all the commensurate magnetic phases of the Kitaev-like models on a 24-site symmetric cluster with periodic boundary conditions. The ordered moment value and spatial orientation defined the zero-temperature phase diagram for the model which was then compared with the diagram obtained via maximal overlap method based on the exact diagonalization (ED) [11]. The length of the moments is the most valuable CMFT result, because it cannot be accessed easily in ED and it explicitly distinguishes between the classical or quantum character of the more complicated orderings. The main results of this part consist of the maps of the ordered moment properties forming the multiple-parameter phase diagram of the models. The hope was that these maps would allow to estimate how far the ground states of the real materials are from the Kitaev spin-liquid regime.

  Part of these results was published in:

  (A) Dorota Gotfryd, Juraj Rusnačko, Krzysztof Wohlfeld, George Jackeli, Jiří Chaloupka, and Andrzej M. Oleś, *Phase diagram and spin correlations of the Kitaev-Heisenberg model: Importance of quantum effects*, Phys. Rev. B. **95**, 024426 (2017).

  (B) Juraj Rusnačko, Dorota Gotfryd, and Jiří Chaloupka, *Kitaev-like honeycomb magnets: Global phase behavior and emergent effective models*, Phys. Rev. B **99**, 064425 (2019).

- **Examining the evolution of the spin-orbital entanglement with increasing spin-orbit coupling**
  For this purpose the simplest setting possible was taken: a spin-orbital chain with two spin and orbital degrees of freedom on every site. The combination of both spin and effective orbital angular momentum to be equal 1/2 with the spin-orbital Hamiltonian consisting of $\mathrm{SU}(2) \otimes \mathrm{SU}(2)$ symmetric Kugel-Khomskii term and the on-site spin-orbit coupling term of the Ising type enabled us to perform extensive exact diagonalization on chains of the length $\mathrm{L} = 4n$, $n = 1,...,5$, allowing for a finite-size scaling. The main results are again the maps in the parameter space of the spin-orbital Hamiltonian, providing information about the evolution of the entanglement and magnetic properties with increasing spin-orbit coupling. Moreover, the detailed, term-by-term derivation of the effective Hamiltonian in large spin-orbit coupling limit, provided an explanation why even the classical spin-orbit coupling can either enhance or suppress the spin-orbital entanglement depending on the Hamiltonian parameters.

  The above results were published in:

  (C) Dorota Gotfryd, Ekaterina M. Pärschke, Jiří Chaloupka, Andrzej M. Oleś, and Krzysztof Wohlfeld, *How spin-orbital entanglement depends on the spin-orbit coupling in a Mott insulator*, Phys. Rev. Research **2**, 013353 (2020).

  (D) Dorota Gotfryd, Ekaterina M. Pärschke, Krzysztof Wohlfeld, and Andrzej M. Oleś, *Evolution of Spin-Orbital Entanglement for Increasing Ising Spin-Orbit Coupling*, Condens. Matter **5**, 53 (2020).

Another aim of this thesis is to summarise the knowledge accumulated so far for the Kitaev-like systems and the spin-orbital entanglement. Hence, the long and detailed *Introduction to Kitaev-like systems* in Chapter 2, as well as the shorter *Introduction to spin-orbital entanglement* in Chapter 4, some technical details in footnotes in Chapters 3, 5, containing the original results, and Appendices A-B.

Chapter 2

Introduction to Kitaev-like systems

In this chapter we will be discussing the physics of Na_2IrO_3 and α-$RuCl_3$, compounds considered to host Kitaev spin liquid (KSL) ground state [7]. Such a state is very attractive for applications in quantum computing because it can be further driven into states involving quantum bits of information (qubits). George Jackeli and Giniyat Khaliullin proposed a mechanism explaining how KSL state could be realized in layered materials containing late transition metal ions sourounded by edge-sharing octahedral oxygen cages [4]. Although further experiments found the materials to possess zigzag long range order instead, their work inspired intense and long lasting interest in these compounds. Further theoretical studies not only brought more validity to the Jackeli-Khaliullin mechanism but also indicated finer interactions moving materials from the spin liquid into the magnetically ordered state. The goal of this chapter is to guide the reader from the onset of the Kitaev-related physics in the above compounds to the present stage of experimental and theoretical research, laying the groundwork for our results to be presented in Chapter 3. While we will touch upon some of the key aspects relevant for the next chapter, the pile of research on the Kitaev-like systems accumulated so far is enormous. Therefore many important results have been omitted. In particular, we focus on Na_2IrO_3 and α-$RuCl_3$, because the research in Chapter 3 was performed with them in mind. However, many other Kitaev candidate materials were proposed and heavily researched over the years, e.g.: α, β, γ-Li_2IrO_3, $H_3LiIr_2O_6$, Cu_2IrO_3, $Cu_3LiIr_2O_6$, $Ag_3LiIr_2O_6$ [12], $Na_3Co_2SbO_6$ [13]. The interested reader is recommended to study the review papers [10, 12, 14] for a more comprehensive view and further resources.

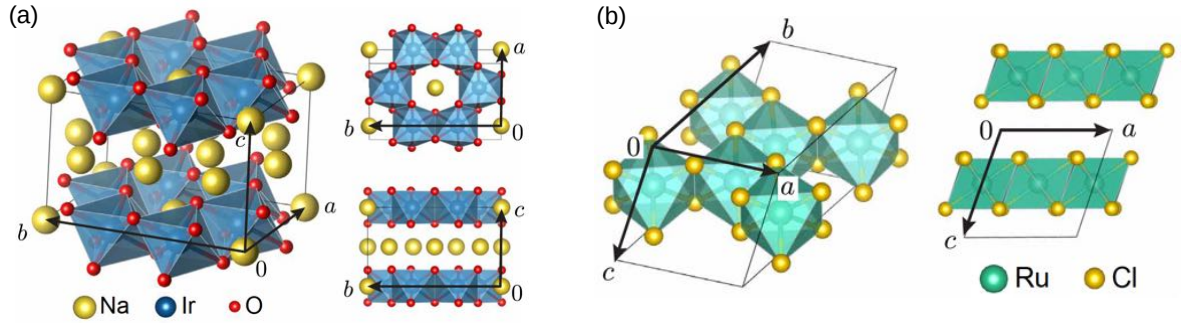

FIGURE 2.1: C2/m structures of quasi two-dimensional Mott-insulating materials (a) Na_2IrO_3 and (b) α-$RuCl_3$, taken from Ref. [10].

2.1 Low-energy physics in the strong spin-orbit coupling limit

Quasi two-dimensional materials Na_2IrO_3 and α-$RuCl_3$ are built from $NaIr_2O_6/RuCl_6$ layers stacked upon each other and, in the case of Na_2IrO_3, alternated with Na layers (Fig. 2.1 (a)). The interactions inside the layers dominate over the inter-layer ones, allowing for the dimensionality reduction by considering the layers containing iridium/ruthenium ions separately. In both cases

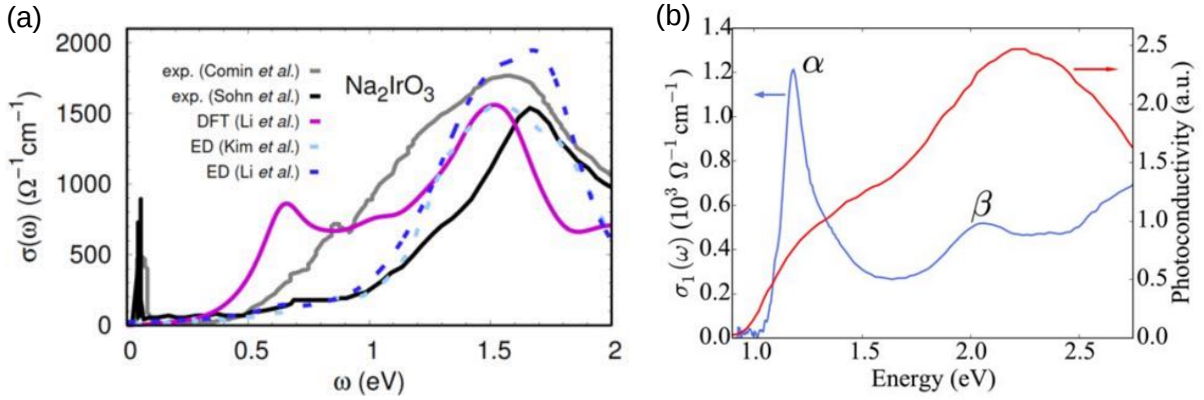

FIGURE 2.2: Optical conductivity for (a) Na_2IrO_3 with experimental and theoretical data reproduced from Refs. [15, 16, 17, 18, 19]) and (b) α-$RuCl_3$ (only the upper part of the charge gap visible on the left). Panels taken from Refs. [10] and [20], respectively.

the said Ir^{4+}/Ru^{3+} transition-metal ions form almost perfect honeycomb lattice. Every site of this lattice is surrounded by octahedral cages built out of oxygen/chlorine ions.[1]

The above materials have shown insulating behaviour in multiple experiments. In particular, optical conductivity [15, 16, 17, 18, 19, 20] (Fig. 2.2) and photoemmision [15, 21, 22, 23] revealed charge gaps of 0.35 eV and 1.1-1.9 eV for Na_2IrO_3 and α-$RuCl_3$, correspondingly.[2] The possible mechanism leading to the opening of the insulating gap in these materials has been under intense discussion, concluding in recognizing them as spin-orbit assisted Mott insulators by the condensed-matter community [10].

2.1.1 Spin-orbit assisted Mott insulators

Let us briefly recall when the Mott-insulating behaviour typically appears. A crystal with odd number of electrons per unit cell would emerge as a metal from the simplest band structure calculations. Yet, if the same system is supplemented with the strong on-site Coulomb interaction U, visibly larger then the bandwidth W, the band around the Fermi energy is split into the upper and lower Hubbard band, opening the insulating gap. This is roughly the behaviour of many $3d$ transition-metal oxides (TMOs), for which U is strong enough to open a gap in the whole 1st Brillouin zone [24].

Although Ru^{3+} and Ir^{4+} ions do have odd number of electrons on the last subshell, their situation is more complex. Their case concerns not $3d$ but $4d$ and $5d$ orbitals, which are progressively more expanded in space. Since the electrons are less localized in the $4d^5$ and $5d^5$ configurations, the realistic values of U for the said ions are much smaller then in the $3d$ case, usually not sufficient for opening the insulating gap. Indeed, many $4d$ and $5d$ transition-metal compounds are normal metals [24].[3]

In a pioneering paper investigating another iridate compound—Sr_2IrO_4, B. J. Kim *et al.* suggested the relativistic on-site spin-orbit coupling (SOC), much stronger then in $3d$ case, to be a crucial factor contributing to the anomalous insulating behaviour of some of the late transition-metal oxides. In this scenario SOC partially separates and tightens the bands around the Fermi

[1] While there are relatively small differences in the length of the three directions of such formed honeycomb lattice, the ideal cubic symmetry O_h of the cages becomes distorted to some extent, which will be discussed later.

[2] Table 1. in Ref. [10].

[3] However, for some $4d$ TMOs weaker U was enough to open a small insulating gap in a typical way [24].

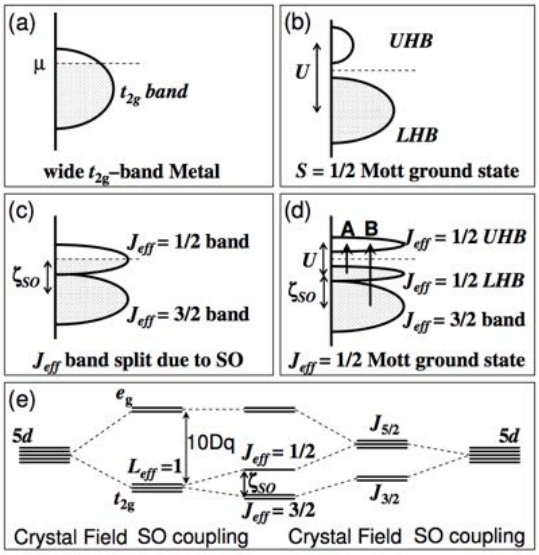

FIGURE 2.3: Schematic representation of the density of states of the $d5^5/t_{2g}^5$ bands of the iridium ions. (a) Wide t_{2g} metallic band resulting from standard band structure calculations. (b) Insulating gap separating upper and lower Hubbard bands (UHB, LHB) appearing in large U limit, unrealistic for $5d$ TMOs. (c) Spin-orbit coupling separating t_{2g} into filled $\tilde{\mathrm{J}} = 3/2$ and half-filled $\tilde{\mathrm{J}} = 1/2$ bands. Here ζ_{SO} is the spin-orbit coupling parameter. (d) Splitting of the $\tilde{\mathrm{J}} = 1/2$ into UHB and LHB by the relatively small U of $5d$ iridates. Resulting gap indicates the $\tilde{\mathrm{J}} = 1/2$ spin-orbit assisted Mott insulator. (e) Possible level splittings due to various interactions appearing in $5d$ TMOs. From the left: in the CF>SOC limit the O_h symmetric crystal field splits $5d$ into empty e_g and almost-filled low-spin t_{2g}^5, which is then further split into $\tilde{\mathrm{J}} = 1/2$ and $\tilde{\mathrm{J}} = 3/2$ states by the spin-orbit coupling, preparing the right conditions for U. From the right: in the SOC > CF limit spin-orbit coupling produces $\tilde{\mathrm{J}} = 3/2$ and $5/2$, which is further split by the crystal field, giving the same $\tilde{\mathrm{J}} = 1/2$ active level. Figure taken from Ref. [24].

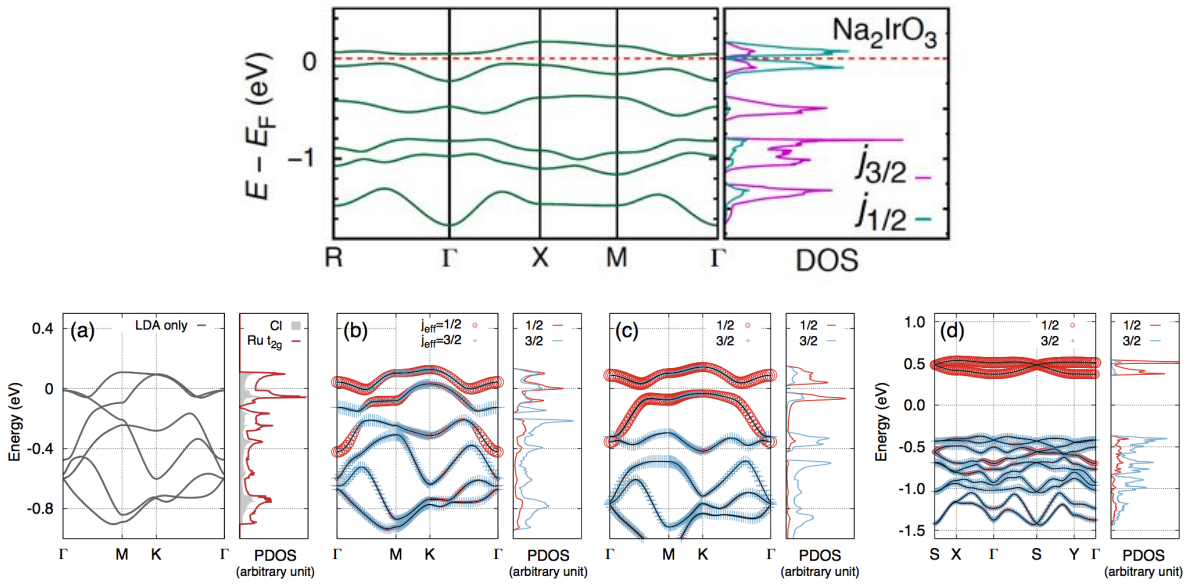

FIGURE 2.4: Upper panels: GGA+SOC band structure and density of states for Na_2IrO_3, taken from Ref. [10]; lower panels: band structure and density of states of α-$RuCl_3$ calculated with (a) LDA, (b) LDA+U, (c) LDA+U+SOC in non-magnetic state, (d)LDA+U+SOC in zigzag magnetic pattern schemes. Taken from Ref. [25].

energy, making them flat enough for the rather small U to split them in the whole 1st Brillouin

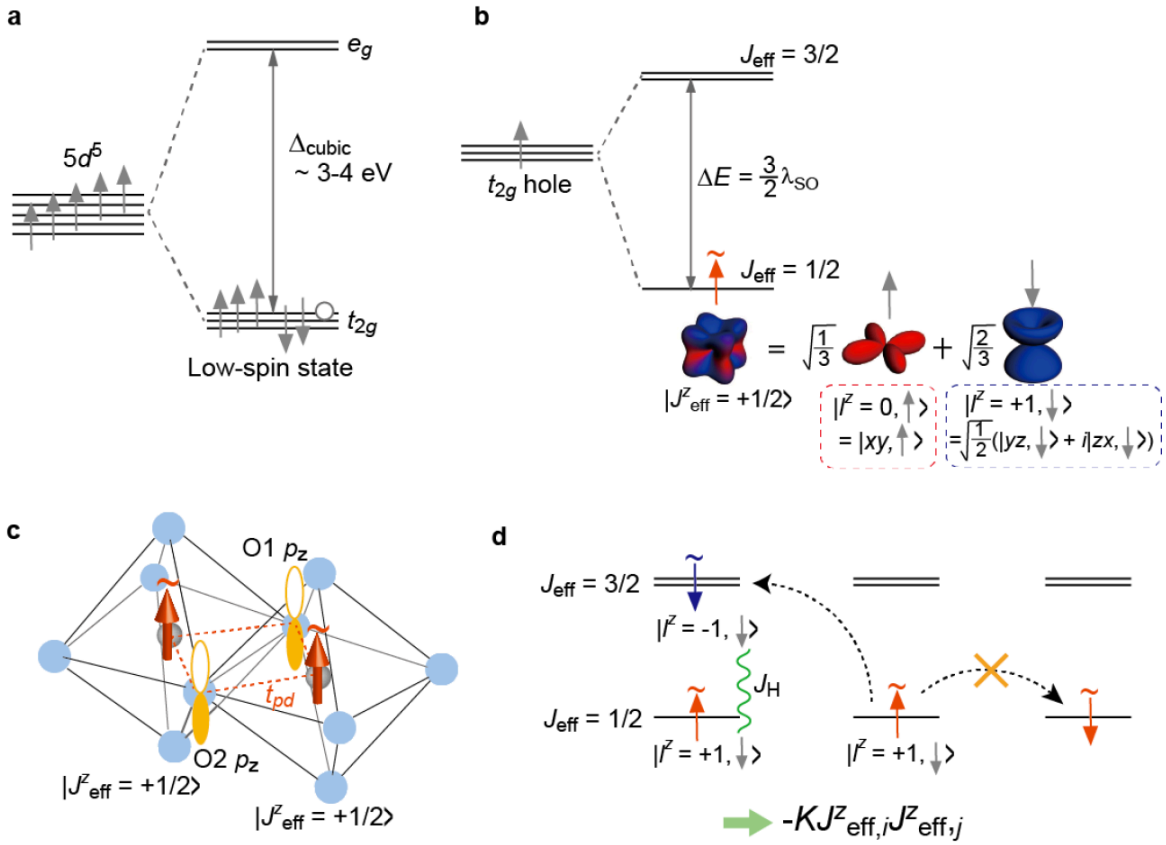

FIGURE 2.5: Local electronic states of the late transition-metal ions with the electron configuration d^5 on the last subshell. Panel (a)—(electron picture) strong cubic crystal field splits the ionic $5d^5$ level and enforces low-spin state in the t_{2g}^5 configuration while the e_g level remains completely empty. The one spin electron "missing" in t_{2g}^5 can be treated as a hole, allowing for utilizing a more convenient hole picture. Panel (b)—(hole picture) splitting of the t_{2g}^5 level by the strong spin-orbit coupling, here denoted as λ_{SO}. The hole stays on the $\tilde{J} = 1/2$ (here J_{eff}) Kramers doublet while the $\tilde{J} = 3/2$ Kramers quartet remains empty. The $\tilde{J}$ pseudospins inherit some of the features of orbitals they are built from, as shown on example of the electron density plot. Panel (c)—two edge-sharing $IrO_6/RuCl_6$ octahedra create 90^o superexchange bonds. The effective interaction axis on each iridium bond is perpendicular to the iridium-oxygen plane encompassing the superexchange bond. Panel (d)—the first-order virtual hopping from one $\tilde{J} = 1/2$ to another $\tilde{J} = 1/2$ and back is reduced due to destructive interference. However, the hopping to neighboring $\tilde{J} = 3/2$ is allowed. The Hund's coupling J_H between two holes enforces the ferromagnetic Ising effective interaction once the upper hole comes back to the $\tilde{J} = 1/2$ level. Figure taken from Ref. [12]

zone [24].[4]

Importantly, SOC is not acting alone—iridium levels are affected by strong cubic crystal field of oxygen octahedra. Namely, the original scheme (Fig. 2.3 (e) and Fig. 2.5 (a)), later adopted and modified for the honeycomb materials, utilizes the dominant crystal field (10Dq≈ 4-3.3 eV [12] and 2-2.2 eV in the Na_2IrO_3 and α-$RuCl_3$, correspondingly[5]) to split the 5d level into empty e_g and almost filled t_{2g} level and enforce the low-spin state. Now it is time for SOC to play its important role in preparing the ground for the insulating behaviour by splitting the t_{2g} level. This can be handled by utilizing both atomic jj and LS regimes. Although the estimated SOC

[4] The reader should realize that even in $5d$ case U is still larger then SOC: realistic U was estimated as 2 eV in [24] and 1.3-1.7 eV in [10] while SOC for Ir^{4+} as 0.4-0.5 eV [10]. The point is that for $5d$ TMOs U is smaller then U for $3d$. The opposite is true for SOC.

[5] Table 1. in Ref. [10].

values for the $5d$ Ir^{4+} and $4d$ Ru^{3+} (0.4-0.5 and 0.1-0.15 eV, respectively) compared with the Hund's coupling for both materials (≈ 0.4 eV) set Na_2IrO_3 as a transition case between jj and LS regimes and α-$RuCl_3$ more as a LS case [10, 12], both schemes provide essentially the same result for the materials in question.[6]

Here we recall the general concept of pseudospins—effective degrees of freedom describing low energy physics, sufficient when the gap between the lowest energy levels and the rest of the spectrum is substantial—in the context of the atomic total angular momentum $\mathbf{J}$. Instead of taking into account the whole d subshell we argue that, since crystal-field gap is large enough to enforce the low spin state, almost filling up t_{2g} level, we are allowed to restrict the SOC considerations to t_{2g} and approximate $\mathbf{J}$ with the pseudospin $\tilde{\mathbf{J}}$. Under SOC the six-fold degenerate t_{2g} level[7] separates into half-filled $\tilde{\mathrm{J}} = 1/2$ Kramers doublet and completely filled $\tilde{\mathrm{J}} = 3/2$ Kramers quartet,[8] visible on Figs. 2.3 (c) and 2.5 (b) in electron and hole picture, respectively.

The above physics is confirmed by the density-functional theory (DFT) studies. In fact, the original Sr_2IrO_4 LDA + SOC and LDA + SOC + U calculations have shown that the $\tilde{\mathrm{J}} = 1/2$ band around the Fermi energy is tight enough to open the insulating gap with the realistic U [24]. Although the honeycomb iridate and ruthenate case was not as clear, *ab initio* calculations for the said materials have also shown the insulating gap [10, 25, 23, 27]. While the trigonal distortion of oxygen/chlorine octahedra plays some role, and in the case of α-$RuCl_3$ larger U produces more prominent gap, even after taking into account the distortions the bands around the Fermi energy are predominantly of $\tilde{\mathrm{J}} = 1/2$ character (Fig. 2.4), giving hope for the presence of Kitaev physics in these materials.

2.1.2 Jackeli-Khaliullin mechanism

We will now focus on the low-energy description of the spin-orbit assisted Mott insulators—the exchange processes for $\tilde{\mathrm{J}} = 1/2$ pseudospins on the neighboring transition-metal ions. In their seminal paper [4] George Jackeli and Ginyiat Khaliullin have shown that for an ideal case of O_h-symmetric IrO_6 octahedra setting the superexchange Ir-O-Ir angle to 90° may result in the emergence of the Kitaev model in $\tilde{\mathbf{J}}$ pseudospins. Below we describe shortly this so-called Jackeli-Khaliullin mechanism.

Since in both Ir^{4+} and Ru^{3+} cases spin-orbit coupling $\lambda \mathbf{S}\cdot\mathbf{L}_p$[9] is strong enough to enforce the formation of $\tilde{\mathbf{J}}$ pseudospins, the interactions between iridium/ruthenium ions are best described in these degrees of freedom. Both Kramers doublet and quartet are expressed in terms of spins and orbitals [4, 10, 12]:

$$\begin{aligned}
\left|\tilde{\mathrm{J}} = \frac{1}{2}, \tilde{\mathrm{J}}^z = +\frac{1}{2}\right\rangle &= \frac{1}{\sqrt{3}}\left(|d_{xy},\uparrow\rangle + |d_{yz},\downarrow\rangle + i\,|d_{zx},\downarrow\rangle\right), \\
\left|\tilde{\mathrm{J}} = \frac{1}{2}, \tilde{\mathrm{J}}^z = -\frac{1}{2}\right\rangle &= -\frac{1}{\sqrt{3}}\left(|d_{xy},\downarrow\rangle - |d_{yz},\uparrow\rangle + i\,|d_{zx}\,\uparrow\rangle\right),
\end{aligned} \tag{2.1}$$

[6] This is especially the case when solely the t_{2g}^5 configuration is considered, for which the Hund's coupling does not play any role. For more information about jj and LS regimes in the context of iridates we recommend a detailed work by Ekaterina M. Pärschke and Rajyavardhan Ray [26].

[7] three-fold orbital and two-fold spin degeneracy.

[8] When trigonal distortion of the octahedra is absent.

[9] The orbital momentum operator projected to t_{2g} subspace is related to orbital momentum operator projected to p subshell, $\mathbf{L}_{t_{2g}} = -\mathbf{L}_p$.

$$\begin{aligned}
\left|\tilde{\mathrm{J}}=\frac{3}{2},\tilde{\mathrm{J}}^z=+\frac{3}{2}\right\rangle &= \frac{1}{\sqrt{2}}\left(-\left|d_{yz},\uparrow\right\rangle - i\left|d_{zx},\uparrow\right\rangle\right),\\
\left|\tilde{\mathrm{J}}=\frac{3}{2},\tilde{\mathrm{J}}^z=+\frac{1}{2}\right\rangle &= \frac{1}{\sqrt{6}}\left(2\left|d_{xy},\uparrow\right\rangle - \left|d_{yz},\downarrow\right\rangle - i\left|d_{zx},\downarrow\right\rangle\right),\\
\left|\tilde{\mathrm{J}}=\frac{3}{2},\tilde{\mathrm{J}}^z=-\frac{1}{2}\right\rangle &= \frac{1}{\sqrt{6}}\left(2\left|d_{xy},\downarrow\right\rangle + \left|d_{yz},\uparrow\right\rangle - i\left|d_{zx},\uparrow\right\rangle\right),\\
\left|\tilde{\mathrm{J}}=\frac{3}{2},\tilde{\mathrm{J}}^z=-\frac{3}{2}\right\rangle &= -\frac{1}{\sqrt{2}}\left(\left|d_{yz},\downarrow\right\rangle - i\left|d_{zx}\downarrow\right\rangle\right),
\end{aligned} \tag{2.2}$$

where $|d_{\alpha\beta}\rangle$, α, $\beta = x$, y, z, are the t_{2g} orbitals with effective orbital quantum number $\mathrm{L}_{t_{2g}} = -\mathrm{L}_p = -1$ and $|\uparrow\rangle$, $|\downarrow\rangle$ are the $\mathrm{S}^z = \pm 1/2$ spin states. As can be seen on Fig. 2.5 (b), the pseudospin electron-density profile inherits some of the features of the orbitals it is built from and the information of the directionality is not completely lost. Below we explain that this has profound consequences for the effective models developed for different bond geometries [4].

To arrive at the effective Hamiltonian written in low energy $\tilde{\mathrm{J}} = 1/2$ degrees of freedom one should realize again that the systems in question are in principle described by the multi-band Hubbard model. As explained in the previous section, we are allowed to take the insulating limit where the on-site Coulomb repulsion U dominates over the hopping parameter t. In fact, even the moderate $U \approx 2$ eV of iridates and ruthenates easily overcomes $t \approx 0.1$-0.2 eV, as estimated from *ab-initio* calculations [10]. Because of the Mott-insulating limit the interactions between the remaining degrees of freedom such as spins, orbitals or pseudospins have to be determined by the virtual hoppings. While a very comprehensive description of this approach can be found in Refs. [8, 10], here we only shortly sketch its two versions. Both of them are based on perturbation theory with t/U as the small parameter.

One way is to first derive the spin-orbital Hamiltonian of the Kugel-Khomskii type and introduce the on-site spin-orbit coupling afterwards. The crucial issue is to produce an intermediate state with two spin holes at one site. For example, if we consider d_i^5-d_j^5 configurations at the transition-metal sites i, j the intermediate state would have been d_i^4-d_j^6 configurations. The virtual spin-hole hoppings from the d_i^5-d_j^5 bond through this intermediate state and back to d_i^5-d_j^5, utilizing also the indirect paths through oxygens, would produce the exchange interactions forming the Kugel-Khomskii Hamiltonian. Of course some of these processes would be excluded because of the Pauli principle, others would give zero contribution because of the destructive interference [4, 12]. The remaining ones would be ordered by the energy they cost. Once the importance of the processes is determined and the series is truncated we can move to the final step of obtaining the effective Hamiltonian—projecting the Kugel-Khomskii expression onto the lowest part of SOC spectrum—the Kramers doublet.[10]

The other approach starts already with the effective pseudospins, i.e. firstly includes on-site spin-orbit coupling and then takes into account the Hubbard U. At the beginning we have one hole at the $\tilde{\mathrm{J}} = 1/2$ level at each site. Such a hole can hop to the Pauli-principle allowed levels on the neighboring sites, including the $\tilde{\mathrm{J}} = 3/2$ and higher levels (Fig. 2.3 (e)) and hop back to the $\tilde{\mathrm{J}} = 1/2$ level. As determined in [4], the first order t^2/U term contains the isotropic Heisenberg contribution. This is exactly the case for Sr_2IrO_4, for which the 180° Ir-O-Ir bond has one unique superexchange path and the process involving $\tilde{\mathrm{J}} = 1/2$ on both iridium sites produces the Heisenberg term in the effective Hamiltonian. However, due to the previously mentioned directionality in the electronic profiles of the pseudospins, for the honeycomb materials with edge-sharing $IrO_6/RuCl_6$ octahedra such-originated Heisenberg term will not survive. Namely, as seen in Figs. 2.5 (c) and 2.6 (d), there are two superexchange paths available in the 90°

[10] We will be utilizing this approach in Chapter 5.

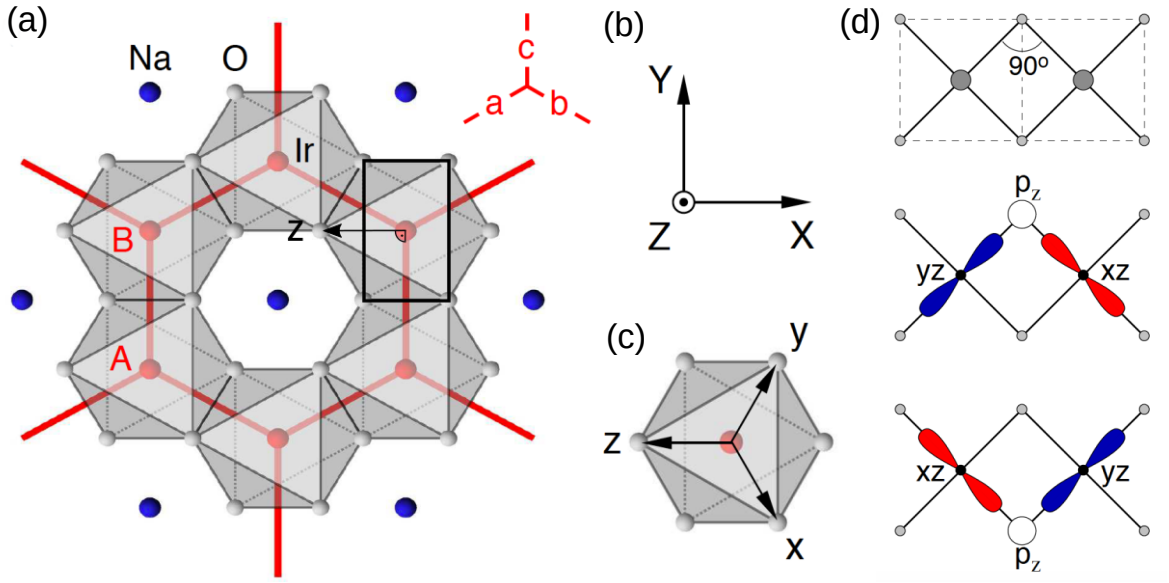

FIGURE 2.6: Panel (a)— top view of $NaIr_2O_6$ plane in Na_2IrO_3. Three types of bonds in the iridium-based honeycomb lattice are denoted by letters a, b, c. Kitaev interaction axis for bond c is perpendicular to the Ir-O-Ir plane (black rectangle) and is marked by z. Kitaev interaction axes for all three bonds meeting at the iridium site are perpendicular to each other, coinciding with the frame related to the cubic symmetry of the octahedron. The top view on such a frame is shown in panel (c). Panel (b)—XYZ frame, in which X and Y axes lie in the honeycomb plane while the Z axis points perpendicularly towards the reader. Panel (d)-edge-sharing oxygen octahedra enforce 90°-geometry of the Ir-O-Ir bond. Below, orbitals participating in the oxygen-assisted hoppings in the said geometry are shown. Panels (a)-(c) taken and modified from Ref. [9], panel (d)—from Ref. [4].

geometry of the Ir-O-Ir / Ru-Cl –Ru bond. The virtual hoppings concerning only $\tilde{J} = 1/2$ in the intermediate (virtual) Ir/Ru states will cancel each other (distructive interference) but the next-order $t^2 J_H/(U^2)$ term will be non zero. Fig. 2.5 (d) illustrates the origin of this higher-order term. A hole hops from $\tilde{J} = 1/2$ on site i to the $\tilde{J} = 3/2$ on site j. At this point, with two holes on site i, the Hund's interaction J_H ensures ferromagnetism and *Isingness* of the effective interaction once the hole returns to its original site [12].

In this way a ferromagnetic Ising term is created at each bond ij, but the orientation of the Ising pseudospins depends on the direction of the bond. Namely, the interaction axis on each bond is perpendicular to the Ir-O-Ir plane setting the bond (Fig. 2.5 (c)). For a better understanding the reader may imagine it on the example of bond c in Fig. 2.6 (a). First one identifies the two oxygens mediating superexchange processes for the bond. Those two oxygens and two iridium sites form the Ir-O-Ir plane (black rectangle). Now, starting from one of the iridium sites one draws a vector perpendicular to the Ir-Ir bond leading to one of the other oxygens outside the plane. We chose the oxygen to the left, lying above the honeycomb lattice. This is the direction of the z axis for the $\tilde{J}_i^z \tilde{J}_j^z$ interaction in $\tilde{J} = 1/2$ pseudospins on bond c. The effective interactions on the a and b bonds can be obtained by a cyclic permutation.

The careful reader might have also noticed that for each iridium site, where all three bonds meet, the axes of these anisotropic interactions are perpendicular to each other. Fig. 2.6 (c) presents the top view on the orthogonal frame formed in this way, coinciding with the cubic frame of oxygen octahedron. Here we draw the reader's attention to the unusual position of the cubic frame. Contrastingly to the well known perovskite transition-metal oxides, where the cubic axes are parallel to the bonds[11] [28], in the honeycomb iridates and ruthenates the oxygen/chlorine octahedra share edges. Thus, cubic frame is rotated up by $\alpha \approx 35.26°$ from the honeycomb

[11] In an ideal case.

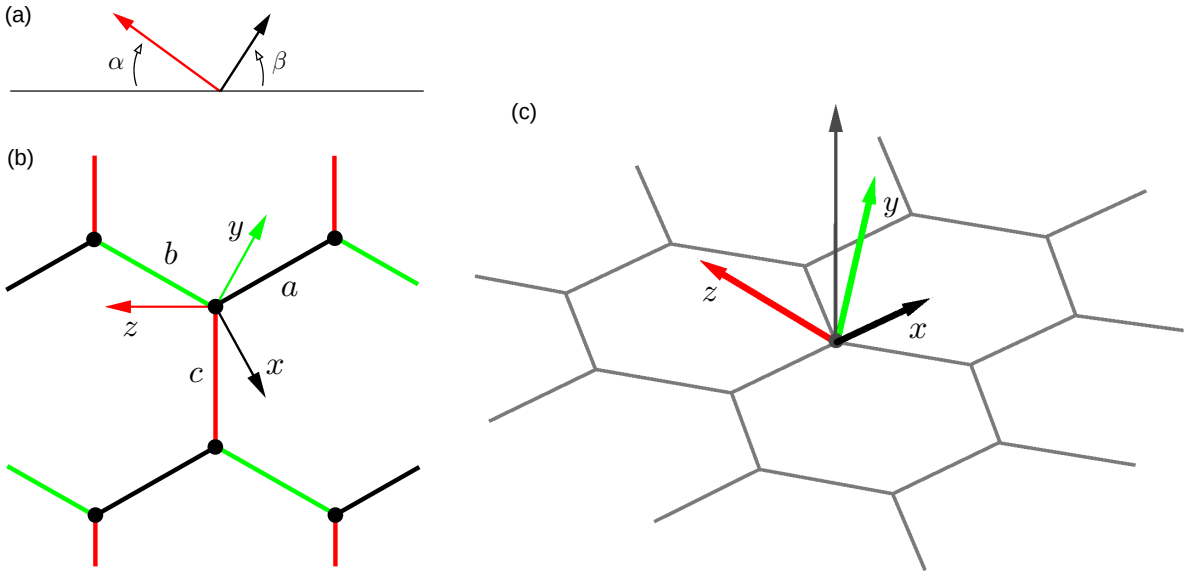

FIGURE 2.7: Arrangement of the Kitaev cubic frame derived for honeycomb iridates and ruthenates. For each bond direction on the honeycomb lattice the suitable Ising-like term $S_i^\gamma S_j^\gamma$ is being assigned, where $\gamma = x, y, z$. As a result each bond is associated with one γ axis. In the Kitaev model derived for iridates and ruthenates those axes have to be rotated up from the honeycomb plane by $\alpha \approx 35.26°$, forming an orthogonal frame identical to the cubic frame of the octahedra. As a result, each γ axis is perpendicular to the suitable bond. Panel (a) demonstrates the projection of the Kitaev axes to the XZ plane, panel (b)—the projection to the honeycomb plane and panel (c)—3D view on the axes. For convenience panel (a) contains also β angle from the honeycomb plane to xy plane ($\beta \approx 54.7°$). The colors of respective axes and bonds are matched to illustrate the common convention $S_i^x S_j^x \to a$, $S_i^y S_j^y \to b$, $S_i^z S_j^z \to c$.

plane containing the Ir-Ir/Ru-Ru bonds. While spotting the orthogonality of the frame may not be easy due to its particular relative position to the honeycomb lattice, Fig. 2.7 provides the projection of the interaction axes to the honeycomb plane and to the vertical XZ plane[12], to further help with the task.

Altogether the anisotropic effective interactions form precisely the famous Kitaev model, due to the different Ising form of each of them *and* the orthogonality relation between the interaction axes. In order to emphasise the orthogonality relation and the unusual position of the interaction axes we will call the *xyz* frame the *Kitaev cubic frame* from now on. In this way the authors of Ref. [4] demonstrated how to apply the exciting Kitaev physics, discussed in the next section, into the transition-metal compounds.

2.2 Kitaev model

The Kitaev model was originally introduced by Alexei Kitaev as an anisotropic spin 1/2 model on the honeycomb lattice [7]. The Ising-like nearest-neighbor interactions $S_i^\gamma S_j^\gamma$, $\gamma = x, y, z$, forming the Hamiltonian

$$\mathcal{H}_{Kitaev} = \sum_{\langle i,j\rangle \perp \gamma} K_\gamma S_i^\gamma S_j^\gamma \tag{2.3}$$

are different for each a, b or c direction of the lattice (Fig. 2.7). Crucially for the Kitaev model, on each site the interaction axes γ from the three surrounding bonds form an orthogonal frame. As mentioned in the previous section, for the version of the model derived for honeycomb iridates and ruthenates these orthogonal axes coincide with the frame related to the cubic symmetry of

[12] XYZ frame is introduced on Fig. 2.6.

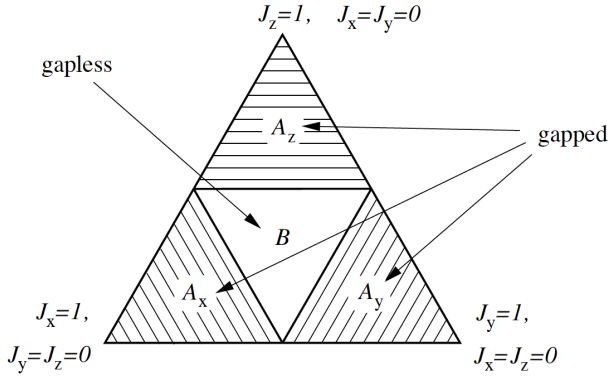

FIGURE 2.8: The phase diagram of the Kitaev model. Here J_γ correspond to K^γ in our notation ($\gamma = x$, y, z). In the A_γ regions of the diagram, where one of the coupling constants dominates over the sum of two others, the ground state is a gapped (topological) Kitaev spin liquid, while in the central region B the spin liquid is gapless. Figure taken from Ref. [7].

oxygen/chlorine octahedra. Namely, this Kitaev cubic frame has its axes always perpendicular to the suitable bonds, rotated up by $\alpha \approx 35.26°$ from the honeycomb plane (Fig. 2.7 (a)).[13]

The Kitaev model drove enormous interest because of the implied possibility of a realisation of qubits via special non-local quasiparticles, supported by the model, that could form a stable quantum memory[14]. Namely, when one of the coupling parameters K_γ is significantly larger then the two others, the system is gapped (Fig. 2.8). The gap protects the excitations building the topological qubits and guarantees resilient memory. When the K_γ parameters are of similar size, the spectrum is gapless, and the excited states become fragile. Acting with magnetic field can however restore the gap even in this case [7]. In this thesis we will be focusing on a symmetric case of the model, with the same coupling parameter K for all directions:[15]

$$\mathcal{H}_{Kitaev} = K \sum_{\langle i,j\rangle \perp \gamma} \mathrm{S}_i^\gamma \mathrm{S}_j^\gamma \tag{2.4}$$

2.2.1 Kitaev spin liquid

The extremely valuable feature of the Kitaev model is its exactly known quantum spin-liquid ground state. In a nutshell, a quantum spin liquid is a highly entangled state whose quantum spatial entanglement[16] shapes it into a massive superposition of different spin configurations [30]. Because of its form it is robust against the local perturbations which can only effectively permute its terms, thus preserving the superposition [30]. Moreover, quantum spin liquid supports non-local, fractional excitations which can only appear in pairs [7, 30, 12]. Painting an even simpler

[13] Because of this symmetric location in relation to the lattice, the 90° angle between the axes is distorted in the top view on the lattice.

[14] Due to the topological protection from decoherence.

[15] The positive (antiferromagnetic, AF) and negative (ferromagnetic, FM) values of K give the same energy values and absolute values of the correlations. In fact, the AF and FM Kitaev models are connected by the unitary transformation [7]: starting from the two sublattices of the AF case, where site i belongs to sublattice A and all its nearest neighbors j belong to sublattice B, we have $\tilde{\mathrm{S}}_i^\gamma = +\mathrm{S}_i^\gamma$, $\tilde{\mathrm{S}}_j^\gamma = -\mathrm{S}_j^\gamma$. Inserting the operators $\tilde{\mathrm{S}}^\gamma$ into Hamiltonian (2.4) produces $-K\sum_{\langle i,j\rangle \perp \gamma} \tilde{\mathrm{S}}_i^\gamma \tilde{\mathrm{S}}_j^\gamma$ —the FM case. Thus the observables calculated for the pure model can be translated from one case to the other.

[16] A purely quantum feature binding the results of the measurement on one subsystem to the results of the measurement of the other subsystem. The entanglement is inherently connected to the quantum superposition and quantum fluctuations and is extensively discussed in Chapters 4 and 5.

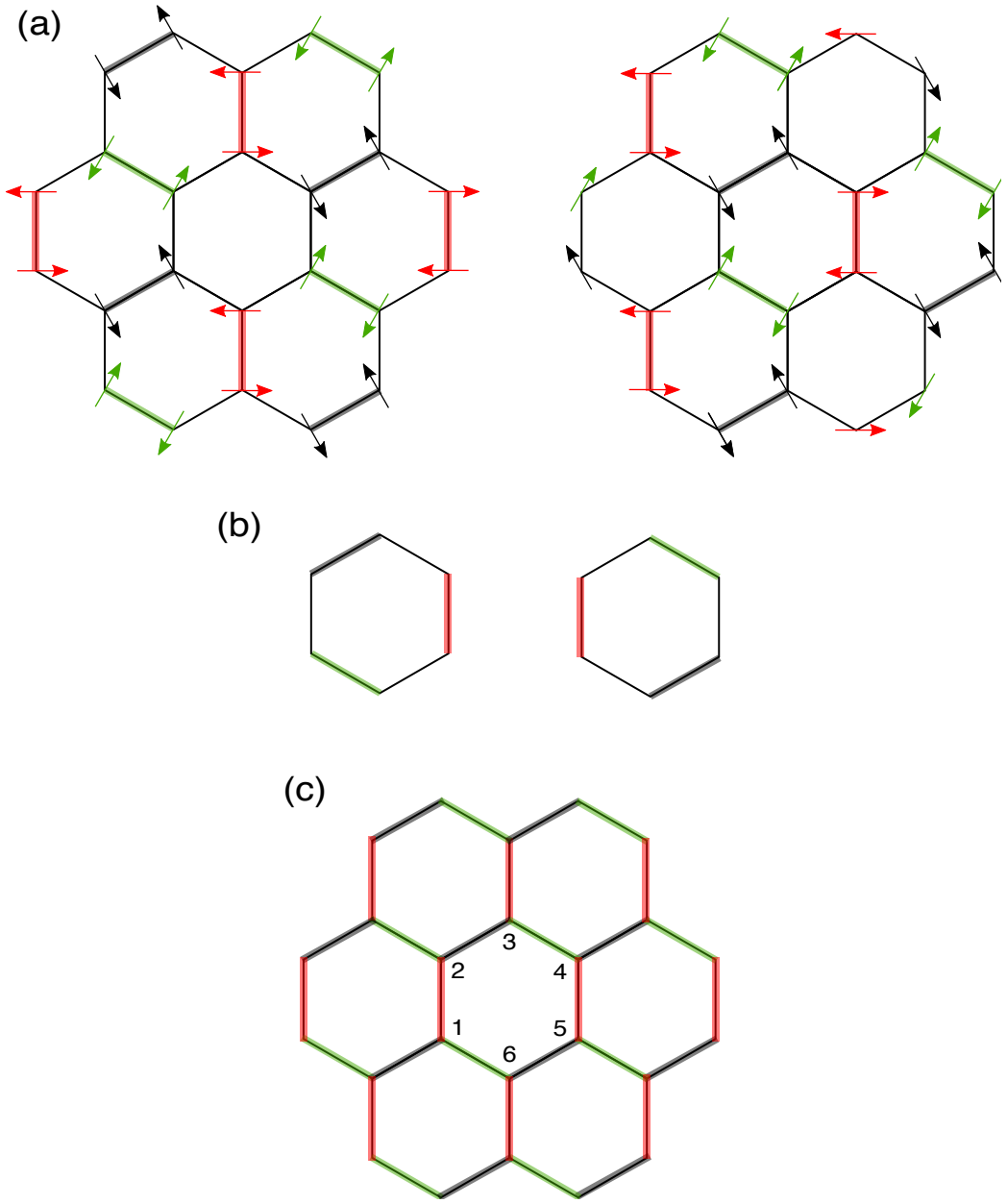

FIGURE 2.9: Structure of the antiferromagnetic Kitaev spin liquid (AF KSL) demonstrated on a 24-site symmetric cluster. Panel (a) provides two examples of the classical spin patterns, with the right pattern translated by one hexagon compared to the left one. The arrows aligned along the $\gamma = x$, y, z directions (cf. Fig. 2.7) are here projected to the honeycomb plane. [For a more complete picture we recommend seeing panels (a) and (b) of Fig. 1 in Ref. [12] and Fig. 8 in the Appendix A of the Ref. [29].] Starting from the outer hexagons on the left pattern only three bonds can have the lowest energy satisfying Kitaev interaction, while three other bonds are not optimized. Such an arrangement results in the central hexagon being satisfied only on the outer bonds. Since the Kitaev spin liquid is a superposition of the above and many similar patterns, all bonds are being satisfied by virtue of quantum superposition. We may imagine the two cases of optimized bonds (panel (b)) being summed up to form a fully optimized spin liquid in panel (c). In fact, the last panel presents the non-zero nearest-neighbor correlations of the Kitaev spin liquid. They form short-range magnetic pattern: $\langle \mathrm{S}_i^x \mathrm{S}_j^x \rangle \neq 0$ on bonds in direction a (black color), $\langle \mathrm{S}_i^y \mathrm{S}_j^y \rangle \neq 0$ on bonds b (green color) and $\langle \mathrm{S}_i^z \mathrm{S}_j^z \rangle \neq 0$ on bonds of type c (red color). This is a characteristic feature making the ground state a special case of spin liquid. Sites 1, ...,6 of the central hexagon are taken into account in the plaquette invariant $\langle \mathrm{W}_p \rangle$ enabling to monitor the topological features, see the main text.

and perhaps naive picture, a crystal still has ordered structure, but the magnetic[17] correlations are short-range only, similarly to the short range interactions in a proper liquid state [31]. In general, quantum spin liquids are typical for 1D systems, where enormous quantum fluctuations usually rule out the magnetic order, and are more difficult to find in higher dimensions.

Following Ref. [12], we first mention a basic example of a 2D quantum spin liquid: the resonating valence bond (RVB) state, introduced as an ansatz for the ground state of the Heisenberg model on the geometrically frustrated kagome and triangular lattices [32]. This frustration can be intuitively understood on the triangular lattice, where it is impossible to construct the classical Néel state, since there is always one site on a triangle which "does not know" how to polarize. The two available options leave one bond unsatisfied, rising the energy. Although the true ground state turned out to be an ordered state acquired by breaking the rotational symmetry of the Heisenberg model by spin polarization differing by 120° between the sites, the RVB state poses an interesting alternative. One could imagine the RVB state as a superposition of patterns of singlets (valence bonds) for which the rotational symmetry is preserved. In each such pattern each singlet is surrounded by the unsattisfied ("unhappy") bonds with zero exchange energy gain [12]. The superposition of singlet patterns ensures a liquid-like fluctuating behavior. In the RVB case the non-local excitations are $\Delta S = 1/2$ spinons. The hypothesised RVB state on the frustrated 2D lattices could be detected by the continuum seen in the dispersion plots,[18] characteristic for 1D Heisenberg spinons. Such picture contrasts with the sharp dispersion curve of the $\Delta S = 1$ magnons expected in 2D, because in the RVB case the magnon decomposes or *fractionalizes* into a pair of spinons [12, 1].

Keeping the well known picture of the RVB state in mind, let us examine which features make the ground state of the Kitaev model a magnetic quantum liquid, following Refs. [12, 30, 31]. In the Kitaev model the frustration on each site is generated by the three conflicting orthogonal interaction axes γ coming from the three bonds meeting at the same site. This frustration is preventing all bonds to be satisfied at once, leading in the classical limit to an infinite degeneracy of the ground state. Namely, there are infinitely many ways to distribute the "happy" bonds, see Fig. 2.9 (a). In each such term the spins arrangement on the "happy" bonds is optimized to the Ising solution in the direction dictated by the γ axis.[19] This can only be done on 1/3 of the bonds,[20] leaving the others unoptimized, similarly to the RVB case [12]. Once we let spins to be fully quantum, the degeneracy is lifted by the formation of a massive superposition of such terms. We can qualitatively imagine the above process by starting with the two patterns in Fig. 2.9 (a) and focusing on how the two possibilities of optimized bonds for a single hexagon [Fig. 2.9 (b)] are being merged to form the characteristic pattern of the nearest-neighbor correlations [Fig. 2.9 (c)]: $\langle S_i^x S_j^x \rangle \neq 0$ on bonds in direction a (black color), $\langle S_i^y S_j^y \rangle \neq 0$ on bonds b (green color) and $\langle S_i^z S_j^z \rangle \neq 0$ on bonds of type c (red color). For the Kitaev spin liquid (KSL) only those nearest-neighbor correlations mimicking the arrangement of the terms in Hamiltonian (2.4) are non-zero.

To have some rough idea how A. Kitaev derived this beautiful exact solution and to see what kind of non-local excitations are supported by KSL, one has to use the slave-particle[21] formalism, which would be of fermionic nature in this case [30, 12]. We take four species of fermions b_i^γ, c_i, with $\gamma = x, y, z$ and the usual fermionic properties

$$\{c_i, c_j^\dagger\} = \{b_i^\gamma, b_j^{\gamma\dagger}\} = \delta_{ij},$$

[17] Spin correlations if the model is applied to spins, pseudospin correlations if the model is applied to effective degrees of freedom.

[18] Spin dynamical structure factor.

[19] One can see it by minimizing classical energy.

[20] On infinite lattice or a cluster with periodic boundary conditions and properly handled double counting.

[21] parton

$$\{c_i^\dagger, c_i^\dagger\} = \{c_i, c_i\} = \{b_i^{\gamma\dagger}, b_i^{\gamma\dagger}\} = \{b_i^\gamma, b_i^\gamma\} = 0, \tag{2.5}$$

along with the unusual ones

$$b_i^{\gamma\dagger} = b_i^\gamma,$$
$$c_i^\dagger = c_i, \tag{2.6}$$

making them so-called Majorana fermions. We translate the spin components into new degrees of freedom according to the recipe

$$\mathrm{S}_i^\gamma = \frac{i}{2} b_i^\gamma c_i \tag{2.7}$$

with an additional constraint $b_i^x b_i^y b_i^z c_i = 1$ to keep the original amount the information.[22] The new Hamiltonian emerges as

$$\mathcal{H}_{Kitaev} = \frac{1}{4} \sum_{\langle i,j\rangle \perp \gamma} K_\gamma b_i^\gamma b_j^\gamma c_i c_j. \tag{2.8}$$

Because the bond operators $u_{ij} = b_i^\gamma b_j^\gamma$ with the eigenvalues $\pm i$ commute with Hamiltonian (2.8), they share with it the eigenbasis,[23] constitute the conserved quantities [30, 12] and set the good quantum numbers for the system. Moreover, one can construct more complex integrals of motion via a product of u_{ij} over each hexagonal plaquette

$$\mathrm{W}_p = 2^6\ \mathrm{S}_1^x\ \mathrm{S}_2^y\ \mathrm{S}_3^z\ \mathrm{S}_4^x\ \mathrm{S}_5^y\ \mathrm{S}_6^z = u_{12}^z u_{23}^x u_{34}^y u_{45}^z u_{56}^x u_{61}^y, \tag{2.9}$$

where we take a suitable spin component S_i^γ compatible with the outer bonds and u_{ij}^γ compatible with the bonds building the hexagon [7, 30] [Fig. 2.9 (c)]. Since there is only one plaquette operator on each hexagon and it has two eigenvalues differing only by sign (± 1), the Z_2 symmetry they represent is conserved by the Hamiltonian because of the commutation relation. It is convenient to order the energies of the Kitaev Hamiltonian according to the set of those conserved eigenvalues over (a considered cluster of) honeycomb lattice. It turns out that the ground state is characterized by the set

$$\{+1, +1, +1, ..., +1\}. \tag{2.10}$$

In other words: all plaquettes give $+1$ [30, 12]. Utilizing the eigenvalues of u_{ij} [12] one obtains the dispersion relation for the c_i fermions. The obtained Dirac-type spectrum is gapless for the isotropic or weakly anisotropic set of K^γ and gapped for $K^\alpha > |K^\beta + K^\gamma|$, α, β, $\gamma = x$, y, z [7, 12] (Fig. 2.8).

Fingerprints of the Kitaev spin liquid in experiments

To know what to look for in the candidate materials one has to simulate the response of the ideal Kitaev system to the experimental probes. Firstly, we focus on the fractionalization of spins into Majorana fermions. The *a priori* artificial transformation (2.7) applied to the Kitaev Hamiltonian creates fractional excitations: the b_i^γ fermions, frozen by the conservation of u_{ij}, and the c_i fermions which can propagate because they are not bound by the conservation law [12]. Thus, the spin really fractionalizes into stationary and itinerant fermions. Moreover, the emergence of the stationary fermions leads to the non-local excitations as the u_{ij} operator gives contribution to *two* plaquette operators on the hexagons sharing the ij bond [30, 12]. Following Ref. [30], we may imagine a non-local excitation as a defect plaquette with the eigenvalue -1. In literature such an object is called a flux or a vison [12]. The non-locality here means that one cannot create a single excitation of that type in the magnetic scattering experiments because

[22] The same size of the Hilbert space.
[23] u_{ij} commute also with one another.

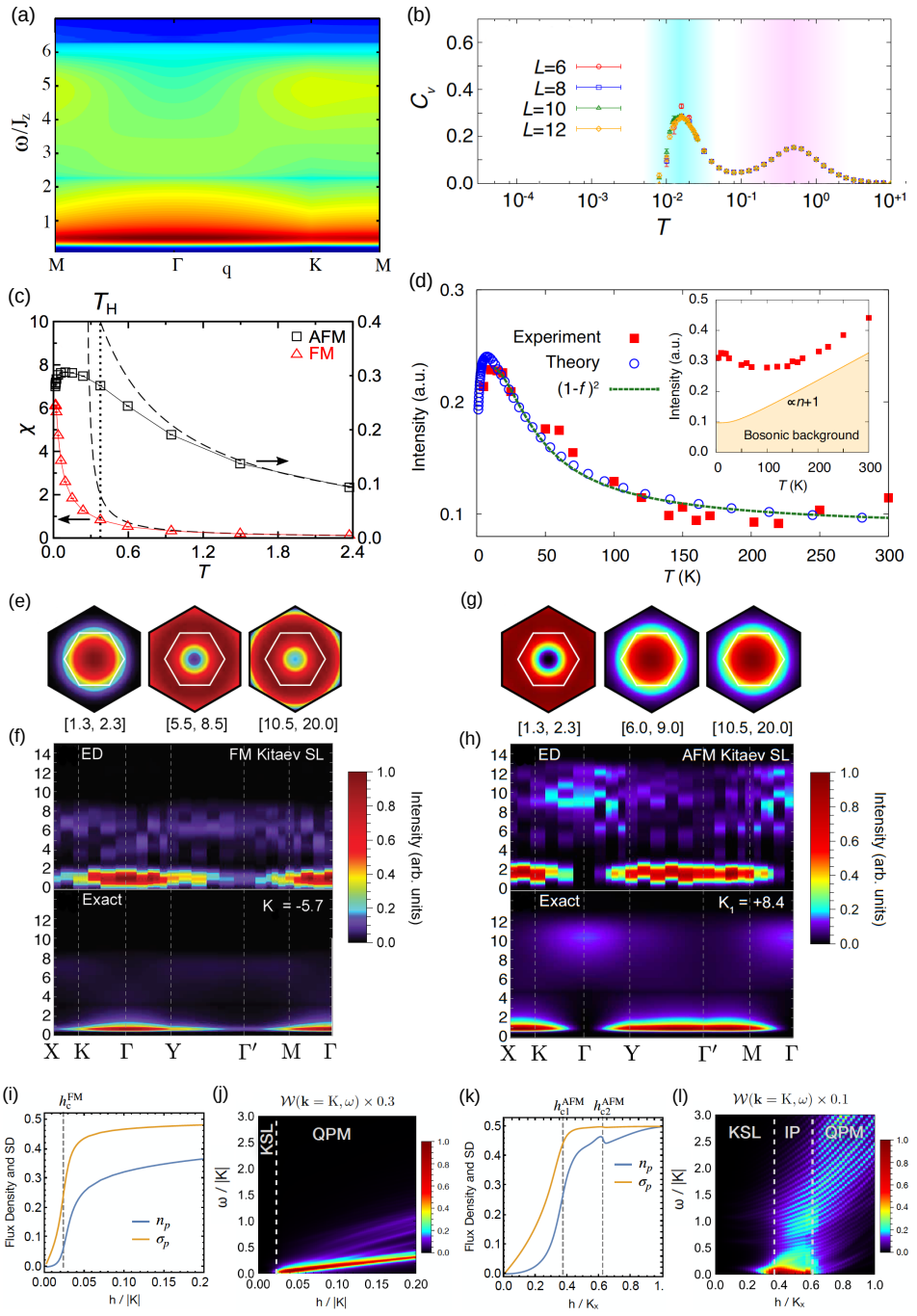

FIGURE 2.10: The response of the FM and AF isotropic Kitaev model (2.4). FM case: (a) —the exact dynamical spin structure factor; (b)—the specific heat (QMC); (c)—the static magnetic susceptibility $\chi(T)$ (CDMFT+CTQMC, FM and AF cases), with the asymptotes of the Curie-Weiss behaviour (dashed lines); (d)—the integrated Raman intensity (QMC on 20 sites, blue circles) and the experimental intensity for α-$RuCl_3$ within 5-12.5 meV (red squares). FM and AF cases: (e), (g)—1st BZ maps of the INS intensity $I(\mathbf{k},\omega)$ integrated over energy range noted below each map [meV] for the FM and AFM model, correspondingly; (f), (h)—$I(\mathbf{k},\omega)$. [The vertical energy axis in meV (ED and LSWT).] The evolution in external magnetic field *perpendicular* to the honeycomb plane (ED): (i), (j)—Z_2-flux density $\hat{n}_p$, its standard deviation σ_p and the dynamical Z_2-flux structure factor $W(\mathbf{k},\omega)$ at $\mathbf{k}$=K for the FM model; (k),(l) the same for the AF gapless model with a small K^γ anisotropy. Panels taken and modified from Refs.: (a)—[33], (b)—[34], (c)—Ref. [35], (d)—[36], (e)-(h)— [37], (i)-(l)—[38].

exciting one spin effectively excites two plaquettes via fractionalization [12]. The excited state with two defect plaquettes would automatically fall into different sector than the ground state because -1 would appear twice in the set of conserved plaquette eigenvalues. The resulting two-flux gap appears in the simulated response of the Kitaev system in inelastic neutron scattering (INS) in the dynamical spin structure factor[24] calculated exactly [33] [Figs. 2.10 (a) , (f), (h)] and via the exact diagonalization [Figs. 2.10 (f), (h)]. In other words: while in the gapped KSL in Fig. (2.8) there is a finite gap separating the ground state from all other states, in the gapless KSL the ground state is connected to the gapless c-fermion excitations but separated from the flux excitations by the two-flux gap.[25] KSL response in Figs. 2.10 (a), (f), (h) reveals flat and intense low-energy bands for certain momentum values and much weaker continuum in higher energies. The integer-spin collective excitations (magnons) are not visible due to their fractionalization [37].

Several other manifestations of fractionalisation of the physical quantities are possible. Special features specific to the localized or itinerant fermions may appear for different temperatures for the two species. Exactly this was considered in the specific heat C_v for the isotropic Kitaev model (2.4) simulated by the quantum Monte Carlo (QMC) method for various cluster sizes. The low-temperature peak shown in Fig. 2.10 (b) is related to the localized Majorana fermions while the high-temperature peak corresponds to the itinerant fermions [34, 12].

As explained earlier, the liquid state emerges from the strong frustration. This can be seen in Fig. 2.10 (c), where the numerical predictions for the static spin susceptibility $\chi(T)$ in both ferromagnetic and antiferromagnetic Kitaev model are presented. For low enough temperatures the susceptibility deviates from the Curie-Weiss mean-field curves (dashed lines), hinting at the frustration and strong quantum effects.

It should be kept in mind that ultimately we are interested in the true gapped phase [7] which stabilizes the non-local flux excitations and therefore is essential for considering stable topological qubits. Although the model derived by G. Jackeli and G. Khaliullin for the honeycomb iridates is isotropic in K^γ and thus gapless, accessing the desired gapped phase is theoretically possible by introducing a perturbation breaking the time-reversal symmetry such as the external magnetic field or more difficult to engineer second-nearest neighbor term [7, 12, 30]. Following Ref. [38], let us here consider the response of Kitaev model to a uniform magnetic field perpendicular to the honeycomb plane. Specifically, we will be following the quantities allowing us to observe the fractionalization more directly: the average value uf the Z_2-flux density

$$\langle \mathrm{n}_p \rangle = \frac{1}{2} \left(1 - \langle \mathrm{W}_p \rangle\right), \tag{2.11}$$

as well as its standard deviation σ_p, monitoring the variations of n_p, and the dynamical Z_2-flux structure factor $\mathrm{W}(\mathrm{K}, \omega)$—i.e. the dynamical correlation of the Fourier transforms of the plaquette operators. While a small magnetic field keeps the flux density at low values close to $\frac{1}{2}\left(1 - \langle +1 \rangle\right) = 0$ obtained for no-field case of the stationary fluxes, a higher field leads to a phase transition into the partially polarized quantum paramagnet (QPM) in the FM Kitaev case [38]. AF Kitaev model behaves differently in the stronger field due to the incompatibility of the AF nearest-neighbor configurations in the liquid state with the FM configurations of the polarized state preffered by the high field [38]. Similarly to the AF Heisenberg case the field has to rotate the antifferomagnetically arranged spins, but because of the frustration the path to the polarized state may be complicated and contain intermediate phases [1]. Namely, the simulations presented in Ref. [38] indicate the presence of the intermediate phase (IP) characterised by the strong low-energy response of $\mathrm{W}(\mathrm{K}, \omega)$.

[24] Proportional to the INS cross section.

[25] If the full spectrum was plotted, including the sectors invisible to spin dynamical observables of INS: ground-state and c-fermion excitations, the gap would be filled.

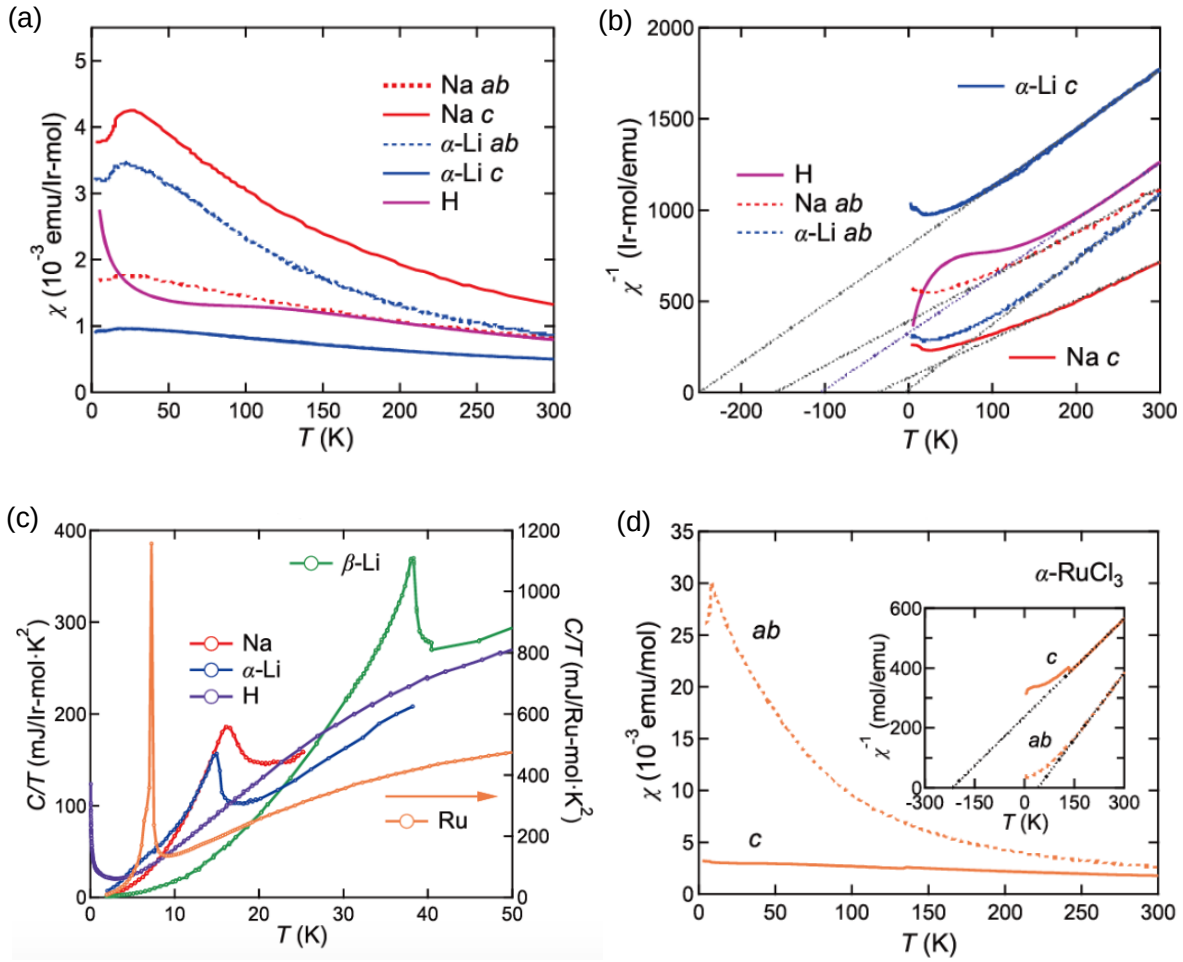

FIGURE 2.11: Experimental magnetic and thermodynamic characteristics of several honeycomb spin-orbit assisted Mott insulators: panel (a)—static magnetic susceptibility $\chi(T)$ for Na_2IrO_3, α-Li_2IrO_3 and $H_3LiIr_2O_6$ measured under the magnetic field in the honeycomb plane (ab =XY) and along out-of-plane (c =Z) direction; panel (b)—$\chi^{-1}(T)$ and the asymptotic Curie-Weiss (black dotted) lines for the same materials; panel (c)—specific heat $C(T)$ measured for Na_2IrO_3, α-Li_2IrO_3, β-Li_2IrO_3, $H_3LiIr_2O_6$ and α-$RuCl_3$; panel (d)—$\chi(T)$ and $\chi^{-1}(T)$ with the asymptotic Curie-Weiss lines (inset) for α-$RuCl_3$; all panels taken and modified from Ref. [12]

2.3 Magnetic state of the honeycomb iridates and ruthenates

It has turned out that the real materials display both the features of long-range magnetic order (LRO) and strong frustration related to the bond anisotropy expected for the Kitaev system. Below we attempted to present a realistic picture of the complex magnetism of the honeycomb materials.

A technical note: following the common custom in the field of the Kitaev-like models we simplify $\tilde{J}_i^\gamma \tilde{J}_j^\gamma$ *to* $S_i^\gamma S_j^\gamma$*, as in the original Kitaev model. Nevertheless we keep the name* $\tilde{J}$ *when referring to the pseudospin as a quantum number in some cases, e.g.* in the context of $\tilde{J} = 1/2 \longleftrightarrow \tilde{J} = 3/2$ *hopping. At the same time we keep the name "pseudospin" insdead of "spin" whenever possible. This seemingly unnecessary complication sets the pseudospins* $\tilde{\mathbf{J}}$*, leading in the strong spin-orbit coupling limit to the Kitaev physics, in a more general context encompassing also Chapters 4 and 5, where both spins and effective pseudospins will be utilized and the interpolation between strong and weak spin-orbit coupling will be discussed.*

2.3.1 Fingerprints of the magnetic order

We start with the evidence of the LRO in Na_2IrO_3 and α-$RuCl_3$. As can be seen in Figs. 2.11 (a) and (d), the low-temperature kinks in the magnetic susceptibility $\chi(T)$ indicate the LRO with at least some of the relations between the magnetic moments being antiferromagnetic[26] and set the Néel temperature T_N[27] at 13-18 K for Na_2IrO_3 and 7-14 K for α-$RuCl_3$ [10, 12].[28] The transition is independently confirmed by a pronounced anomaly in the specific heat, visible around T_N [Fig. 2.11 (c)] [12].

2.3.2 Fingerprints of the Kitaev physics

Despite the LRO, signatures of strong frustration are also present in these materials. Comparing the $\chi(T)$ predictions for the Kitaev model [Fig. 2.10 (c) with Fig. 2.11 (a), (b) and (d)], where Curie-Weiss asymptotes are plotted in χ^{-1} regime, we notice some resemblance of the real materials' susceptibility curves to the ideal Kitaev ones. In both model and material cases the deviation from the Curie-Weiss mean-field magnetic susceptibility is well visible, allowing for an estimate of the upper range of the magnetic interactions at 100-200 K [12]. Hence, in both Na_2IrO_3 and α-$RuCl_3$ the module of the Weiss temperature $|\Theta|$ is much larger than T_N, which is one of the simplest expermental fingerprints of the strong frustration [1].

Notably, the materials in question display strong magnetic anisotropy ($\chi^{c=\mathrm{Z}} \gg \chi^{ab=\mathrm{XY}}$ for Na_2IrO_3 and $\chi^{ab=\mathrm{XY}} \gg \chi^{c=\mathrm{Z}}$ for α-$RuCl_3$) in low temperatures. Moreover, Θ estimates also strongly depend on the direction of the magnetic field, changing sign from the AF to FM one in the α-$RuCl_3$, or even reach infinitesimal values, signalling cancellation of different interactions. The complex situation wrapped up in Table 1. of Ref. [12] suggests sensitivity of the interactions to the details of the electronic structure. The standing out feature here is the directional anisotropy of Θ and χ hinting at some bond-anisotropy in the interactions [12].[29]

The latter was further investigated by B. J. Kim's group via the diffuse magnetic X-ray scattering, which brought direct evidence of the dominant bond-directional interactions in Na_2IrO_3 [39]. Namely, the reciprocal-space pseudospin-pseudospin correlations $\langle \mathrm{S}^{\gamma}_{\mathbf{q}} \mathrm{S}^{\gamma}_{\mathbf{-q}} \rangle$ recovered from the dynamical spin structure factor show the directional dependence. For example, following the green line in Fig. 2.12 (d), corresponding to $\langle \mathrm{S}^{x}_{\mathbf{q}} \mathrm{S}^{x}_{\mathbf{-q}} \rangle$ correlation, one can see that the maximal intensity of this correlation is confined to $\Psi \in [180, 300]^{\circ}$. Cyclic rotation by 120° leads to the maximum in $\langle \mathrm{S}^{y}_{\mathbf{q}} \mathrm{S}^{y}_{\mathbf{-q}} \rangle$ [yellow line] and further to the maximum in $\langle \mathrm{S}^{z}_{\mathbf{q}} \mathrm{S}^{z}_{\mathbf{-q}} \rangle$ [blue line]. Since at each site of the honeycomb lattice bonds are spread by 120°, it proves that the most prominent magnetic interactions in Na_2IrO_3 are bond-anisotropic [39]. Although the Kitaev interaction seems to be the largest of them, as it will be explained later, there are other anisotropic interactions that influence the direction of the magnetic moment [39].

The diffuse magnetic X-ray scattering provides more comprehensive understanding of the frustration in Na_2IrO_3: although the ground state of the material is not Kitaev spin liquid, the long range order survives only at the lowest temperatures. While the dominant Kitaev magnetic interaction is not strong enough to enforce fully liquid massive superposition, it is still powerful enough to keep a remnant of this state, the superposition of the ordering patterns above the Néel temperature [39].

Frustration and anisotropic behaviour were also searched for in α-$RuCl_3$. Inelastic neutron scattering (INS) [40, 41] and THz spectroscopy [42] experiments revealed an interesting continuum of excitations above the low-energy $\Delta \mathrm{S} = 1$ magnon appearing below T_N. Upper subpanel of the Fig. 2.13 (e) shows both the experimentally observed magnon and the continuum above it.

[26] See Fig. 6.13 in Ref. [1] for purely antiferromagnetic case.

[27] Here we follow the popular convention to call the ordering temperature for the phase containing some antiferromagnetic component T_N.

[28] Strong sample dependency [10, 12].

[29] This anisotropy suggests the presence of anisotropic interactions more complex then Kitaev [10].

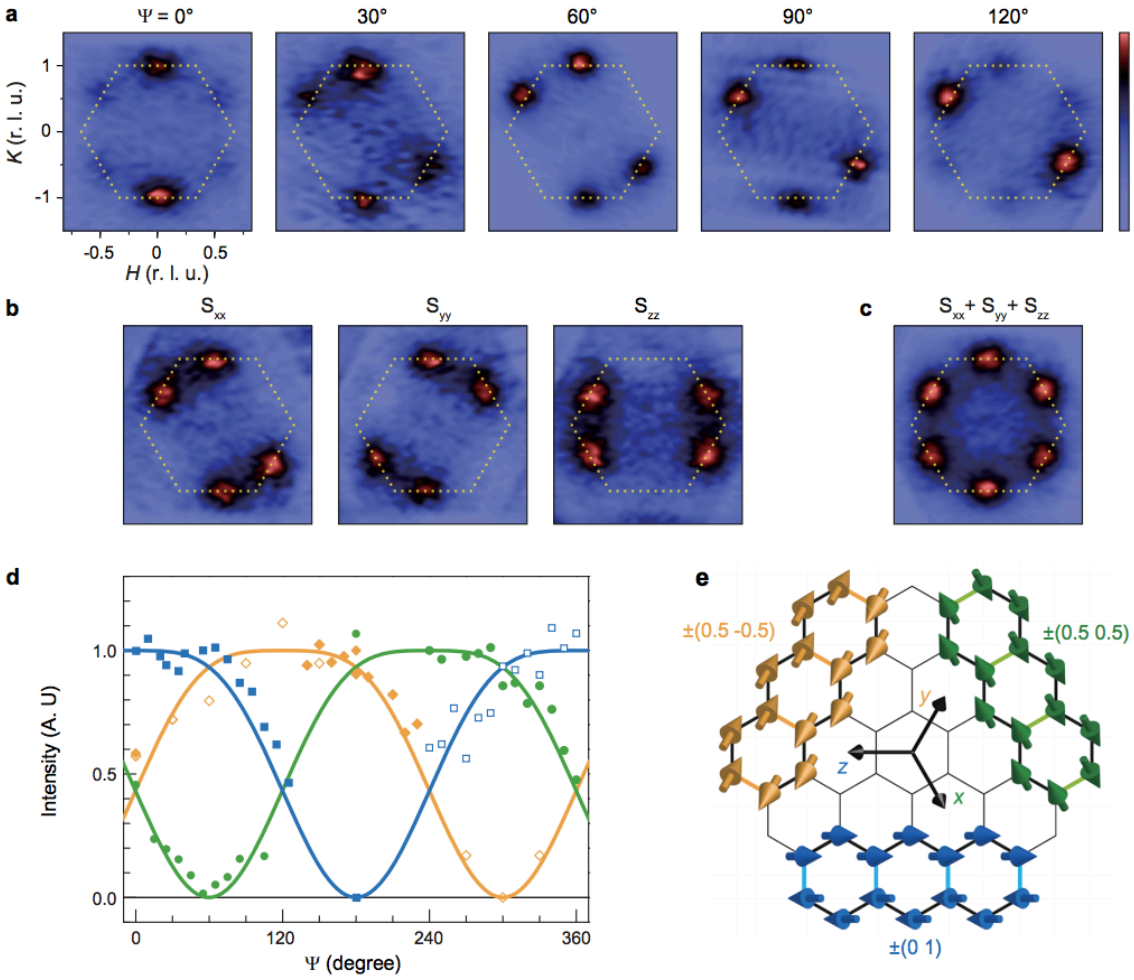

FIGURE 2.12: Diffuse magnetic X-ray scattering results for Na_2IrO_3. Panel (a)—T=17 K intensities probed for several values of the azimuthal angle Ψ, starting from -X direction [see Fig. 2.6 (b) for the XYZ frame], panels (b), (c)—static pseudospin correlations extracted from (a), panel (d)—angular dependence of the measured intensities with the fitted theoretical intensities for the zigzag patterns presented in panel (e). Figure taken from Ref. [39].

The magnon manifests itself as a wave-like dispersive object around the Γ point for the low energy regime 1-4 meV. Importantly, when moving away from the Brillouin zone center the intensity of the magnon fades. Moreover, the INS experiments revealed that the mysterious continuum had a star –like shape when integrated over its energy range [40] [Fig. 2.13 (a)], contrary to a more simple shapes of the continua of the FM and AF Kitaev models [Fig. 2.10 (e) and (g)], but in agreement with the continuum of the so-called J-K-Γ-J_3 model [Fig. 2.13 (b)] [37], which will be addressed in detail in Sec. 2.5.

Initially the continuum was explained by fractionalization of magnons into the Majorana fermions, also suggested in Ref. [36] via integration of QMC Raman intensity for FM Kitaev model over α-$RuCl_3$-relevant part of the spectrum [Fig. 2.10 (d)]. However, the intensity calculated for the J-K-Γ-J_3 model via ED showed the one-magnon line dissolving into the continuum away from the zone center [Fig. 2.13 (d)], similarly to Fig. 2.13 (b). Comparison between ED and linear spin wave theory (LSWT), which considers only the non-interacting sharp magnons, revealed the connection between the continuum and the interaction between magnons. Hence, the continuum does not seem to be a manifestation of the fractionalization of magnons into the Majorana fermions, but rather the multi-magnon effect enforced by the Γ interaction [37].

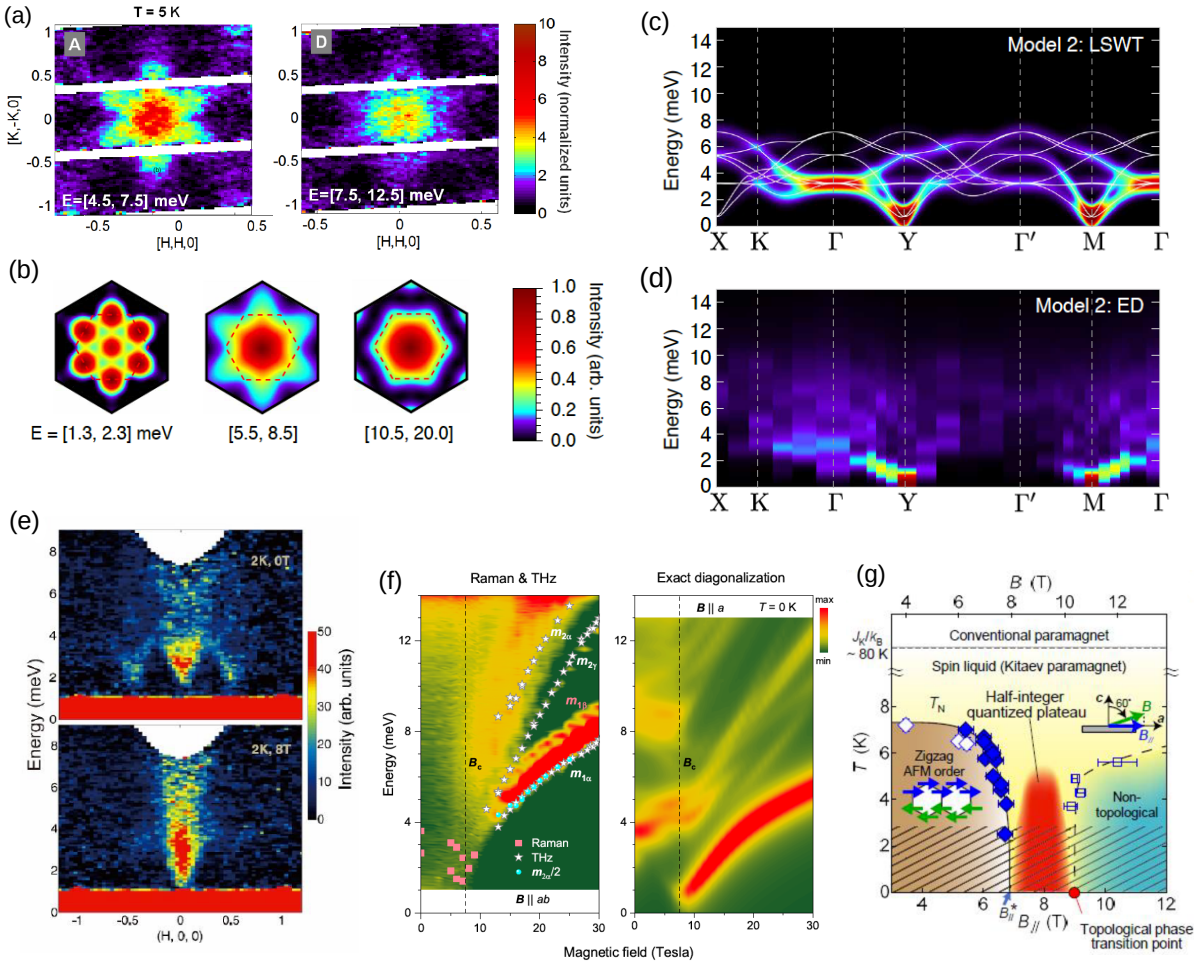

FIGURE 2.13: α-$RuCl_3$ in magnetic experiments: panel (a)—1st BZ maps of the inelastic neutron scattering (INS) single-crystal intensities $I(\mathbf{k},\omega)$ integrated over the energy ranges given in the inset. Panel (b)—$I(\mathbf{k},\omega)$ maps integrated over the energy ranges in meV given below each map, calculated via exact diagonalization (ED) for 24 sites and the minimal model for the material—the J-K-Γ-J_3 model (see Sec. 2.5). Panel (c), (d)—$I(\mathbf{k},\omega)$ for the J-K-Γ-J_3 model calculated via linear spin wave theory (LSWT) and ED, respectively. Panel (e)—INS $I(\mathbf{k},\omega)$ in zero and 8T magnetic field along X axis [in honeycomb plane, see Fig. 2.6 (b) for the XYZ frame]. Panel (f)—Raman and THz spectroscopy intensity (experimental on the left subpanel and ED simulated on the right subpanel) measured/calculated for the field in the honeycomb plane. Panel (g)—a sketch of the magnetic field-temperature phase diagram, where $B_{||}$ is the magnetic field set in the honeycomb plane. Panels taken and modified from Refs.: (a)—[40], (b)-(d)—[37], (e)—[41], (f)—[43] (g)— [44].

.

2.3.3 Engineering the liquid state

Although the KSL ground state has not been found in real materials so far, the accumulated evidence of strong frustration opens the question how close to the Kitaev limit the real materials are. Would it be possible to drive them into the quantum spin-liquid state by suppressing the long-range order via experimentally accessible means: magnetic field, pressure or doping [12]?

In recent years several experimental and theoretical groups have been searching for the KSL in the magnetically induced materials. Firstly, both classical and quantum simulations suggest that introducing a magnetic field pointed in an arbitrary direction will suppress the zero-field magnetic order for the strong enough field [45] and ultimately lead to the ferromagnetically polarized state in the infinite-field limit. As mentioned earlier for the Kitaev model, the path to

polarization may be quite complicated in the presence of the frustrated interactions. Indeed, several experiments reported not only the suppression of LRO-characteristic sharp magnon features while leaving the continuum intact for the field ≈ 7.5 T in honeycomb plane [41, 43] [lower subpanel of Fig. 2.13 (e)], but also the half-integer thermal Hall effect was recognised in the thermal conductivity measurements. An intermediate topological phase for the in-plane field $\in [7, 9]$ T and temperature below 5K [44] can be seen on the phase diagram in Fig. 2.13 (g). However, further Raman and THz-spectroscopic results [43] revealed more details of the continuum [left subpanel of Fig. 2.13 (f)], no definite evidence of fractionalization seems to hold above B_{crit}. Instead, the magnetic field in the honeycomb plane induces a quantum disordered state (QDS) with only partial polarization [43].

Under pressure the so-far analyzed materials [46, 47, 48, 49, 50] undergo a transition into a dimerized state in which pairs of iridium/ruthenium ions form strong molecular bonds instead localized pseudospin moments. This is an undesirable effect, since one would rather hope for the compression of the honeycomb layers while keeping the Ir/Ru bond anisotropy minimal. This would save the pseudospins and strengthen the hopping paths leading to the Kitaev term, hopefully moving the material towards the spin-liquid regime [12].

While conventional doping[30] of Na_2IrO_3 with Li has been moderately successful in enlarging the frustration regime, lowering T_N, and increasing $|\Theta|$ [10], chemical modification with ions of the same valence is effectively acting as a more sophisticated pressure experiment. Namely, chemical modification of Li_2IrO_3 with hydrogen leads to the crystalisation of $H_3LiIr_2O_6$ [51]. The new material has more packed honeycomb layers, which suppress the LRO. Indeed, in Fig. 2.11 (a) susceptibility curve labeled as H does not have a kink while $\chi^{-1}(T)$ diverge from the Curie-Weiss line in a profoundly different manner than the other materials [Fig. 2.11 (b)]. These and other features may be fingerprints of quantum spin liquid, differing however from the KSL.[31] The material is currently still under investigation [12]

2.3.4 More on the magnetic order

Below we dive deeper into the magnetic order fingerprints, focusing on the character of LRO in Na_2IrO_3 and α-$RuCl_3$. Single crystal neutron and X-ray diffraction determined the magnetic order of both materials as a colinear zigzag pattern [52, 53, 54, 55, 56]. Within $NaIr_2O_6$/ $RuCl_6$ layers such a pattern is built out of the antiferromagnetically connected ferromagnetic zigzag chains, as illustrated in Fig. 2.12 (e). While Na_2IrO_3 displays antiferromagnetic coupling between the layers, in case of α-$RuCl_3$ the stacking faults appearing extremely easily in the samples (due to weak inter-layer van der Vaals couplings) make the full 3D order difficult to identify [54, 57].

In both materials magnetic order was determined by analyzing the Bragg peak corresponding to the propagation wave vector of magnetic order parameter—(0,1,0.5) in the1st Brillouin zone of the C2/m-symmetric structure. Irreducible representations analysis for the C2/m group and (0,1,0.5) vector allowed to further compare the experimental peaks to the possible magnetic patterns. Only the zigzag pattern reproduced the experimental intensities of the considered magnetic peaks [52, 54].

Magnetic moment value

Importantly for the results presented in this thesis, the neutron diffraction (ND) provided the value of the magnetic moment per magnetic atom in the ordered phase below T_N: $0.22\mu_B$/Ir

[30] Replacing some ions with the ions of lower/higher valence then the original ones to introduce more electrons/holes to the system.

[31] E.g. by different, not anomalous specific heat.

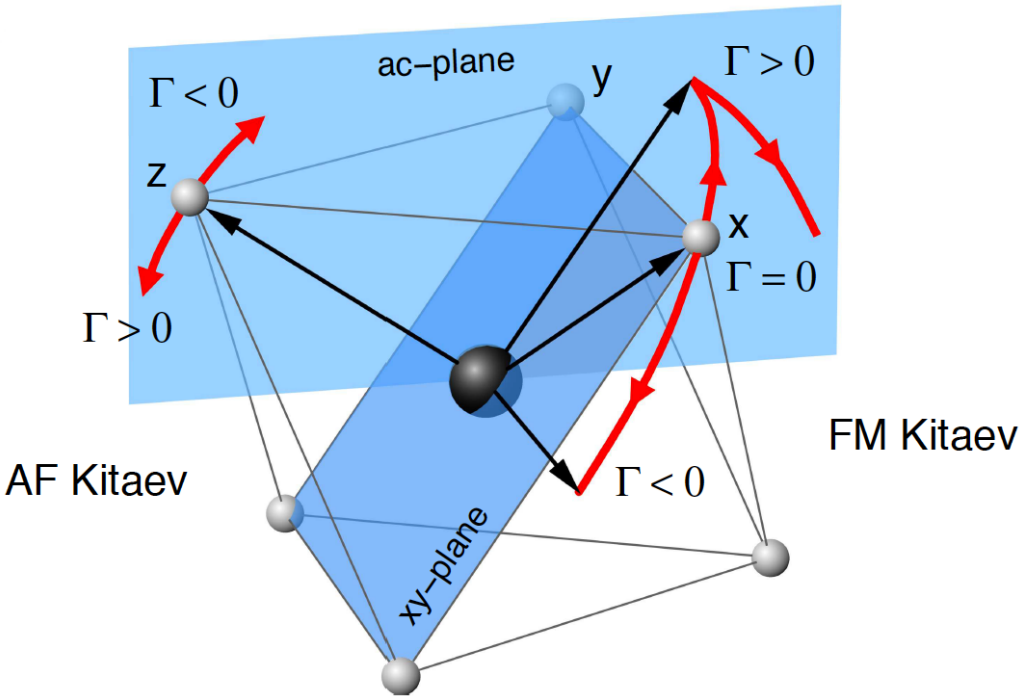

FIGURE 2.14: Direction of the ordered moment in the J-K-Γ-Γ' model for the ferromagnetic zigzag chains running along the a and b bonds. Here ac denotes the XZ plane. Figure taken from Ref. [11].

[52] and 0.4-0.7μ_B/Ru [54], considerably lower than the 1μ_B/atom corresponding to the atomic J $= \frac{1}{2}$.

Magnetic moment direction

When considering the direction of the magnetic moment we will be referring to the orthogonal XYZ frame presented in Fig. 2.6 (b).[32] For both Na_2IrO_3 and α-$RuCl_3$ the moment lies in the XZ plane, denoted in Fig. 2.14 as ac,[33] pointing significantly above the honeycomb plane. Resonant elastic X-ray scattering (REXS) experiments for both Na_2IrO_3 [39] and α-$RuCl_3$ [58] determined the orientation of the **N** vector related to the magnetic moment.[34] The angle within honeycomb plane, ϕ_N, is equal 0° for both materials.[35] In case of Na_2IrO_3 the angle from the honeycomb plane to **N** vector, α_N, equals 44.3°[39]. For α-$RuCl_3$ REXS gives the out-of-plane angle $\alpha_N = (32 \pm 3)°$ while the neutron diffraction provides an analogical angle for the proper magnetic moment **M**, $\alpha_M \approx 35°$ [57].

As the materials in question display the magnetic LRO in low temperatures, a careful derivation of the effective model became important to estimate how close to the Kitaev spin liquid the real materials are. Below we present some, by no means complete, scope of the effective Hamiltonians considered for the honeycomb systems, focusing especially on the Kitaev-Heisenberg and J-K-Γ-Γ' Hamiltonians, due to their relevance for the results presented in this thesis.

[32] X and Y in the honeycomb plane, Z—out-of –plane direction.
[33] In Ref. [11] *abc* denotes XYZ frame, *not* the crystallographic frame.
[34] We elaborate on the relation in Sec. 3.5.
[35] When ϕ_N starts from the +X direction. Both Refs. [39, 58] use the opposite convention, starting from the −X, hence 180° value in those papers.

2.4 Kitaev-Heisenblerg model

Since the ferromagnetic Kitaev spin liquid state is quite resistant to small perturbations [7], there was hope that derivation of the effective model for the honeycomb materials will result in a finite spin-liquid window, making the KSL state easier to utilize in applications. Indeed, in subsequent papers [5, 6] Jiří Chaloupka, George Jackeli and Giniyat Khaliullin presented the phase diagram of the emerging Kitaev-Heisenberg (KH) model, for which two spin-liquid windows were visible.

The Kitaev-Heisenberg Hamiltonian has the form

$$\mathcal{H} = K \sum_{\langle i,j\rangle\perp\gamma} \mathrm{S}_i^\gamma \mathrm{S}_j^\gamma + J \sum_{\langle i,j\rangle} \mathbf{S}_i \mathbf{S}_j, \tag{2.12}$$

where both J and K coupling constants can take positive or negative values, leading to the AF or FM contributions. The new Heisenberg interaction may originate from a direct Ir-Ir overlap (the AF case) or the not yet considered indirect hopping between the t_{2g} and e_g iridium orbitals and subsequent Hund's coupling (the FM case) [5, 6].[36] The Kitaev term could be derived from the $\tilde{\mathrm{J}} = 1/2 \longleftrightarrow \tilde{\mathrm{J}} = 3/2$ hopping[37] and the following Hund's interaction, already described in Sec. 2.1.2, (the FM case) or the above mentioned $t_{2g} \longleftrightarrow e_g$ hopping. Finally, a more complicated process involving meeting of the two holes on oxygen site as well as a cyclic hopping through Ir-O –Ir-O plaquette contributes to both the AF Heisenberg and FM Kitaev terms [5, 6]. For more details Fig. 2 of Ref. [6] is recommended.

Maybe it is a good place to make a technical remark: over the years different conventions of parametrising the Kitaev-Heisenberg Hamiltonian were introduced. The form (2.12) is currently the most popular, but originally the Hamiltonian was defined as

$$\mathcal{H} = 2K \sum_{\langle i,j\rangle\perp\gamma} \mathrm{S}_i^\gamma \mathrm{S}_j^\gamma + J \sum_{\langle i,j\rangle} \mathbf{S}_i \mathbf{S}_j, \tag{2.13}$$

where the rescaling of the K parameter was designed to emphasise the hidden symmetries of the model.

2.4.1 Phase diagram

Below we discuss the phase diagram of the KH model, replotted from Ref. [6] in Fig. 2.15. The diagram was based on the exact diagonalization (ED) on the symmetric 24-site cluster, compatible with the magnetic cells of all ordered phases. The shape of the cluster is shown on the mini-drawings surrounding the diagram. The phase boundaries are compatible with Hamiltonian (2.13), with the polar parametrization

$$K^2 + J^2 = 1 \longrightarrow J = \cos\varphi,\ K = \sin\varphi,\ \varphi \in [0, 2\pi]. \tag{2.14}$$

The azimuthal angle φ starts and ends at $J = +1$ AF Heisenberg limit, reaches $K = +1$ AF Kitaev limit for $\varphi = \pi/2$, $J = -1$ FM Heisenberg limit for $\varphi = \pi$ and $K = -1$ FM Kitaev limit for $\varphi = 3\pi/2$.

LRO phases

In the Kitaev-Heisenberg model the long-range magnetic order can only be collinear. In fact, there are four types of possible classical patterns: Néel, zigzag, FM and stripy, as depicted on

[36] It should not be confused however with the previously described cancelled-out original isotropic exchange between $\tilde{\mathrm{J}} = 1/2$ states via two possible Ir-O-Ir paths.

[37] Since both $\tilde{\mathrm{J}} = 1/2$ and $\tilde{\mathrm{J}} = 3/2$ states arise from the splitting of the t_{2g} orbital by the spin-orbit coupling one could also say "$t_{2g} \longleftrightarrow t_{2g}$" hopping.

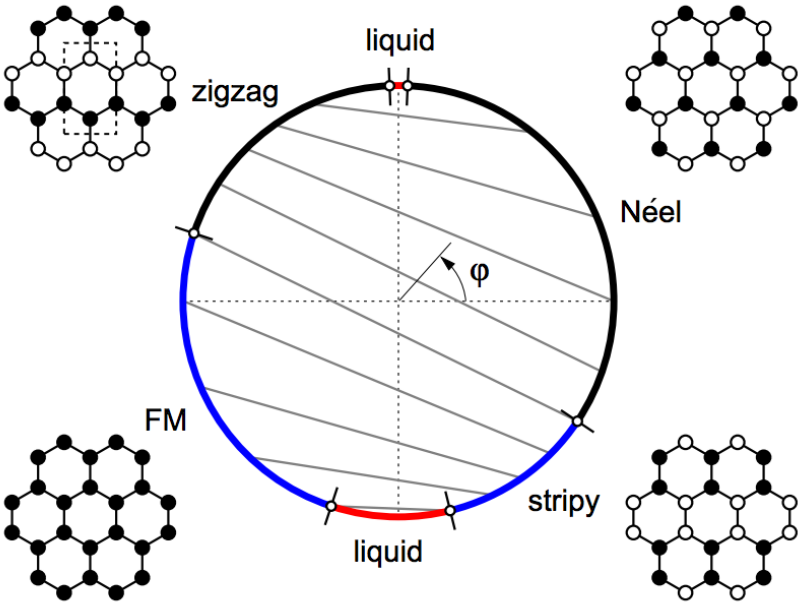

FIGURE 2.15: Ground-state based phase diagram of the Kitaev-Heisenberg model.The mini-drawings present the magnetic patterns characteristic for four magnetically ordered phases: Néel, zigzag, FM and stripy. The filled and empty circles represent the ± projection of the pseudospin on the z axis. Magnetically ordered regions with the explicit or hidden AF tendencies are marked in black, the phases with the FM tendencies are depicted in blue and spin-liquid regions are presented in red. Some of the dual points on the diagram are connected by grey lines to emphasise the usefulness of the $\mathcal{T}_4$ transformation. The figure copied from Ref. [6].

the mini-drawings surrounding the diagram. However, the Kitaev-Heisenberg Hamiltonian is quantum, therefore in the ground state these patterns are "dressed" in a suitable amount of quantum fluctuations, depending on the ratio between competing J and K terms.[38]

For purely-Heisenberg model the SU(2) symmetry could be broken in any direction in the ground state. It is no longer the case when the Kitaev term is added to the Hamiltonian, because of different interaction axis on bonds in the a, b and c direction. Since the Kitaev interaction axes reduce the SU(2) symmetry, the pseudospins oriented along any of these axes will have the highest coefficient in the ground state. For collinear LRO patterns the same axis is chosen for the whole pattern. In this way six highest-probable versions of each pattern can be selected. This is a very simplistic description of the order-from-disorder mechanism [1].

For completeness below we present also magnetic unit cells and reciprocal-lattice pictures of the discussed magnetic patterns.

Bragg spots for the magnetic patterns

The honeycomb net, though commonly called a lattice, is not a real Bravais lattice because of the non-equivalence of the two types of its sites.[39] Therefore, the 1st Brillouin zone of the honeycomb lattice, shown as the inner hexagon in Fig. 2.16 (a), is often obtained by treating one of the triangular sublattices as a lattice with a two-ion basis. Moreover, every magnetic periodic

[38] In contrast to the one-dimensional case, where the enormous quantum fluctuations suppress the long-range order in the nearest-neighbor antiferromagnetic Heisenberg model [1], for the two-dimensional lattices without geometrical frustration the Néel pattern, "dressed" in still significant amount of quantum fluctuations, forms long-range order. The latter happens also in the case of honeycomb lattice.

[39] One species would be equivalent to the other after the π rotation of the surrounding sites.

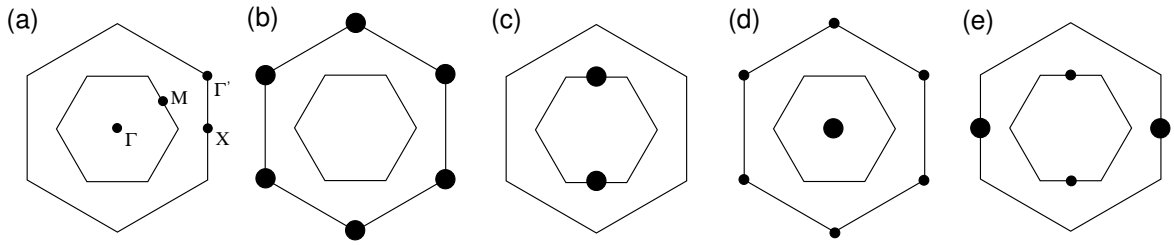

FIGURE 2.16: Panel (a)—1st Brillouin zones of the honeycomb lattice (the inner hexagon) and the triangular lattice created by adding a site at the center of each hexagon (the outer hexagon). Panels (b-e)—reciprocal pictures of the collinear patterns with the pseudospins (anti)parallel to the z axis: (b) Néel, (c) zigzag, (d) FM and (e) stripy. A reciprocal picture of the Kitaev spin liquid will be discussed separately.

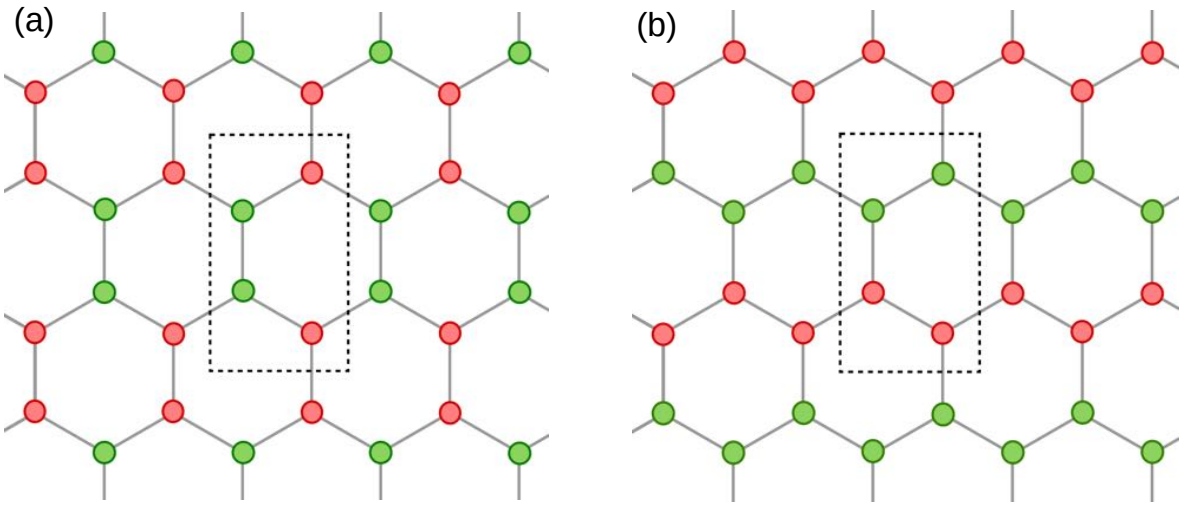

FIGURE 2.17: Magnetic unit cells for the (a) stripy and (b) zigzag patterns. The red and green circles represent the antiparallel orientation of the pseudospins.

pattern can be reduced to its magnetic unit cell, which, when repeated, can recreate the pattern. Such cells can be relatively small, e.g. the two-site cells of the FM and Néel patterns, or larger, as the stripy and zigzag cells depicted in Fig. 2.17. Since the Néel and FM patterns transformed to the reciprocal lattice via the Fourier transform produce Bragg spots outside of the 1st Brillouin zone of the honeycomb lattice, it is customary to show also the 1st Brillouin zone of another triangular lattice emerging after adding a site in the center of each hexagon. This is the outer hexagon in Fig. 2.16 (a). The other panels present the reciprocal-lattice pictures obtained for patterns aligned along the z axis. The order of patterns follows the growth of φ parameter on the phase diagram.

KSL windows

The highly desirable Kitaev spin-liquid phase spreads around the two Kitaev limits of the phase diagram. As expected, the FM KSL state occupies a large region around $\varphi = 3\pi/2$, winning over the energetic competition with the less quantum-fluctuating FM and stripy phases. The AF liquid window around $\varphi = \pi/2$ is much narrower because the quantum spin liquid competes there with also strongly quantum-fluctuating phases of the AF type [6]. [The meaning of the AF/FM "type" will be explained in the section below.]

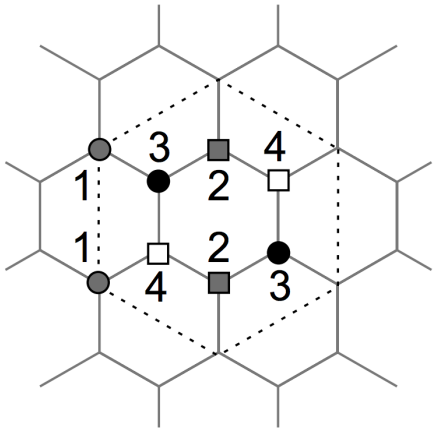

FIGURE 2.18: Four sublattices introduced in the T_4 transformation. Figure taken from Ref. [9].

$\mathcal{T}_4$ transformation, self-duality and the hidden SU(2) points

As mentioned earlier, the Kitaev-Heisenberg Hamiltonian has some hidden symmetries. Substituting the pseudospin operators in the Hamiltonian with a set of the new pseudospins, related to the old ones via $\mathbf{S}_i = \mathcal{R}_i^{-1}\mathbf{S}_i'$, where $\mathcal{R}_i$ is symmetry operation matrix, leads in general to a new form of the Hamiltonian. Sometimes such transformation is so powerful, that it is able to transform the Hamiltonian onto itself [9]. Such a transformation is called self-dual. Crucially, self-duality guarantees that the eigenstate properties such as the amount of quantum fluctuations will be the same for every two points connected by the transformation. Although the ground state for the linked points may look very different in the original basis, the self-dual connection between Hamiltonian forms guarantees existence of a basis in which ground state A will coincide with ground state B.

It turns out that rotating pseudospins in Hamiltonian (2.12) in a particular way links every point on the phase diagram with its self-dual equivalent on the very same diagram, see grey lines in Fig. 2.15. The referred self-dual transformation of the Kitaev-Heisenberg model is known in literature as $\mathcal{T}_4$ [59, 5, 6, 9] and consists of four different rotations for the four sublatices:

$$\begin{aligned}
(\mathrm{S}^{x'},\mathrm{S}^{y'},\mathrm{S}^{z'}) &= (\mathrm{S}^{x},-\mathrm{S}^{y},-\mathrm{S}^{z}) && \pi\text{-rotation around } x \text{ axis on sublattice 1,}\\
(\mathrm{S}^{x'},\mathrm{S}^{y'},\mathrm{S}^{z'}) &= (-\mathrm{S}^{x},\mathrm{S}^{y},-\mathrm{S}^{z}) && \pi\text{-rotation around } y \text{ axis on sublattice 2,}\\
(\mathrm{S}^{x'},\mathrm{S}^{y'},\mathrm{S}^{z'}) &= (-\mathrm{S}^{x},-\mathrm{S}^{y},\mathrm{S}^{z}) && \pi\text{-rotation around } z \text{ axis on sublattice 3,}\\
(\mathrm{S}^{x'},\mathrm{S}^{y'},\mathrm{S}^{z'}) &= (\mathrm{S}^{x},\mathrm{S}^{y},\mathrm{S}^{z}) && \text{identity operation on sublattice 4.}
\end{aligned} \tag{2.15}$$

The above sublattices are represented by circles and squares in Fig. 2.18.

$\mathcal{T}_4$ transformation proved to be a very practical tool because it reduces the range of coupling parameters for which the calculations have to be performed. It is enough to cover half of the phase diagram and utilize $\mathcal{T}_4$ to transfer the whole information from the calculated part to the missing part [9]. It can save computational memory and time or be used for cross-checking the results, filtering out the effects of numerical instabilities and other artifacts.

Most importantly, two particular points in zigzag and stripy phases are directly related via $\mathcal{T}_4$ to AF and FM SU(2) (i.e. purely-Heisenberg) points. One can notice that by following the grey lines coming from $\varphi = 0$ and π in Fig. 2.15. In the convention of Eq. (2.13) the hidden AF and FM SU(2) points are located at $\varphi = 3\pi/4$ and $7\pi/4$, correspondingly. By showing the Néel-zigzag and FM-stripy relations, the transformation reveals the AF character of the zigzag and FM character of the stripy phases of the Kitaev-Heisenberg model.

As the experimental results on Na_2IrO_3 and α-$RuCl_3$ were accumulating, it became clear

that the direction of the pseudospins in the zigzag order supported by the Kitaev-Heisenberg model is too divergent from the experimental data. Namely, pseudospins forming zigzag patterns in the ED-based ground state point either towards x, y or z axes, in contrast to the experimental moments lying in the XZ plane, *in between* the x and y axes.[40] Therefore, revisiting the derivation of the effective Hamiltonian became necessary. Nevertheless, the Kitaev-Heisenberg model remains an important part of the family of the Kitaev-like models because on one hand it is easy to handle in perturbative and numerical approaches and, on the other hand, it is highly nontrivial due to the directional frustration manifested by the Kitaev term and the competition between Kitaev and Heisenberg terms.

2.5 More complex Kitaev-like models

Spin-liquid vs LRO properties of real materials strongly depend on the ratio of various microscopic characteristics, such as the length of the Ir-Ir/Ru-Ru bonds and the distortions of oxygen/chlorine octahedra. This is because the details of the crystal structure are the first selectors deciding on the relative strength of the hopping paths yielding coupling parameters in the effective model. As expected, the structural imperfections of Na_2IrO_3 and α-$RuCl_3$ resulted in their huge, 25/29-parameter effective Hamiltonians [60]. Such models, although more precise, would be challenging to process numerically, therefore it was important to decide which terms could be omitted without diverging too far from the experimental results. As a consequence, over the recent years multiple sets of minimal models for the materials in question were proposed. Below we cite the ones from Ref. [60] as an example:

- K-J_3 model for Na_2IrO_3 with $|J_3/K| \approx 0.4$ and $K < 0$, $J_3 > 0$, where J_3 stands for the Heisenberg third-neighbor coupling.
- J-K-Γ-J_3 model for α-$RuCl_3$ with $(J, K, \Gamma, J_3) = (-0.5, -5, +2.5, +0.5)$ meV. Importantly, both J and K have a FM sign , contrary to Γ and J_3 [60, 61, 45, 38].

Although these and other models [62, 63, 64, 65, 66, 67, 68] pinpoint the values of the parameters of the two materials, it is beneficial to see the surroundings of these points on the phase diagram.[41] Just for α-$RuCl_3$ the effective Hamiltonian has four parameters, when taking into account only the strongest interactions. Other studies, however, [66, 69] suggested the importance of the trigonal distortion effect, represented partly by the so-called Γ' term or even a second-neighbor Kitaev term. Full phase diagram of the J-K-Γ-Γ'-J_3 model would provide a comprehensive picture of the LRO/spin-liquid tendencies, helping with engineering a quantum spin liquid, either starting from the positions of Na_2IrO_3 and α-$RuCl_3$ or designing a new material.

Considering the complexity of the five-parameter phase diagram we will first introduce the sub-diagrams of:

- the J-K-Γ model [8],
- the J-K-Γ-Γ' model—classical phase diagram and selected patches of the quantum phase diagram published in Refs. [70, 9, 11, 71, 38],
- the J-K-Γ-J_3 model—selected patches of the classical and quantum phase diagrams from Refs. [37, 60, 61, 45, 38],

leaving a more detailed discussion, including the information we brought to the table for Chapter 3.

[40] See Sec. 2.3.4 for a reminder.

[41] We note that some of the references provide characteristics of close neighborhood of the proposed parameter points.

2.5.1 Phase diagram of the J-K-Γ model

In case of the perfect $IrO_6/RuCl_6$ octahedra the C_3 pseudospin and lattice[42] symmetry at each Ir/Ru site still allows for an additional nearest-neighbor term besides the J and K [8]. The symmetric off-diagonal exchange Γ enriches the Hamiltonian into the form (in the case of bond c)

$$\mathcal{H}|_c = \begin{pmatrix} \mathrm{S}_i^x & \mathrm{S}_i^y & \mathrm{S}_i^z \end{pmatrix} \begin{pmatrix} J & \Gamma & 0 \\ \Gamma & J & 0 \\ 0 & 0 & J+K \end{pmatrix} \begin{pmatrix} \mathrm{S}_j^x \\ \mathrm{S}_j^y \\ \mathrm{S}_j^z \end{pmatrix} =$$

$$= J\mathbf{S}_i \cdot \mathbf{S}_j + K\mathrm{S}_i^z\mathrm{S}_j^z + \Gamma(\mathrm{S}_i^x\mathrm{S}_j^y + \mathrm{S}_i^y\mathrm{S}_j^x). \tag{2.16}$$

Due to the C_3 symmetry the expressions for bonds a and b are accessible via a cyclic permutation of x, y and z components. For clarity we present the generic bond expression below

$$\mathcal{H}|_\eta = J\mathbf{S}_i \cdot \mathbf{S}_j + K\mathrm{S}_i^\gamma\mathrm{S}_j^\gamma + \Gamma(\mathrm{S}_i^\alpha\mathrm{S}_j^\beta + \mathrm{S}_i^\beta\mathrm{S}_j^\alpha), \tag{2.17}$$

where α, β and $\gamma \in (x, y, z)$ are specific for the bonds of $\eta = a$, b or c direction perpendicular to γ [8].

In the Kitaev-related physics it has become a tradition to represent the coupling parameters in terms of the trigonometric functions. Below we explain a popular convention for models with three parameters and beyond, which is utilized in this and subsequent chapter.

A quick guide to the circular maps

One may imagine J, K and Γ parameters as axes of the 3D coordinate frame. Then, extending the polar parametrization of the Kitaev-Heisenberg model to the spherical one, we obtain:

$$\begin{aligned} J &= \sin\theta\cos\varphi, \\ K &= \sin\theta\sin\varphi, \\ \Gamma &= \cos\theta, \end{aligned} \tag{2.18}$$

which confines the energy scale to a unit sphere

$$J^2 + K^2 + \Gamma^2 = 1. \tag{2.19}$$

In principle, one could produce a spherical distribution of the J, K and Γ parameters—the result would be a globus-like object for which one could calculate a phase diagram. A more practical solution—a two dimensional map requires some kind of projection. Out of multiple options known from cartography, we describe the two filling the circle created by the azimuthal angle φ with the information about the *vertical* axis Γ. Namely, one may perform a straight forward projection of the (J, K, Γ) points on the sphere onto the horizontal JK plane by plotting their J and K positions. The strength of the Γ term may then be recreated using the normalization (2.19). Alternatively, we may plot the points in terms of φ as the anglular and $\theta = \arccos(\Gamma)$ as the *radial* variable.

The second solution was introduced in the Ref. [8] and we will be following this convention. Fig. (2.19) explains how any random point on the sphere is mapped onto the full horizontal circle. It is easy to imagine that the points close to $\Gamma = \pm 1$ poles will project close to the center of the circle, where θ has to be small to give $\cos\theta \approx 1$ values, while the points with smaller Γ component will be projected further and further towards the outer $J^2 + K^2 = 1$ circle, where

[42] At each Ir/Ru site the rotation of the pseudospin components *and* bond direction by 120° enables transfer between one-bond terms of the anisotropic effective Hamiltonian analogically to the pure Kitaev model.

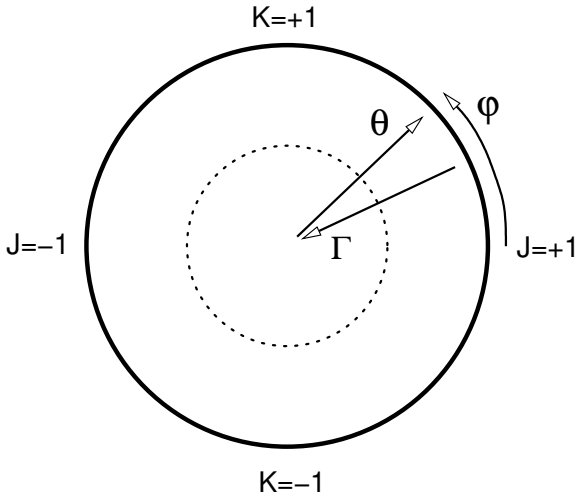

FIGURE 2.19: A guide to circular maps utilizing the trigonometric parametrization of the coupling parameters of the Kitaev-like models [including the Γ parameter].

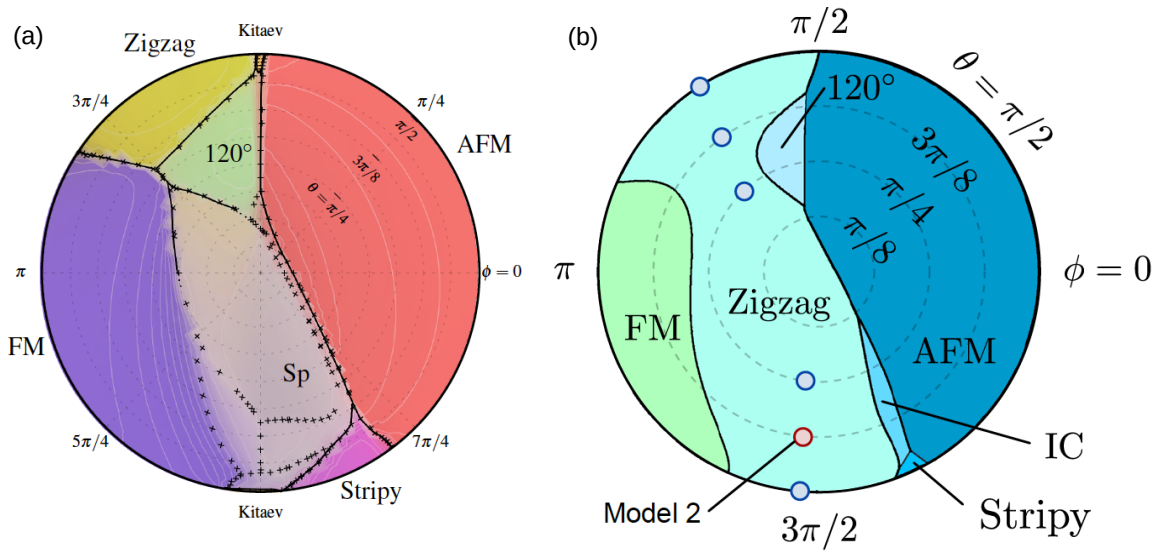

FIGURE 2.20: Representable slices of the J-K –Γ-Γ′-J_3 phase diagram known from literature. (Here $\phi = \varphi$, $\theta = \vartheta$.) Panel (a)— phase diagram of the J-K-Γ model for the $\Gamma \geq 0$ case. The Néel phase in red, the FM phase in dark-violet, the zigzag phase in dark yellow, and the stripy phase in pink. Non-collinear patterns: 120° (vortex) and spiral (Sp) in light green and light violet, respectively. The KSL regions are (barely) visible in orange color. Panel (b)—$J_3 = +0.088$ slice of the phase diagram of the J-K-Γ-J_3 model. IC label stands for the incommensurate spiral region. The red point represents the estimated α-$RuCl_3$ position in the coupling-parameter space mentioned at the beginning of Sec. 2.5. Exact-diagonalization based panels (a) and (b) taken from Refs. [8] and [37], correspondingly.

the Kitaev-Heisenberg limit is reached. As a result, on such a map the value of Γ effectively increases when moving towards the center of the circle. After this initial geometric exercise it is time introduce the phase diagram of the J-K-Γ model.

Phase diagram

The first phase diagram of the J-K-Γ model [8] consisted of the classical (Monte Carlo-based) and quantum (exact-diagonalization-based) circles. Here we refer to the quantum part [Fig. 2.20

(a)] because its phase boundaries reflect the strong frustration in the model more adequately. The reader may recognise the familiar collinear phases: the vast Néel (red) and FM (violet) regions as well as the smaller stripy (pink) and zigzag (yellow) patches. All those phases start from their respective Kitaev-Heisenberg arcs on the outer $\Gamma = 0$ circle.

Introducing the non-diagonal Γ term to the Hamiltonian not only rotates the pseudospins from one of the Kitaev cubic axes xyz [11, 69] but also allows non-collinear tendencies in certain parameter ranges. In particular, the non-collinear phase in the middle of the phase diagram was detected and interpreted as the 120°-order with some internal three-sublattice structure [8]. The phase was further recognised as a vortex one due to the hidden SU(2) point, called the vortex point, at the boundary with the Néel phase, revealed by the 6-sublattice transformation $\mathcal{T}_6$ [9]. We will elaborate on the $\mathcal{T}_6$ transformation in Sec. 2.5.2 and on its relation to the whole vortex phase—in Chapter 3. For now though we refer the reader to Fig. 2.21 (c) for the example of a possible vortex pattern at the vortex point.

The non-collinear tendencies are not restricted to the vortex phase. According to early papers, a faint tendency towards the zigzag ordering visible close to the middle of the circle acquires the non-collinear behaviour (diffusion of yellow and light violet/grey colors) and further changes into the incommensurate phase with a spiral component (Sp) in the $J > 0$, $K < 0$ quarter fn Fig. 2.20 (a). We will examine the above issues in Chapter 3.

Finally, the KSL regions spread slightly from the corresponding AF and FM KSL windows on the outer Kitaev-Heisenberg circle when the small Γ values are included, which is indicated in orange on Fig. 2.20 (a). As will be disclosed later, those are not the only spin-liquid tendencies on the diagram.

2.5.2 Phase diagram of the J-K-Γ-Γ' model

Allowing for the trigonal compression of the oxygen / chlorine octahedra suplements the nearest-neighbor J-K-Γ Hamiltonian with the negative off-diagonal Γ' term [70, 10]. The full nearest-neighbor form is presented below for the bond in direction c [70]

$$\mathcal{H}|_c = \begin{pmatrix} \mathrm{S}_i^x & \mathrm{S}_i^y & \mathrm{S}_i^z \end{pmatrix} \begin{pmatrix} J & \Gamma & \Gamma' \\ \Gamma & J & \Gamma' \\ \Gamma' & \Gamma' & J+K \end{pmatrix} \begin{pmatrix} \mathrm{S}_j^x \\ \mathrm{S}_j^y \\ \mathrm{S}_j^z \end{pmatrix} = \tag{2.20}$$

$$= J\mathbf{S}_i \cdot \mathbf{S}_j + K\mathrm{S}_i^z\mathrm{S}_j^z + \Gamma(\mathrm{S}_i^x\mathrm{S}_j^y + \mathrm{S}_i^y\mathrm{S}_j^x) + \Gamma'(\mathrm{S}_i^x\mathrm{S}_j^z + \mathrm{S}_i^z\mathrm{S}_j^x + \mathrm{S}_i^y\mathrm{S}_j^z + \mathrm{S}_i^z\mathrm{S}_j^y). \tag{2.21}$$

For completeness, we provide the generic form for any bond direction:

$$\mathcal{H}|_\eta = J\mathbf{S}_i \cdot \mathbf{S}_j + K\mathrm{S}_i^\gamma\mathrm{S}_j^\gamma + \Gamma(\mathrm{S}_i^\alpha\mathrm{S}_j^\beta + \mathrm{S}_i^\beta\mathrm{S}_j^\alpha) + \Gamma'(\mathrm{S}_i^\alpha\mathrm{S}_j^\gamma + \mathrm{S}_i^\gamma\mathrm{S}_j^\alpha + \mathrm{S}_i^\beta\mathrm{S}_j^\gamma + \mathrm{S}_i^\gamma\mathrm{S}_j^\beta). \tag{2.22}$$

When calculating the phase diagram one of the possible conventions is to keep the J, K and Γ parameters normalized to a unit sphere [as for the J-K-Γ model] while allowing Γ' to change freely. With such constraints the parameter space forms a cylinder which one can then cut for the selected values of Γ', obtaining the Γ' =const. slices of the diagram.

Phase diagram

Judging from Γ' slices of the classical phase diagram as well as patches of the quantum phase diagram (cf. Figs. 2 and 3 in Ref. [70], respectively), one can already grasp some general tendencies caused by the Γ' term. While $\Gamma > 0$, $\Gamma' < 0$ allows vortex and lower zigzag regions to spread, suppressing other phases, $\Gamma' > 0$ promotes robust Néel and FM regions. Since even a more comprehensive picture of this diagram, clarifying the form of possible magnetic patterns

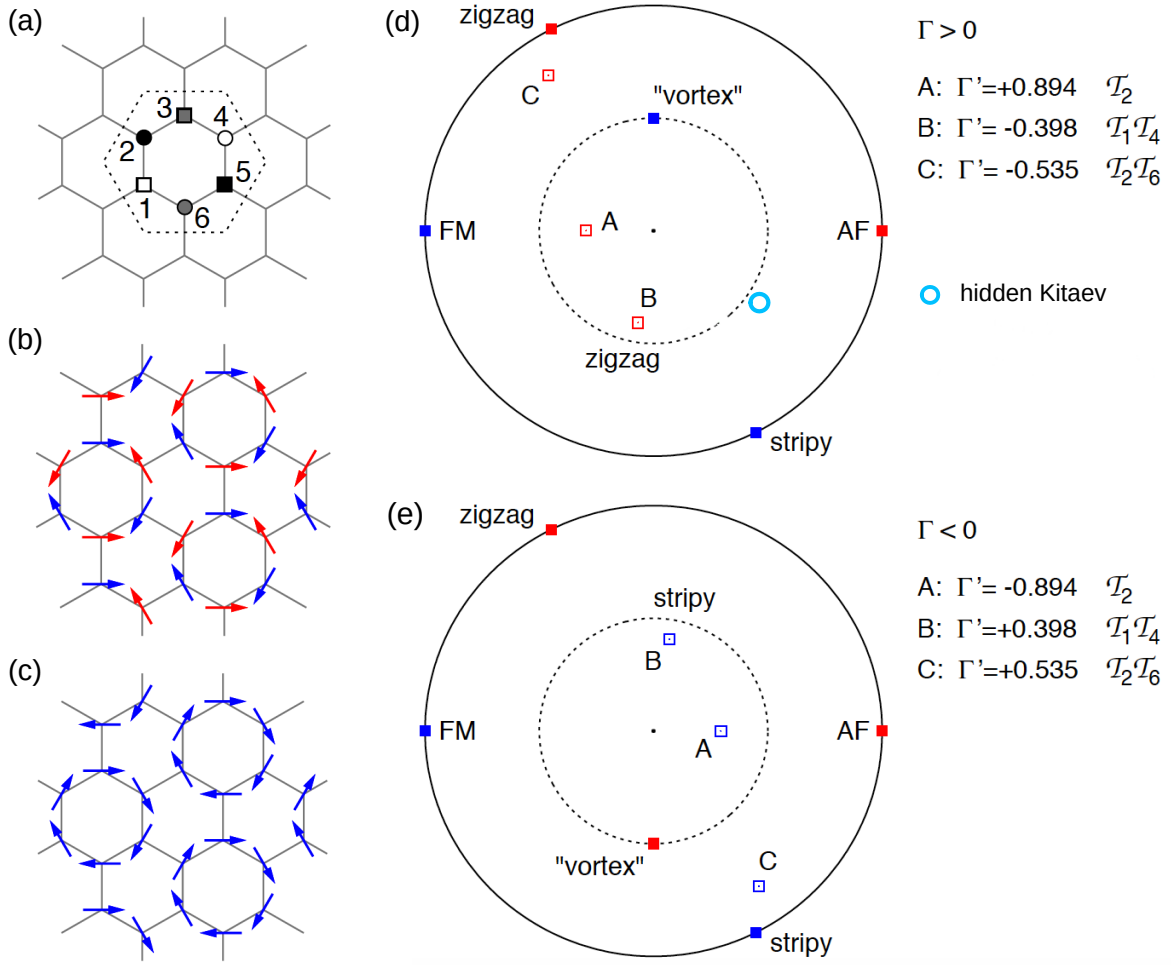

FIGURE 2.21: Selected hidden symmetries of the J-K-Γ-Γ'-J_3 model. Panel (a)—6 sublattices of the $\mathcal{T}_6$ transformation; panels (b), (c)— examples of the vortex patterns at the vortex SU(2) points for $\Gamma < 0$ ($\Gamma > 0$), respectively, where in case (b) the pseudospins marked by the different colors can be rotated to an opposite orientations by $\mathcal{T}_6$. Panels (d), (e)— special points for the $\Gamma > 0$ ($\Gamma < 0$) cases projected on the J-K-Γ plane, respectively. The points connected to AF and FM SU(2) points are denoted by red and dark blue with their Γ' values given in the legend. Light blue circle denotes hidden AF Kitaev point, as presented in Refs. [29, 38]. All panels taken and modified from Ref. [9].

and including internal structures within each phase will be presented in Chapter 3, we did not include the figures from Ref.[70], but the interested reader is recommended to examine them.

Hidden symmetries of the model

As nicely put in Ref. [12], multiple sets of (J, K, Γ, Γ', J_3) parameters roughly reproduce the properties of Na_2IrO_3 and α-$RuCl_3$. Therefore, a further verification of the estimated values of the parameters depends also on the global and local tendencies on the phase diagram. Having a comprehensive knowledge about as extensive portion of the diagram as possible is a rather challenging task, hence, some guidelines where to look at firstly would be of great value. Fortunately, such guidelines do exist in the form of the hidden symmetries even in the J-K-Γ-Γ' model [9].

In general, such symmetries may concern special points or even finite regions with surprisingly simple Hamiltonian, but even in the former case those special points may be considered as "sources" of a particular phase [9]. Below we shortly describe the symmetries of J-K-Γ-Γ' model, the transformations leading to them and the deep consequences for the real materials they bring [9], leaving the rest of the hidden dualities and their extensive discussion for Chapter 3.

Before we introduce the transformations, we once again bring back the XYZ frame, related to the xyz frame by the rotation matrix

$$\mathcal{R}_{\mathrm{XYZ}} = \begin{pmatrix} \frac{\sqrt{6}}{6} & \frac{\sqrt{6}}{6} & -\frac{\sqrt{6}}{3} \\ -\frac{\sqrt{2}}{2} & \frac{\sqrt{2}}{2} & 0 \\ \frac{\sqrt{3}}{3} & \frac{\sqrt{3}}{3} & \frac{\sqrt{3}}{3} \end{pmatrix} \tag{2.23}$$

As illustrated on Fig. 2.6 (b), X and Y axes lie in the honeycomb plane while the Z axis points perpendicularly, "towards the reader". Equipped with the two convenient frames we move towards the transformations.

$\mathcal{T}_1$ transformation

The only transformation mapping the J-K-Γ-Γ' model onto itself is the global π-rotation around the Z axis [9], it is therefore the simplest to present it in the XYZ frame:

$$(\mathrm{X}', \mathrm{Y}', \mathrm{Z}') = (-\mathrm{X}, -\mathrm{Y}, \mathrm{Z}) \tag{2.24}$$

Despite its simplicity, the transformation proved to be extremely useful because, similarly to the $\mathcal{T}_4$ transformation for the Kitaev-Heisenblerg model, it allows to transfer all the physical quantities of a given point to its self-dual counterpart. For a convenient check of the self-dual partner of any point at the phase diagram we refer to the $\mathcal{T}_1$ matrix form from Ref. [9]:

$$\begin{pmatrix} J \\ K \\ \Gamma \\ \Gamma' \end{pmatrix}' = \begin{pmatrix} 0 & +\frac{4}{9} & -\frac{4}{9} & +\frac{4}{9} \\ 0 & -\frac{1}{3} & +\frac{4}{3} & -\frac{4}{3} \\ 0 & +\frac{4}{9} & +\frac{5}{9} & +\frac{4}{9} \\ 0 & -\frac{2}{9} & +\frac{2}{9} & +\frac{7}{9} \end{pmatrix} \begin{pmatrix} J \\ K \\ \Gamma \\ \Gamma' \end{pmatrix}. \tag{2.25}$$

In that regard we describe two applications of the above transformation to real materials:

Zigzag SU(2) points

$\mathcal{T}_1$ connects upper and lower zigzag regions and, in particular, the hidden AF SU(2) point of the Kitaev-Heisenberg model with the hidden AF SU(2) point lying in the extended neighborhood of the estimated positions of the parameters for real materials [9] [points marked as "zigzag" and "B" in Fig. 2.21 (d)]. As a result, pseudospins aligning along one of the x, y or z axes in the zigag phase of the pure Kitaev-Heisenberg model experience rotation to a more experimentally acceptable direction [39, 58]. We will return to this issue in Chapter 3.

Hidden Kitaev points

Another important result provided by the $\mathcal{T}_1$ transformation is the determination of the self-dual partners of the original Kitaev points [9]. Transforming the AF Kitaev point via Eq. (2.25) locates the hidden AF Kitaev point at $J = \Gamma = 4/9K'$, $K = -1/3K'$, $\Gamma' = -2/9K'$, where K' is the coupling parameter of the original point, resulting in $J = \Gamma \approx 0.624$, $K \approx -0.468$, $\Gamma' \approx -0.312$ in our parametrisation (2.18). Due to the self-duality this point maintains the antiferromagnetic character[43] inherited from the original point. Crucially for application to real materials, the K parameter is negative for the transformed point. In fact, the hidden AF Kitaev point lies relatively close to the predicted values of the coupling parameters for Na_2IrO_3 and α-$RuCl_3$. Moreover, because of the self-duality, the whole AFM KSL region has its hidden "sibling" region around the above hidden point. While we will be analysing this region in detail in Sec.

[43] I.e. $K' > 0$.

3.4.6, we would like to mention a recent Ref. [38] in which an interpolation between the hidden AF Kitaev region and one of the currently established α-$RuCl_3$ locations was presented. The reader can find more on this problem in Sec. 2.6.

The FM Kitaev point $K = -1$ has its self-dual partner in the less experimentally interesting $\Gamma < 0$ part of the diagram. Namely, the hidden FM Kitaev point is located at $J = \Gamma = -4/9K'$, $K = 1/3K'$, $\Gamma' = +2/9K'$. Analogically to the AF KSL region, the much larger FM KSL phase should also have its $\mathcal{T}_1$ representation around this point. While the characteristics of the currently investigated materials do not lie anywhere close to the region, this may change in the future. If so, the larger size of the hidden FM KSL region might facilitate tuning the new material into the spin-liquid state. Thus, the $\mathcal{T}_1$ transformation opened new paths for the realization of the Kitaev physics in the transition-metal oxides.

Now we will introduce other transformations leading to the hidden SU(2) points and the points themselves.

$\mathcal{T}_2$ transformation

In this transformation pseudospins in one of the sublattices are rotated by π around the Z axis, just like in the $\mathcal{T}_1$ case, while the pseudospins in the other sublattice remain unaffected [9]:

$$\begin{aligned}(\mathrm{X}', \mathrm{Y}', \mathrm{Z}') &= (-\mathrm{X}, -\mathrm{Y}, \mathrm{Z}) \qquad \pi \text{ rotation around the Z axis on sublattice A,} \\ (\mathrm{X}', \mathrm{Y}', \mathrm{Z}') &= (\mathrm{X}, \mathrm{Y}, \mathrm{Z}) \qquad \text{identity operation on sublattice B.}\end{aligned} \tag{2.26}$$

$\mathcal{T}_6$ transformation

The six pseudospin rotations can be decomposed into the (anti)cyclic permutations of the components and inversions in the original xyz frame [9]:

$$\begin{aligned}(\mathrm{S}^{x'}, \mathrm{S}^{y'}, \mathrm{S}^{z'}) &= (\mathrm{S}^{x}, \mathrm{S}^{y}, \mathrm{S}^{z}) && \text{sublattice 1,} \\ (\mathrm{S}^{x'}, \mathrm{S}^{y'}, \mathrm{S}^{z'}) &= (-\mathrm{S}^{y}, -\mathrm{S}^{x}, -\mathrm{S}^{z}) && \text{sublattice 2,} \\ (\mathrm{S}^{x'}, \mathrm{S}^{y'}, \mathrm{S}^{z'}) &= (\mathrm{S}^{y}, \mathrm{S}^{z}, \mathrm{S}^{x}) && \text{sublattice 3,} \\ (\mathrm{S}^{x'}, \mathrm{S}^{y'}, \mathrm{S}^{z'}) &= (-\mathrm{S}^{x}, -\mathrm{S}^{z}, -\mathrm{S}^{y}) && \text{sublattice 4,} \\ (\mathrm{S}^{x'}, \mathrm{S}^{y'}, \mathrm{S}^{z'}) &= (\mathrm{S}^{z}, \mathrm{S}^{x}, \mathrm{S}^{y}) && \text{sublattice 5,} \\ (\mathrm{S}^{x'}, \mathrm{S}^{y'}, \mathrm{S}^{z'}) &= (-\mathrm{S}^{z}, -\mathrm{S}^{y}, -\mathrm{S}^{x}) && \text{sublattice 6.}\end{aligned} \tag{2.27}$$

Fig. 2.21 (a) explains how to cover the honeycomb lattice with the above sublattices. The $\mathcal{T}_6$ transformation not only leads to the hidden SU(2) points but also provides more insight about the Kitaev term, which will be discussed in Chapter 3.

Remaining hidden SU(2) points

The above transformations and their combinations also bring in the new hidden SU(2) points. On the external Kitaev –Heisenberg circle of Fig. 2.21 (d) and (e) the hidden SU(2) points are marked by red and blue filled squares. For Γ and $\Gamma' \neq 0$ the new points appear. Since Γ values estimated for iridates and ruthenates remain in the positive range, we are mainly interested in Fig. 2.21 (d). The remaining SU(2) points for $\Gamma > 0$ are found by the $\mathcal{T}_2$ (A), $\mathcal{T}_2\mathcal{T}_6$ (C) and $\mathcal{T}_6$ transformations ("vortex").

The vortex point has a rather peculiar coupling parameters $J = 0$, $K = \Gamma$, $\Gamma' = 0$ representing only the bond-anisotropic interactions, that nevertheless fit so well together that they form the SU(2) symmetry [9]. Namely, the vortex point in Fig. 2.21 (d) is connected to the FM SU(2)

point [see Fig. 2.21 (c) for an example of the vortex pattern allowed there]. In contrast, the vortex point in Fig. 2.21 (e) for $\Gamma < 0$ is related to the AF SU(2) point.

Finally, in Fig. 2.21 (e) there remains a hidden SU(2) point with the features of stripy ordering (B), fitting well within the non-zero stripy region for $\Gamma < 0$ and connected to the original stripy point of the Kitaev-Heisenberg model. As will be shown in Chapter 3, those and other special points are not mere theoretical curiosities. They serve as pronounced "topographic" features, explaining to a large extent the complicated trends on the phase diagram.

2.5.3 Phase diagram of the J-K-Γ-J_3 model

Further-neighbor Heisenberg interactions also tend to stabilize the zigzag order [62, 37, 65]. According to Ref. [37], third nearest neighbor J_3 coupling is the strongest among them for both Na_2IrO_3 and α-$RuCl_3$. Comparison of Fig. 2.20 (a) and (b) reveals a substantial reaction of the system to a small positive $J_3 \sim 0.1$. The two zigzag regions merge and broaden, which, along with the still large Néel region, suppresses the other phases on the diagram [37]. We will continue this discussion in Chapter 3, where we will present more data further confirming this tendency.

2.6 Recent developements

We would like to point out a very interesting theoretical development concerning the hidden symmetries and the evolution of α-$RuCl_3$ in the external magnetic field proposed recently in Ref. [38]. As described in Sec. 2.2.1, application of the magnetic field directed perpendicularly to the honeycomb plane for (a) AF Kitaev model leads to the appearance of an intermediate phase (IP), while (b) nothing particularly interesting exists above FM KSL. Ref. [38] shows that utilizing special site-dependent field rotated according to the four-sublattice scheme in case (a) produces the result (b) and *vice versa*. Perhaps more importantly, another path to the field-induced intermediate phase is provided. Ref. [38] shows that strong enough uniform perpendicular field is not only able to produce the IP phase above the KSL around the hidden AF Kitaev point, but also its range spreads above the zigzag phase in the α-$RuCl_3$ location (see Fig. 11 there for the phase diagram of the model interpolating between the hidden AF Kitaev and α-$RuCl_3$ point).

Finally, we would like to mention other interesting developements of the Kitaev-related physics that do not directly influence the results in the following chapter, but the interested reader may find them inspiring. The Kitaev-Heisenberg model may be also considered for the kagome [72] and triangular [73] lattices. One could study the behaviour of its ground state from the 1D chain, through a ladder, up to proper 2D honeycomb lattice [74, 75], or consider the system's behaviour in finite temperature via the tensor networks [76]. The effective models for other candidate materials could also be explored, e.g. α-Li_2IrO_3 [77] or very promising $Na_3Co_2SbO_6$ with less-extended $3d$ orbitals [13]. Even bosonic version of the Kitaev model for the d^4 electronic configuration [78] may be considered.

As the reader could see, the field of the Kitaev-related physics has a short but intense history. Such a dynamic development led to the accumulation of quite a bulk of knowledge, hence this long introduction. We hope that the material condensed within this chapter allowed to build solid background about some of the current problems in the field and will be useful for the reader in the future. We tried to keep the amount of details at bay, leaving however enough to build strong experimental and theoretical arguments for the LRO and spin-liquid tendencies as well as provide some understanding of the frustration and quantum spin liquid phenomena. In the following chapter we will present our input to the field.

Chapter 3

Magnetic ordered moment studies for Kitaev-like models.

3.1 Magnetic ordered moment in the effective models

Understanding magnetic properties of late transition-metal compounds such as Na_2IrO_3 or α-$RuCl_3$ requires several layers of approximations. To paint a still relatively simple picture we start from the magnetic Ir^{4+}/Ru^{3+} ions forming the honeycomb lattice. In zero temperature the magnetic moments $\mathbf{M}_i$ appearing at every site of the lattice can potentially form a magnetically ordered or disordered state. The strength and spatial orientation of these magnetic moments define the magnetic order in the system as the order parameter for particular magnetic phase sums up the moments over suitable sublattices. Such a simple description masks however the fact that the behaviour of $\mathbf{M}_i$ is influenced by the properties of oxygen/chlorine octahedra encapsulating the transition metal ions.

Why should one engage into such an intricate problem though? As the reader remembers from Sec. 2.3, Na_2IrO_3 and α-$RuCl_3$ do not have a spin-liquid ground state but display long range zigzag order instead. Interestingly however, on the phase diagram of the J-K-Γ-Γ' model (2.22) the zigzag regions touch both the explicit Kitaev spin-liquid windows around the $K \pm 1$ Kitaev points as well as the hidden one around the hidden AF Kitaev point. It is therefore important for quantum computing applications to know how far from the liquid windows the real materials are. This can be understood by taking experimental orientations of the magnetic patterns (Sec. 2.3.4) and pointing out where in the zigzag regions on the diagram those particular orientations appear. Owning a dense *map* of the precise properties of the ordered moments at each point of the J-K-Γ-Γ'-J_3 phase diagram would enable such a comparison. This would allow us to narrow down the pool of model parameters set by multiple *ab-initio* studies, greatly simplifying further calculations, and to provide more precise data for groups exploring driving those materials into the spin-liquid state (Sec. 2.3.3).

Since we are interested in details of such a map, we have to keep in mind that the Kitaev-like models are written in terms of pseudospins $\tilde{\mathbf{J}}$—the appropriate degrees of freedom for materials with the strong crystal-field splitting and spin-orbit coupling dominating over interactions between t_{2g} electrons on neighboring ions [4]. Here we would like to connect the dots and briefly sketch the relation between $\tilde{\mathbf{J}}$ and $\mathbf{M}$:

In case of a coupling between spin and orbital degrees of freedom the total angular momentum is formed

$$\mathbf{J} = \mathbf{L} + \mathbf{S}, \tag{3.1}$$

and the suitable magnetic moment is in general *not* parallel to $\mathbf{J}$ [79]:

$$\mathbf{M} = \mathbf{L} + 2\mathbf{S}. \tag{3.2}$$

Specific assumptions considered for Na_2IrO_3 and α-$RuCl_3$ can simplify this situation considerably. In an ideal case, the cubic crystal field originating from the oxygen/chlorine octahedra splits the d subshell of Ir^{4+}/Ru^{3+} ions into e_g and t_{2g} and the spin-orbit coupling further filters

out the degeneracy. As mentioned in Sec. 2.1.1, the low spin state, appearing because of a large crystal-field gap, allows us to focus entirely on the t_{2g} orbital. Then, instead of considering the $\mathbf{L}$ operator projected to the whole d subshell ($\mathbf{L}_d$), we may consider just its t_{2g}-restricted part ($\mathbf{L}_{t_{2g}}$). It turns out that $\mathbf{L}_{t_{2g}}$ is proportional to the $\mathbf{L}$ operator projected to the p subshell ($\mathbf{L}_p$). In other words, the set of matrices $\mathrm{L}^{\gamma}_{t_{2g}}$ for any set of orthogonal axes γ are proportional to L^{γ}_{p} matrices, differing from it only by the minus sign. Thus, for t_{2g} orbitals we can replace quantum number $\mathrm{L}_d = 2$ with effective quantum number $\mathrm{L}_{t_{2g}} = -\mathrm{L}_p = -1$.[1]

In real materials oxygen/chlorine cages may not have an ideal octahedral shape. In case of the honeycomb iridates and ruthenates, where the imperfect octahedra share edges, on the top of the cubic crystal-field splitting a trigonal distortion[2] Δ appears, leading up to further splitting of the t_{2g} subshell. Since the trigonal distortion occurs along the direction perpendicular to the honeycomb plane, it is the easiest to label it by Z, utilizing the XYZ frame from Fig. 2.6 (b). Taking the trigonal Z axis as the quantization axis, one may also include the trigonal distortion into the Kramers doublet [4, 11][3]

$$\left|\tilde{\mathrm{J}} = \frac{1}{2}, \tilde{\mathrm{J}}^{\mathrm{Z}} = +\frac{1}{2}\right\rangle = +\sin\vartheta|0,\uparrow_{\mathrm{Z}}\rangle - \cos\vartheta|+1,\downarrow_{\mathrm{Z}}\rangle, \tag{3.3}$$

$$\left|\tilde{\mathrm{J}} = \frac{1}{2}, \tilde{\mathrm{J}}^{\mathrm{Z}} = -\frac{1}{2}\right\rangle = -\sin\vartheta|0,\downarrow_{\mathrm{Z}}\rangle + \cos\vartheta|-1,\uparrow_{\mathrm{Z}}\rangle, \tag{3.4}$$

where $\tilde{\mathrm{J}}^{\mathrm{Z}} = \pm 1/2$, $\uparrow_{\mathrm{Z}}$, $\downarrow_{\mathrm{Z}}$, and 0, ± 1 correspond to the Z projection of the pseudospin, spin and $\mathrm{L}_{t_{2g}}$ of a hole, respectively. The so-called spin-orbit mixing angle ϑ is related to the trigonal distortion by

$$\tan(2\vartheta) = \frac{2\sqrt{2}}{1+\delta}, \tag{3.5}$$

$$\delta = \frac{2\Delta}{\lambda}, \tag{3.6}$$

where λ is the ionic spin-orbit coupling parameter [11]. In the hole picture the single-ion Hamiltonian reads then as follows

$$\mathcal{H}_{ion} = +\lambda \mathbf{L}_p \cdot \mathbf{S} - \Delta \left(\mathrm{L}^{\mathrm{Z}}_p\right)^2, \tag{3.7}$$

where the first term holds an effective spin-orbit interaction and the second term describes the trigonal splitting of orbitals. As will be shown below, the presence or absence of trigonal distortion deeply affects the relationship between $\tilde{\mathbf{J}}$ and $\mathbf{M}$.

Now, the magnetic moment can be described as

$$\mathbf{M} = \mathbf{L}_{t_{2g}} + 2\mathbf{S} = -\mathbf{L}_p + 2\mathbf{S}. \tag{3.8}$$

By calculating the matrix elements of $\mathrm{L}^{\mathrm{Z}}_p$, S^{Z} and $\tilde{\mathrm{J}}^{\mathrm{Z}}$ in the Kramers basis (3.3-3.4) we may simplify the above formula. Obviously,

$$\left\langle \tilde{\mathrm{J}}^{\mathrm{Z}} = \pm\frac{1}{2}\right| \tilde{\mathrm{J}}^{\mathrm{Z}} \left|\tilde{\mathrm{J}}^{\mathrm{Z}} = \pm\frac{1}{2}\right\rangle = \pm\frac{1}{2}, \tag{3.9}$$

[1] We use capital letters, similarly to e.g. Ref. [12], to be more consistent with the LS scheme and not to confuse the less-experienced reader with the small letters, possibly misinterpretted as coming from the jj scheme. We are aware that in the ground state for the materials in question both schemes converge and that the most popular convention for quantum numbers utilizes small letters.

[2] Of the octahedra.

[3] Here we follow consistently the notation from Ref. [11].

while

$$\left\langle \tilde{\mathrm{J}}^{\mathrm{Z}} = \pm\frac{1}{2}\right| \mathrm{L}_p^{\mathrm{Z}} \left|\tilde{\mathrm{J}}^{\mathrm{Z}} = \pm\frac{1}{2}\right\rangle = \pm\cos^2\vartheta = \pm\frac{1}{2}\left(2\cos^2\vartheta\right), \tag{3.10}$$

$$\left\langle \tilde{\mathrm{J}}^{\mathrm{Z}} = \pm\frac{1}{2}\right| \mathrm{S}^{\mathrm{Z}} \left|\tilde{\mathrm{J}}^{\mathrm{Z}} = \pm\frac{1}{2}\right\rangle = \pm\frac{1}{2}\left(\sin^2\vartheta - \cos^2\vartheta\right). \tag{3.11}$$

Hence, $\mathrm{L}_p^{\mathrm{Z}} = 2\cos^2\vartheta\tilde{\mathrm{J}}^{\mathrm{Z}}$ and $\mathrm{S}^{\mathrm{Z}} = \left(\sin^2\vartheta - \cos^2\vartheta\right)\tilde{\mathrm{J}}^{\mathrm{Z}}$. Moreover, due to the Eckart -Wigner theorem we can also write that $\mathbf{L}_p = 2\cos^2\vartheta\tilde{\mathbf{J}}$, $\mathbf{S} = \left(\sin^2\vartheta - \cos^2\vartheta\right)\tilde{\mathbf{J}}$ [11]. Then, the magnetic moment can be written as

$$\mathbf{M} = 2\left(\sin^2\vartheta - 2\cos^2\vartheta\right)\tilde{\mathbf{J}}. \tag{3.12}$$

When $\Delta = 0$, the spin-orbit mixing angle $\vartheta \approx 35.26°$, leading to $\mathbf{L}_p = 4\tilde{\mathbf{J}}/3$, $\mathbf{S} = -\tilde{\mathbf{J}}/3$, which simplifies $\mathbf{M}$ considerably

$$\mathbf{M} = -2\tilde{\mathbf{J}}. \tag{3.13}$$

Thus, when the trigonal distortion is absent the effective picture given by formula (3.13) makes the magnetic moment on every iridium/ruthenium site antiparallel to the pseudospin $\tilde{\mathbf{J}}$ [11]. This simplification would allow for a more direct comparison between the theoretical predictions and experimental findings. However, when the trigonal distortion is present,[4] a non-zero angle appearing between $\mathbf{M}$ and $\tilde{\mathbf{J}}$ makes the comparison between theory and experiment more challenging.

Our strategy in the current chapter is to first analyse the orientation and absolute value of the pseudospins $\tilde{\mathbf{J}}$ for the Kitaev-like models. Once this discussion is complete, we will use a translation of the orientation of the magnetic moments to the orientation of the pseudospins obtained in Ref. [11] to specify the windows of Hamiltonian parameters applicable for Na_2IrO_3 and α-$RuCl_3$ and discuss the compatibility of these windows with the *ab initio* results.

Finally, let us also state three important technical remarks:
Similarly to Chapter 2, below we will denote $\tilde{\mathbf{J}}$ *pseudospin as* $\mathbf{S}$ *to be consistent with the dominant convention in the literature.* Then, formula (3.13) reads as

$$\mathbf{M} = -2\mathbf{S}. \tag{3.14}$$

The second remark concerns what exactly is understood by the "ordered moment" in this chapter. It coincides with the general definition of the order parameter of the magnetic phases [1]. In the context of Kitaev-like models we can define the expression

$$\mathcal{S} = \frac{1}{\mathrm{I}}\sum_{\mathrm{I}}\frac{1}{\mathrm{N_I}}\sum_{i\in\mathrm{I}}^{\mathrm{N_I}}\begin{pmatrix}\mathrm{sgn}\left(\langle \mathrm{S}_i^x\rangle\right)\langle \mathrm{S}_i^x\rangle \\ \mathrm{sgn}\left(\langle \mathrm{S}_i^y\rangle\right)\langle \mathrm{S}_i^y\rangle \\ \mathrm{sgn}\left(\langle \mathrm{S}_i^z\rangle\right)\langle \mathrm{S}_i^z\rangle\end{pmatrix}. \tag{3.15}$$

A particular magnetic pattern can be split into I sublattices, where the pseudospins belonging to each sublattice have the same spatial orientation. Then, inside each of the sublattices one can sum the averages weighted by their sign, so that there is no cancellation of terms. The factor 1/I brings the normalization over the number of sublattices while the factor $1/\mathrm{N_I}$—over the number of sites inside each sublattice. In the end, the summation over all sublattices is performed. Expression (3.15) works not only for the trivial cases of the ferromagnetic and Néel patterns, but also it returns a non-zero vector for the more complex patterns like vortex [Fig. 2.21 (b) and (c)], which has six sublatices to be summed over.

[4] For now we remind the reader that in the nearest-neighbor-restricted Kitaev-like Hamilttonian (2.22) $\Delta \neq 0$ is represented by the Γ' term [70]; we will return to this issue at the end of this chapter.

Part the results presented in this chapter was published in two papers:

- [80] Dorota Gotfryd, Juraj Rusnačko, Krzysztof Wohlfeld, George Jackeli, Jiří Chaloupka, and Andrzej M. Oleś, *Phase diagram and spin correlations of the Kitaev-Heisenberg model: Importance of quantum effects*, Phys. Rev. B. **95**, 024426 (2017), [a multi-method analysis for the Kitaev-Heisenberg model],
- [29] Juraj Rusnačko, Dorota Gotfryd, and Jiří Chaloupka, *Kitaev-like honeycomb magnets: Global phase behavior and emergent effective models*, Phys. Rev. B **99**, 064425 (2019), [a multi-method analysis for the J-K-Γ-Γ'-J_3 model].

3.2 Methods

Here we will explain how the orientation and absolute value of the ordered moment can be obtained. In order to recognise magnetic order of the quantum system one needs access to the ground state. Since Kitaev-like models keep the combined C_3 pseudospin and lattice symmetry at each iridium/ruthenium site intact, the superposition in their ground state will often[5] contain six terms with the largest coefficients. The sources of this phenomenon are bond-anisotropic terms such as Kitaev, Γ and Γ', that invoke selection of the easy axis by the order-by-disorder mechanism. In the simplest Kitaev-Heisenberg case the three equivalent easy axes that could be selected from all other possible directions will be the Kitaev interaction axes $\gamma = x,\ y,\ z$ [11]. Along each of these axes pseudospins can be arranged in two ways, hence six equivalent magnetic patterns with the largest probability. Therefore, we could say that the ground state of Kitaev-like models emulates the perfectly isolated microscopic sample of the materials in question.

However, measuring magnetic ordered moment in a crystal sample gives a particular Bragg spot in case of the long-range order, which means that one direction is selected. This is due to the spontaneous symmetry breaking (SSB) phenomena [1, 81] which would here concern C_3 discrete symmetry. The proper analytical approach to SSB requires introducing a weak magnetic field to the magnetization formula for an *infinite* system and then taking the field to zero from above [81]. Unfortunately, for the complicated Kitaev-like models such approach is highly impractical.

A reasonable way to obtain the ordered moment requires performing the numerics on the largest and most symmetric cluster and supplementing it with the analytics at those selected points where the Hamiltonian simplifies [5, 6, 9, 29]. At this point the choice of the numerical method depends on what information is more important to us: we can choose a method keeping as much of the quantum superposition in the ground state as possible, which would result in very accurately estimated orientations of the pseudospins but the ordered moment value would not be easily accessible. We can also polarize the boundary of the cluster and obtain the value of the ordered moment in a self-consistent manner, but the price for disturbing quantum fluctuations of the microscopic system would be worse precision in the direction of the moments and a possible struggle with the convergence. Below we describe both of these aproaches, inevitably putting more details to the latter, which the author of the thesis was utilizing.

3.2.1 Exact diagonalization

Exact diagonalization (ED) literally means numerical diagonalization of the Hamiltonian matrix. Full exact diagonalization produces complete energy spectrum and eigenstates of a given Hamiltonian, but is possible only on smaller systems, up to 16 sites for (pseudo)spin 1/2.[6] Larger systems, necessary for the Kitaev-like models, require turning to the Lanczos method [82]. With a smartly chosen and carefully tested truncating condition the latter method produces a ground

[5] This concerns especially Kitaev-Heisenberg model where long-range order is exclusively collinear.

[6] For very symmetric Hamiltonians like Heisenberg the size accessible for full ED may be even larger.

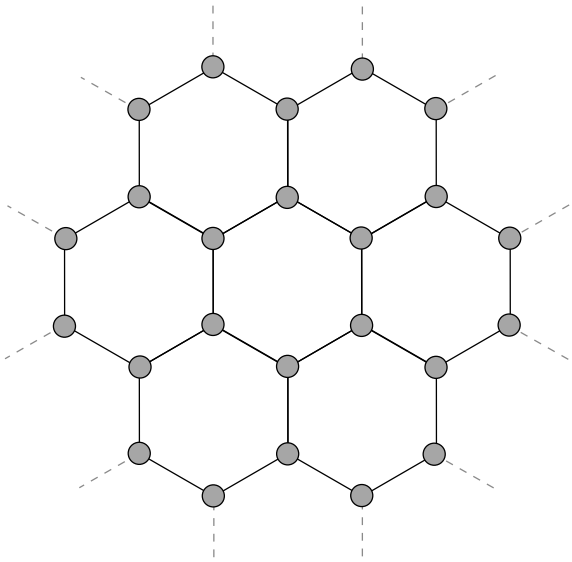

FIGURE 3.1: 24-site symmetric cluster of the honeycomb lattice with periodic boundary conditions.

state which is very well converged to the full-ED ground state. The smallest cluster compatible with all the collinear and most of the non-collinear magnetic patterns that would also not favour any particular direction is the 24-site cluster, presented in Fig. 3.1.

Importantly, the ED method equipped with the suitable periodic boundary conditions (PBC) treats all bonds equally, ensuring a less-biased,[7] fully quantum ground state. In the simplest, non-degenerate case it produces a state containing the superposition of different magnetic patterns.[8] The dominant coefficients stand before the symmetry-allowed versions of the magnetic order suitable for the particular set of the Hamiltonian parameters. This means two possibilities of the pseudospins' orientation for a given direction multiplied by the coefficients with the same absolute value, resulting in $\langle \mathrm{GS}|\mathbf{S}_i|\mathrm{GS}\rangle = 0$. However, the characteristics of the ordered moment can be still obtained from the ground state utilizing the methods listed below.

Correlation matrix method

In this standard approach the ordered moment direction is found by diagonalizing

$$\langle \mathrm{S}^{\alpha}_{-\mathbf{Q}} \mathrm{S}^{\beta}_{\mathbf{Q}} \rangle, \tag{3.16}$$

where α, $\beta = x$, y, z, and taking the direction of the largest eigenvector. Unfortunately, for a significant part of the parameter space the method is unable to uniquely identify the direction due to the degenerate eigenvalues appearing because of the above-mentioned equal coefficients multiplying equivalent patterns in the ground state. Furthermore, finite size effects mix in some contributions of the equivalent patterns into the correlation matrix for the selected $\mathbf{Q}$ vector that would ideally represent only one of those patterns. The reader is advised to visit Appendix A of Ref. [11] for details.

Maximal overlap method

This method, introduced in Ref. [11], utilizes classical arrangements of the pseudospin "arrows", the so-called spin – coherent states. To produce such a state with a particular orientation of the

[7] For completeness we note that there exists some PBC-related bias—PBC filter out the configurations with the magnetic unit cells larger than the size of the cluster. Without the PBC, however, one calculates the state of an isolated cluster instead of approximating macroscopic crystal.

[8] For a quantum Hamiltonian.

"arrows", one has to rotate "arrow up" in the z direction into a new direction n. If direction n is given by spherical angles θ, ϕ then $n = (\sin\theta\cos\phi,\ \sin\theta\sin\phi,\ \cos\theta)$ and the rotated "arrow" has the form

$$|\theta,\phi\rangle = e^{-i\phi \mathrm{S}^z} e^{-i\theta \mathrm{S}^y} |\uparrow\rangle. \tag{3.17}$$

The spin-coherent state is a direct product of the "arrows" given by formula (3.17)

$$|\Psi\rangle = |\theta_1,\phi_1\rangle \otimes |\theta_2,\phi_2\rangle \otimes ... \otimes |\theta_\mathrm{N},\phi_\mathrm{N}\rangle = \prod_{i=1}^{\mathrm{N}} |\theta_i,\phi_i\rangle, \tag{3.18}$$

where the multiplication is executed over all sites of the cluster. For the collinear phases the pattern with the largest overlap with the ground state sets the ordered moment direction. Such a pattern has the maximal probability of being realized in the system with the ground state $|\mathrm{GS}\rangle$, given by

$$\mathcal{P}(\theta,\phi) = |\langle\Psi|\mathrm{GS}\rangle|^2. \tag{3.19}$$

For non-collinear phases, introduced by the Γ term, $(\theta_i,\ \phi_i)$ may differ from site to site. Therefore, one has to search for the pattern with maximal $\mathcal{P}(\theta_i,\phi_i)$ and extract directions (θ_i,ϕ_i) for the pseudospin at each site i. Such examination is done in an iterative way, by the global and local optimization algorithms. As a result, the maximal probability-based phase diagram can be produced.

Such calculations were performed by Jiří Chaloupka and Juraj Rusnačko and published together with the cluster mean-field theory results of the author of this thesis in Ref. [29].

3.2.2 Self-consistent cluster mean-field theory

Self-consistent cluster mean-field theory (CMFT) is the simplest junction of exact-diagonalization and mean-field approaches [83]. At the beginning, we divide the system into two non-equivalent parts, as illustrated on Fig. 3.2. The first part consist of the grey sites which will be experiencing a fully quantum Hamiltonian with the "operator-operator" terms only. The second part is built from the black sites, directly exposed on the effective (molecular) magnetic fields [1] emanating from the empty squares. Those are the matching black sites from the periodic copies of the cluster. The effective fields are applied by the mean-field part of the CMFT Hamiltonian. Altogether, the CMFT Hamiltonian for the nearest-neighbor Kitaev-like model consists of:

$$\mathcal{H} = \sum_{\text{internal bonds}} \mathcal{H}_\mathrm{IN} + \sum_{\text{MF bonds}} \mathcal{H}_\mathrm{MF}, \tag{3.20}$$

with

$$\mathcal{H}_\mathrm{IN}|_\eta = J\mathbf{S}_i\cdot\mathbf{S}_j + K\mathrm{S}_i^\gamma\mathrm{S}_j^\gamma + \Gamma\left(\mathrm{S}_i^\alpha\mathrm{S}_j^\beta + \mathrm{S}_i^\beta\mathrm{S}_j^\alpha\right) \tag{3.21}$$

$$+\Gamma'\left(\mathrm{S}_i^\alpha\mathrm{S}_j^\gamma + \mathrm{S}_i^\gamma\mathrm{S}_j^\alpha + \mathrm{S}_i^\beta\mathrm{S}_j^\gamma + \mathrm{S}_i^\gamma\mathrm{S}_j^\beta\right), \tag{3.22}$$

$$\mathcal{H}_\mathrm{MF}|_\eta = J\mathbf{S}_i\langle\mathbf{S}_j\rangle + K\mathrm{S}_i^\gamma\langle\mathrm{S}_j^\gamma\rangle + \Gamma\left(\mathrm{S}_i^\alpha\langle\mathrm{S}_j^\beta\rangle + \mathrm{S}_i^\beta\langle\mathrm{S}_j^\alpha\rangle\right) \tag{3.23}$$

$$+\Gamma'\left(\mathrm{S}_i^\alpha\langle\mathrm{S}_j^\gamma\rangle + \mathrm{S}_i^\gamma\langle\mathrm{S}_j^\alpha\rangle + \mathrm{S}_i^\beta\langle\mathrm{S}_j^\gamma\rangle + \mathrm{S}_i^\gamma\langle\mathrm{S}_j^\beta\rangle\right), \tag{3.24}$$

where α, β and $\gamma \in \{x,\ y,\ z\}$ are defined for each $\eta = a$, b or c bond direction perpendicular to γ. For example, $\mathcal{H}_\mathrm{IN}$ and $\mathcal{H}_\mathrm{MF}$ on the c-bonds will have the form

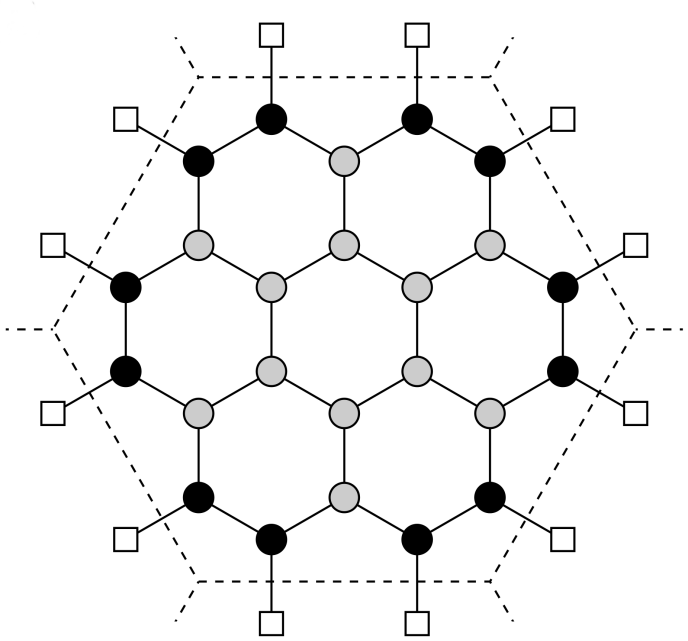

FIGURE 3.2: 24-site symmetric cluster with periodic boundary conditions treated in a mean-field way. While the grey sites experience a fully quantum Hamiltonian, the black sites are exposed to the effective field produced by their periodic neighbors, here denoted as the empty squares. Figure has been published in Ref. [80].

$$\mathcal{H}_{\mathrm{IN}}|_c = J\mathbf{S}_i \cdot \mathbf{S}_j + K\mathrm{S}_i^z\mathrm{S}_j^z + \Gamma\left(\mathrm{S}_i^x\mathrm{S}_j^y + \mathrm{S}_i^y\mathrm{S}_j^x\right) \tag{3.25}$$

$$+\Gamma'\left(\mathrm{S}_i^x\mathrm{S}_j^z + \mathrm{S}_i^z\mathrm{S}_j^x + \mathrm{S}_i^y\mathrm{S}_j^z + \mathrm{S}_i^z\mathrm{S}_j^y\right), \tag{3.26}$$

and

$$\mathcal{H}_{\mathrm{MF}}|_c = J\mathbf{S}_i\langle\mathbf{S}_j\rangle + K\mathrm{S}_i^z\langle\mathrm{S}_j^z\rangle + \Gamma\left(\mathrm{S}_i^x\langle\mathrm{S}_j^y\rangle + \mathrm{S}_i^y\langle\mathrm{S}_j^x\rangle\right) \tag{3.27}$$

$$+\Gamma'\left(\mathrm{S}_i^x\langle\mathrm{S}_j^z\rangle + \mathrm{S}_i^z\langle\mathrm{S}_j^x\rangle + \mathrm{S}_i^y\langle\mathrm{S}_j^z\rangle + \mathrm{S}_i^z\langle\mathrm{S}_j^y\rangle\right). \tag{3.28}$$

Similarly to the usual mean-field approach, the method is self-consistent, therefore it needs the initial polarization of the boundary to produce effective fields. In principle, the ansatz could be random, but ordered patterns, obtained e.g. from the maximal overlap method, significalntly accelerate the calculations. Once the suitable ansatz for the boundary is chosen, we diagonalize the full Hamiltonian by ED. The resulting ground state may be polarized to various extent, depending on the coupling parameters values. It may contain less quantum fluctuations than the one emerging from pure ED. The first iteration is closed by calculating new averages $\langle\mathrm{S}_i^\gamma\rangle$ in this ground state. In each iteration the averages obtained in the previous step are applied to the mean-field part of the Hamiltonian. Once the averages in two subsequent iterations are equal up to the desired precision, the calculations can stop. In our calculations, after exiting the loop, we corrected the ground state energy by the $\langle\mathrm{S}_i^\alpha\rangle\langle\mathrm{S}_j^\beta\rangle$ terms to fully fit the mean-field approximation on the boundary bonds[9]

[9]Computational tip: here α and β can be also equal. Appropriate summation and considering the symmetries of the system allows for using just one of the first two terms in the formula (3.29).

$$\mathrm{S}_i^\alpha \mathrm{S}_j^\beta \approx \mathrm{S}_i^\alpha \langle \mathrm{S}_j^\beta \rangle + \langle \mathrm{S}_i^\alpha \rangle \mathrm{S}_j^\beta - \langle \mathrm{S}_i^\alpha \rangle \langle \mathrm{S}_j^\beta \rangle. \tag{3.29}$$

At this point it is important to understand the mechanism of obtaining stable pseudospin averages in CMFT. Polarization of the boundary literally reduces quantum fluctuations on the black sites. Although only these external sites directly experience the effective fields, through indirect polarization the resulting averages may be non-zero[10] inside the cluster. The scale of this effect depends on the specific values of the model parameters as well as the size and geometry of the cluster, but, in general, the further from the boundary a site is, the less polarized its pseudospin should be—the value of the average will be decreasing. In other words, the central part of the cluster should contain the largest amount of quantum fluctuations. For the 24-site symmetric cluster the central hexagon is the most quantum. If other frustration-related effects are excluded,[11] all the observables, including the pseudospin averages and energy, taken from this region will be the most reliable.

CMFT bias

The initial polarization, however, is also responsible for the downside of the method. While for the purely-Heisenberg nearest-neighbor model the effect is just the overestimated length of the average vector,[12] which can be corrected to some extent by considering values from the most inner part of the cluster, introducing the bond-anisotropic Kitaev, Γ and Γ' terms creates a more complicated case. The heart of the trouble lies in the bond anisotropy: in the simplest Kitaev-Heisenberg case for each direction on the honeycomb lattice there is an additional mean-field term from the Kitaev part, consisting of one pseudospin component only. For instance, for bond a the extra mean field comes from the $K\mathrm{S}_i^x\langle \mathrm{S}_j^x \rangle$ term. As a result, a quantum pseudospin on the external site i experiences stronger "pulling" in one direction. Considering the full cluster, pseudospins on some of the black sites will be pulled more in x, some in y, and some in z direction, corresponding to the a, b, and c boundary bonds. Such a setting results in slower convergence and canting tendency for patterns that would emerge as purely collinear from the maximal overlap method based on ED. Nevertheless, with some careful inspection some of the CMFT bias can be removed and undesired effects corrected. We will explain this in detail when analysing the particular results.

Linearized CMFT

A full CMFT procedure can be quite time– and memory-consuming, it is therefore benefitial to try out a linearized CMFT in the context of the Kitaev-like models. To linearize the method we take one iteration of the CMFT loop and consider the outcoming averages $\langle \mathrm{S}_i^\alpha \rangle_{out}$ as functions of the initial averages $\langle \mathrm{S}_j^\beta \rangle_{ini}$.[13] We expand the $\langle \mathrm{S}_i^\alpha \rangle_{out}\left(\langle \mathrm{S}_j^\beta \rangle_{ini}\right)$ mappings and take into account only the linear terms $(\mathrm{F})_{kl}\langle \mathrm{S}_j^\delta \rangle_{\mathrm{ini}}$, where

$$(\mathrm{F})_{kl} = \frac{\partial \langle \mathrm{S}_i^\gamma \rangle_{out}}{\partial \langle \mathrm{S}_j^\delta \rangle_{ini}}, \quad \begin{cases} \gamma = x & k = i \\ \gamma = y & k = 12 + i \\ \gamma = z & k = 24 + i \end{cases}, \quad \begin{cases} \delta = x & l = j \\ \delta = y & l = 12 + j \\ \delta = z & l = 24 + j \end{cases}, \tag{3.30}$$

cf. Fig 3.3. This is because in the general case, necessary for the Hamiltonian containing Γ and Γ', a vector describing all the initial averages on the external sites $\langle \mathrm{S}_j^\delta \rangle_{ini}$ has $3 \times 12 = 36$

[10] With some effort the averages can be reduced to 0 in the disordered phases.

[11] This will be discussed in the context of the CMFT results for the J-K-Γ-Γ' model.

[12] The detailed comparison of the ordered moment value for the Heisenberg model on the honeycomb lattice obtained by various methods will be shown later in this chapter.

[13] α, β, $\delta = x$, y, z.

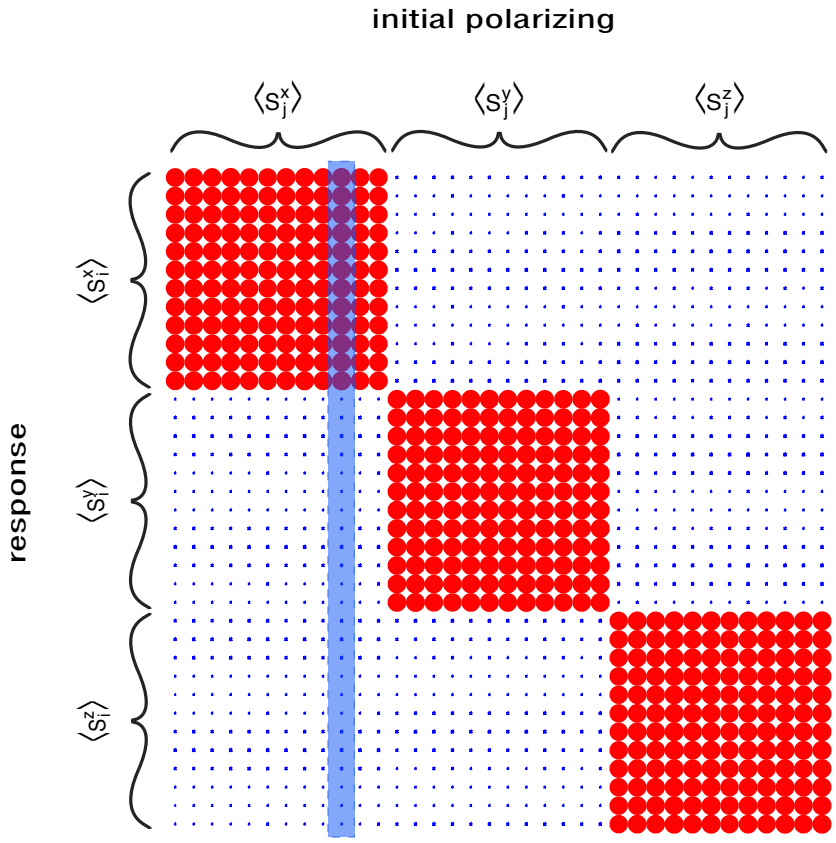

FIGURE 3.3: Example of the linearization matrix F for a 24-site cluster in the general case of the Kitaev-like Hamiltonian. The matrix represents the linear response of the external sites to the separate, single-site and single-component polarization. The blue rectangle marks a response of the whole system to the polarization of a particular component at a particular site. The size of the filled circles represents the strength of the response while the color is connected to the sign of the derivative (blue $\rightarrow -$, red$\rightarrow +$).

coefficients for the 24-site cluster. As a result, the elements $(\mathrm{F})_{kl}$ form a 36×36 matrix F. This matrix records the linear response of all the black sites to the subsequent one-site and component polarizations. For example, the column highlighted in blue represents the response of all the pseudospin components to the initial polarization of just one of them: $\langle \mathrm{S}_m^{\beta} \rangle$, where m is the chosen site and β—the chosen pseudospin component.[14]

To predict the CMFT result we diagonalize this relatively small [15] matrix, take the eigenvalues λ_i, i =1,...,36, and recreate the nth step in the CMFT loop as $(\lambda_i)^n$. For any solution to stabilize, λ_{max}, corresponding to the strongest response of the system, must not only be positive but also larger than one, otherwise $(\lambda_{max})^n$ will converge to zaro. If λ_{max} is larger than one we can predict the pseudospin pattern by looking at the corresponding eigenvector, written in the same basis as $\langle \mathbf{S}_i \rangle$, making the task extremely easy. If λ_{max} is smaller than one there is no magnetic order within the linear approximation. It is worth mentioning that $\lambda_i < 0$ correspond to the oscillations of averages during the iterations. This is caused by the different signs of $(\lambda_i)^n$,

[14] Here we remind the less-experienced reader that the overall appearance of the matrix depends on the convention of indexing the external sites.

[15] Compared to the full Hamiltonian.

flipping the averages for odd and even ns. Therefore, by running the linearized procedure first one can be warned about the potential stability problems before deciding whether to engage in the full CMFT calculations for the selected set of the coupling parameters.

3.2.3 Testing the method for the Kitaev-Heisenberg model and 6 sites

Here we will test the linearized CMFT for a small system and the simplest of Kitaev-like models supporting magnetically ordered phases.

CMFT settings for the Kitaev-Heisenberg model

As it was mentioned earlier, in case of the Kitaev-Heisenberg model the cubic x, y and z axes are selected by the order-by-disorder mechanism as the possible easy axes. For each magnetic phase the pseudospins can align along those three degenerate directions, making six versions of the magnetic patterns with the maximal coefficients in the ED-based ground state. Thus, the ordered moments will orient along the x or y or z axis with maximal probability.[16] As a result, formula

$$\mathbf{S}_i\langle\mathbf{S}_j\rangle \approx \mathrm{S}_i^{\gamma}\langle\mathrm{S}_j^{\gamma}\rangle \tag{3.31}$$

should be no longer an approximation. Here we utilize the most intuitive convention

$$\mathbf{S}_i\langle\mathbf{S}_j\rangle = \mathrm{S}_i^{z}\langle\mathrm{S}_j^{z}\rangle. \tag{3.32}$$

Results for 6 sites

A single hexagon[17] serves as a toy model here—a first test how well the predictions from the linearized CMFT (left panel of Fig. 3.4) match the results of the full method (right panel of the same figure). It turned out that eigenvectors associated with $\lambda_{max} > 1$ described magnetic patterns from the literature: Néel, zigzag, FM and stripy [5, 6].[18] The solution given by the full CMFT matched the linearization rather well, stabilizing the above-mentioned magnetic patterns.

The task was not easy, however, due to certain features of such a small system. Namely, the magnetic unit cells for more complicated patterns such as zigzag or stripy are built from 4 sites, see Fig. 2.17. 6 sites are not suitable to fully establish those phases because the 4-site cells need to be repeated in a periodic lattice. This makes clusters of $4n$ sites optimal from the magnetic point of view.

On the other hand, from the CMFT perspective it would be simpler to have only one species of sites directly affected by the mean field. This is not the case for 4 and 8 sites,[19] where some sites would have two bonds with mean-field interaction. In contrast, 6 sites have the mean field applied in a simple way. Both of these conditions are first met by the $4 \cdot 6 = 24$-site cluster.

The above points sum up to a geometric bias affecting the extent of each magnetic phase. For the single hexagon the zigzag and stripy phases cannot occupy similarly broad regions in the parameter space as visible on the phase diagram based on a 24– site cluster. Instead, both linearized and full CMFT indicate that significantly suppressed magnetic phases give way to two disorder regions, denoted in grey color. In those regions no λ_i is above 1. Moreover, some of the

[16] The only exceptions are the Heisenberg points.

[17] With periodic boundary conditions similar to that for a 24-site cluster.

[18] The reader may look back at Figs. 2.15 and 2.16 in the Chapter 2. Note the small discrepancy: two variants of stripy patterns in case of linearized CMFT on 6 sites.

[19] 8 sites could have some advantage here due to the two full 4-site magnetic cells available, however CMFT would be more complicated in this case: 2 sites with 2 mean-field bonds each, another 2 sites with no mean-field bonds and 4 sites with 1 mean-field bond. Such a complicated system would probably have its own disadvantages. Similar problems would occur for 4 sites. It seems no small system is perfectly suited for CMFT on Kitaev-like models.

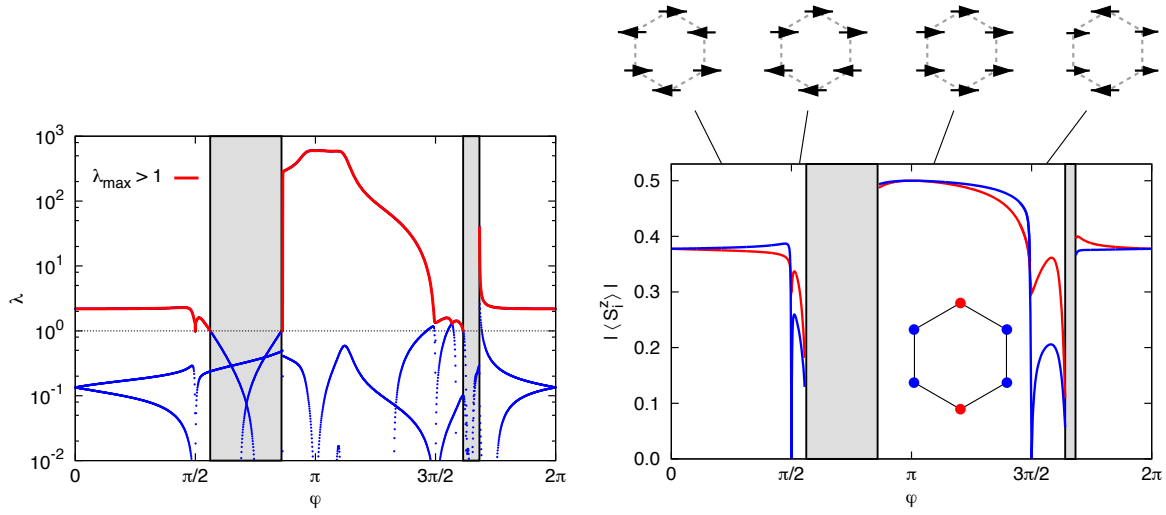

FIGURE 3.4: CMFT results for the Kitaev-Heisenberg model on a 6-site cluster. φ, visible on the horizontal axes of both panels, is the polar angle $\in [0, 2\pi]$ in the parametrization $J = \cos\varphi$, $K = \sin\varphi$ of Hamiltonian (2.12). Left panel presents all the eigenvalues of linearization matrix F (blue color) and marks the largest one of them, λ_{max}, in red when $\lambda_{max} > 1$, predicting the stabilizing tendency. φ intervals for which no λ_i is above 1 are marked in grey—for those parameter values linearized CMFT does not predict any stable order. Right panel presents the stable result from the full CMFT—the pseudospin norm. As explained in the main text, in case of Kitaev-Heisenberg model $|\langle S_i^z \rangle|$ represent the full averages. Red and blue colors mark the results for two species of nonequivalent sites: red sites receive additional portion of effective field from the Kitaev term, which is present only on the c mean-field bonds, while blue sites experience the field only from the Heisenberg part. Magnetic orderings appearing in the Kitaev-Heisenberg phase diagram for 6 sites are shown above the right panel. Again, the disordered regions are marked by grey color. Figure has been published in Ref. [80].

λ_i are below 0[20], causing sign oscillations from iteration to iteration. One of the consequences of this effect was the need to introduce strong damping into the CMFT loop in order to stabilize the stripy phase.

Finally, λ_{max} for the ferromagnetic case is much larger than λ_{max} for the Néel phase. A similar effect is visible in $|\langle S_i^z \rangle|$ coming from the full CMFT. Quantum fluctuations suppress pseudospin moments in the dressed Néel phase, confirming its quantum character. Unfortunately, λ_{max} and $|\langle S_i^z \rangle|$ in the zigzag and stripy phases are of even smaller magnitude. The reason is again the size of the system—6 sites are not enough to accommodate the 4 sublattices of the $\mathcal{T}_4$ transformation properly,[21] which breaks the exact Néel-zigzag and FM-stripy mappings. Here it is clearly the cluster to be blamed since full CMFT is plagued by the same effect. As a closing observation we mention that the Kitaev spin-liquid windows are here reduced to the two Kitaev points $\varphi = \pi/2$, $3\pi/2$.

The above results confirm that the system is simply too small for the strongly frustrated Kitaev-related physics to fully develop and cannot be utilized for systematic analysis of the models in question. Nevertheless, the linearized CMFT as a method proved to be quite useful. Not only did it predict the extent of the magnetic phases and their classical/quantum character rather consistently with the full CMFT, but also it pointed out possible disordered windows and regions where obtaining a stable solution may be challenging. By comparing both approaches we also see that the nonlinear effects do not play an important role in this case.

[20] Not plotted because of the logarithmic scale.
[21] Cf. Fig. 2.18.

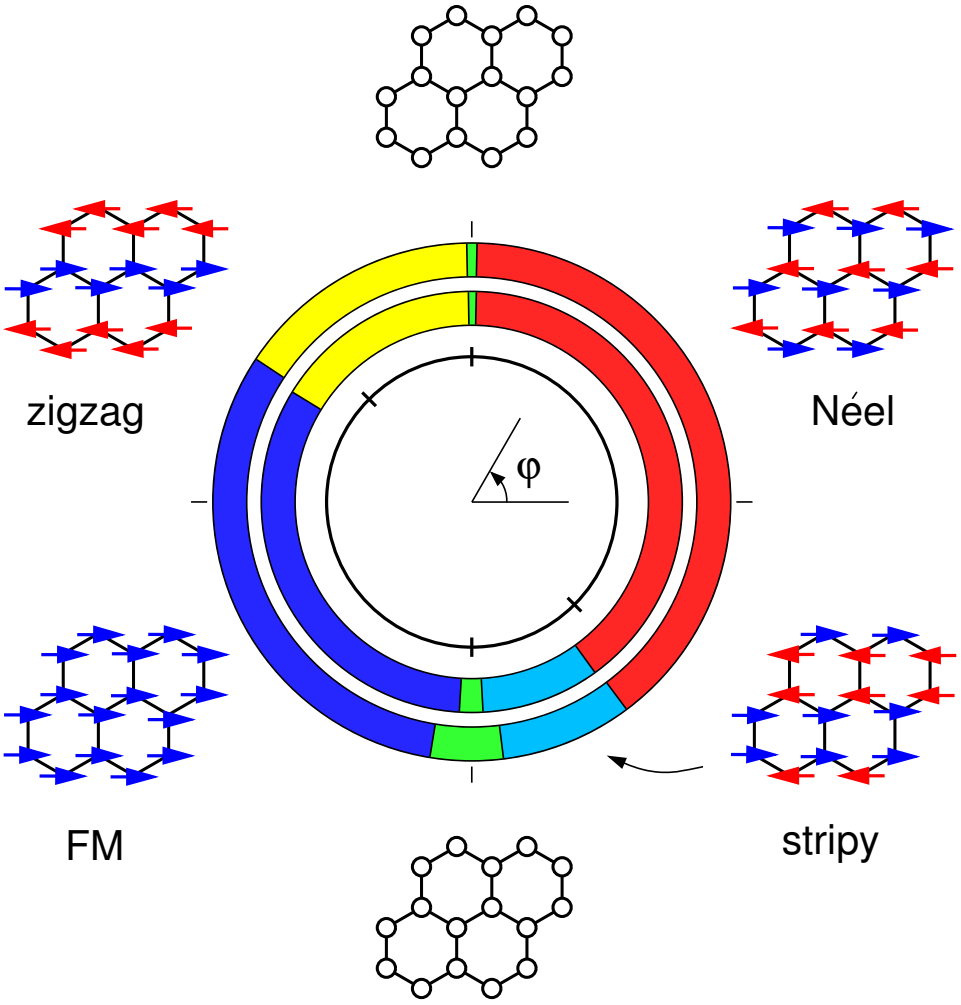

FIGURE 3.5: Composite phase diagram of the Kitaev-Heisenberg model on a 24-site cluster. $\varphi \in [0, 2\pi]$ is the polar angle in the parametrization $J = \cos\varphi$, $K = \sin\varphi$ of Hamiltonian (2.12). AF and FM Heisenberg [SU(2)] and Kitaev points are marked by short black sticks outside the diagram rings. The mini-drawings present magnetic orderings in suitable regions, here aligning along the z axis to fit CMFT settings. The range of the Néel phase is shown in red, zigzag—in yellow, FM—in dark blue and stripy—in light blue. Green is reserved for the Kitaev spin-liquid regions. Inner black circle represents classical diagram, middle ring—the full CMFT, and outer ring—the ED-based boundaries recalculated from Fig. 2.15 of Ref. [6] to fit the current parameter convention. Figure has been published in Ref. [80].

3.3 CMFT results for the Kitaev-Heisenberg model on the 24-site cluster

3.3.1 Composite phase diagram

Contrary to the above 6-site test, when evaluating Kitaev-Heisenberg model on a cluster compatible with both the magnetic unit cells and the $\mathcal{T}_4$ transformation we can expect the ordered phases to occupy broader regions of the parameter space. Such an effect is visible on the original ED-based phase diagram in Fig. 2.15. To make a comparison with the CMFT data, we recalculated this result in the currently used convention of the coupling parameters[22] and prepared the composite phase diagram, presented in Fig. 3.5.

Before we dive into details of the CMFT result on 24 sites we will briefly sketch the key features of the phase diagram. Stable solution from the full CMFT algorithm (middle ring in Fig.

[22] Compare eqs. (2.12) and (2.13).

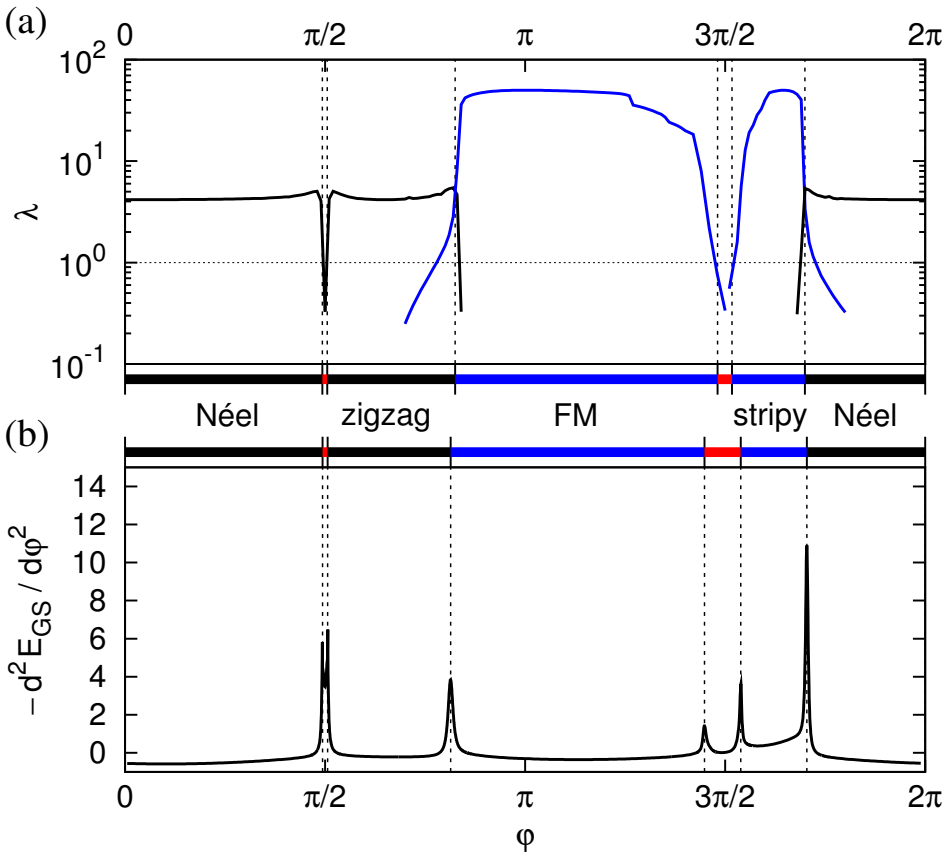

FIGURE 3.6: Panel (a)—results of the simplified linearized CMFT procedure. λ values were obtained for the Néel, zigzag, FM and stripy patterns on the 24-site cluster. If the maximal $\lambda > 1$, then the corresponding order will stabilize within the simplified linear approximation. Here the red color marks Kitaev spin-liquid phase while the $\mathcal{T}_4$ FM-stripy and Néel-zigzag mappings are indicated in blue and black, respectively. Panel (b) replots the second derivative of the ED-based ground-state energy from Ref. [6], providing peaks roughly at the phase transitions shown by the linearized CMFT. Figure has been published in Ref. [80].

3.5) reproduces the long-range ordered Néel, FM, zigzag and stripy phases within the boundaries reasonably consistent with the previous ED-based diagram (outer ring in Fig. 3.5). As will be shown in detail later, discrepancies between zigzag-FM, stripy-Néel and even long-range order/ Kitaev spin liquid (LRO/KSL) boundaries around $K = +1$ are quite small. However, LRO/KSL boundaries around $K = -1$ FM Kitaev point are visibly shifted and the Kitaev spin-liquid region is considerably smaller in CMFT. This is caused by the initial polarization and thus reduction of quantum fluctuations on the boundary bonds. As a part of the CMFT bias it has to be taken into account in conclusions.

The key information to be taken from the composite diagram is the pronounced difference in size between the two spin-liquid regions. While the feature has already been explained in Ref. [6], by connecting the stability of the Kitaev spin liquid against the LRO perturbation to the amount of quantum fluctuations in the LRO states competing with it, now the evidence is stronger, supported also by the perturbation-theory and CMFT results. While the issue will be thoroughly examined in section 3.3.3, now we will present the data leading to the diagram, focusing strongly on the ordered moment characteristics.

3.3.2 Ordered moment

Linearized CMFT

We start the ordered moment analysis with the linearized CMFT. For the 24-site calculations we again utilize $S_i^z\langle S_j^z\rangle$ mean-field decoupling as the exact expression when polarizing the system. The executed here modified version of the linearization procedure starts with the ansatz tuned to the particular magnetic pattern and concerning all 12 external sites. Then, a single iteration of the CMFT loop is executed on those sufficiently small $\langle S_j^z\rangle_{ini}$, differing only by a sign. Characteristic $\lambda_{pattern}$ for the particular ordering is calculated as a normalized sum over the external sites

$$\lambda_{pattern} = \frac{1}{n}\sum_{j=1}^{n} \mathrm{sgn}\left(\langle S_j^z\rangle_{ini}\right) \frac{\langle S_j^z\rangle_{out}}{|\langle S_j^z\rangle_{ini}|}. \tag{3.33}$$

In this simple way the F matrix has been reduced to a single number, but the now less general procedure has to be performed for each initial pattern separately. Surprisingly, this maximally simplified attempt gave reasonable results, setting the phase boundaries well matched to the ED estimates. It becomes quite evident when comparing the vertical lines in Fig 3.6 (a) with the ones in Fig 3.6 (b), where the second derivative of ED-based ground state energy, $-\mathrm{d}^2\mathrm{E_{GS}}(\varphi)/\mathrm{d}\varphi^2$, is replotted from Ref. [6]. The only exception is the FM Kitaev spin-liquid region, which became strongly reduced in the linearized CMFT.

What is also quite striking in the presented result is the preservation of the Néel-zigzag and FM-stripy mappings despite the reduction of the quantum fluctuations. The reader may recognise it by comparing the magnitude of λ_{Neel} and λ_{zigzag} as well as λ_{FM} and λ_{stripy}. In fact, λ_{FM} and λ_{stripy} (blue lines) reach roughly one order of magnitude larger values then λ_{Neel} and λ_{zigzag} (black lines). This predicts, within the linear approximation, that the stabilized ordered moment should be largely reduced in the Néel/ zigzag case and will remain close to the classical 0.5 in the FM/stripy case. Thus, we obtained yet another confirmation of strongly quantum AF character of the zigzag phase and the classical FM character of the stripy phase in the pure Kitaev-Heisenberg model.[23]

Full CMFT

Because the spatial orientation of pseudospins is reduced to the x, y or z cubic axes, the task is to the estimate the absolute value of the ordered moment. In CMFT calculations we again choose z axis as the initial orientation of the averages. Then, $S_i^z\langle S_j^z\rangle$ is enough to capture the mean-field approximation on the boundary bonds and the resulting stable $|\langle S_i^z\rangle|$ build the ordered moment (3.15). Fig. 3.7 (b) presents the ordered moment values summed over the different set of sites. Namely, solid green lines depict the values taken from the central hexagon of the 24-site cluster while the dashed green lines mark the values from sites lying further from the cluster's center. The moment denoted by the solid lines is the most reduced due to the strongest quantum fluctuations in the central hexagon.

Again quite strikingly, the CMFT-based ordered-moment data is compatible with the $\mathcal{T}_4$ transformation. Similarily to the linearized CMFT, also here the Néel-zigzag and FM-stripy mappings survive. The reader may recognise roughly the same values in the Néel and zigzag regions, strongly reduced by the quantum fluctuations, as well as a far more classical FM and stripy values. In particular, the CMFT algorithm recognises the hidden AF and FM SU(2) points, lying in the zigzag and stripy phases, correspondingly.

[23] Because the method is extremely simplified and the author of the thesis was rather inexperienced at the time of the calculations, the results around the right side of the FM phase, i.e. close to the boundary with the spin liquid, seem not to be ideally optimized, probably due to the premature truncation of the Lanczos algorithm. We suspect that with a more careful monitoring of the numerical calculations one could obtain a smoother curve.

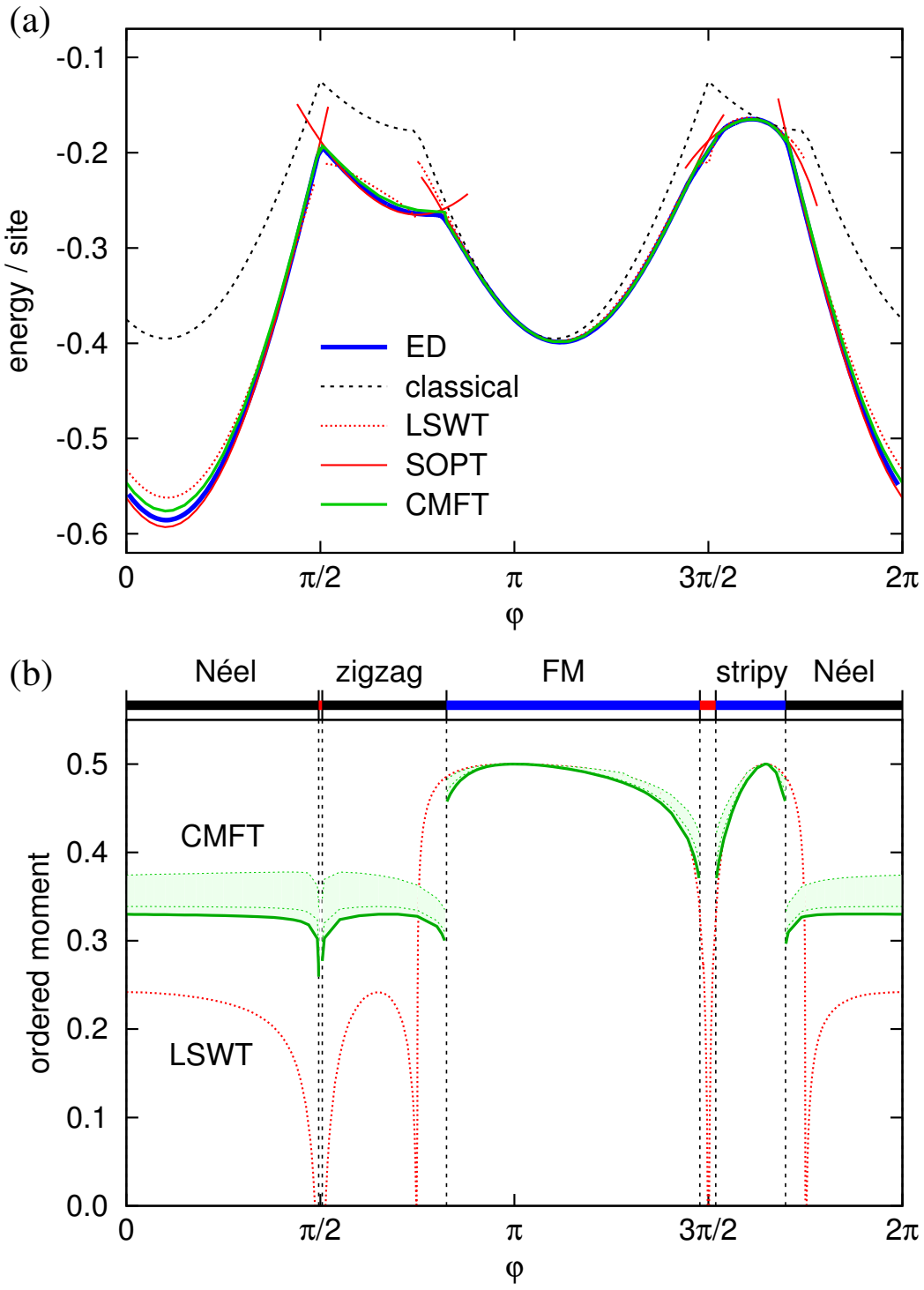

FIGURE 3.7: Panel (a) presents the ground-state energy of the Kitaev-Heisenberg model obtained via different methods: ED on 24-sites (blue, [6]), classical estimates (black dashed), LSWT (red dotted), second-order perturbation theory (solid red) and CMFT (green line). The CMFT-based value was recovered from the nearest neighbor correlations within the central hexagon (see Appendix A.1). Panel (b) provides the CMFT and LSWT-based ordered moment values. The CMFT-based values are taken from: the central hexagon (solid green) or the intermediate and external sites (dashed green). The LSWT-based values are denoted by the dotted red line. Figure has been published in Ref. [80].

AF and FM SU(2) points

Let us begin the investigation of the details with the explicit AF SU(2) point at $\varphi = 0$, where we also have access to the estimates provided by other methods.[24] Table 3.1 compares those

[24]Calculated for the Heisenberg model on honeycomb lattice.

Method	**Value for $J = +1$, $K = 0$**	**References**
m^2 from ED on 24-sites	0.450	[83]
CMFT 24-sites (boundary sites)	0.374	[80]
CMFT 24-sites (central hexagon)	0.330	[80]
High-order expansion	0.307	[84, 85]
m^2 from finite-size scaling, ED	0.270	[83]
m^2 from QMC	0.268	[86, 87, 88]
LSWT	0.248	[89, 80]

TABLE 3.1: Ordered moment value at the AF SU(2) point. Table published in Ref. [80].

estimates, starting with the highest values. It is visible that m^2 approximation on the 24-sites provides a largely overestimated value, seemingly close to the classical Néel value in the Ising model. Among the 24-site calculations CMFT-based value extracted from the central hexagon "wins", with also the high-order expansion estimate being quite close. However, the value obtained by the finite-size scaling of the ED data is much lower[25] and it is supported by the similarly low estimate by the Quantum Monte Carlo-based m^2. The lowest value, obtained using the linear spin wave theory (LSWT), is probably underestimated due to the harmonic nature of the approximation. One can only speculate that the value in the thermodynamic limit would be rather reduced, somewhere between the central-hexagon CMFT and the finite-size-scaling for ED/QMC estimates. Unfortunately, obtaining a stable solution on clusters exceeding 24 sites is even more costly, making reliable CMFT-based finite-size scaling practically impossible.

Before moving to the fully frustrated regime we briefly examine the explicit FM SU(2) point (at $\varphi = \pi$), for which both the CMFT and LSWT produce the correct 0.5 value. The red dotted line in Fig. 3.7 (b) shows that around this fluctuation-free point as well as for the $\mathcal{T}_4$-dual stripy point the values predicted by CMFT and LSWT also coincide. The high accuracy of the LSWT result in the FM and stripy regions may be attributed to the small amount of quantum fluctuations indicated also by the more exact methods such as ED. The bias coming from the harmonic approximation in LSWT case or from the polarization of the boundary in CMFT case is simply not large enough to spoil the results. The situation changes when one moves towards the Kitaev points.

Frustrated neighborhood of the liquid regions

Close to the liquid regions the growing bond frustration emanating from the stronger Kitaev term suppresses the ordered moment. This effect seems to be promoted way too much within the LSWT in the Kitaev spin liquid for the positive (AF) K, suggesting broader antiferromagnetic liquid region, while the space for FM KSL with the negative K becomes even narrower than in the CMFT picture. It seems that the KSL/LRO boundaries provided by the LSWT are highly affected by the approximation. Perhaps including a carefully selected interacting-magnon terms[26] could balance the above tendencies. In the frustrated regions the central-hexagon CMFT and high-order expansion [84, 85] estimates seem more realistic. As the general conclusions for the ordered moment in the neighborhood of the liquid regions we would like to emphasize how frustrated those regions are and how difficult it is to obtain the least biased results consistent with the $\mathcal{T}_4$ mapping.

[25] Not all clusters chosen for the ED-based scaling were symmetric enough—they could introduce geometrical bias.

[26] Higher-order terms.

3.3.3 KSL/LRO transitions

In what follows, we would like to examine the KSL/LRO transitions even more extensively. A good understanding of these transitions is important in the context of driving the existing materials into the spin-liquid phase or synthesizing a new material fitting in one of the liquid windows of the Kitaev-like models. Already on the composite phase diagram in Fig. 3.5 the large FM KSL region dominates over the quite tiny but still finite AF one. This striking difference in size, shown by both ED and CMFT, is also an effect related to the quantum fluctuations, which influence not only the extent of the phases but also the character of the transitions. Below we elaborate on those differences, confirming the suggestions first made in Ref. [6]. Let us first sketch those effects by means of the second-order perturbation theory (SOPT).

Ground-state energy

By SOPT ground-state energy we mean the classical contribution to the energy of each magnetic pattern and its second-order correction.[27] These are the first and second terms in the expressions below:

$$\mathrm{E}_{Neel} = -\frac{1}{8}(K+3J) - \frac{1}{16}(K+3J), \tag{3.34}$$

$$\mathrm{E}_{zigzag} = -\frac{1}{8}(K-J) - \frac{1}{16}(K-J), \tag{3.35}$$

$$\mathrm{E}_{FM} = +\frac{1}{8}(K+3J) + \frac{1}{16}\frac{K^2}{K+2J}, \tag{3.36}$$

$$\mathrm{E}_{stripy} = +\frac{1}{8}(K-J) + \frac{1}{16}\frac{(K+2J)^2}{K}. \tag{3.37}$$

In the Néel and zigzag cases the ratio of quantum and classical terms, $r_{q/c} = \mathrm{E}_q/\mathrm{E}_c$, is fixed to 1/2. This means that quantum fluctuations contribute with 1/3 of the total energy of each pattern. The effect is visible in Fig. 3.8 (a), where the classical energies E_c for suitable patterns are depicted by the dashed lines while the total energies $\mathrm{E}_{pattern} = \mathrm{E}_c + \mathrm{E}_q$ are marked in blue. By comparing the blue energies to the green (spin-liquid) one,

$$\mathrm{E}_{\mathrm{KSL}} = \frac{3}{2}(K+J)\langle \mathrm{S}^\gamma \mathrm{S}^\gamma \rangle_{Kitaev}, \tag{3.38}$$

where $\langle \mathrm{S}^\gamma \mathrm{S}^\gamma \rangle_{Kitaev} \approx \pm 0.131$ is an analytical estimate from Ref. [91], we see that the Néel and zigzag phases have enough quantum fluctuations to quickly overcome even the very quantum spin liquid. As a result, the AF KSL window is rather tiny.

In contrast, Fig. 3.8 (b) reveals the non-trivial $r_{q/c\ FM}$ behaviour for the FM and stripy patterns. Quick calculation estimates the energy ratio as

$$r_{q/c\ FM} = \frac{1}{2}\frac{K^2}{(6J^2+5JK+K^2)}, \tag{3.39}$$

and

$$r_{q/c\ stripy} = \frac{1}{2}\frac{(2J+K)^2}{K(K-J)}, \tag{3.40}$$

respectively for the FM and stripy cases. The maximal value 1/2 is reached only when $J = 0$—at the FM Kitaev point. When allowing $|J| > 0$, which means moving to the left or to the right

[27] In perturbation theory for Kitaev-Heisenberg model we treat all the terms of the Kitaev-Heisenberg Hamiltonian containing $\mathrm{S}_i^z \mathrm{S}_j^z$ as the unperturbed part $\mathcal{H}^{(0)}$ and the terms containing spin flips as a perturbation $\mathcal{H}'$. The first non-zero corrections are of second order. For the specific details of SOPT calculations for the model the reader may study a nicely written summary in Ref. [90].

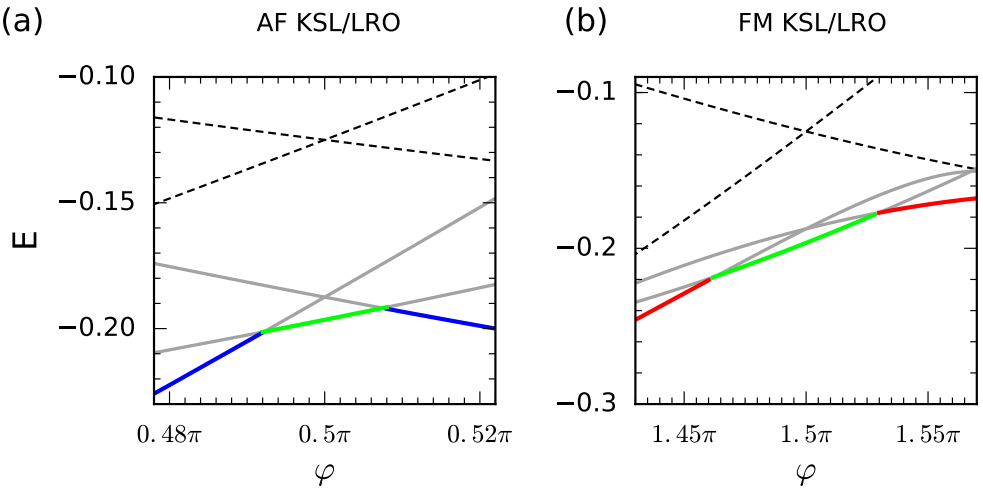

FIGURE 3.8: Classical energies and their second-order quantum corrections in the vicinity of (a) the AF Kitaev point at $\varphi = 0.5\pi$ and (b) the FM Kitaev point at $\varphi = 1.5\pi$. Panel (a) contains classical Néel and zigzag contributions (dashed lines) and their SOPT-corrected quantum versions (blue). Long-range order (LRO) energies are compared to the analytical estimate of the spin liquid contribution (green). Analogically, panel (b) contains the FM and stripy SOPT-corrected energies (red). The plots are based on formulae (3.34)-(3.37), (3.38).

from the Kitaev point, the ratio in the ordered states decreases rapidly, until it reaches 0 at the FM explicit and hidden SU(2) points [5, 6]. The significantly reduced level of those quantum fluctuations sets a suitable background for the spin liquid to spread, as the liquid state has lower energy than the more classical FM and stripy states. Therefore, in $K < 0$ case the KSL region is much larger than in the $K > 0$ case. Attentive reader might have also noticed some asymmetry of the FM KSL region. In fact, the shorter part $\varphi \in [1.5, 1.539]\pi$ maps exactly via the $\mathcal{T}_4$ transformation to the longer $\varphi \in [1.448, 1.5]\pi$ part, so the apparent asymmetry is related to the fundamental symmetry of the model.

We complete the ground-state energy analysis by discussing energy estimates provided by different methods in the whole range of the parameters of the model. Such examination is important because the accuracy of the ground-state energy influences the distribution of the phase boundaries, since the pattern with the lowest energy wins the competition. Fig. 3.7 (a) stores the energy per site calculated by means of ED, CMFT, SOPT, LSWT, as well as the classical energy values.[28] It is quite evident that all the methods which include some form of quantum fluctuations are relatively close to the ED result. The SOPT and central-hexagon CMFT lines (details in Appendix A.1) run very close to the ED line even in the AF regions, where the LSWT struggles a bit. We were thus justified to utilize the SOPT for sketching the tendencies in the neighborhood of the Kitaev-points.

Pseudospin correlations

As mentioned earlier, quantum fluctuations influence not only the size of the spin-liquid windows but also the nature of the KSL/LRO transitions. This will be now illustrated by the pseudospin correlations, plotted in Fig. 3.9. The correlations provide additional information about the characteristics of each phase. For example, the diverging blue and red lines ($\langle \mathrm{S}_i^\gamma \mathrm{S}_j^\gamma \rangle$ for the nearest-neigbor Kitaev correlation on each bond and $\langle \mathrm{S}_i^\alpha \mathrm{S}_j^\alpha \rangle$, $\langle \mathrm{S}_i^\beta S_j^\beta \rangle$ for the complementary nearest-neighbor correlations) in the FM phase shown in Fig. 3.9 (a) illustrate how sensitive to

[28] The $\mathrm{S}_i^z \mathrm{S}_j^z$ terms, with suitable coupling parameters for each bond, averaged over each magnetic pattern.

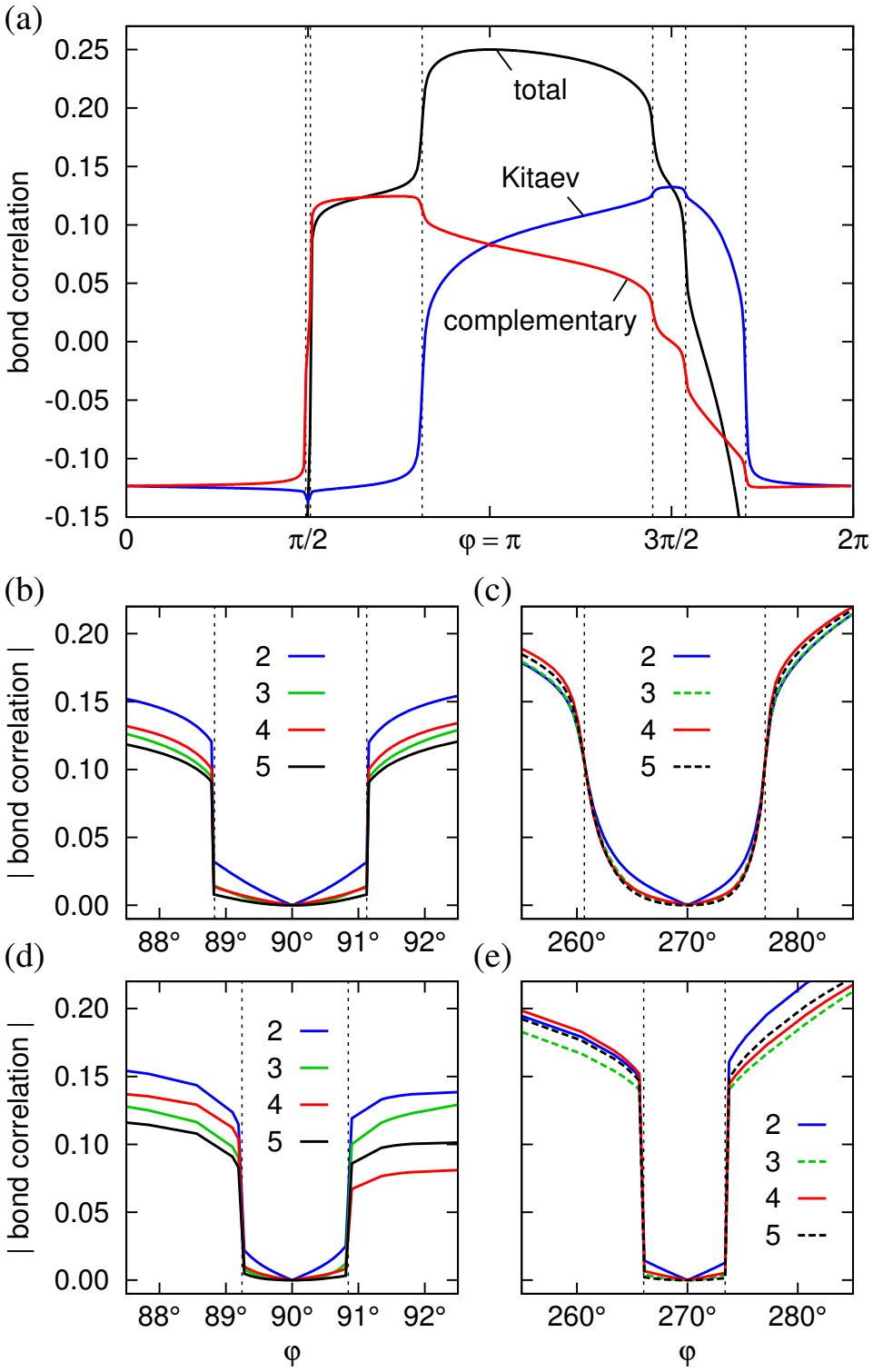

FIGURE 3.9: Pseudospin correlations for the Kitaev-Heisenberg model. (a)—nearest-neighbor ED-based correlations: $\langle \mathbf{S}_i \cdot \mathbf{S}_j \rangle$-in black, correlations of the components active in the Kitaev interaction $\langle \mathrm{S}_i^{\gamma} \mathrm{S}_j^{\gamma} \rangle$—in blue and complementary pseudospin components $\langle \mathrm{S}_i^{\alpha} \mathrm{S}_j^{\alpha} \rangle$, $\langle \mathrm{S}_i^{\beta} \mathrm{S}_j^{\beta} \rangle$—in red. On panels (b)-(e), containing further-neighbor correlations $|\langle \mathbf{S}_i \cdot \mathbf{S}_j \rangle|$ calculated via ED and CMFT, colors correspond to different neighbors: the ED-based correlations around the AF KSL phase (b) and the FM KSL phase (c), the CMFT-based correlations in the AF KSL (d) and the FM KSL case. Figure has been published in Ref. [80].

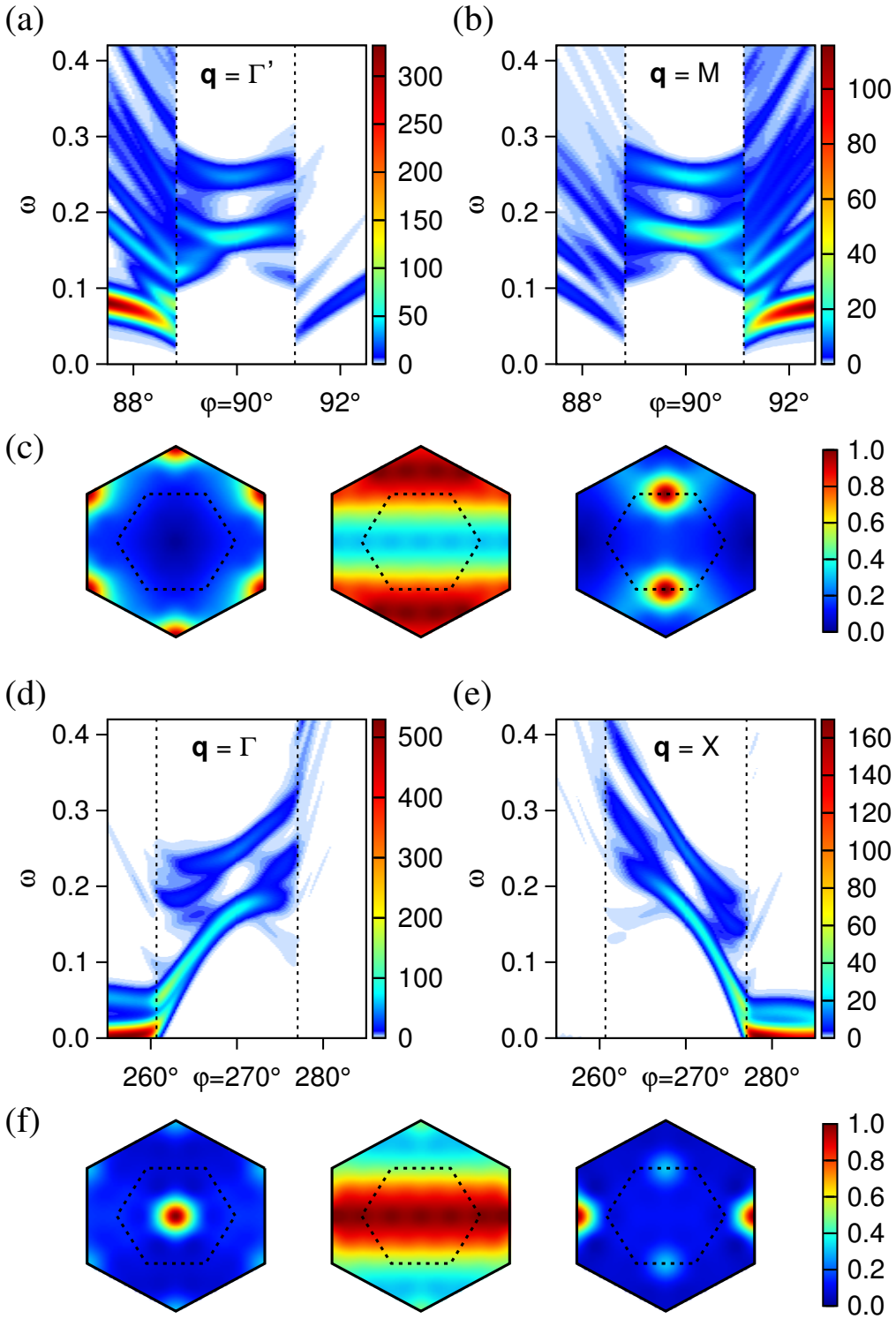

FIGURE 3.10: Spin dynamics around the KSL/LRO transitions in the Kitaev-Heisenberg model. (a), (b)—dynamical spin susceptibility $\chi''(\mathbf{q},\omega)$ in the neighborhood of the AF Kitaev point for the wavevector of the Néel and zigzag order ($\mathbf{q} = \Gamma'$ and M). (c)—spin structure factor $\langle S^z_{-\mathbf{q}} S^z_{\mathbf{q}} \rangle$ calculated at $\varphi = 87.5°$, 90°, and 92.5° as representative for the Néel, KSL and zigzag phases. (d), (e)—$\chi''(\mathbf{q},\omega)$ plots around the FM Kitaev point at $\mathbf{q} = \Gamma$ and X characteristic for the FM and stripy orderings. (f)— structure factors for the FM, KSL and stripy patterns at $\varphi = 255°$, 270°, and 285°. Figure has been published in Ref. [80].

the parameter changes the FM (and stripy) phase is compared to the Néel (and zigzag) phase. This should be kept in mind as the robustness of the AF phases changes dramatically once the

Γ parameter is introduced in other Kitaev-like models in Sec. 3.4.

Moreover, the correlations allow us to verify the green regions of the composite phase diagram in Fig. 3.5 as the critical cases of KSL [92], since the only significant nearest-neighbor components in those regions are the Kitaev correlations [cf. maximal |blue| curve vs infinitesimal |red| curve values in Fig. 3.9 (a)]. This is complemented by the also infinitesimal further-neighbor correlations on Fig. 3.9 (b)-(e).

Our current discussion focuses on the latter panels. It is natural to imagine a first-order-like transitions[29] in Fig. 3.9 (b), where the ED-based correlations are plotted around the AF Kitaev point. For the non-zero but sufficiently small J[30] further-neighbor correlations perturb the liquid state. Not enough, however, to enforce the LRO, which appears abruptly for larger $|J|$, when the correlations suddenly jump to the much higher values. This contrasts with the ED prediction for the neighborhood of the FM Kitaev point in Fig. 3.9 (c). There, at the boundary of a broader liquid region, further-neighbor correlations continuously climb to obtain the LRO values.

We do not observe the above-mentioned difference in the behaviour in the CMFT-based correlations around the AF vs FM KSL/LRO transitions [Fig. 3.9 (d) and (e), correspondingly]. Although there is a small resemblance between Fig. 3.9 (c) and (e) in how the correlations lines run close to each other in the LRO regions, the smooth correlation curves do not appear in the CMFT. The reason lies in the extreme difficulty with the continuous connection of the *de facto* isolated-cluster result inside the liquid window[31] with the PBC result in the ordered regions. Open boundary conditions bring stronger finite-size effects, feeding discontinuity at the boundary. Still, values taken from the central hexagon reproduce well the spin-liquid features in the green regions, giving some rough verification of the spin-liquid phases, but the fine beauty of the FM KSL/LRO transition is lost.

Spin structure factor and spin susceptibility

Fourier transform of the pseudospin correlations is proportional to the differential crossection of the magnetic neutron scattering

$$\langle \mathrm{S}^{\alpha}_{-\mathbf{q}} \mathrm{S}^{\beta}_{\mathbf{q}} \rangle = \frac{1}{\mathrm{N}} \sum_{\mathbf{R}_i, \mathbf{R}_j} \left\langle e^{i\mathbf{q}\cdot(\mathbf{R}_i - \mathbf{R}_j)} \mathrm{S}^{\alpha}_i \mathrm{S}^{\beta}_j \right\rangle \propto \frac{\mathrm{d}^2\sigma(\mathrm{E}, \mathbf{q})}{\mathrm{dEd}\Omega}, \tag{3.41}$$

where N is the size of the system, $\mathbf{R}_i$ and $\mathbf{q}$ are the direct and reciprocal lattice vectors and α, $\beta \in \{x, y, z\}$ [90]. Here we exploit the static spin structure factor $\langle \mathrm{S}^z_{-\mathbf{q}} \mathrm{S}^z_{\mathbf{q}} \rangle$ to illustrate how each pattern looks in the reciprocal lattice, as utilized by the scattering experiments. The reader may recall Fig. 2.16 where the expected reciprocal pictures of the magnetic patterns were presented. Now we may compare those images to the patterns emerging from $\langle \mathrm{S}^z_{-\mathbf{q}} \mathrm{S}^z_{\mathbf{q}} \rangle$ averaged over the 24-site-ED ground state. The extreme subplots in Fig. 3.10 (c) and (f) reveal (correspondingly) the Néel, zigzag, FM and stripy patterns, in accordance with Fig. 2.16. Central subplots in Fig. 3.10 (c) and (f) depict $\langle \mathrm{S}^z_{-\mathbf{q}} \mathrm{S}^z_{\mathbf{q}} \rangle$ for AF and FM KSL. The characteristic wave-like images appear because in the Kitaev spin liquid only the nearest-neighbor correlations of the specific γ components on a given bond direction are finite.[32] For such a short-range pattern the interference of many further and further-neighbor terms, typical for the LRO focused peaks, does not occur and we are left with the wave-like behaviour of $\langle \mathrm{S}^{\gamma}_{-\mathbf{q}} \mathrm{S}^{\gamma}_{\mathbf{q}} \rangle$ for each γ.[33]

Pseudospin dynamics in the Kitaev-Heisenberg model can be described by the dynamical spin susceptibility. In general, we use the magnetic susceptibility to measure the response of the

[29] It is just an analogy, we are obviously in zero temperature.

[30] φ sufficiently close to 0.5π.

[31] In KSL $\langle \mathrm{S}^z_i \rangle$ are zero, creating open boundary conditions.

[32] Basic description of KSL can be found in Sec. 2.2.1.

[33] For example, the only non-zero correlations on c bonds—$\langle \mathrm{S}^z_i \mathrm{S}^z_j \rangle$ set the direction ‖Y, that can be seen on $\langle \mathrm{S}^z_{-\mathbf{q}} \mathrm{S}^z_{\mathbf{q}} \rangle$ plot as the wave vector of a wave in reciprocal space (reciprocal of reciprocal is direct).

system after it was excited by a magnetic perurbation. In the very definition of dynamical spin susceptibility

$$\chi_{\gamma\gamma}(\mathbf{q},\omega) = i\int_0^\infty \left\langle \mathrm{GS}\left|\left[\mathrm{S}^\gamma_{\mathbf{q}}(t),\mathrm{S}^\gamma_{-\mathbf{q}}(0)\right]\right|\mathrm{GS}\right\rangle e^{i\omega t}\mathrm{d}t, \tag{3.42}$$

the reader may notice how $\mathrm{S}^\gamma_{-\mathbf{q}}(0)$ operator excites the system from the ground state $|\mathrm{GS}\rangle$ at time $t = 0$. Then, after some time t operator $\mathrm{S}^\gamma_{\mathbf{q}}(t)$ is measured. For $\omega > 0$ the imaginary part of the above formula can be written as the resolvent

$$\chi''_{\gamma\gamma}(\mathbf{q},\omega) = -Im\left\langle \mathrm{GS}\left|\mathrm{S}^\gamma_{\mathbf{q}}\frac{1}{\omega+\mathrm{E_{GS}}-\mathcal{H}+i\delta}\mathrm{S}^\gamma_{-\mathbf{q}}\right|\mathrm{GS}\right\rangle, \tag{3.43}$$

which can be reformulated into a sum over the excited states $|\mathrm{EX}_i\rangle$,[34] enabling the numerics.

$$\chi''_{\gamma\gamma}(\mathbf{q},\omega) = \pi\sum_i \left|\left\langle \mathrm{EX}_i\left|\mathrm{S}^\gamma_{-\mathbf{q}}\right|\mathrm{GS}\right\rangle\right|^2 \delta\left(\omega-\mathrm{E_{EX}}i\right). \tag{3.44}$$

Here we would like to focus on the certain features of $\chi''_{\gamma\gamma}(\mathbf{q},\omega)$ results for the 24-site cluster, providing further insight into the AF and FM KSL/LRO transitions. The results are presented in Fig. 3.10 (a), (b) and (d), (e), correspondingly for the neighborhood of the AF and FM KSL.

For the AF case, if we start from the LRO side and follow $\chi''_{\gamma\gamma}$ behaviour in Fig. 3.10 (a) or (b) we will see a pronounced pseudo-Goldstone mode for the wave vector suitable for selected LRO.[35] Next, we will observe a level crossing to a phase with a rather stable pseudospin gap, signalling an abrupt change from the LRO to KSL.

FM case presents a substantially different behaviour. Starting with the KSL/LRO dotted lines in Fig. 3.10 (d)-(e), a gapless magnon *gradually* gains a pseudospin gap, until it reaches the FM Kitaev point. We can look at this picture also in the opposite way— when the Kitaev Hamiltonian is being perturbed with the Heisenberg interaction and $|J|$ grows, the pseudospin gap is decreasing. Consequently, further-neighbor correlations are slowly increasing, until they reach the LRO values (already reported in Fig. 2 of Ref. [5]).

Before we summarize the KSL/LRO transitions, we would like to emphasise that χ'' reveals only the *magnetic* excitations— the gaps presented here are the pseudospin gaps. The above result is consistent with the fact that we are using the symmetric Kitaev term with a single K coupling producing *gapless* Kitaev spin liquid when considering all the excitations, including the fermionic ones [7]. The reader may consult Sec. 2.2.1 for a recollection.

Summary of KSL/LRO transitions

From correlations and $\chi''_{\gamma\gamma}$ plots we see that AF and FM KSL/LRO transitions are fundamentally different. Antiferromagnetic case reminds the 1st-order transition with its level crossings and discontinuities. The tough energetic competition between the highly fluctuating AF LRO phases and the AF KSL leads to the suppression of KSL to the tiny region of the phase diagram where finally the spin liquid wins. The ferromagnetic case is much more gradual, with the gapless LRO modes continuously connected to the pseudospin gap at the Kitaev point and the smooth behaviour of correlations. The liquid solution does not have to compete to such an extent with the less fluctuating FM LRO phases, hence the KSL may spread much further.

Unfortunately, the CMFT method is able to only partially show the difference between the analysed regions. While the AF KSL/LRO transition is reproduced rather well, the FM case suffers. The liquid region is somewhat smaller then in the ED-based results and the subtleties of the FM KSL/LRO transition are lost.

[34] Here the excitation energies $\mathrm{E_{EX}}i$ are normalized to the ground-state energy.

[35] Small pseudo-gaps in the LRO phases result from the finite-size effects of a 24-site cluster. More details in Ref. [80].

3.4 CMFT results for the J-K-Γ-Γ' model on the 24-site cluster

Similarly to the Kitaev-Heisenberg model in the previous section, we will now present the composite phase diagram of the J-K-Γ-Γ' model defined by Eq. (2.22). We will examine the ordered moment characteristics obtained via various analytical and numerical methods.[36] In what follows we will discuss the emerging discrepancies and identify the puzzle pieces forming the reasonably coherent picture. We will start with a sketch of the quantum and classical trends in the parameter space visible on the λ_{max} maps produced by the linearized CMFT. Subsequently, we will move towards a more thorough analysis incorporating the strength, spatial orientation and probabilities of different magnetic patterns. Those trends can be followed on:

- the maximal probability maps (the maximal-overlap method);
- the maps of the norm of the ordered moment $|\mathcal{S}|$, as in the formula (3.15) (full CMFT);
- the maps of the spatial orientation of the pseudospins (both the maximal overlap and the full CMFT methods);
- the stability maps of the collinear patterns.

The reader may find a quick guide how to read the circular maps in Sec. 2.5.1

The most complex $\Gamma' = 0$ slice of the phase diagram will be analysed in great detail, revealing a multi-layered structure of the subphases and special patches within the phases already known from Fig. 2.20 (a). Then, we will monitor how the system responds to the increasing value of $|\Gamma'|$ in the following slices. We will explain the emerging tendencies by exploiting the analytical arguments such as the classical-energy minimization and the distance from the special points and patches, where the peculiar ordered moment characteristics can have a more fundamental source. Once the general trends are grasped, we will turn our full focus to the above-mentioned points and manifolds, exploring their origin and meaning to a further extent. In this way the two completely classical manifolds, the Ising-Kitaev-compass model as well as a separate compass point will be analytically justified. Together with the already-known hidden SU(2) points, the above-mentioned results will provide us with a deeper understanding of the tendencies occurring on the phase diagram.

Finally, we will compare the spatial orientation and strength of the magnetic moments of the honeycomb iridates and ruthenates[37] and the obtained here pseudospins. This will allow us not only to narrow down the parameter windows for the said materials, but also to verify their other presumed characteristics, related to the amount of quantum fluctuations in the selected windows and the adjacent area.

3.4.1 Linearized CMFT

Before we start the general analysis within the linear approximation of CMFT, let us provide few more methodological details. For the J-K-Γ-Γ' model the full version of the algorithm described in Sec. 3.2.2 was chosen in order to accommodate the non-collinear tendencies observed already in Refs. [8, 70, 9] as well as the predicted deviation of the moments from the Kitaev cubic axes. For each parameter point the linear response to the polarization of one pseudospin component at a single external site at a time was collected. Going through all the external sites and pseudospin components resulted in the 3×12 sets of the 3×24 $\langle \mathrm{S}_i^{\gamma} \rangle_{out}$ estimates. From this pool only the external-site averages entered the F matrix (3.30). The key idea of the linear response is that the

[36] Sec. 3.2.
[37] See Sec. 2.3.4.

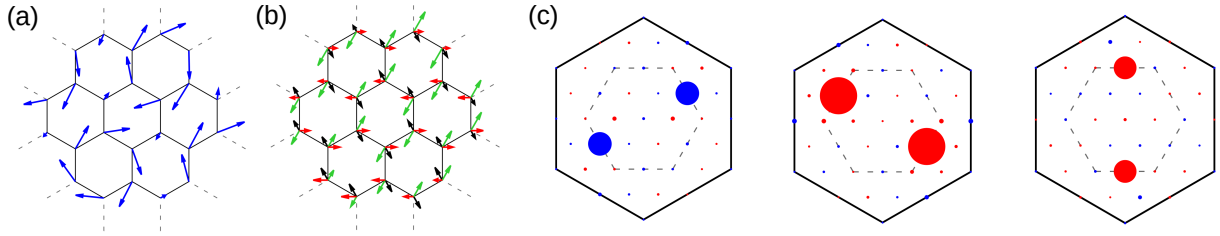

FIGURE 3.11: An example of a pattern read out from the eigenvector corresponding to λ_{max} in the linearized CMFT. Panel (a)—the pattern restored for the 24 sites by the procedure described in the main text for a point in the upper zigzag region close to the external Kitaev-Heisenberg circle. Panel (b)—the projection of the blue arrows from the panel (a) to the Kitaev cubic axes. The x-projection marked in black, the y-projection—in green and the z-projection—in red color. Panel (c)—the Fourier transforms of these projections into the reciprocal lattice. The red/blue color marks the positive/negative signal in the "Bragg" peak.

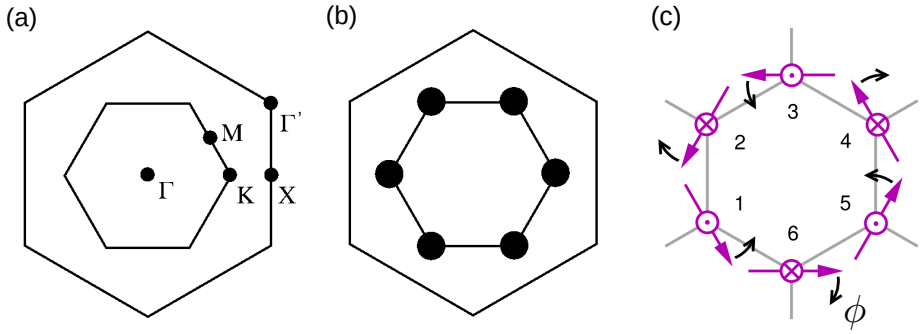

FIGURE 3.12: Panel (a)—the 1st Brillouin zone of the honeycomb lattice (the inner hexagon) and the triangular lattice created by adding a site at the center of each hexagon (the outer hexagon); panel (b)—the reciprocal picture of a vortex pattern; panel (c)—the convention of the azimuthal angle ϕ for the in-plane patterns. Panel (c) taken from Fig. 10 of Ref. [29].

eigenvector corresponding to the maximal eigenvalue of F, $\lambda_{max} > 1$, represents the magnetic pattern on the external sites that would stabilize after n iterations. While these 12 sites would be in principle enough to identify an ideal collinear pattern, one could make it easier for the non-collinear or even just slightly canted cases by performing an additional step: from all the 72 outcoming $\langle \mathrm{S}_i^\gamma \rangle_{out}$ averages for each 36 initially polarized $\langle \mathrm{S}_j^\delta \rangle_{ini}$ a 72×36 response matrix F′ can be formed. Then, by acting with F′ on the 36-component eigenvector, one can reconstruct magnetic pattern $\{\mathbf{P}_i\}$ for all 24 sites.

CMFT bias

This careful approach proved to be extremely useful as the linearized CMFT brought quite puzzling results. Namely, the independent initial polarizations added up to the strongly non-collinear patterns in the parameter regions previously recognized to yield collinear phases [8, 90]. The most affected turned out to be the zigzag phase, for which further inspection revealed a decomposition of the real-space vortex-like pattern (Fig. 3.11 (a)) into a sum of the three zigzag patterns $\{\mathrm{P}_i^\gamma\}$ in the pseudospin components, denoted by different colors in Fig. 3.11 (b).

The above effect is a direct consequence of the action of the bond-anisotropic part of the mean field (the K, Γ and Γ' terms in Eq. (3.24)). One could intuitively understand this by considering just the Kitaev mean-field term on the 3 species of the external sites, each attached to the mean-field bond in either a, b or c direction. The 4 sites with the mean-field bonds in the direction a will experience an effective magnetic field from the x component $\mathrm{S}_i^x \langle \mathrm{S}_j^x \rangle$. Similarly, the 4 sites

with the mean-field bonds in the direction b will be exposed to the field from the y component and the last 4 sites connected to the c-type bonds will be affected by the z component. Thus, for each species a different pseudospin component in the average will be preferred and ultimately a non-collinear tenendency will emerge.[38] Having verified that for a large part of the parameter space the fully quantum J-K-Γ-Γ' Hamiltonian would have promoted a ground state in a form of the superposition of collinear patterns, we consider the effect method-related and a part of the CMFT bias.

Consequently, we predict that the CMFT bias would be the strongest in those parameter regions where a significant part of the quantum fluctuations within the ED-based ground state would come from satisfying the bond-anisotropic part of the Hamiltonian by forming a quantum superposition of the collinear patterns. For such a situation, replacing the operator-operator K, Γ, Γ' terms by their mean-field analogues would reduce the superposition of the proper collinear patterns, differing by the rotation by 120°, to the superposition of the collinear pseudospin-component patterns, rotated by 120° for each $\langle \mathrm{S}^{\gamma} \rangle$. These 3 patterns would then form a non-collinear pattern in $\langle \mathbf{S}_i \rangle$. Hence, applying the mean-field approach with $\langle \mathbf{S}_i \rangle$ to the bond-anisotropic terms cannot result in the collinear averages without additional constrains, which we will impose on the full CMFT approach.

The recognition of zigzag tendencies in the P_i^x, P_i^y and P_i^z components in Fig. 3.11 (b) (black, green and red arrows, respectively) requires quite some effort. To make the process more efficient we transformed the components to the reciprocal space. Fig. 3.11 (c) presents $\mathrm{P}_{\mathbf{q}}^x$, $\mathrm{P}_{\mathbf{q}}^y$ and $\mathrm{P}_{\mathbf{q}}^z$ calculated for all the symmetry-allowed $\mathbf{q}$-points compatible with the 24-site cluster visible on Fig. 3.11 (a) and (b).[39]

Unfortunately, another, more intricate aspect of the CMFT bias has also emerged. At the first glance, the linearized CMFT should respect the C_3 pseudospin-lattice symmetry. We were polarizing each pseudospin component at a time and the F matrix should reflect it. Indeed, the C_3 matrix took the block-diagonal form in the eigenbasis of F. Importantly, the irreducible representations of the C_3 group are of the E and A types. Our linearized results revealed a splitting between two Es and one A, instead of the expected 3 degenerate cases. Moreover, in some special regions the splitting was so strong, that it lead to the mixing of the eigenvalues representing the excited states.

Quantum/classical trends on the λ_{max} maps

Because of all the above disadvantages only a rough recognition of the phases was possible within the linearized CMFT approach.[40] We have confirmed that the $\Gamma' = 0$ slice in Fig. 3.13 approximately agrees with Fig. 2.20 (a), predicting the spread of the collinear phases of the Kitaev-Heisenberg model towards the center of the circle, and the appearance of the second zigzag region and the non-collinear vortex phase. The other slices predict further growth of the vortex and the lower zigzag regions at the expense of the FM, Néel, upper zigzag and stripy phases. In the next section we will verify whether these coarse predictions are justified.

Moreover, even these strongly hampered results allowed for reasonable predictions concerning the quantum vs classical tendencies on the diagram. Such information can be read out from the maximal-eigenvalue plots in Fig. 3.14, for which the color of each point is proportional to the amount of the quantum fluctuations in the system. Interestingly, the λ_{max} maps reveal a quite extreme landscape:

[38] Γ and Γ' change the direction in which the 4 species are being "pulled".

[39] All the results presented in Fig. 3.11 were suitably rescaled for the reader's convenience. In fact, the arrows in Fig. 3.11 (b) are of the magnitude 10^{-4} because they are the outcome of a single iteration of the CMFT loop after the initial polarization of the order of 10^{-3} in a fairly quantum parameter point close to the zigzag SU(2) point.

[40] A comparison of the P_q^{γ} images to the ideal patterns shown in Fig. 2.16 allowed us to approximately identify the phases.

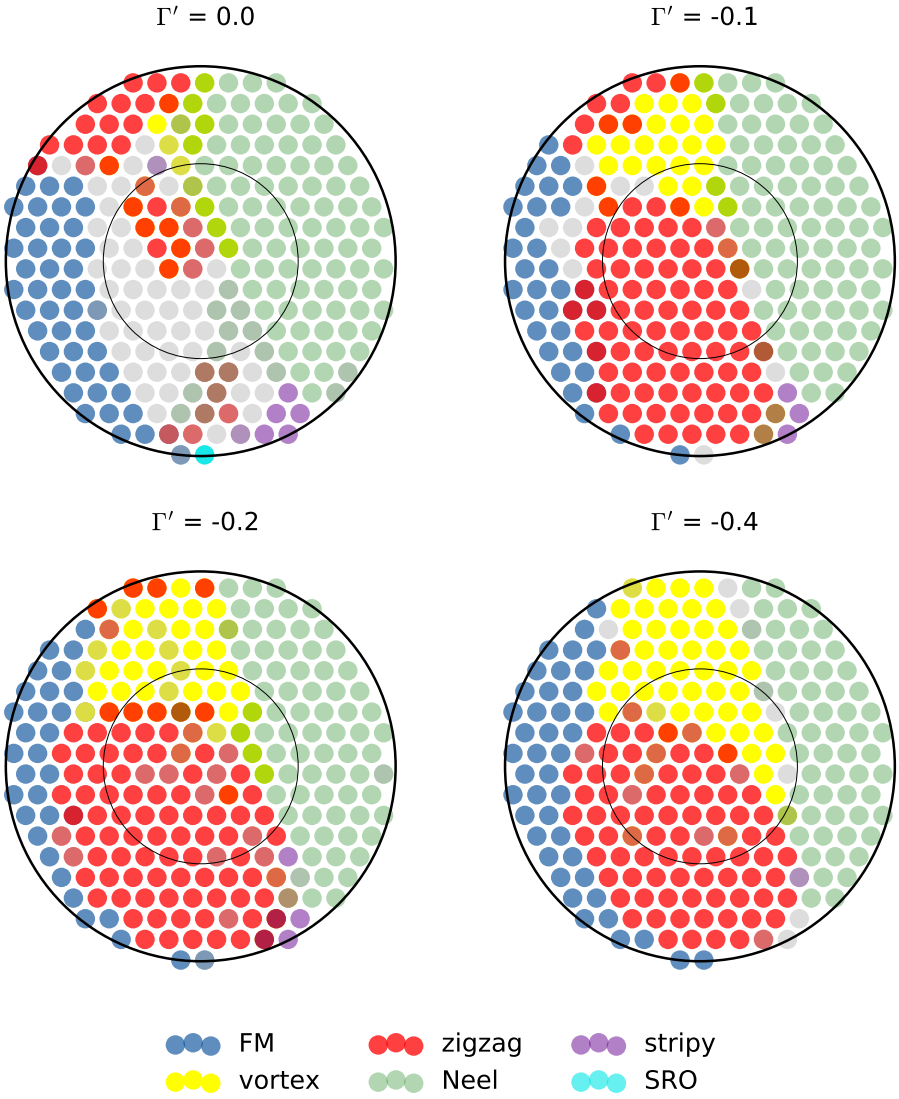

FIGURE 3.13: A sketch of the phase diagram of the J-K-Γ-Γ' model (2.22) based on the linearized CMFT. The eigenvectors corresponding to λ_{max} provide the magnetic patterns with the highest chances for stabilization in the full CMFT procedure. Those magnetic tendencies are denoted by colors in the legend. In particular, SRO denotes the short-range order tendencies detected as a wave-like pattern in one of the P^{γ}_{q} components.

- The brown/red regions in the central part and close to the left side of the slices experience a strong response exceeding the linear regime. The initial polarization at the 10^{-3} level results in the λ_{max} response crossing 10^4, which indicates a classical behaviour with the vanishing quantum fluctuations.[41] These regions may be imagined as "high mountain ranges" of the parameter space.

- Progressively, the yellow/green regions represent a moderate response with the growing fluctuations.

- The light up to dark-blue regions of the smaller λ_{max} values, reduced by the significant quantum fluctuations. Despite that, the LRO is still stabilizing there within the linear approximation ($\lambda_{max} > 1$). They can be imagined as "flat lowlands".

[41] The less quantum fluctuations the easier the system polarizes, resulting in a stronger response.

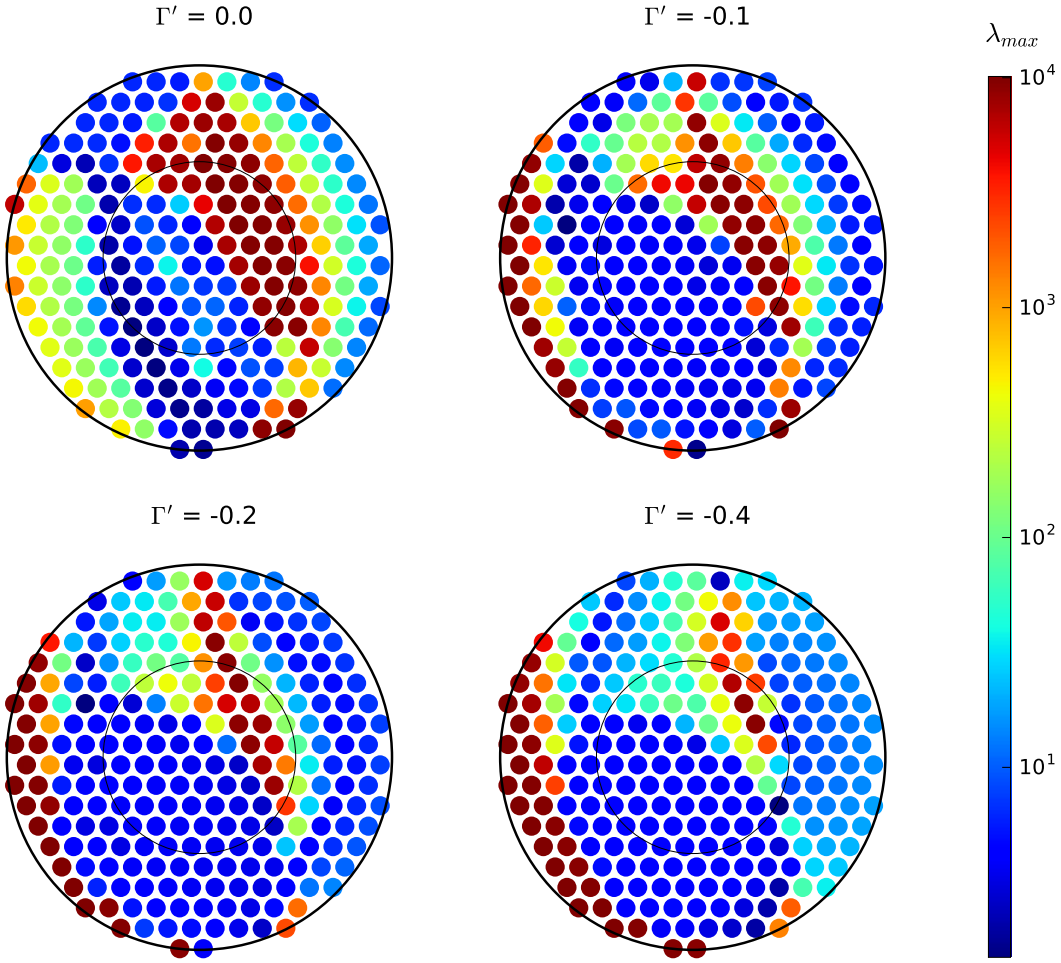

FIGURE 3.14: The λ_{max} plots for the selected Γ' slices of the J-K-Γ-Γ' model (2.22). Each colored circle provides information about the λ_{max} value (colorbar) for a unique set of the J, K, Γ values represented by the center of each circle.

- Few almost black spots where λ_{max} is equal to or is even smaller than one.[42] In the latter case no LRO can appear within the linear approximation. Some of these extremely quantum areas coincide with the parameter regions where the spin-liquid characteristics were previously reported [8, 93]. Some will be further recognised as the boundary, unstable patches between the FM and zigzag regions and a highly fluctuating patch within the extended neighborhood of the hidden AF Kitaev point at the $\Gamma' = -0.4$ slice. The reader may picture them as small "lakes" of various shape.

Although the amount of information that could be taken from the linearized CMFT has been somewhat disappointing and the details of the patterns could not be trusted, the λ_{max} maps seem not to be affected much by the CMFT bias. Indeed, they contain reliable information about the quantum vs classical character of each phase that can be qualitatively translated to the strength of the ordered moment, just as in the Kitaev-Heisenberg case. In the next step we will extend the insight into those tendencies by introducing more refined maps based on the maximal-overlap and the full CMFT methods.

[42] Not distinguished because of the logscale.

More technical remarks

Before we move towards further results let us provide few technical remarks:

In the J-K-Γ-Γ' model the symmetry-allowed but non-diagonal $\Gamma\left(\mathrm{S}_i^{\alpha}\mathrm{S}_j^{\beta}+\mathrm{S}_i^{\beta}\mathrm{S}_j^{\alpha}\right)$ and $\Gamma'\left(\mathrm{S}_i^{\alpha}\mathrm{S}_j^{\gamma}+\mathrm{S}_i^{\gamma}\mathrm{S}_j^{\alpha}+\mathrm{S}_i^{\beta}\mathrm{S}_j^{\gamma}+\mathrm{S}_i^{\gamma}\mathrm{S}_j^{\beta}\right)$ terms[43] will be tilting the pseudospins from the cubic axes preferred by the Kitaev term. Accommodating such a behaviour required utilizing significantly more degrees of freedom in both the maximal-overlap and the CMFT methods. Namely, the orientation of each classical pseudospin $\mathbf{n}_i$ translated to the spherical angles reads as

$$\mathbf{n}_i = (\mathrm{n}_i^{\mathrm{X}}, \mathrm{n}_i^{\mathrm{Y}}, \mathrm{n}_i^{\mathrm{Z}}) = (\sin\theta_i\cos\phi_i, \sin\theta_i\sin\phi_i, \cos\theta_i), \tag{3.45}$$

where X, Y lie in the honeycomb plane while Z is the perpendicular direction, see Fig. 2.6 (b). This reduces the number of parameters in the maximal-overlap method to 48 for the 24-site cluster. Although this could be further simplified for collinear orderings such as Néel or zigzag, the non-collinear tendencies promoted by the Γ and Γ' terms enforce the 48-parameter space of $\{\phi_i, \theta_i\}$ [29].

Even more computationally challenging becomes the CMFT method. Since the cubic axes are no longer the easy axes, $\mathbf{S}_i\langle\mathbf{S}_j\rangle \approx \mathrm{S}_i^z\langle\mathrm{S}_j^z\rangle$ becomes a very poor approximation. Consequently, the general formula (3.24), stabilizing the full $\langle\mathbf{S}_i\rangle$ vectors has to be utilized as the mean-field part. We will be reading out the spatial orientation of the ordered moment $\mathcal{S}$ given by formula (3.15) in an analogous way as in the maximal-overlap method

$$\frac{\mathcal{S}}{|\mathcal{S}|} = (\sin\theta\cos\phi, \sin\theta\sin\phi, \cos\theta) \tag{3.46}$$

for the collinear and

$$\frac{\mathcal{S}}{|\mathcal{S}|}|_{\text{sublattice I}} = (\sin\theta_i\cos\phi_i, \sin\theta_i\sin\phi_i, \cos\theta_i) \tag{3.47}$$

for the non-collinear orderings.

In both cases, when presenting the results we will utilize a convention in which the azimuthal (honeycomb plane) angle ϕ starts from the +X direction and we will reduce its range to $[0, 180]^\circ$, while θ will be translated into an angle from the plane to the pattern: $\alpha = 90^\circ - \theta$.

Site-averaging over the external sites

Linearized CMFT gave us a notice about the strong canting tendencies appearing even in the collinear regions due to the bond-anisotropic part of the mean field. To compensate this effect an averaging over the external sites after each iteration of the CMFT loop was introduced in the full CMFT algorithm.[44] In this way the excess value filling up different $\langle\mathrm{S}_i^{\gamma}\rangle$ for each direction of the mean-field bonds became evenly spread among all external sites, promoting collinearity from iteration to iteration.

3.4.2 Composite phase diagram of the J-K-Γ model

Here we will prove that the rough sketch presented in Fig. 3.13 is actually corroborated by the more sophisticated approaches.

[43] $\alpha, \beta, \gamma \in \{x, y, z\}$ according to a cyclic permutation suitable for a particular bond direction.

[44] Explicitly: the outcoming averages were summed up and normalized.

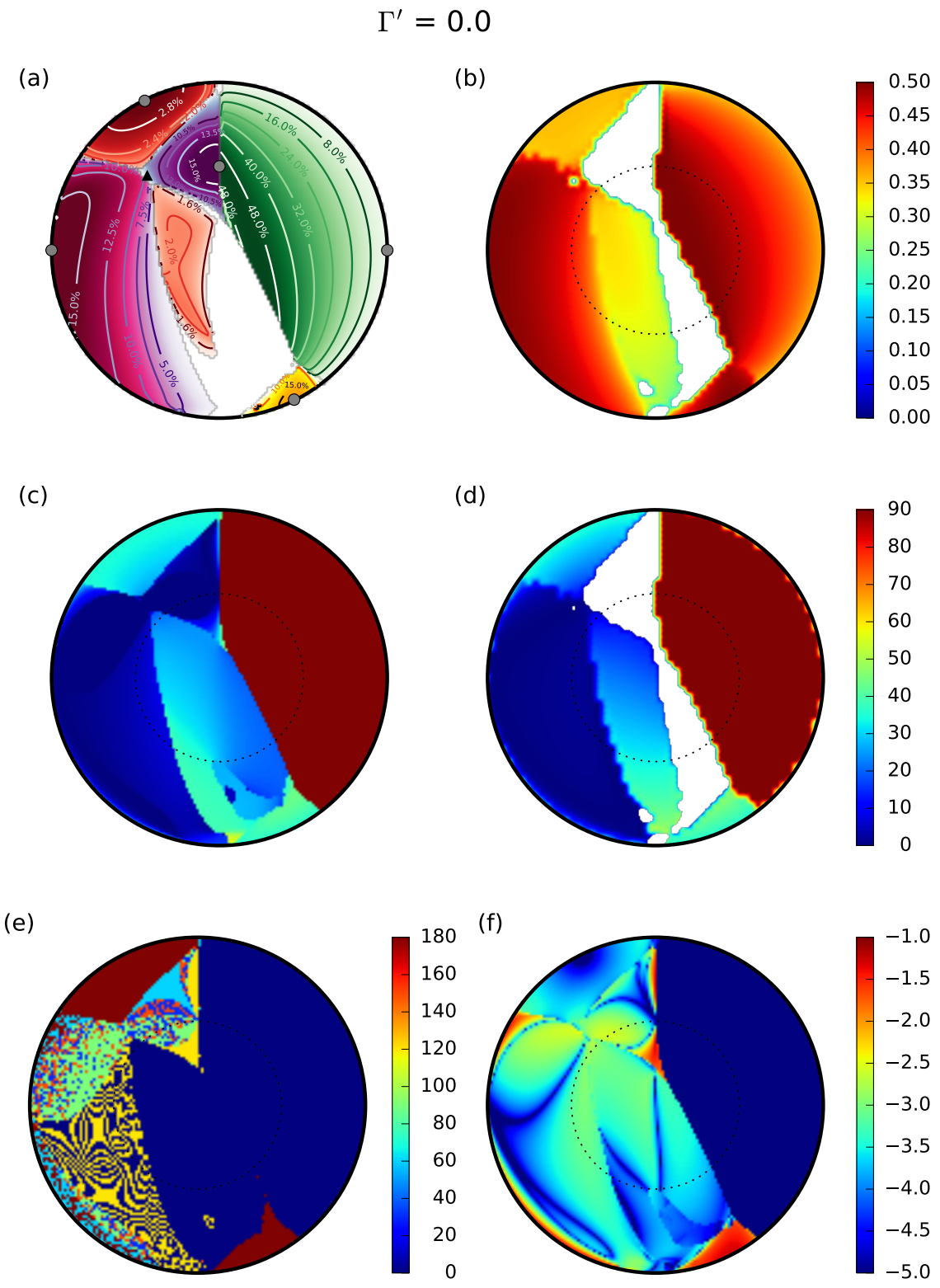

FIGURE 3.15: The $\Gamma' = 0$ slice of the composite phase diagram: (a)—patterns with the maximal probability in the ground state: pink—FM, yellow —stripy, green—Néel, red—zigzag and violet —vortex. The grey circles/black triangle indicate the SU(2)/compass points. (b)—the ordered moment value for the 24 sites via the full CMFT. (c)-(d)—the angle α [in °] from the honeycomb plane to the pattern for the maximal-overlap and CMFT methods, correspondingly. (e)-(f)—the azimuthal angle ϕ [in °] within the honeycomb plane and $\log_{10}|\tilde{\lambda}_{max}|$ stability map for the maximal-overlap method.

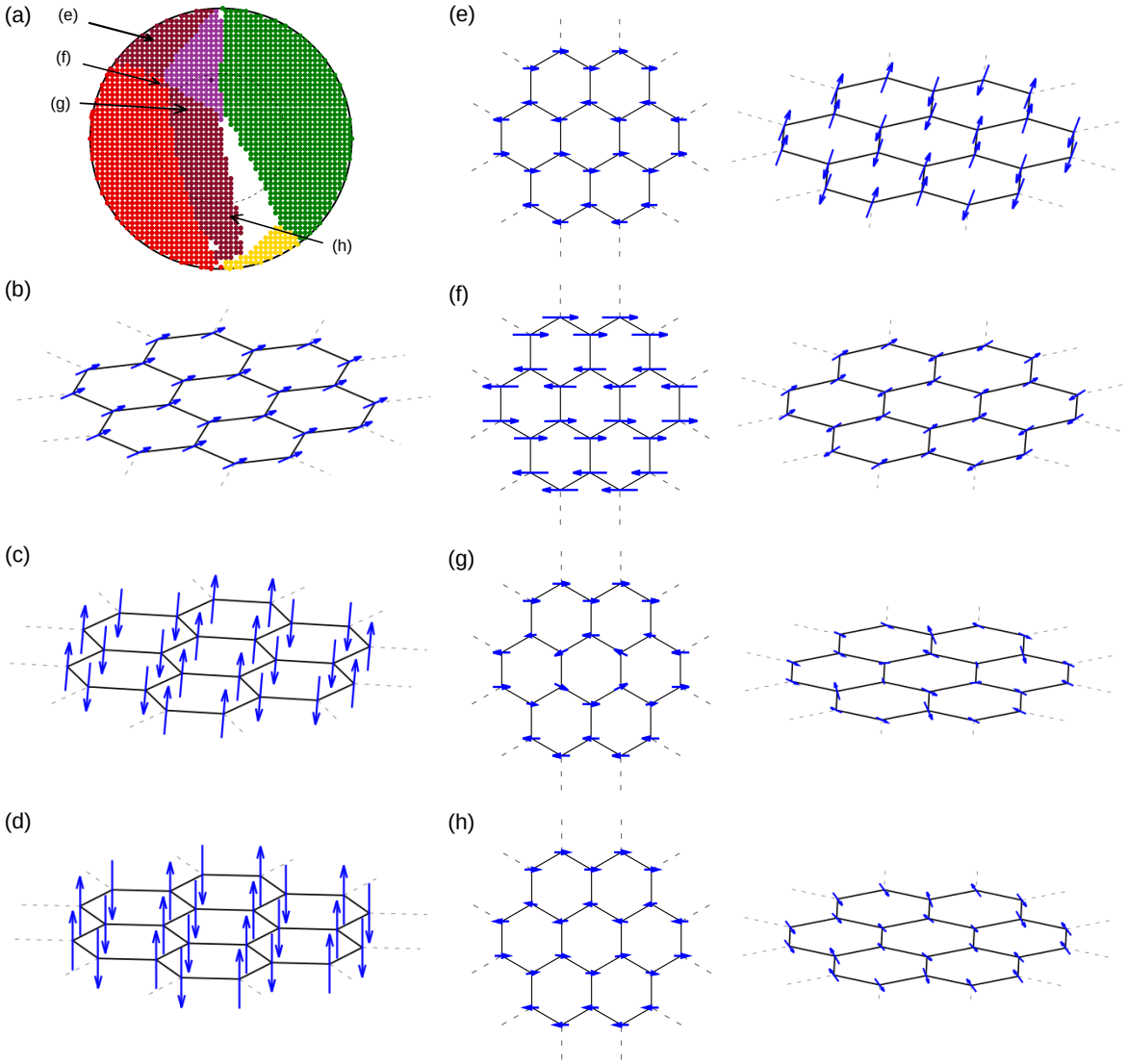

FIGURE 3.16: The representative full CMFT results [panels (b)-(h)] with their positions on the $\Gamma' = 0$ slice [panel (a)]. Panel (a) presents the exclusively CMFT phase diagram with the boundaries determined by the ground-state energy comparison. Here red represents the FM, yellow—the stripy, green—the Néel, dark brown—the zigzag, violet —the vortex stabilized patterns. The dark-violet point inside the vortex phase corresponds to the vortex-a variant, see Fig. 3.17 and the main text. Panels (b), (c), (d) show the typical orientation of the FM/stripy/Néel pattern inside the $\Gamma' = 0$ slice, respectively. Panels (e)-(h) present the tendencies inside the zigzag phase.

Ferromagnetic phase

It is reasonable to start the analysis from the most classical FM phase, massively spread around the FM SU(2) point. The reader may locate this point as the grey circle at $J = -1$, $K = \Gamma = 0$ in Fig. 3.15 (a). The FM region is roughly consistent between Figs. 3.13 and 3.15, representing the maximal-overlap and the full CMFT results for the $\Gamma' = 0$ slice.[45] Among them, Fig. 3.15 (a) recognises the phases based on the pattern with the maximal overlap with the ground state. Just like in the basic quantum mechnics, the overlap provides the plotted probability of the winning pattern.

[45] Linearized CMFT did not give a definite prediction at the "eastern" FM boundary, and indeed, the probability of the FM pattern decreases there significantly.

Interestingly, on the external Kitaev-Heisenberg circle the FM configuration has the probability 1/6. This feature is closely related to the ordered moment direction. Namely, for the Kitaev-Heisenberg model 1/6 is the maximal available probability for any pattern because the ground state contains 6 versions of a given collinear arrangement, differing by the alignment along one of the Kitaev cubic axes. Hence, a probability reaching 1/6 signals the vanishing quantum fluctuations if the pseudospins are arranged along the Kitaev axes. The effect is further confirmed by the strongly classical ordered moment value (Fig. 3.15 (b)), reaching 0.5 at the FM SU(2) point.

However, almost immediately after the Γ term is introduced the ferromagnetic moments tilt towards the honeycomb plane. This can be seen on the maps of the angle α between the honeycomb plane and the pattern, estimated by the maximal overlap (Fig. 3.15 (c)) and the CMFT methods (Fig. 3.15 (d)). A deeper understanding of this behaviour may come from the classical energy E_c:[46]

$$\mathrm{E}_{cFM} \propto 3J + K - \Gamma + \Gamma\left(\mathrm{n}^x + \mathrm{n}^y + \mathrm{n}^z\right)^2, \tag{3.48}$$

where $\mathbf{n}$ is the direction of the classical pseudospins normalized to one, here described in relation to the Kitaev cubic axes. Let us consider three examples of the FM pattern direction to see what orientation would minimize E_c:

- The FM pattern perpendicular to the honeycomb plane projects in equal proportions to the Kitaev cubic xyz axes.[47] Utilizing formula (2.23) one obtains $\left(\mathrm{n}^x + \mathrm{n}^y + \mathrm{n}^z\right)^2 = (3\times\frac{1}{\sqrt{3}})^2 = 3$. This leads to $-\Gamma + 3\Gamma = 2\Gamma$—a large positive contribution for $\Gamma > 0$ considered for the real materials.

- The pseudospins lying along one of the cubic axes, e.g. z, produce $-\Gamma + \Gamma(0+0+1)^2 = 0$.

- Finally, $\mathbf{n} \parallel -\mathrm{X}$ leads to $\left(\mathrm{n}^x + \mathrm{n}^y + \mathrm{n}^z\right)^2 = \left(-\frac{\sqrt{6}}{6} - \frac{\sqrt{6}}{6} + \frac{\sqrt{6}}{3}\right)^2 = 0$, where we again used formula (2.23) for the projections. In this configuration the orientation-independent $-\Gamma$ term is not hampered by the positive Γ contribution. By virtue of the C_3 symmetry, we would obtain the same effect considering $\mathbf{n}$ aligned along positive and negative projections of each of the Kitaev cubic axes to the honeycomb plane. Moreover, since $\left(\mathrm{n}^x + \mathrm{n}^y + \mathrm{n}^z\right)^2$ can be reduced to the square of the scalar product $\mathrm{Z}\cdot\mathbf{n}$[48], any direction within the honeycomb plane brings the term to zero from orthogonality. The honeycomb plane minimizes the classical energy, guaranteeing $3J - \Gamma + \Gamma\left(\mathrm{n}^x + \mathrm{n}^y + \mathrm{n}^z\right)^2$ to be strongly negative for the negative J and positive Γ.

This is not the end of the discussion of the ferromagnetic phase though. In fact, in the more quantum maximal overlap method few ferromagnetic subphases are distinguishable based on the directional details. By comparing Fig. 3.15 (c) and (e), where the azimuthal angle ϕ is presented, one notices that the honeycomb plane prefers the orientation along the bonds: $\phi = 30°$, $90°$, $150°$ for the a, c, b bonds, respectively. In contrast, the orientation slightly above the plane ($\alpha \approx 10°$) is correlated with the alignment perpendicular to the bonds: $\phi = 0°$, $60°$, $120°$, $180°$ in our settings.

The CMFT-based patterns mostly lie in the honeycomb plane. Only close to the outer rim of the slice the α angle stays at a non-zero level [Fig. 3.15 (d)]. This can be easily justified by the

[46] In this method we treat the pseudospins as classical vectors, of the length 1 for convenience. For a chosen pattern, eg. zigzag with the FM a, b bonds and the AF c bonds, one isolates its magnetic unit cell, along with the PBC. Each bond of the cell contributes to the Hamiltonian consisting of the classical scalar product in case of the Heisenberg term, and the products of the classical projections to the suitable axes for the anisotropic terms. It is energetically favorable for the pseudospins to align along the directions set by the most negative Hamiltonian terms.

[47] The (111) direction in the Kitaev cubic axes, the Z direction in the XYZ axes.

[48] Better visible as $(1,1,1)\cdot(\mathrm{n}^x, \mathrm{n}^y, \mathrm{n}^z)$.

reduction of the quantum fluctuations on the mean-field bonds. It is much easier for the classical energy to stabilize the in-plane orientation with the weaker quantum fluctuations. An example of the stabilized CMFT result in the region can be examined in Fig. 3.16 (b). Even though with this we end the description of the FM phase on the $\Gamma' = 0$ slice, the reader will soon realise that there is much more to discover when $\Gamma' < 0$.

Stripy phase

As mentioned in Secs. 2.4.1 and 3.3.2, on the external Kitaev-Heisenberg circle the $\mathcal{T}_4$-partner of the FM phase is the stripy phase. Consequently, all the ordeded moment characteristics are connected for the two phases, including the spatial direction. This is no longer the case once the Γ term is activated, breaking the self-duality of the $\mathcal{T}_4$ mapping. While the moments preserve their classical FM character, evidenced by the very high probability and moment value in the whole stripy region, reaching correspondingly 1/6 and ≈ 0.5 at the stripy SU(2) point, the moments do not bend towards the honeycomb plane but tilt slightly above the Kitaev cubic axes instead. An example of the stripy pattern stabilized within the CMFT is shown in Fig. 3.16 (c).

Néel phase

In the next step, we move towards the Néel phase [the green region in Fig. 3.15 (a)], for which the classical energy

$$\mathrm{E}_{cNeel} \propto -3J - K + \Gamma - \Gamma(\mathrm{n}^x + \mathrm{n}^y + \mathrm{n}^z)^2, \tag{3.49}$$

is minimized by the maximal contribution from $(\mathrm{n}^x + \mathrm{n}^y + \mathrm{n}^z)^2$, guaranteed by the direction perpendicular to the honeycomb plane. Fig. 3.16 (d) showcases this orientation based on the CMFT result. It is evident in Fig. 3.15 (c) and (d) that even very small Γ values are able to rotate the moments to the Z direction.[49]

Interestingly, the growing Γ also makes the Néel phase increasingly classical, evidenced by the growing probability and ordered moment value. For the Z direction there are only two possibilities of any collinear pattern, each of them carrying maximally 50% probability. Fig. 3.15 (a) and (b) as well as the $\Gamma' = 0$ panel of the Fig. 3.14 indicate the existence of a special manifold[50] starting at the vortex SU(2) point, for which the ordered moment characteristics are *exactly* classical: the Néel probability = 50%, the ordered moment value = 0.5 and λ_{max} dramatically exceeds the linear regime.[51] The explanation of this extraordinary behaviour, presented in detail in Sec. 3.4.5, is quite remarkable: all the pseudospin-flipping terms applicable to the Néel pattern in the out-of-plane direction cancel, making the pattern purely classical. Therefore, the Néel phase of the J-K-Γ model encompasses both the classical Néel state near the center of the slice and the highly-dressed Néel pattern close to the external Kitaev-Heisenberg circle.

Zigzag phase via the maximal overlap method

On the external Kitaev-Heisenberg circle the $\mathcal{T}_4$-partner of the Néel phase is the zigzag phase. The linearized CMFT confirmed the expanse of the original upper zigzag region and the appearance of another, lower zigzag patch once $\Gamma > 0$.[52] Prompted by the linearized CMFT troubles, we will start the description with the ED-based results to set a reliable reference picture. The easiest to notice are the low zigzag probabilities [the red regions in Fig. 3.15 (a)] in comparison to the neighboring phases. This suggests that, even more than in the pure Kitaev-Heisenberg case, the

[49] Since the Z direction is a pole for the azimuthal angle ϕ, the zero value on Fig.3.15 (e) is just a convenience-this angle is not well defined for the out-of-plane direction.

[50] A curved surface in the parameter space.

[51] Reaching the range 10^4 for the initial polarization of 10^{-3}.

[52] Cf. Figs. 2.20 and 3.13.

zigzag phase is strongly fluctuating. Indeed, many patterns compete in the ground state and the maximal probability does not cross 3%.

In the upper zigzag phase the highest probability values are concentrated around the zigzag SU(2) point, and the whole upper region seems to emanate from there. With the growing Γ, the ordered moment rotates down from one of the Kitaev cubic axes towards the honeycomb plane, as schematically shown on the left side of the Fig. 2.14. Fig. 3.15 (c) reveals the moment continuously diverging from the z axis ($\alpha \approx 35.26°$) down to $\approx 30°$ at the boundary of the region, while the azimuthal angle remains fixed to $\phi = 180°$ in Fig. 3.15 (e).

The lower zigzag region has its source at another zigzag SU(2) point at $\Gamma' = -0.398$ [9].[53] For the $\Gamma' = 0$ slice the region is characterized by the even lower probability than in the upper zigzag case. Importantly, in the lower zigzag region the moment rotates up from $\alpha \approx 25°$ to slightly above 30° at the "southern" zigzag boundary, while the azimuthal angle is zero. In other words, the moment stays in the vertical XZ plane, equidistant from the x and y axes, as illustrated on the right side of the Fig. 2.14.

In the present slice the maximal overlap method keeps the two zigzag regions separate. Moreover, a careful examination of the maximal probability data revealed that the two zigzag regions as well as the FM and vortex phases, meet at a special point marked as a black triangle in Fig. 3.15 (a). As it will be thoroughly described in Sec. 3.4.6, at this point the J-K-Γ Hamiltonian reduces to the proper compass model.

Stability map

While in Fig. 3.15 (a) only the collinear zigzag tendencies in the lower zigzag region are shown, Fig. 2 in Ref. [29] reveals the non-collinear zigzag tendencies just below it. The instability of the collinear zigzag against the non-collinear effects was also inspected via the Hessian matrix. Such a matrix is formed from the second derivatives of the maximal collinear probability with respect to the 48 angles $\{\phi_i, \theta_i\}$. A true stable maximal probability of the collinear pattern would generate negative Hessian eigenvalues, while the appearance of a positive eigenvalue would indicate a potential instability in some direction. Thus, the maximal eigenvalue $\tilde{\lambda}_{max} < 0$ guarantees that all the other eigenvalues have to be also negative and the pattern is stable—no need to consider the non-collinear patterns in such a case. In contrast, $\tilde{\lambda}_{max} > 0$ suffices to destabilize the pattern in one direction, prompting a need for a more elaborate pattern optimization with respect to the full 48-parameter set. It has been verified that not only the probability of the collinear zigzag below the "southern" border of the lower zigzag region, but also the maximal collinear probability in the whole white area in Fig. 3.15 (a) results in the positive maximal eigenvalue patches.

In order to cover also the finer structure inside each phase, a map of $\log_{10}|\tilde{\lambda}_{max}|$ was plotted in Fig. 3.15 (f). There, a dark-blue color indicates that as $\log_{10}|\tilde{\lambda}_{max}| \to -\infty$ and $|\tilde{\lambda}_{max}| \to 0$, some of the 48 degrees of freedom are being released. One can recognise the already-mentioned subphases of the FM region, with their boundaries meeting at the FM SU(2) point where any orientation of the FM pattern is allowed and only the collinearity constraints hold. Surprisingly, no fine structure is found inside the stripy phase. The seemingly puzzling dark-blue color of the entire Néel region is just an artifact of the indeterminacy of the ϕ angle for the Néel pattern along the Z direction.

Returning to the zigzag phase, an expected release of the degrees of freedom is observed around the zigzag SU(2) point in the upper zigzag region. The collinear and non-collinear tendencies in the lower region are indeed separated by a blue boundary. We leave the stability inspection in the non-collinear, non-zigzag regions for the further sections, now moving on to the full CMFT results for the zigzag phase.

[53] Cf. Fig. 2.21 (d).

Zigzag phase via the full CMFT

While the CMFT results for the FM, stripy and Néel phases on the $\Gamma' = 0$ slice are reliable, the zigzag averages still experience some bias, even with the site-averaging included. Fig. 3.16 (a) presents all the points where the collinear and vortex patterns stabilized within the full CMFT algorithm. The colors indicate the orderings with the lowest ground-state energy. In particular, the two zigzag regions are marked in dark brown. When comparing this CMFT-only phase diagram to the stability map in Fig. 3.15 (f), one could hypothesize that the "northern" part of the lower zigzag region contains the collinear patterns while the non– collinear tendencies accumulate in the "southern" part. Unfortunately, this is not exactly the case for the CMFT data. We will therefore analyse the emerging tendencies in detail, providing 4 representative results [Fig. 3.16 (e)-(h)] with their location on the phase diagram marked in Fig. 3.16 (a).

While the results in the upper zigzag region are rather collinear and could be trusted [Fig. 3.16 (e)], the lower zigzag region becomes problematic again. Namely, the non-collinear canting tendencies appear mainly in its "northern" and "eastern" part [Fig. 3.16 (g)], belonging to the collinear region according to the maximal overlap method. In contrast, the most "southern" region, where the non-collinear trends were expected, turns out to be much more collinear [Fig. 3.16 (h)].

Even though the overall situation is much better than if the averages were allowed to freely respond to the anisotropic mean field,[54] the details of the lower zigzag region remain biased in the CMFT case. The anisotropic mean-field and the site-averaging together reduce the quantum fluctuations in a way that leads to a misrepresentation of the collinear/non-collinear tendencies in this originally strongly bond-frustrated quantum region. This is the main reason why we decided not to present the CMFT $\Gamma' = 0$ slice in Ref. [29] and opted for a more thrustworthy $\Gamma' = -0.1$ case instead. As the reader will see in Sec. 3.4.3, supplementing K and Γ with Γ' reduces the frustration, providing an opportunity for the CMFT to perform better in those slices.

Nevertheless, when carefully extracted, some information about the ordered moment can be trusted. By evaluating formula (3.15) over the 24 sites we obtained, in our opinion, the most reliable ordered moment value for the zigzag phase in the $\Gamma' = 0$ slice. This is what is presented in Fig. 3.15 (b). The other explored possibilities: the central hexagon and the external sites, can be found in Appendix A.2. While the moment from the external sites has expectedly overestimated value, the moment from the central hexagon, though appealingly the lowest, has shown undesired tendencies that we attribute to the detectable non-collinear canting appearing inside the cluster. Therefore, in contrast to the pure Kitaev-Heisenberg case, the central hexagon turned out not to be an optimal option. In general, the moment value is smaller in the lower zigzag region and visibly decreases in its "southern" part. This confirms the conclusion driven from the probablility evolution: the ground state in the region is very quantum, with the fluctuations appearing mainly as a way to overcome the frustration caused by the bond-selective K and Γ terms.

Fortunately, the spatial orientation of the zigzag pattern can also be trusted when taken from the most collinear external sites. Indeed, the CMFT-based α map [Fig. 3.15 (d)] reveals similar trends as in the maximal-overlap case [Fig. 3.15 (c)]. The less quantum conditions generated by the boundary mean field cause α to change at a slightly higher rate than in the maximal-overlap case, but this bias is easy to manage and does not disqualify the results.

There is one more caveat one should be aware of when inspecting the CMFT result. Namely, the zigzag pattern actually reaches the honeycomb plane in the narrow island between the two zigzag regions. The zigzag island can be easily identified in Fig. 3.16 (a), where it is represented by the two points.[55] One may inspect the pattern stabilizing there in Fig. 3.16 (f). Because

[54] This would probably result in the non-colliear patterns everywhere. We base this conclusion on the patterns emerging from the linearized CMFT and the initial tests of the full CMFT without the site-averaging.

[55] In the chosen density of the parameter-space covering. Whether within the higher resolution a bridge would stabilize between the upper and lower zigzag remains an open question. In any case, the island is a side effect of the method.

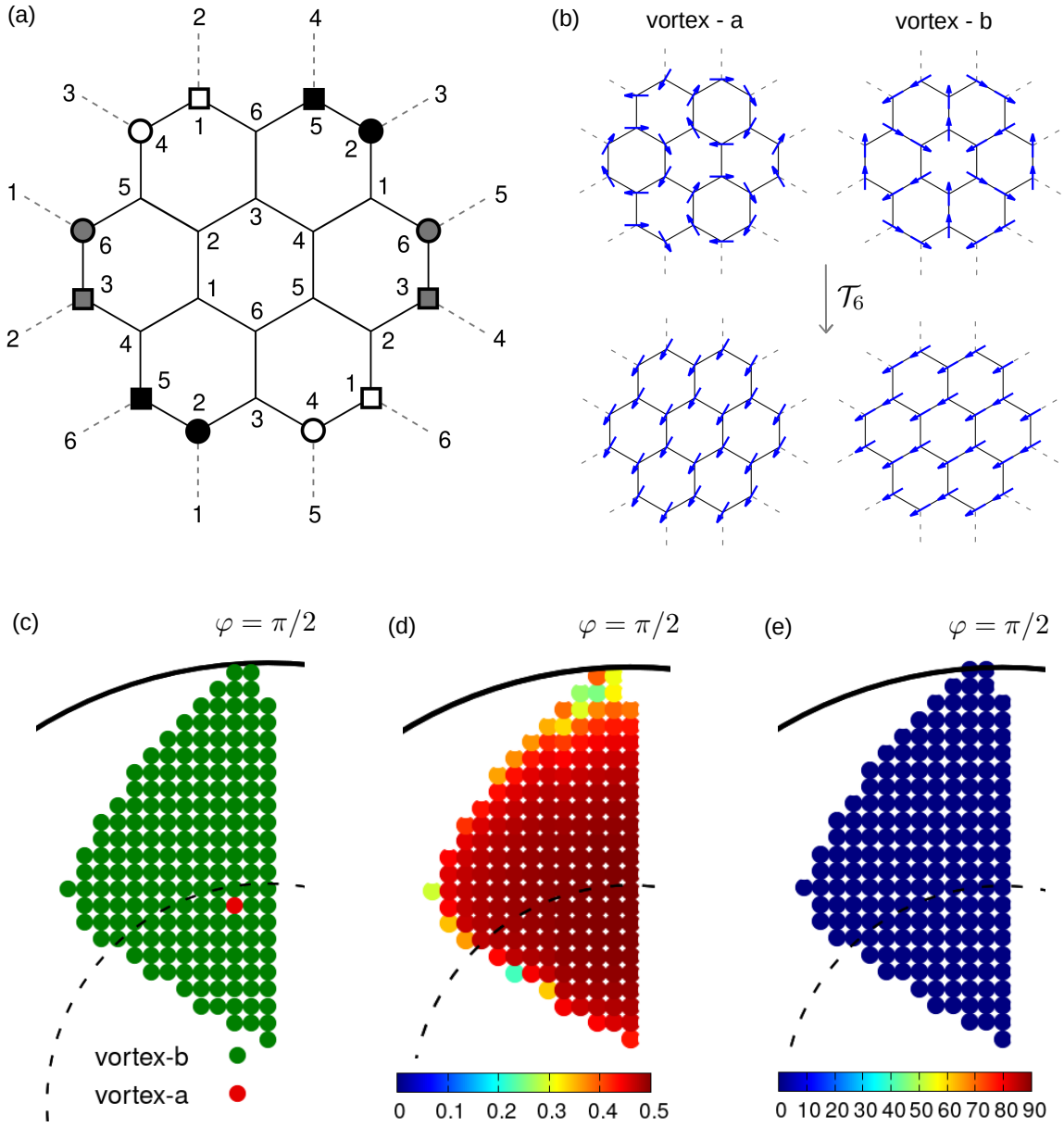

FIGURE 3.17: The CMFT setup and results for the vortex phase in the $\Gamma' = 0$ slice. Panel (a)—the distribution of the 6 sublattices required by the $\mathcal{T}_6$ transformation on the 24-site embedded cluster. The assignment of the external sites to the 6-sublattice site-averaging is additionally marked by the geometrical symbols. Panel (b)—the CMFT results in a close neighborhood of the vortex SU(2) point: the vortex-a/vortex-b patterns and the FM patterns obtained from them via $\mathcal{T}_6$. Panels (c), (d), (e)—the distribution of the vortex-a and vortex-b variants, the ordered moment value and the α angle [in °], respectively.

of the mean field and the site-averaging, the ground state in the island looses enough quantum fluctuations to stabilize the LRO. Moreover, the island and its close neighborhood make the only area where the zigzag moment value becomes more classical, jumping towards ca. 0.4 in Fig. 3.15 (b). However, since the maximal-overlap and the semi-analytical results at the compass point look different, we consider this a method-related effect.

Vortex phase

In Sec. 2.5.1 we have mentioned a non-collinear region identified by the 120°-order in Ref. [8]. Here we present a detailed, multi-method study of the phase, partially published in Ref. [29]. We begin with the vortex SU(2) point ($J = 0$, $K = \Gamma = 1/\sqrt{2}$), marked by the grey circle in the middle of the violet region in Fig. 3.15 (a). Although at this point the SU(2) continuous symmetry guarantees an infinite number of the possible patterns,[56] all of them must have a particular 6-sublatice structure in order to be transformed into a suitable FM pattern via the $\mathcal{T}_6$ transformation (2.27). Fig. 3.17 (b) provides two representative examples of the allowed patterns: vortex-a and vortex-b. These patterns are the actual converged CMFT results at/in the close neighborhood of the vortex point, before and after the $\mathcal{T}_6$ transformation.

At the vortex point the CMFT could run without the site-averaging because of the anisotropic mean field summing up into the SU(2) symmetry.[57] However, in order to obtain stable vortex patterns in the whole vortex region revealed by the maximal overlap method (the violet color in Fig. 3.15 (a)), we have incorporated a special kind of the boundary site-averaging into the full CMFT algorithm. Fig. 3.17 (a) illustrates the distribution of the 6 sublattices on the 24-site cluster with periodic boundary conditions. We are interested in the external sites belonging to the same sublattice, marked by the matching symbols on the panel. The site-averaging was performed within each such subset, preserving the 6-sublattice structure, and the patterns from the maximal overlap method were used to polarize the external sites.

Let us now compare the results of the both methods. The whole violet region in Fig. 3.15 (a) emanates from the vortex point and is divided into several subphases where vortex-a or vortex-b has the maximal probability, depending on the ratio of the Hamiltonian parameters. The subphases can be identified by the azimuthal angle ϕ (Fig. 3.15 (e)). The in-bond arrangement of vortex-b is captured by $\phi = 30°$, 90° and 150°, while ϕ for vortex-a reaches 0°, 60°, 120°, 180°. The small difference in probability between the two patterns together with the $\log_{10}|\tilde{\lambda}_{max}|$ trends in Fig. 3.15 (f) suggest soft transitions between the two variants. For the maximal overlap method vortex-b always lies in the honeycomb plane (Fig. 3.15 (c)) while vortex-a may have a staggered Néel component in the Z direction for the points close to the boundary with the Néel phase.

The general vortex boundaries are similar within the CMFT method. We begin their inspection from the whole stabilized vortex result in Fig. 3.17 (c). To set the boundaries between this region and the collinear phases, we have compared their ground-state energies. The outcome is visible in Fig. 3.16 (a). As the reader might have noticed, however, we do not include the CMFT-based vortex data explicitly in the composite diagram in Fig. 3.15. The reason is the distribution of the vortex-a and vortex-b subphases, strikingly different from the maximal-overlap case, and our suspicion that the CMFT-based vortex result is not complete.

In order to understand it, let us examine Fig. 3.17 (e). There, the moment direction is bound to the honeycomb plane, differing slightly from the maximal-overlap result. Such an outcome was caused by taking the vortex-a and vortex-b ansaetze always perfectly in the honeycomb plane and the site-averaging strongly suppressing the out-of-plane tendencies. Such an approach had both the positive and the negative consequences: on one hand, the 6-sublattice site-averaging produced perfect vortex patterns and allowed the vortex phase to stabilize in the region almost identical to the maximal-overlap case. On the other hand, the energy comparison led to the overwhelming dominance of vortex-b in the CMFT result, with only one vortex-a point winning the competition close to the vortex SU(2) point.[58] Because the site-averaging turned out to be so powerful in this case, we suspect that the present study is incomplete. Perhaps the ansaetze with a varying vertical component would enable vortex-a to expand into the boundary region

[56] ED on a finite cluster produces the ground state containing their smaller, orthogonal subset.
[57] At any SU(2) point the CMFT performs well.
[58] In the presented parameter – space covering.

with the Néel phase, similarly to the maximal-overlap case. We acknowledge, however, that such a task could be rather tiresome and the outcome might not be worth the effort.

Nevertheless, both methods brought solid evidence of a classical character of the vortex region in the $\Gamma' = 0$ slice. Similarly to the FM and stripy phases, the probability saturates there at $1/6 \approx 16\%$—the maximal possible value for the pattern without quantum fluctuations considering the FM-vortex $\mathcal{T}_6$ connection. Importantly, the classical character is directly confirmed by the high ordered moment values (Fig. 3.17 (d)), reaching 0.5 at the vortex point. Thus, all the so-far-analysed LRO phases except zigzag become strongly classical in the $\Gamma' = 0$ slice.

We would like to conclude the description of the vortex phase with the analytical arguments, as presented in Ref. [29]. We will consider the influence of the 4 special points surrounding the vortex phase in the $\Gamma \geq 0$ part of the J-K-Γ-Γ' parameter space:

1. The already-mentioned vortex SU(2) point in Fig. 3.15 (a), of a hidden FM nature.
2. The hidden AF SU(2) point appearing for $\Gamma' = -0.535$, marked by C in Fig. 2.21 (d) and by a black circle in Fig. A.4 (j). This point supports both vortex variants, but the ground state is strongly quantum because of the AF character of the point.
3. The also already-mentioned compass point at $K = \Gamma = -J > 0$, $\Gamma' = 0$, marked as a black triangle in Fig. 3.15 (a).
4. The compass-like point for $\Gamma' = -0.603$, denoted by an empty triangle in Fig. A.4 (k).

The hidden SU(2) symmetry of the points 1. and 2. enables many patterns in the ground state, as long as they are $\mathcal{T}_6/\mathcal{T}_2\mathcal{T}_6$-compatible, respectively. Leaving these points however selects the vortex-a or vortex-b patterns, depending on the proximity to the two compass points. At the point 3. the J-K-Γ-Γ' model simplifies to the proper compass model on the honeycomb lattice which has the interaction axes in the honeycomb plane, along the suitable bonds. Consequently, in the neighborhood of this point the in-bond vortex-b alignment of the pseudospins is favoured. In contrast, at the point 4. the model simplifies to a compass-like model, with the interaction axes also in the honeycomb plane but perpendicular to the bonds. Naturally, this promotes vortex-a in the neighborhood of the point. The compass points are a part of the Ising-Kitaev-compass model hiding within the J-K-Γ-Γ' Hamiltonian and will be discussed in detail in Sec. 3.4.6.

The white area

The mysterious white area on the panels of the Fig. 3.15 hosts the incommensurate pseudospin arrangements [8, 94]. Indeed, the maximal overlap method revealed various spiral patterns in the majority of the white region between the Néel and zigzag phases. Moreover, additional 32-site calculations in the unstable, "southern" part of the lower zigzag region, *performed by Jiří Chaloupka*, verified that the zigzag tendencies become incommensurate when the cluster is large enough.[59]

Another omitted feature of the $\Gamma' = 0$ slice is the lower part of the vertical $J = 0$ line, where the FM Kitaev term is perturbed by the growing Γ interaction. The spin-liquid tendencies appearing on that line were recently published in Refs. [93, 95]. The ED calculations in the reciprocal space revealed the characteristic, wave-like background below the LRO peaks in the close neighborhood of the line as well as the LRO tendencies summing up to a rather prominent wave-like pattern on the line, suggesting the spin-liquid state. The reader is referred to Fig. 3 of Ref. [29] for more details.

Although the full CMFT results for $\Gamma' = 0$ fit roughly to the above image, several details are clearly not trustworthy. The zigzag phase stabilized by the CMFT exceeds the boundaries of the

[59] See Ref. [29] for a detailed discussion.

stable zigzag phase from the maximal-overlap method. In particular, it crosses $J = 0$ line, which seems to be a true boundary for the zigzag phase for larger clusters.

KSL regions

The most intensively investigated KSL regions stretch around the explicit Kitaev points $K = \pm 1$ at the very top and bottom of the $\Gamma' = 0$ slice [8, 10]. The maximal probability map around the AF Kitaev point [see Appendix A of Ref. [29]] reveals a tiny U-shaped patch where the short-range patterns of the type illustrated in Fig. 2.9 (a), characteristic for the S $\to \infty$ limit of the Kitaev model, are favoured with the probability below 0.1%. Therefore, we take it as a trace of the liquid behaviour, even though the maximal overlap method is not best suited for the highly-entangled quantum spin-liquid phases. At the border with the LRO phases the probability has a significant jump to 1% and more. This is consistent with the further-neighbor correlations and spin susceptibility (χ'') analysis for the Kitaev-Heisenberg model around the AF Kitaev point in Sec. 3.3.3. We expect a more nuanced behaviour around the FM Kitaev point due to the fingerprints of the stronger bond-directional frustration and liquid behaviour in the adjacent incommensurate regions, as explained above.

3.4.3 Composite phase diagram of the J-K-Γ-Γ' model

The precise description of the imperfect real materials requires considering many more hopping paths, leading to several new terms in the effective Hamiltonian.[60] For practical reasons, however, one has to disregard the smaller coupling parameters. Below we analyse the influence of the small negative Γ' values,[61] related to the trigonal compression of the oxygen octahedra.[62]

Ferromagnetic phase

In the presence of $\Gamma' < 0$, the classical energy

$$\mathrm{E}_{cFM} \propto 3J + K - \left(\Gamma + 2\Gamma'\right) + \left(\Gamma + 2\Gamma'\right)\left(\mathrm{n}^x + \mathrm{n}^y + \mathrm{n}^z\right)^2, \tag{3.50}$$

will promote the out-of-plane arrangement of the FM moments when $2|\Gamma'| > \Gamma$. Namely, the direction-independent $-\left(\Gamma + 2\Gamma'\right)$ term will become positive while the $\left(\Gamma + 2\Gamma'\right)\left(\mathrm{n}^x + \mathrm{n}^y + \mathrm{n}^z\right)^2$ term—negative. In this situation, the out-of-plane direction maximizing $\left(\mathrm{n}^x + \mathrm{n}^y + \mathrm{n}^z\right)^2$ minimizes the classical energy. In Figs. 3.18-3.19 (c) and (d) such a situation, corrected by the quantum effects, takes place near the external $\Gamma = 0$ circle. The subphase boundaries are also well visible on the stability maps (Figs. 3.18-3.19 (f)). As we will elaborate in Sec. 3.4.5, for the certain parameter ranges the quantum fluctuations in the out-of-plane direction cancel out completely, leading to the purely classical manifolds. Hints of such a manifold inside the FM region away from the SU(2) point can be examined in Figs. 3.18-3.19 (a), where part of the out-of-plane subphase carries $> 48\%$ probability, as well as in Fig. 3.18 (b), where the CMFT-based ordered moment value also becomes classical in the out-of-plane subphase.

Néel phase

In contrast, in the Néel phase the Γ-Γ' competition leads to the emergence of the in-plane subphase. On the classical-energy level

$$\mathrm{E}_{cNeel} \propto -3J - K + \left(\Gamma + 2\Gamma'\right) - \left(\Gamma + 2\Gamma'\right)\left(\mathrm{n}^x + \mathrm{n}^y + \mathrm{n}^z\right)^2, \tag{3.51}$$

for $\Gamma' < 0$, $2|\Gamma'| > \Gamma$ the $\left(\Gamma + 2\Gamma'\right)$ term will become negative. Hence, the minimal energy will be reached by reducing the positive $-\left(\Gamma + 2\Gamma'\right)\left(\mathrm{n}^x + \mathrm{n}^y + \mathrm{n}^z\right)^2$ term. This is achieved in the in-plane direction, just as for the ferromagnet in the J-K-Γ model. In fact, it is even possible to distinguish the decrease in probability (Figs. 3.18-3.19 (a)) and ordered moment value (Fig. 3.18 (b)) in the boundary region.[63] It is caused by the major release of the degrees of freedom and the rise of the quantum fluctuations at the corresponding $\Gamma = -2\Gamma'$ arc. With the equation giving $\Gamma = 0.2$ and 0.4 for $\Gamma' = -0.1$ and -0.2, respectively, a progression of the boundary region towards the center of the slices is observed in Figs. 3.18-3.19. Fig. A.4 reveals the full extent of this trend.

[60] See Sec. 2.5.

[61] See Sec. 2.5.2.

[62] During the execution of this project first papers with the customized *ab-initio* studies started emerging. Ref. [60] suggested that the Γ' influence could be omitted in the minimal models for Na_2IrO_3 and α-$RuCl_3$. However, given the relation of Γ' to the trigonal distortion, we think that Γ' slices still bring valuable information about the trends of the magnetic ordering. This is supported by several recent experimental and theoretical developements taking into account the Γ' term. Following the *ab-initio* suggestions we have kept the Γ' values sufficiently small.

[63] We stress that, similarly to the $\Gamma' = 0$ slice, the less appealing appearance of the CMFT-based α map in Fig. 3.18 (d) is due to the actual results. The less quantum Hamiltonian promoted the intermediate regions of the moderate α values between the FM and AF subphases.

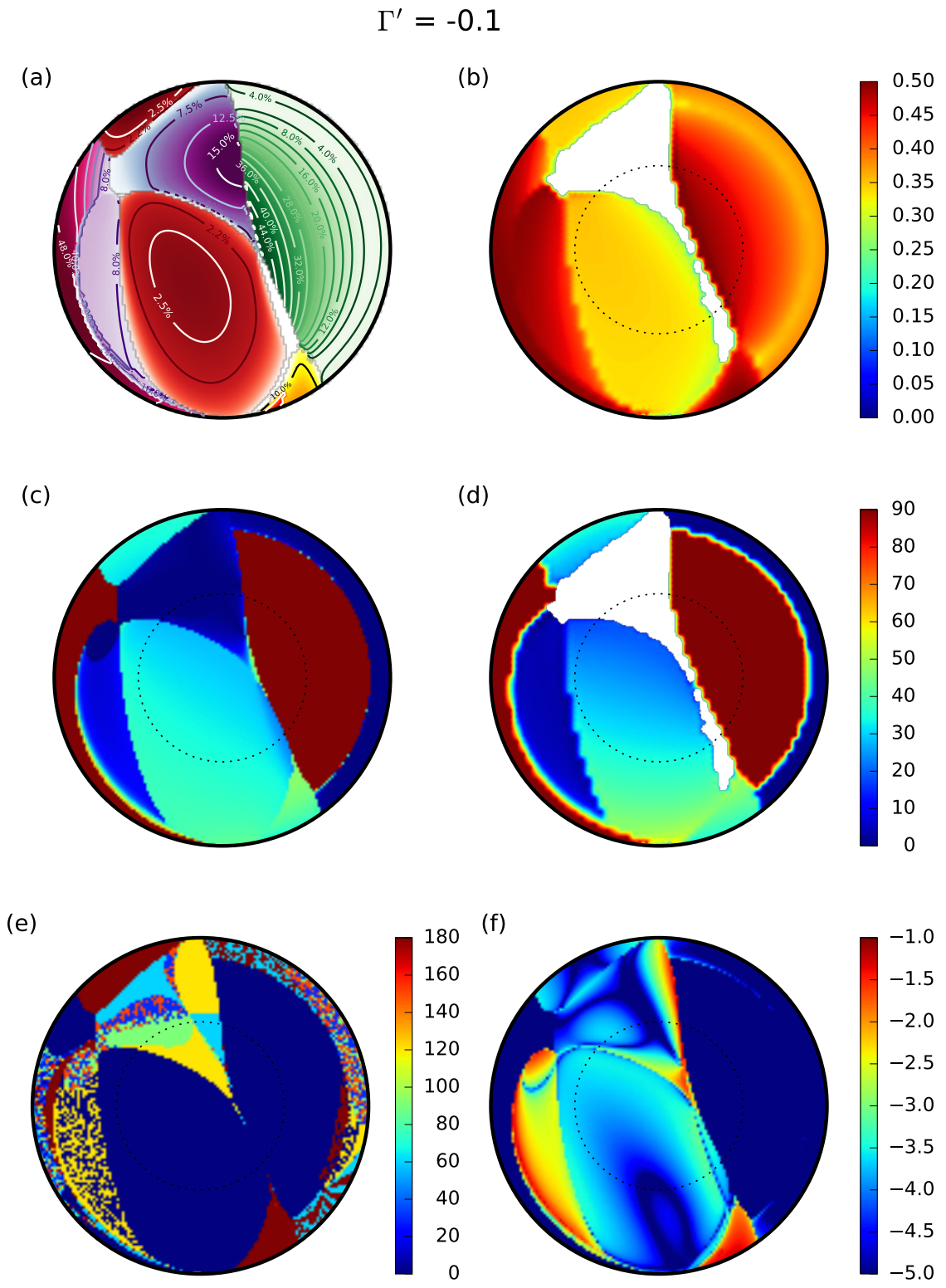

FIGURE 3.18: The $\Gamma' = -0.1$ slice of the composite phase diagram. (a)—the patterns with the maximal probability in the ground state: pink—FM, yellow —stripy, green—Néel, red—zigzag and violet — vortex. (b)—the ordered moment value for the 24 sites via the full CMFT. (c), (d)—the α angle from the honeycomb plane to the pattern for the maximal overlap and CMFT methods, correspondingly. (e), (f)—the azimuthal angle ϕ within the honeycomb plane and the $\log_{10}|\tilde{\lambda}_{max}|$ stability map for the maximal overlap method.

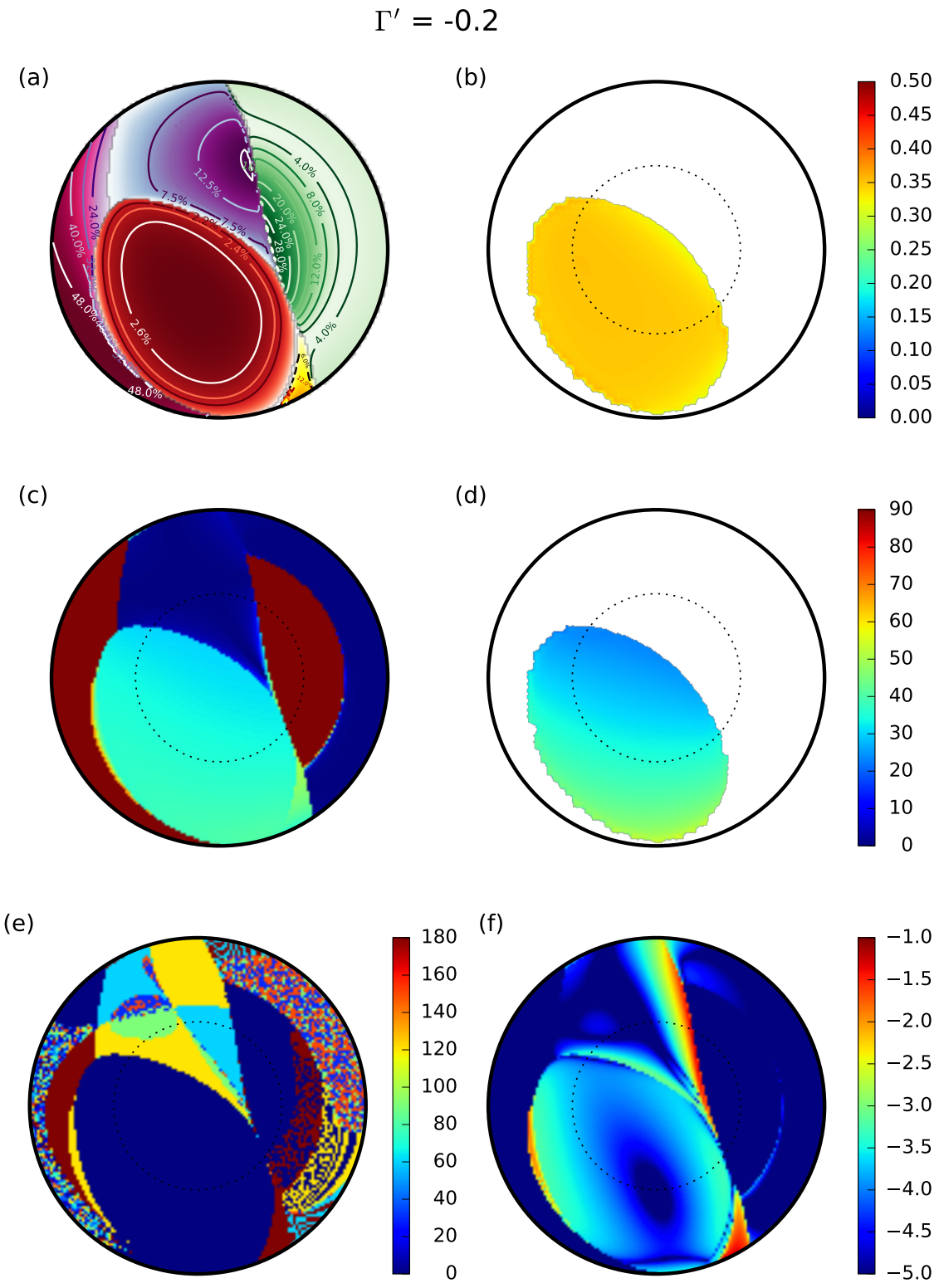

FIGURE 3.19: The $\Gamma' = -0.2$ slice of the composite phase diagram. (a)—the patterns with the maximal probability in the ground state: pink—FM, yellow —stripy, green—Néel, red—zigzag and violet —vortex. (b)—the ordered moment value for the 24 sites via the full CMFT. (c), (d)—the α angle from the honeycomb plane to the pattern for the maximal overlap and CMFT methods, correspondingly. (e), (f)—the azimuthal angle ϕ within the honeycomb plane and the $\log_{10}|\tilde{\lambda}_{max}|$ stability map for the maximal overlap method.

Stripy phase

Although the small Γ' values suppress the stripy phase considerably, the character of the phase remains unaffected. The stripy probability is still rather high, hinting the preservation of the classical character, no subphases develop and the moment direction evolves slowly in Γ in a similar fashion as before.

Zigzag phase

With the growing $|\Gamma'|$ the upper zigzag region regresses. The maximal overlap and CMFT methods are in accordance here, showing no visible trace of the upper zigzag region already at $\Gamma' = -0.2$. This may be attributed to the growing distance from the zigzag SU(2) point of the pure Kitaev-Heisenberg model.

In contrast, the lower zigzag region spreads massively in the central part of the slices, with the probability/ordered moment value somewhat higher than on the $\Gamma' = 0$ slice. This translates into slightly less quantum fluctuations in the ground state but still enough to preserve the quantum character of the phase. This can be attributed to another zigzag SU(2) point at $\Gamma' = -0.398$, denoted by B in Fig. 2.21 (d) and by a black circle in Fig A.4 (i). Similarly to the $\Gamma' = 0$ slice, the moment direction is located in the XZ plane, with $\phi = 0°$ (Figs. 3.18-3.19 (e)) and the α starting at $\approx 30°/20°$ in the "northern" part of the lower zigzag region and slowly rotating up to $\approx 40°/55°$ for the maximal-overlap/CMFT method (Figs. 3.18, 3.19 (c), (d)). The above moment direction is closer to the experimental estimates and will be discussed in detail in Sec. 3.5.

Vortex phase

Negative Γ' allows the vortex phase to expand. The moments remain in the honeycomb plane for most of the vortex region, with only a faint vertical component appearing near the boundaries with the Néel and lower zigzag phases. A careful inspection of the maximal-overlap patterns reveals a vortex-a dominance under the negative Γ' influence. Its source is the already-mentioned compass-like point at $\Gamma' = -0.603$, with the compass interaction axes oriented in the honeycomb plane, perpendicular to the bonds, and thus promoting the patterns with such pseudospin arrangements.

Being aware of the soft mode between the vortex subphases as well as the CMFT struggle for the $\Gamma' = 0$ slice, we did not attempt to stabilize the vortex phase via the full CMFT. More maximal-overlap-based slices, revealing also the evolution of other phases in Γ' can be examined in Appendix A.4.

3.4.4 Influence of J_3

Below we shortly describe the evolution of the phases under the influence of the third-neighbor Heisenberg term (J_3). The interested reader may find a more detailed description in Ref. [29].

The positive J_3 values suggested by the *ab-initio* methods [60] force the third-neighbor pseudospin pairs to align antiferromagnetically. Hence, the Néel and zigzag patterns fulfilling this condition dominate on the $J_3 > 0$ slices (Fig. 3.20). While the regions of the explicit or hidden FM character: FM, stripy and vortex are considerably reduced or even vanished, the AF regions consolidate: the Néel region expands even more than in the $J_3 = \Gamma' = 0$ slice while the upper and lower zigzag regions merge.

The moment direction inside the united zigzag region evolves from the moderate α values in the z-axis neighborhood towards the honeycomb plane. There, the zigzag probability grows substantially, the moment can easily rotate from $\phi = 180°$ to $0°$ and start tilting up again, towards the $(x + y)/\sqrt{2}$ direction and beyond.

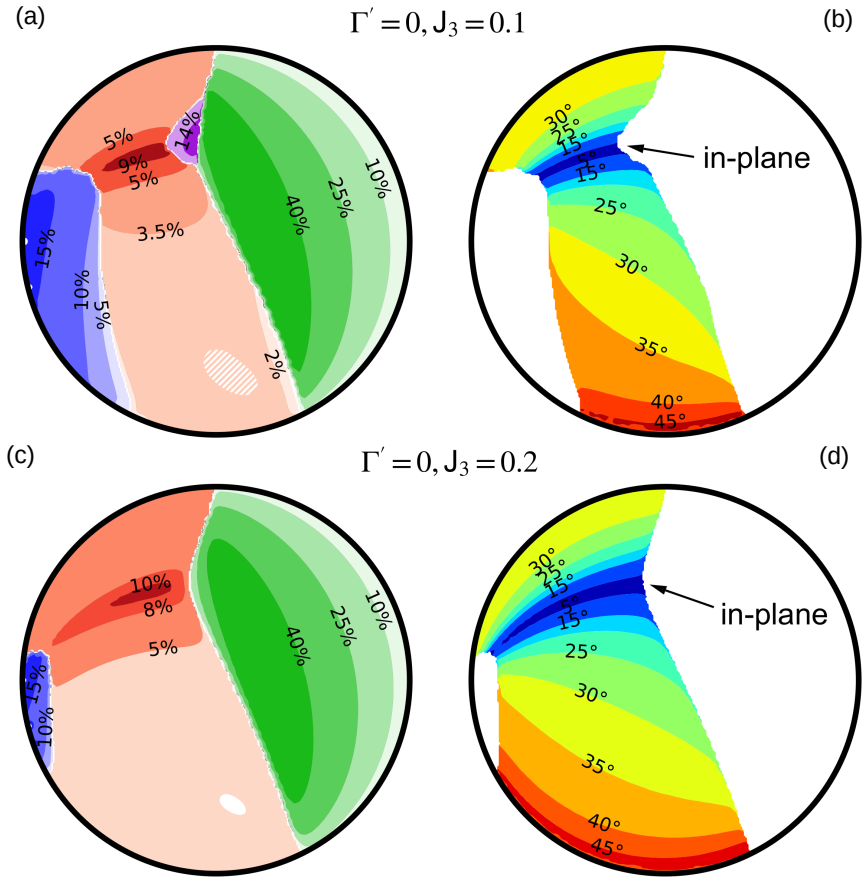

FIGURE 3.20: The $J_3 > 0$, $\Gamma' = 0$ slices of the phase diagram via the maximal overlap method. Panels (a), (c)—the patterns with the maximal probability in the ground state: blue—FM, green—Néel, red—zigzag, violet—vortex; panels (b), (d)—the α angle from the honeycomb plane to the pattern. Figure published in Ref. [29].

Although a combination of the overlapping projects and the general slowness of the full CMFT approach prevented us from producing the $J_3 \neq 0$ slices, in Appendix A.3 we have prepared a setup for the inclusion of the J_3 term into the CMFT algorithm for the interested reader to utilize. Based on the general tendencies provided by the classical energy and maximal overlap methods we do think that calculating the J-K-Γ-J_3 slices should be easier than the problematic J-K-Γ slice. For example, the zigzag region has higher maximal probability with than without J_3. Moreover, the new term is bond-isotropic, which could reduce the artificial non-collinear tendencies observed so far in the CMFT results.

3.4.5 Classical manifolds

Following the growing Γ value towards the center of the $\Gamma' = J_3 = 0$ slice results in the increase of the Néel probability (Fig. 3.15 (a)) and the ordered moment value (Fig. 3.15 (b)). The trend culminates within the centrally located special line defined by the formula

$$3J + K - \Gamma - 2\Gamma' = 0, \tag{3.52}$$

for which both characteristics reach the classical values 50% and 0.5, respectively.[64] This is not the only strictly fluctuation-free manifold on the diagram. A more careful inspection revealed

[64] Here we follow the custom of keeping the probability in the percentage notation.

that one of the FM subphases close to the outer rim of the $\Gamma' < 0$ slices hides another region with no quantum fluctuations in the ground state, set by the equation

$$K + 2\Gamma - 2\Gamma' = 0. \tag{3.53}$$

Interestingly, the classical state appears only when formulae (3.52)-(3.53) enter the regions in which the magnetic pattern is oriented perpendicularly to the honeycomb plane. The reason behind this becomes more clear in a reference frame providing the vertical projection of the J-K-Γ-Γ' exchange. Formula

$$\begin{pmatrix} \mathrm{S}^x \\ \mathrm{S}^y \\ \mathrm{S}^z \end{pmatrix} = \underbrace{\begin{pmatrix} \frac{1}{\sqrt{6}} & -\frac{1}{\sqrt{2}} & \frac{1}{\sqrt{3}} \\ \frac{1}{\sqrt{6}} & \frac{1}{\sqrt{2}} & \frac{1}{\sqrt{3}} \\ -\sqrt{\frac{2}{3}} & 0 & \frac{1}{\sqrt{3}} \end{pmatrix}}_{\mathcal{R}^{-1}_{\mathrm{XYZ}}} \underbrace{\begin{pmatrix} \cos\varphi_\eta & \sin\varphi_\eta & 0 \\ -\sin\varphi_\eta & \cos\varphi_\eta & 0 \\ 0 & 0 & 1 \end{pmatrix}}_{\mathcal{R}_{\mathrm{XY}}} \begin{pmatrix} \mathrm{S}^{\mathrm{X}} \\ \mathrm{S}^{\mathrm{Y}} \\ \mathrm{S}^{\mathrm{Z}} \end{pmatrix}$$

$$= \begin{pmatrix} \frac{1}{\sqrt{6}} & -\frac{1}{\sqrt{2}} & \frac{1}{\sqrt{3}} \\ \frac{1}{\sqrt{6}} & \frac{1}{\sqrt{2}} & \frac{1}{\sqrt{3}} \\ -\sqrt{\frac{2}{3}} & 0 & \frac{1}{\sqrt{3}} \end{pmatrix} \begin{pmatrix} \mathrm{S}^{\mathrm{X}}\cos\varphi_\eta + \mathrm{S}^{\mathrm{Y}}\sin\varphi_\eta \\ -\mathrm{S}^{\mathrm{X}}\sin\varphi_\eta + \mathrm{S}^{\mathrm{Y}}\cos\varphi_\eta \\ \mathrm{S}^{\mathrm{Z}} \end{pmatrix} \tag{3.54}$$

translates the pseudospin operators on each site between the projections to the Kitaev cubic axes (xyz) and to the XYZ axes.[65] The relation between the two frames is transparent in Fig. 3.21 (b). In the new frame the XY plane coincides with the honeycomb plane while the Z versor points upwards, exactly in the (111) direction according to the Kitaev frame. While $\mathcal{R}^{-1}_{\mathrm{XYZ}}$[66] translates the interaction on the bond $\eta = c$, in order to accommodate the less trivial transformation for the bonds a and b one has to rotate the S^{X} and S^{Y} projections by the angle φ_η distinguishing the a and b directions from the c direction. φ_η equals 0, $2\pi/3 = 120^o$, and $4\pi/3 = 240^o = -120^o$ for $\eta = c$, a and b direction, correspondingly. As shown in Ref. [9], inserting the above relations to the J-K-Γ-Γ' Hamiltonian (2.22) results in the new bond form

$$\begin{aligned} \mathcal{H}_{\mathrm{XYZ}}|_\eta = {} & J_{\mathrm{XY}}(\mathrm{S}^{\mathrm{X}}_i\mathrm{S}^{\mathrm{X}}_j + \mathrm{S}^{\mathrm{Y}}_i\mathrm{S}^{\mathrm{Y}}_j) + J_{\mathrm{Z}}\mathrm{S}^{\mathrm{Z}}_i\mathrm{S}^{\mathrm{Z}}_j \\ & + A\left((\mathrm{S}^{\mathrm{X}}_i\mathrm{S}^{\mathrm{X}}_j - \mathrm{S}^{\mathrm{Y}}_i\mathrm{S}^{\mathrm{Y}}_j)\cos\varphi_\eta - (\mathrm{S}^{\mathrm{X}}_i\mathrm{S}^{\mathrm{Y}}_j + \mathrm{S}^{\mathrm{Y}}_i\mathrm{S}^{\mathrm{X}}_j)\sin\varphi_\eta\right) \\ & - B\left((\mathrm{S}^{\mathrm{X}}_i\mathrm{S}^{\mathrm{Z}}_j + \mathrm{S}^{\mathrm{Z}}_i\mathrm{S}^{\mathrm{X}}_j)\cos\varphi_\eta + (\mathrm{S}^{\mathrm{Y}}_i\mathrm{S}^{\mathrm{Z}}_j + \mathrm{S}^{\mathrm{Z}}_i\mathrm{S}^{\mathrm{Y}}_j)\sin\varphi_\eta\right), \end{aligned} \tag{3.55}$$

with the coupling parameters

$$J_{\mathrm{XY}} = J + \frac{1}{3}(K - \Gamma - 2\Gamma'), \tag{3.56}$$

$$J_{\mathrm{Z}} = J + \frac{1}{3}(K + 2\Gamma + 4\Gamma'), \tag{3.57}$$

$$A = \frac{1}{3}(K + 2\Gamma - 2\Gamma') \tag{3.58}$$

[65] A quick reminder: on the honeycomb lattice the nearest-neighbor bonds may have the $\eta = a$, b or c direction. The bond-directional Kitaev term has a different interaction axis on each of the η bonds, following the scheme: $\eta = a \to \gamma = x$, $b \to y$, $c \to z$ in the $\mathrm{S}^\gamma_i\mathrm{S}^\gamma_j$ expression. Since at any site i connected by all three bonds η these interaction axes γ form the 90° angles between one another it is convenient to utilize them as a reference frame. We call this frame the "Kitaev cubic frame" in this thesis, because for the Kitaev model derived for the iridates and ruthenates it coincides with the frame related to the cubic symmetry of the oxygen/chlorine octahedra. For more details see the last paragraphs of Sec. 2.1.2.

[66] Cf. formula 2.23 for $\mathcal{R}_{\mathrm{XYZ}}$.

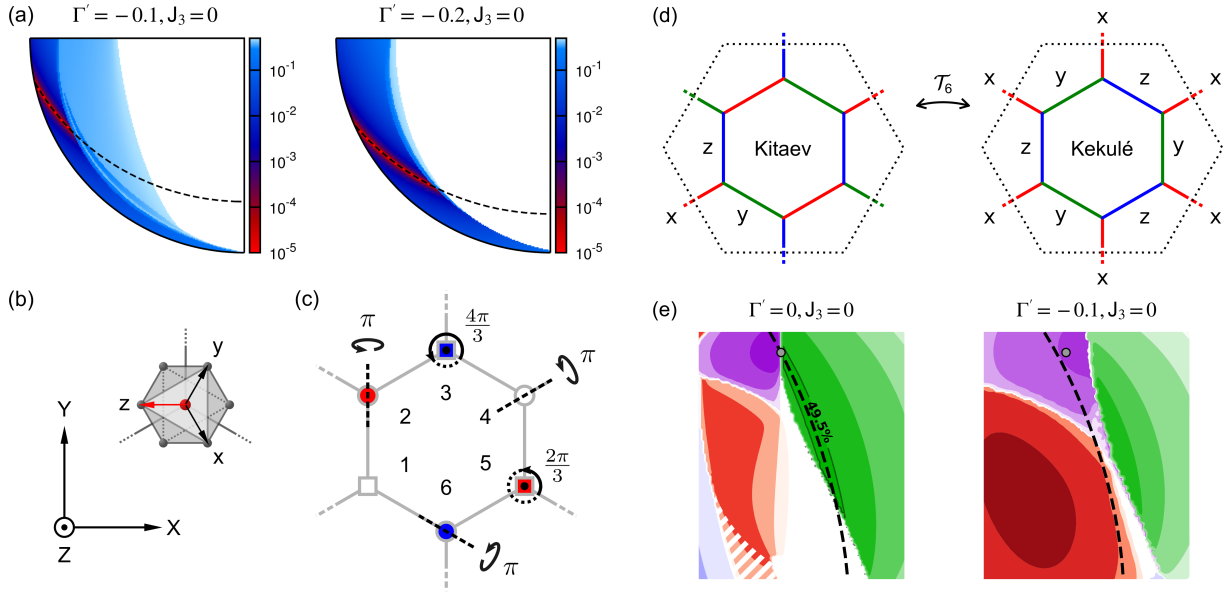

FIGURE 3.21: The new classical manifolds in the J-K-Γ-Γ' phase diagram. Panel (a) demonstrates the fit of the $K + 2\Gamma - 2\Gamma' = 0$ lines to the 50% probability patches within the subphase of the FM pattern oriented perpendicularly to the honeycomb plane. To make the difference between the exact and approximate 50% more pronounced, the dominant probability $\mathcal{P}$ is plotted in the form of $\log_{10}(0.5 - \mathcal{P})$ on the maps. Panel (b) illustrates the relation between two orthogonal frames: the Kitaev cubic frame xyz with each axis rotated up by $\approx 35.26°$ from the honeycomb plane and the frame consisting of the X and Y axes within the plane and the Z axis in the out-of-plane direction. Panel (c) presents the effect of the $\mathcal{T}_6$ transformation on the pseudospins belonging to the specific sublattices. The moments on every second site (sublattices 1, 3, and 5) experience a rotation along the vertical axis by 0, 240° and 120°, respectively. The rest of the sublattices (2, 4, 6) encounter the 180° rotation around the suitable bonds. Panel (d) captures how $\mathcal{T}_6$ releases the $\mathrm{S}_i^\gamma \mathrm{S}_j^\gamma$ interactions in the Kitaev term ($\gamma = x, y, z$) from the simple assignment to the bond direction $\eta = a, b, c$. The left scheme illustrates the Kitaev distribution of the Ising interactions: $\mathrm{S}_i^x \mathrm{S}_j^x$ on bond a, here in red, $\mathrm{S}_i^y \mathrm{S}_j^y$ on the green bond b, and $\mathrm{S}_i^z \mathrm{S}_j^z$ on the blue bond c. The right scheme shows how after the transformation the $\mathrm{S}_i^y \mathrm{S}_j^y$ and $\mathrm{S}_i^z \mathrm{S}_j^z$ bonds form the green & blue benzene-like rings, connected by the $\mathrm{S}_i^x \mathrm{S}_j^x$ interaction, forming the Kekulé-Kitaev term. Panel (e) uncovers the classical manifold within the Néel (111)=Z subphase. While for the $\Gamma' = J_3 = 0$ slice the $3J + K - \Gamma - 2\Gamma' = 0$ line fits perfectly into the fluctuation-free manifold, allowing for $\Gamma' < 0$ moves the line away from the vertically oriented Néel subphase, thus allowing for the quantum fluctuations to enter the ground state. Figure has been published in Ref. [29].

$$B = \frac{\sqrt{2}}{3}(K - \Gamma + \Gamma'). \tag{3.59}$$

Having the Hamiltonian with the Z direction isolated, we may now analytically inspect the mysterious manifolds, starting with the more transparent FM one.

Ferromagnetic case

We will now inspect which terms in Hamiltonian (3.55) are activated by the FM pattern in the Z direction and which of them have the potential to dress the pattern in quantum fluctuations, reducing its probability. This can be easily achieved by utilizing the operators explicitly responsible for the fluctuations—the pseudospin-flip operators in the Z direction: S^+ and S^-. By substituting $\mathrm{S}^\mathrm{X} = (\mathrm{S}^+ + \mathrm{S}^-)/2$, $\mathrm{S}^\mathrm{Y} = -i(\mathrm{S}^+ - \mathrm{S}^-)/2$ into formula (3.55) we obtain the

Hamiltonian form

$$\begin{aligned}\mathcal{H}_{\mathrm{XYZ}}|_\eta = &\frac{J_{\mathrm{XY}}}{2}(\mathrm{S}_i^+\mathrm{S}_j^- + \mathrm{S}_i^-\mathrm{S}_j^+) + J_{\mathrm{Z}}\mathrm{S}_i^{\mathrm{Z}}\mathrm{S}_j^{\mathrm{Z}} \\ &+ \frac{A}{2}\left((\mathrm{S}_i^+\mathrm{S}_j^+ + \mathrm{S}_i^-\mathrm{S}_j^-)\cos\varphi_\eta + i(\mathrm{S}_i^+\mathrm{S}_j^+ - \mathrm{S}_i^-\mathrm{S}_j^-)\sin\varphi_\eta\right) \\ &- \frac{B}{2}\left[\left((\mathrm{S}_i^+ + \mathrm{S}_i^-)\mathrm{S}_j^{\mathrm{Z}} + \mathrm{S}_i^{\mathrm{Z}}(\mathrm{S}_j^+ + \mathrm{S}_j^-)\right)\cos\varphi_\eta - i\left((\mathrm{S}_i^+ - \mathrm{S}_i^-)\mathrm{S}_j^{\mathrm{Z}} + \mathrm{S}_i^{\mathrm{Z}}(\mathrm{S}_j^+ - \mathrm{S}_j^-)\right)\sin\varphi_\eta\right].\end{aligned} \tag{3.60}$$

One can immediately notice that the FM state is an eigenstate of the J_{Z} term. While all the other terms contain some sort of the pseudospin-flip combinations, not all of them can act on the above state. For example, the J_{XY} term can be excluded right away. The A and B terms are more intricate to verify. Although both of them can in principle act on the FM state, the bond-dependent trigonometric factors suggest that shifting from the one-bond towards the one-site picture may lead to their cancellation. We will guide the reader trough such an analysis.

The Hamiltonian for a finite cluster contains a summation over all nearest-neighbor (NN) pairs of sites

$$\mathcal{H}_{\mathrm{cluster}} = \sum_{\langle ij\rangle\perp\gamma}\mathcal{H} = \sum_{\langle ij\rangle\perp x}\mathcal{H}_a + \sum_{\langle ij\rangle\perp y}\mathcal{H}_b + \sum_{\langle ij\rangle\perp z}\mathcal{H}_c. \tag{3.61}$$

By writing the sums over the nearest neighbors in terms of the double independent sums over sites ($\sum_{\langle ij\rangle} \to \sum_i\sum_j$) one changes the perspective from the bonds to the sites. Following the example in Fig. 3.22 (a), we will now comprehend all the bonds connected to the site no 4 together. Let us write the first part of both A and B expressions in formula (3.60) for the site no 4 and all the 3 bonds connected to it

$$\frac{A}{2}(\mathrm{S}_4^+\mathrm{S}_1^+\cos 120^\circ + \mathrm{S}_4^+\mathrm{S}_2^+\cos 240^\circ + \mathrm{S}_4^+\mathrm{S}_3^+\cos 0), \tag{3.62}$$

$$\frac{B}{2}(\mathrm{S}_4^+\mathrm{S}_1^{\mathrm{Z}}\cos 120^\circ + \mathrm{S}_4^+\mathrm{S}_2^{\mathrm{Z}}\cos 240^\circ + \mathrm{S}_4^+\mathrm{S}_3^{\mathrm{Z}}\cos 0). \tag{3.63}$$

Whereas there is not much to improve in expression (3.62), we are actually able to simplify formula (3.63) considerably. Noticing that for the FM state the S^{Z} operator produces the same eigenvalue on every site, we end up with

$$\pm\frac{1}{2}\frac{B}{2}\mathrm{S}_4^+(\cos 120^\circ + \cos 240^\circ + \cos 0) = \pm\frac{1}{2}\frac{B}{2}\mathrm{S}_4^+(-\frac{1}{2} - \frac{1}{2} + 1) = 0. \tag{3.64}$$

We apply similar procedure to other sub-terms in the expression B, noticing that $\sin 120^\circ + \sin 240^\circ + \sin 0 = \sqrt{3}/2 - \sqrt{3}/2 + 0 = 0$. Thus, the B term cancels out on every site of the honeycomb lattice due to the destructive summation over all bonds connected to the site.

As a result, only the A term can effectively disrupt the FM pattern along the Z direction. By setting $A = 0$ one obtains condition (3.53) for the fluctuation-free FM manifold that spans from small to moderate negative Γ' values. Fig. 3.21 (a) demonstrates the ideal fit of the $K + 2\Gamma = -0.1 \cdot 2$ and $K + 2\Gamma = -0.2 \cdot 2$ lines to the patches of the 50% probability, the 0.5 moment value and $\lambda_{max} \geq 10^4$, confirming the above explanation of their origin. The reader may consult Appendix A.4 for more examples. Finally, the FM classical manifold survives the addition of the very small AF third-neighbor Heisenberg interaction to the Hamiltonian as long as the FM subphase along the Z direction exists.

Summing up, the classical FM manifold appears away from the FM SU(2) points when condition (3.53) enters the FM subphase with the moments oriented perpendicularly to the honeycomb plane.

Néel case

Moving on to the more complex classical manifold within the Néel || Z subspace, one may notice that it begins at the vortex point which is a hidden Heisenberg ferromagnet. At this point, the SU(2) symmetry offers an infinite choice of patterns, restricted however by the compatibility with the $\mathcal{T}_6$ transformation.[67] In particular, the Néel configuration along the Z direction also fulfills this condition. In the context of the pseudospins polarized along the vertical direction it is essential to understand what $\mathcal{T}_6$ actually does to the pattern and the Hamiltonian. We start with the pattern analysis.

Fig. 3.21 (c) illustrates in a simple way the effect of the $\mathcal{T}_6$ transformation on the specific sublattices. The moments on every second site (sublattices 1, 3, and 5) experience the rotation along the vertical axis by 0, 240° and 120°, respectively. The rest of the sublattices (2, 4, 6) encounter the 180° rotation around the suitable bonds. For the Néel pattern polarized along the Z direction this translates into no change for the sublattices 1, 3, 5 and a pseudospin flip on the sublatices 2, 4, 6, transforming Néel into a ferromagnet along Z. Thus, we assembled the first link to the already understood FM case.

The second link will emerge from the Hamiltonian analysis. In order to clearly illustrate what happens, we will devote a moment to transform Hamiltonian (2.22) on the bonds selected in Fig. 3.21 (c). We start from the bond 2-3 in the direction a. For consistency with formulae (2.27) we first rewrite the J-K-Γ-Γ' Hamiltonian substituting the names of the Kitaev axes from γ to $\gamma' = x'$, y', z'

$$\begin{aligned}\mathcal{H}|_{23} = J\left(\mathrm{S}_2^{x'}\mathrm{S}_3^{x'} + \mathrm{S}_2^{y'}\mathrm{S}_3^{y'} + \mathrm{S}_2^{z'}\mathrm{S}_3^{z'}\right) + K\mathrm{S}_2^{x'}\mathrm{S}_3^{x'} \\ + \Gamma\left(\mathrm{S}_2^{y'}\mathrm{S}_3^{z'} + \mathrm{S}_2^{z'}\mathrm{S}_3^{y'}\right) + \Gamma'\left(\mathrm{S}_2^{y'}\mathrm{S}_3^{x'} + \mathrm{S}_2^{x'}\mathrm{S}_3^{y'} + \mathrm{S}_2^{z'}\mathrm{S}_3^{x'} + \mathrm{S}_2^{x'}\mathrm{S}_3^{z'}\right).\end{aligned} \tag{3.65}$$

Then we apply $\mathcal{T}_6$ as in formula (2.27), obtaining

$$\begin{aligned}\tilde{\mathcal{H}}|_{23} = -\Gamma\left(\mathrm{S}_2^x\mathrm{S}_3^x + \mathrm{S}_2^y\mathrm{S}_3^y + \mathrm{S}_2^z\mathrm{S}_3^z\right) + (-J - K + \Gamma)\mathrm{S}_2^y\mathrm{S}_3^y \\ - J\left(\mathrm{S}_2^x\mathrm{S}_3^z + \mathrm{S}_2^z\mathrm{S}_3^x\right) - \Gamma'\left(\mathrm{S}_2^y\mathrm{S}_3^z + \mathrm{S}_2^z\mathrm{S}_3^y + \mathrm{S}_2^x\mathrm{S}_3^y + \mathrm{S}_2^y\mathrm{S}_3^x\right),\end{aligned} \tag{3.66}$$

where we insered $0 = +\Gamma\mathrm{S}_2^y\mathrm{S}_3^y - \Gamma\mathrm{S}_2^y\mathrm{S}_3^y$ to establish the new Heisenberg interaction. The emerging Hamiltonian is of the Kitaev-like $\tilde{J}$-$\tilde{K}$-$\tilde{\Gamma}$-$\tilde{\Gamma}'$ form, with the new coupling parameters related to the old by

$$(\tilde{J}, \tilde{K}, \tilde{\Gamma}, \tilde{\Gamma}') = (-\Gamma, -J - K + \Gamma, -J, -\Gamma'). \tag{3.67}$$

Crucially though, the anisotropic terms are arranged as for the b bond direction, e.g. the $\tilde{K}$ term consists of $\mathrm{S}_2^y\mathrm{S}_3^y$. In other words, the $\mathrm{S}_2^{x'}\mathrm{S}_3^{x'}$ expression in the Kitaev term transforms into $\mathrm{S}_2^y\mathrm{S}_3^y$. Subsequently, we inspect the bond 4-3 in direction b. Repeating the procedure for the suitable sublattices, we transform the initial form

$$\begin{aligned}\mathcal{H}|_{43} = J\left(\mathrm{S}_4^{x'}\mathrm{S}_3^{x'} + \mathrm{S}_4^{y'}\mathrm{S}_3^{y'} + \mathrm{S}_4^{z'}\mathrm{S}_3^{z'}\right) + K\mathrm{S}_4^{y'}\mathrm{S}_3^{y'} \\ + \Gamma\left(\mathrm{S}_4^{z'}\mathrm{S}_3^{x'} + \mathrm{S}_4^{x'}\mathrm{S}_3^{z'}\right) + \Gamma'\left(\mathrm{S}_4^{z'}\mathrm{S}_3^{y'} + \mathrm{S}_4^{y'}\mathrm{S}_3^{z'} + \mathrm{S}_4^{y'}\mathrm{S}_3^{x'} + \mathrm{S}_4^{x'}\mathrm{S}_3^{y'}\right)\end{aligned} \tag{3.68}$$

into

$$\begin{aligned}\tilde{\mathcal{H}}|_{43} = -\Gamma\left(\mathrm{S}_4^x\mathrm{S}_3^x + \mathrm{S}_4^y\mathrm{S}_3^y + \mathrm{S}_4^z\mathrm{S}_3^z\right) + (-J - K + \Gamma)\mathrm{S}_4^z\mathrm{S}_3^z \\ - J\left(\mathrm{S}_4^y\mathrm{S}_3^x + \mathrm{S}_4^x\mathrm{S}_3^y\right) - \Gamma'\left(\mathrm{S}_4^z\mathrm{S}_3^x + \mathrm{S}_4^x\mathrm{S}_3^z + \mathrm{S}_4^z\mathrm{S}_3^y + \mathrm{S}_4^y\mathrm{S}_3^z\right),\end{aligned} \tag{3.69}$$

[67] Cf. formulae (2.27).

where the $\tilde{K}$ term contains now the $S_4^z S_3^z$ interaction as if the bond was in the c direction. Similarly, we obtain the $S_6^x S_3^x$ preference in the $\tilde{K}$ term[68] vs the original $S_6^{z'} S_3^{z'}$ and $S_4^y S_5^y$ vs $S_4^{z'} S_5^{z'}$. The last two examples prove that this is not a simple permutation of the Kitaev exchange in reference to the bond direction. Indeed, the right part of the Fig. 3.21 (d) reveals the benzene-like structures in the two pseudospin components connected by the bond interaction in the third component. Thus, the new bond-anisotropic $\tilde{K}$ term bears the so-called Kekulé-Kitaev interaction [96, 9, 29]. We may therefore call the $\tilde{J}$-$\tilde{K}$-$\tilde{\Gamma}$-$\tilde{\Gamma}'$ form obtained via $\mathcal{T}_6$ the Kekulé-Kitaev-like or the extended Kekulé-Kitaev model. Via this detailed inspection one could see that the $\mathcal{T}_6$ transformation preserves the bond anisotropy, changing only its distribution on the bonds.

In hope that the reader has now a better grasp on what the $\mathcal{T}_6$ transformation is capable of concerning the pattern and the Hamiltonian, we return to the analysis of the special Néel manifold. In the Néel || Z subphase $\mathcal{T}_6$ transforms the J-K-Γ-Γ' Hamiltonian into the Kekulé-Kitaev-like Hamiltonian. Its ground state is the classical FM pattern in the Z direction, which we also obtain by applying $\mathcal{T}_6$ to the Néel || Z pattern. Hence, after the transformation we may proceed as in the FM case. Since there are still 3 different anisotropic Hamiltonians along the 3 bonds connected at one site, the trigonometric terms should sum up to zero in the term of type B. Alternatively, we may substitute parameters (3.67) into the condition for the classical FM manifold (3.53) and get the condition (3.52) for the fluctuation-free Néel manifold as a result. While on the $\Gamma' = J_3 = 0$ slice of the Fig. 3.21 (e) formula (3.52) fits perfectly into the saturated patch within the Néel ||Z subphase, on the $\Gamma' = -0.1$ slice the line runs already outside the borders of the vertically ordered region. Appendix A.4 provides more evidence of the suppression of the classical state by $\Gamma' < 0$ and its expansion with $\Gamma' > 0$.

Perhaps the curious reader has been wondering whether the classical Néel state is related to the Ising interaction. The answer is yes, but only at one point of the classical manifold, deep in the $\Gamma' > 0$ part of the phase diagram. The AF Ising point with the Ising interaction axis along the Z direction has the coordinates: $K = 0$, $J = \Gamma = \Gamma' = \sqrt{2}/2 \approx 0.707$[69] and is denoted as an empty square in Fig. 3.23 (a) and Fig. A.4 (b). The point is also a part of another manifold, for which the four parameters of the J-K-Γ-Γ' Hamiltonian can be reduced to one parameter along each bond. Below we discuss this manifold in detail.

3.4.6 Ising-Kitaev-compass model

In this section we will focus on those special points and manifolds, for which the J-K-Γ-Γ' Hamiltonian can be simplified to the one with a bond-dependent interaction axis. The concept of an interaction axis can be easily understood by imagining the Ising Hamiltonian $\sum_{\langle ij \rangle} S_i^z S_j^z$, which has the same interaction axis on every nearest-neighbor bond. Note, that we have already introduced a more complex example in the form of the Kitaev model. There, on each bond in the direction η the Ising interaction $S_i^\gamma S_j^\gamma$ sets the axis in the direction γ. Below, we will first describe the most accessible example we have identified—the compass model, and then move on to the more demanding cases requiring a formalized approach.

Separate compass point

As already mentioned in Sec. 3.4.2, there exists a tiny patch for which both zigzag regions as well as the FM and vortex regions meet in Fig. 3.15 (a). In fact, although very low, their non-zero probabilities reduce the region to a single point, marked by a black triangle at

$$K = \Gamma = -J = \frac{1}{\sqrt{3}} \approx 0.577 \tag{3.70}$$

[68] Better visible in Fig. 3.17 (a).

[69] In our parametrisation.

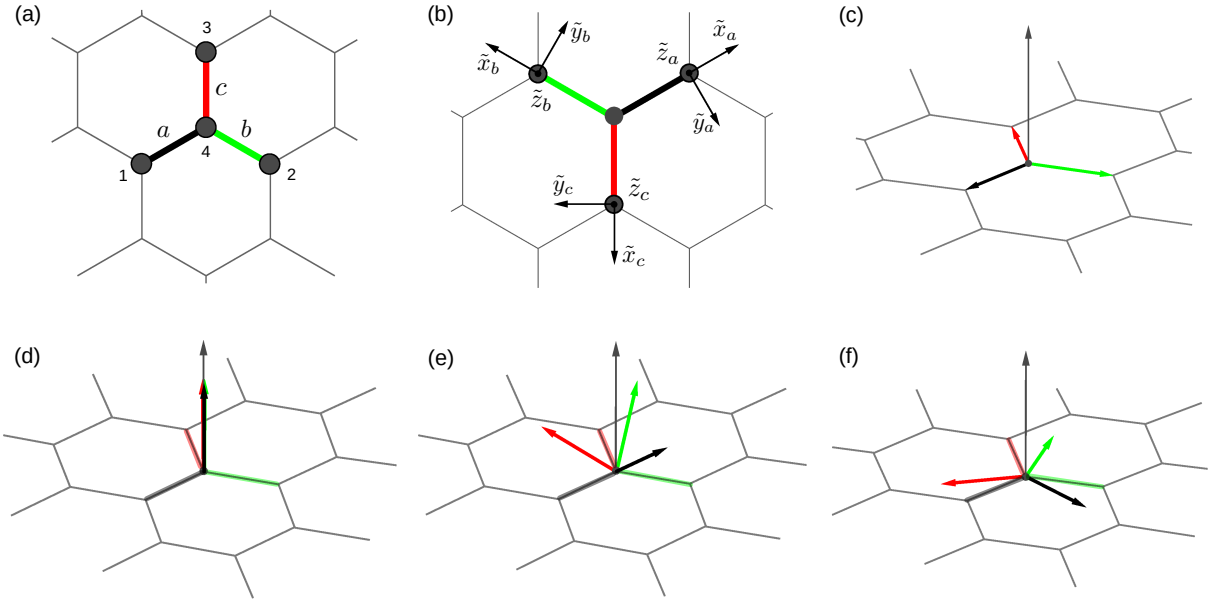

FIGURE 3.22: Panel (a) illustrates the three bonds connecting the site no 4. with the neighboring sites j, with the bond directions $\eta = a, b, c$, discussed in the context of cancelation of term (3.63) on every site of the honeycomb lattice. Panel (b) introduces the rotating reference frame γ_η, defined in relation to the bond direction η. In this frame, the x_η versor lies always along the bond, y_η is perpendicular to it within the honeycomb plane, and z_η coincides with the (111) =Z (out-of-plane) direction. Panel (c) presents the true compass model with the bond interaction axis x_η. Panels (d)-(f) illustrate the "umbrella" effect of the Ising-Kitaev-"compass" model: when the umbrella of interaction axes is closed, the Ising model with the universal interaction axis along the Z direction emerges (panel (d)). Opening the umbrella leads to the bond anisotropy and frustration, eventually reaching the Kitaev model with its orthogonal interaction axes (panel (e)) and finishing with the "compass" model, whose interaction axes are in the honeycomb plane but along y_η.

in our parametrisation. At this degenerate point Hamiltonian (2.22) reduces to the one-term formula at each bond. By inserting the conditions: $\Gamma' = 0$ and (3.70) to the matrix $\mathcal{H}_{pars}$ of the Hamiltonian coupling parameters, extracted from the formulae of type (2.20), one obtains matrices of the lower rank

$$\mathcal{H}_{pars}|_a = \begin{pmatrix} J+K & \Gamma' & \Gamma' \\ \Gamma' & J & \Gamma \\ \Gamma' & \Gamma & J \end{pmatrix} = \begin{pmatrix} 0 & 0 & 0 \\ 0 & -K & K \\ 0 & K & -K \end{pmatrix}, \tag{3.71}$$

$$\mathcal{H}_{pars}|_b = \begin{pmatrix} J & \Gamma' & \Gamma \\ \Gamma' & J+K & \Gamma' \\ \Gamma & \Gamma' & J \end{pmatrix} = \begin{pmatrix} -K & 0 & K \\ 0 & 0 & 0 \\ K & 0 & -K \end{pmatrix}, \tag{3.72}$$

$$\mathcal{H}_{pars}|_c = \begin{pmatrix} J & \Gamma & \Gamma' \\ \Gamma & J & \Gamma' \\ \Gamma' & \Gamma' & J+K \end{pmatrix} = \begin{pmatrix} -K & K & 0 \\ K & -K & 0 \\ 0 & 0 & 0 \end{pmatrix}. \tag{3.73}$$

The diagonalization of the above matrices provides a pseudospin rotation to a different frame for different bond directions.[70] Fig. 3.22 (b) demonstrates these eigenframes for each bond. Namely, the x_η axes are parallel to the given bond direction η, the y_η axes lie in the honeycomb plane, perpendicularly to the bond, and the z_η axes coincide with the (111)=Z direction. From now on we will call the γ_η set a *rotating reference frame*.

[70] A diagonalization of a symmetric matrix is essentially a rotation operation.

At point (3.70) matrices (3.71)-(3.73) have only one non-zero eigenvalue corresponding to the eigenvector x_η

$$\tilde{\mathcal{H}}_{pars}|_\eta = \begin{pmatrix} -2K & 0 & 0 \\ 0 & 0 & 0 \\ 0 & 0 & 0 \end{pmatrix}. \tag{3.74}$$

This means that the effective interaction on each bond is of the ferromagnetic[71] Ising type, with the interaction axis along the x_η eigenvector. One may symbolically write it as

$$\mathcal{H} = -2K \sum_{\langle ij\rangle||\eta} \mathrm{S}_i^{x_\eta}\mathrm{S}_j^{x_\eta} = -2K \left(\sum_{\langle ij\rangle||a} \mathrm{S}_i^{x_a}\mathrm{S}_j^{x_a} + \sum_{\langle ij\rangle||b} \mathrm{S}_i^{x_b}\mathrm{S}_j^{x_b} \sum_{\langle ij\rangle||c} \mathrm{S}_i^{x_c}\mathrm{S}_j^{x_c} \right) \tag{3.75}$$

or in a more elegant way

$$\mathcal{H} = -2K \sum_{\langle ij\rangle \in \mathrm{NN}} (\mathbf{S}_i \cdot \mathbf{r}_{ij})(\mathbf{S}_j \cdot \mathbf{r}_{ij}), \tag{3.76}$$

where $\mathbf{r}_{ij}$ connects sites i and j and is therefore parallel to x_η. Fig. 3.22 (c) reveals that this is in fact a true compass model on the honeycomb lattice, for which the interaction axes lie in plane, along the bonds [97, 98, 99].

In contrast to the Kitaev model in Fig. 3.22 (e), here the interaction axes are not orthogonal, allowing for some overlap between the S^{x_η} projections. This in turn creates an overlap of the interactions, diverging the ground state from KSL.[72] In fact, there is an ongoing discussion about its nature, with different authors proposing the Néel state [97], a dimerized state [98], a superposition of dimers [99], a quantum spin liquid [100] or even a valence-bond solid [101]. The existence of the effective compass Hamiltonian justifies the meeting of the four LRO regions in this degenerate point.

Ising-Kitaev-"compass" line

Continuing the exploration of the Hamiltonian with the bond-dependent interaction axis we will now take a more general approach. By rewritting the matrix of the coupling parameters of the J-K-Γ-Γ' Hamiltonian in the rotating frame γ_η one obtains the same $\mathcal{H}_{pars}$ for all bond directions $\eta = a, b, c$.

$$\tilde{\mathcal{H}}_{pars}|_\eta = \begin{pmatrix} J-\Gamma & 0 & 0 \\ 0 & J+\frac{2K}{3}+\frac{\Gamma}{3}-\frac{4\Gamma'}{3} & \frac{\sqrt{2}}{3}(K-\Gamma+\Gamma') \\ 0 & \frac{\sqrt{2}}{3}(K-\Gamma+\Gamma') & J+\frac{K}{3}+\frac{2\Gamma}{3}+\frac{4\Gamma'}{3} \end{pmatrix}. \tag{3.77}$$

However, in the general case the rotating frame does not provide the full eigenbasis of the matrix (3.77), so the matrix has to be further diagonalized. In order to achieve a single-axis Hamiltonian one has to find the parameter range in which only one of the three possible eigenvalues would be non-zero. Then, one would have a single-axis interaction in the direction of the corresponding eigenvector.

From the above block-diagonal structure one can immediately extract the first eigenvalue $\lambda_1 = J - \Gamma$, corresponding to the x_η eigenvector providing the interaction axis. While at this stage one can already claim that the remaining possibilities are restricted to the $y_\eta z_\eta$ planes, to know more one has to diagonalize the second block. After the diagonalization the set of the

[71] $K = +1/\sqrt{3} \to -2K < 0 \to$ FM.

[72] For numerics it is convenient to project back to the orthogonal frame.

eigenvalues is complete:

$$\lambda_1 = J - \Gamma, \tag{3.78}$$

$$\lambda_2 = J + \frac{1}{2}\left(K + \Gamma + \sqrt{(K-\Gamma)^2 + 8\Gamma'^2}\right), \tag{3.79}$$

$$\lambda_3 = J + \frac{1}{2}\left(K + \Gamma - \sqrt{(K-\Gamma)^2 + 8\Gamma'^2}\right). \tag{3.80}$$

If λ_1 is the only non-zero eigenvalue, the interaction axis is in the honeycomb plane, along the suitable η bond, producing a true compass model. It has turned out that this happens only when $\Gamma' = 0$, precisely at the degenerate point described in the previous section.

λ_2 and λ_3 form a special subset of eigenvalues—they are the two roots of the determinant polynomial of the eigenproblem of the second block, differing only by a sign before the square root. This ensures that, when $\Gamma = J$ is inserted and any of the formulae (3.79)-(3.80) is compared to zero, the same condition arises

$$\Gamma'^2 = J(J+K). \tag{3.81}$$

Importantly, the condition is for the square of Γ'—the left side is always positive. Such an outcome can be generated by either both $J > 0$ and $J + K > 0$ or both $J < 0$ and $J + K < 0$. It is convenient to rewrite formulae (3.79)-(3.80) together as

$$\lambda_{2,3} = J + \frac{J+K}{2} \pm \underbrace{\sqrt{(K-J)^2 + 8\Gamma'^2}}_{>0}. \tag{3.82}$$

One can easily see that for $J > 0$, $J + K > 0$ all the terms in formula (3.82) are positive. Hence, the expression can be reduced to zero only when the minus sign before the square root is chosen. This is the $\lambda_3 = 0$, $\lambda_2 \neq 0$ case. Contrastingly, in the $J < 0$, $J + K < 0$ case the first two terms are negative while the square root remains positive, leading to the choice of the plus sign and $\lambda_2 = 0$, $\lambda_3 \neq 0$. In the suitable cases, after inserting condition (3.81), the non-zero eigenvalue in formula (3.82) simplifies to $3J + K$. Through the $\Gamma = J$ condition the sign of Γ is determined by the sign of J. Therefore, for the experimentally relevant $\Gamma > 0$ and non-zero Γ' we obtain a condition for a line

$$\Gamma = J,\ J > 0,\ \Gamma'^2 = J(J+K),\ J + K > 0, \tag{3.83}$$

with only $\lambda_2 = 3J + K \neq 0$. Because λ_2 is positive, the resulting interaction is antiferromagnetic. Similarly, $\Gamma < 0$, $\Gamma' \neq 0$ enforces the line

$$\Gamma = J,\ J < 0,\ \Gamma'^2 = J(J+K),\ J + K < 0, \tag{3.84}$$

with $\lambda_3 = 3J + K < 0$.

For either λ_2 or $\lambda_3 \neq 0$ the interaction axis lies in the $y_\eta z_\eta$ plane. To determine the direction more precisely one has to examine the eigenvector corresponding to the chosen λ_i. Perhaps the easiest to interpret eigenvector forms appear when one utilizes the fact that the second block of matrix (3.77) is a real, symmetric, 2×2 matrix. Then, in order to diagonalize it is enough to rotate in 2D. But since we do not know a priori where to rotate exactly, let us first write the general rotated form and find the necessary condition afterwards. We start from the two arbitrary orthogonal vectors in the $y_\eta z_\eta$ plane

$$\mathbf{v}_2 = \begin{pmatrix} \sin\tilde{\theta} \\ \cos\tilde{\theta} \end{pmatrix}, \tag{3.85}$$

$$\mathbf{v}_3 = \begin{pmatrix} -\cos\tilde{\theta} \\ \sin\tilde{\theta} \end{pmatrix}, \tag{3.86}$$

where $\tilde{\theta}$ is the deviation from the z_η =Z vertical axis. Taking $\mathbf{v}_2$ and $\mathbf{v}_3$ as the columns of the rotation matrix $\mathcal{R}$, we may write

$$\begin{aligned}\mathcal{H}' &= \mathcal{R}^T\mathcal{H}\mathcal{R} \\ &= \begin{pmatrix} \sin\tilde{\theta} & \cos\tilde{\theta} \\ -\cos\tilde{\theta} & \sin\tilde{\theta} \end{pmatrix} \begin{pmatrix} J+\frac{1}{3}(2K+\Gamma-4\Gamma') & \frac{\sqrt{2}}{3}(K-\Gamma+\Gamma') \\ \frac{\sqrt{2}}{3}(K-\Gamma+\Gamma') & J+\frac{1}{3}(K+2\Gamma+4\Gamma') \end{pmatrix} \begin{pmatrix} \sin\tilde{\theta} & -\cos\tilde{\theta} \\ \cos\tilde{\theta} & \sin\tilde{\theta} \end{pmatrix},\end{aligned} \tag{3.87}$$

where here $\mathcal{H}$ is restricted to the second block of matrix (3.77). Executing (3.87) results in

$$\mathcal{H}' = \begin{pmatrix} A & C \\ C & B \end{pmatrix}, \tag{3.88}$$

where

$$A = \frac{1}{6}\left(3\left(2J+K+\Gamma\right)+\left(-K+\Gamma+8\Gamma'\right)\cos(2\tilde{\theta})+2\sqrt{2}\left(K-\Gamma+\Gamma'\right)\sin(2\tilde{\theta})\right), \tag{3.89}$$

$$B = \frac{1}{6}\left(3\left(2J+K+\Gamma\right)+\left(K-\Gamma-8\Gamma'\right)\cos(2\tilde{\theta})+2\sqrt{2}\left(-K+\Gamma-\Gamma'\right)\sin(2\tilde{\theta})\right), \tag{3.90}$$

$$C = \frac{1}{6}\left(2\sqrt{2}\left(-K+\Gamma-\Gamma'\right)\cos(2\tilde{\theta})+\left(-K+\Gamma+8\Gamma'\right)\sin(2\tilde{\theta})\right). \tag{3.91}$$

To obtain the diagonal form it is enough to set $C = 0$, which leads to

$$\tan(2\tilde{\theta}) = -2\sqrt{2}\frac{(K-\Gamma+\Gamma')}{-K+\Gamma+8\Gamma'}. \tag{3.92}$$

Once the condition $\Gamma = J$ is applied we obtain

$$\tan(2\tilde{\theta}) = 2\sqrt{2}\frac{(-J+K+\Gamma')}{J-K+8\Gamma'} = 2\sqrt{2}\left(\frac{9\Gamma'}{J-K+8\Gamma'}-1\right), \tag{3.93}$$

as in Ref. [29]. This condition binds $\mathbf{v}_{2,3}$ to the previously shown eigenvalues $\lambda_{2,3}$. For completeness, we comment that the standard diagonalization scheme would result in a direct $\mathbf{v}_{2,3}(J,K,\Gamma,\Gamma')$ dependence, leaving $\tilde{\theta}$ to be determined from the ratio of the y_η and z_η components.

Note, that when playing with formulae (3.85)-(3.92), we were not putting any restrictions on the Hamiltonian parameters. Hence, formula (3.92) describes the evolution of the two effective interaction axes $\mathbf{v}_{2,3}$ when moving anywhere on the J-K-Γ-Γ' phase diagram. Enforcing $\Gamma = J$ restricts the domain to the three-dimensional surface in the four-dimensional parameter space. In our parametrisation, for $\Gamma > 0$, one may imagine it as a piece of paper standing inside the J-K-Γ-Γ' cylinder. The piece would be curved along the horizontal direction[73] and placed in the $J > 0$ part, spanning for both the positive and negative Γ' values.

Similarly, for the $\Gamma < 0$ cylinder, the surface would be found in the $J < 0$ half. Thus, formula (3.93) describes the evolution of the two axes $\mathbf{v}_{2,3}$ on such a surface. By setting further conditions, we bound the movement to the non-trivial cuts through the $J = \Gamma$ surfaces —the lines (3.83)-(3.84). The reader may examine the shape of the currently more experimentally relevant line (3.83) in Fig. 3.23 (a), where the positive and negative Γ' branches were projected on the separate J-K –Γ circles for convenience.[74] Since the lines keep only one of the eigenvalues non-zero, there is only one interaction axis to monitor.

[73] Represented by J, K and Γ.

[74] Notably, the whole $\Gamma > 0$ line stretches out into positive and negative Γ'.

Finally, one can write the Hamiltonian with the bond-dependent interaction axis as

$$\mathcal{H}_{\mathrm{IKc}} = \tilde{K} \sum_{\langle i,j\rangle \in \mathrm{NN}} (\mathbf{S}_i \cdot \mathbf{n}_\eta)(\mathbf{S}_j \cdot \mathbf{n}_\eta), \tag{3.94}$$

where $\tilde{K} = 3J + K$ is the emerging coupling parameter with the antiferromagnetic sign for the line (3.83) and the ferromagnetic sign for the line (3.84). For $\Gamma > 0$ the versor $\mathbf{n}_\eta = \mathbf{v}_2/||\mathbf{v}_2||$ defines a unique interaction axis for each bond direction η. The abbreviation IKc refers to the Ising-Kitaev-"compass" model, named after the special points the lines (3.83)-(3.84) cross. We emphasise that along the full length of the lines this model has a unique interaction axis per bond.

As we will show below, what varies is the direction of the axis, leading to the above-mentioned special cases. Although $\tilde{\theta}$ is in principle enough to describe the physical consequences of the axis orientation, to distinguish between the true compass and "compass" cases we provide also the azimuthal angle $\tilde{\phi}$. Because of the bond-dependency of the interaction axis, we opt for the convention where $\tilde{\phi}$ is counted from the suitable η bond. Thus, following Ref. [29], we can rewrite $\mathbf{n}_\eta$ in the spherical parametrization of the rotating frame as

$$\mathbf{n}_\eta = \begin{pmatrix} \sin\tilde{\theta}\cos\tilde{\phi} \\ \sin\tilde{\theta}\sin\tilde{\phi} \\ \cos\tilde{\theta} \end{pmatrix}, \tag{3.95}$$

and in the XYZ frame as

$$\mathbf{n}_\eta = \begin{pmatrix} -\sin\tilde{\theta}\sin(\tilde{\phi}+\varphi_\eta) \\ \sin\tilde{\theta}\cos(\tilde{\phi}+\varphi_\eta) \\ \cos\tilde{\theta} \end{pmatrix}. \tag{3.96}$$

Umbrella effect

In order to understand what the Hamiltonian (3.94) consists of, we will be analysing the evolution of its interaction axis $\mathbf{n}_\eta$ along the experimentally more relevant $\Gamma > 0$ line (3.83). Note however, that similar examination is possible on the $\Gamma < 0$ case. Let us now refocus on a selected site of the honeycomb lattice. Any such site is connected by three bonds differing by the direction η. At the chosen site, we will be following an "umbrella" consisting of the three ribs—the interaction axes $\{\mathbf{n}_\eta\}$, coming from the three bonds, and the main handle—the Z$= z_\eta$ axis. We will monitor the degree of opening of such an umbrella by the $\tilde{\theta}$ angle.

When the umbrella is closed for $\tilde{\theta} = 0$, Hamiltonian (3.94) has the interaction axes along the Z$= z_\eta$ versor perpendicular to the honeycomb plane, regardless of the bond direction. This situation, illustrated in Fig. 3.22 (d), corresponds to the AF Ising model along Z. The Ising point, already encountered in the last paragraph of Sec. 3.4.5, is located at $K = 0$, $J = \Gamma = \Gamma' = \tilde{K}/3 = +\sqrt{2}/2$[75] and marked by an empty square in Figs. 3.23 (a)-(c) and A.4 (b).

Now, we will begin tho open the umbrella, evolving the system from the Ising model to a continuous family of the models with the bond-dependent interaction-axis. Before we start, let us point out few important geometrical dependencies on line (3.83).

1. During the evolution, $\mathbf{n}_\eta$ will remain perpendicular to the suitable η bonds, since rotation is constrained to the $y_\eta z_\eta$ planes.

2. The positive and negative $\tilde{\theta}$ values are related to the coherent 180° rotation of the interaction axes around the Z axis. This is in fact the self-dual $\mathcal{T}_1$ transformation, already

[75] In our parametrisation.

mentioned in Sec. 2.5.2.[76] Since the transformation maps the whole J-K-Γ-Γ' model onto itself, by utilizing the above rotation we obtain the self-dual partner of every point in the phase diagram possessing the same experimental properties. Even more remarkably, for any point on the IKc line (3.83) the $\mathcal{T}_1$ transformation keeps its self-dual partner also on that line. In particular, the Ising point is its own self-dual partner because $\tilde{\theta}$ is equal zero for this case.

No matter whether we follow the positive or negative $\tilde{\theta}$ branch in Fig. 3.23 (b), as soon as we make $\tilde{\theta} \neq 0$, the interactions become bond-anisotropic, introducing frustration to the system. As we open the umbrella further and further, at $\tilde{\theta} = \pm\arccos(1/\sqrt{3}) \approx \pm 54.74^\circ$ we reach the Kitaev model with its orthogonal set of interaction axes shown in Fig. 3.22 (e). $\tilde{\theta} \approx +54.74^\circ$ corresponds to the parameters: $J = \Gamma = \Gamma' = 0$, $K = \tilde{K} = +1$, leading to the original AF Kitaev point (a black point at the very top of Fig. 3.23 (a)-(b)).[77] $\tilde{\theta} \approx -54.74^\circ$ identifies the self-dual partner of the AF Kitaev point—the hidden, π-rotated AF Kitaev point, denoted by an empty circle in Figs. 3.23 (a)-(c) and A.4 (c). The point has coordinates: $J = \Gamma = 4K'/9$, $K = -K'/3$, $\Gamma' = -2K'/9$, where K' is here the coupling parameter of the original AF Kitaev point. This results in $J = \Gamma \approx 0.624$, $K \approx -0.468$, $\Gamma' \approx -0.312$ in our parametrisation.

By opening the umbrella even further we should be able to reach the honeycomb plane at $|\tilde{\theta}| = 90^\circ$, this time with the interaction axes along y_η versors (Fig. 3.22 (f)). This Hamiltonian is in fact equivalent to the compass Hamiltonian discussed in Sec. 3.4.6 up to the azimuthal rotation by 90°.[78] In order to emphasise this small caveat we call it the "compass" Hamiltonian. The "compass" point, marked by an empty triangle in Figs. 3.23 (a) and A.4 (k), is located at $J = \Gamma = \tilde{K}/6$, $K = \tilde{K}/2$, $\Gamma' = -\tilde{K}/3$ which gives $J = \Gamma \approx 0.302$, $K \approx 0.905$, $\Gamma' \approx -0.603$ in our parametrization. Note, that the above values are reached for both the positive and the negative sign of $\tilde{\theta}$. This is because, similarly to the Ising point, the "compass" point is also its own self-dual partner. All the other points, with the interaction axes lying neither in the honeycomb plane nor in the Z direction, are characterized by $|\tilde{\theta}| \in (0, 90^\circ)$. One can easily imagine, that if we push the $|\tilde{\theta}|$ value beyond 90°, we will obtain repeating solutions, e.g. the already-discussed explicit AF Kitaev point[79] is repeated at the bottom of Fig. 3.23 (b) for $\tilde{\theta} \approx (+54.74 + 35.26 + 35.26)^\circ \approx +125.26^\circ$. Therefore, one can summarise that $|\tilde{\theta}| \in [0, 90^o]$ represents a complete solution for the line.

As a final comment we add that while searching for the discussed Hamiltonians we could not fully follow the scheme possible for the hidden SU(2) points (Sec. III A of Ref. [9]). There, one could start from the matrix of the Heisenberg coupling parameters

$$\mathcal{H}'_{ij} = \begin{pmatrix} \pm J' & 0 & 0 \\ 0 & \pm J' & 0 \\ 0 & 0 & \pm J' \end{pmatrix} \tag{3.97}$$

and apply it to the formula

$$\mathcal{H}_{ij} = \mathcal{R}_i \mathcal{H}'_{ij} \mathcal{R}_j^T, \tag{3.98}$$

where $\mathcal{H}_{ij}$ denotes the matrix of the explicit J-K-Γ-Γ' Hamiltonian, $\mathcal{R}_i$ is an identity matrix and $\mathcal{R}_j$ is restricted by $\mathcal{H}_{ij} = J'\mathcal{R}_j^T$. After determining the J, K, Γ, Γ' parameters in $\mathcal{H}_{ij}$ for the

[76] On one hand, rotating any vector by 180° around the Z axis will naturally change the sign of the angle between the vertical axis and the vector. One may imagine this by rotating the z Kitaev cubic axis to land in between x and y. On the other hand, because $\tilde{\theta}$ is a function of the coupling parameters, changing them according to the $\mathcal{T}_1$ transformation results in the sign change $\tilde{\theta} \to -\tilde{\theta}$.

[77] The Kitaev interaction axes were previously described in Sec. 2.2 by $\alpha = 90^\circ - \tilde{\theta} \approx 35.26^\circ$, defined from the honeycomb plane.

[78] The physical properties of the ground state do not depend on the azimuthal angle $\tilde{\phi}$ but on the overlap between the pseudospin projections to the interaction axes dictated by $\tilde{\theta}$.

[79] $J = \Gamma = \Gamma' = 0$, $K = +1$.

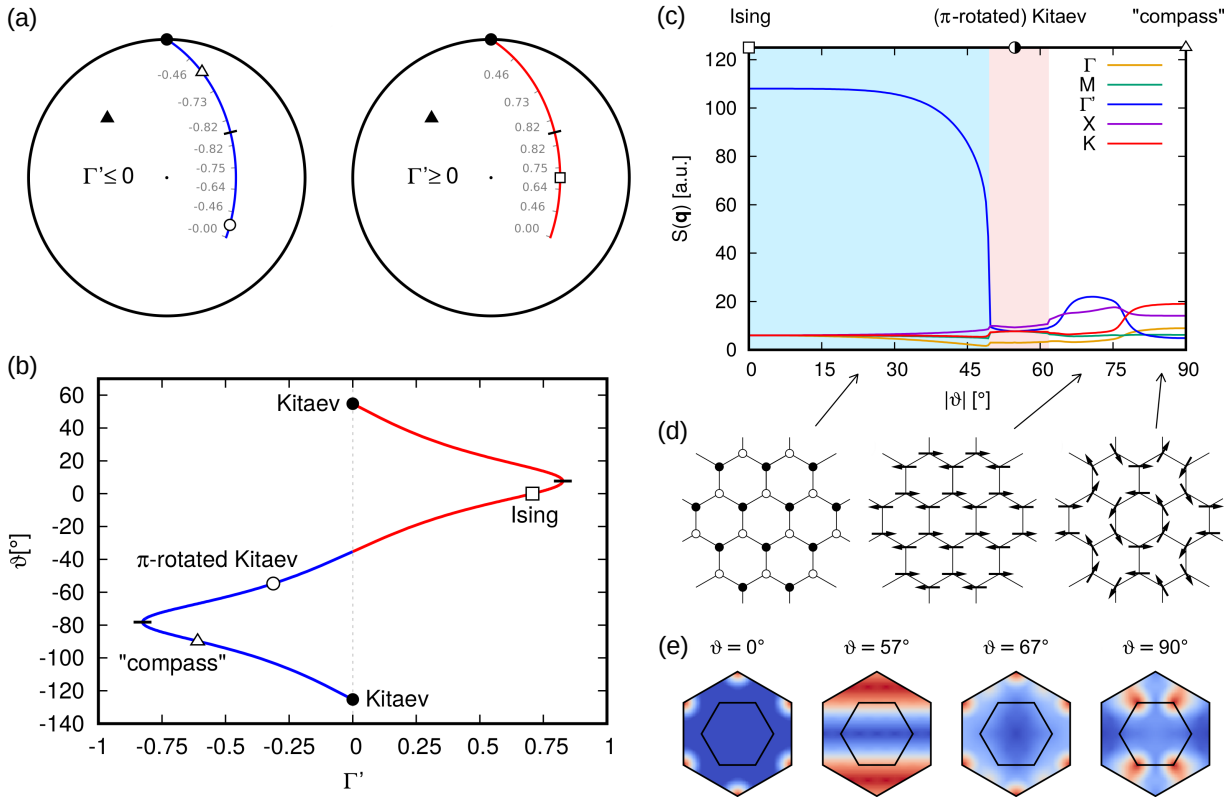

FIGURE 3.23: Panel (a)—the $\Gamma' \leq 0$ and $\Gamma' \geq 0$ branches of the $\Gamma > 0$ line (3.83), projected separately onto the same (J, K, Γ) circle. The Γ' values are denoted on the attached scales while the special points are marked by: an empty square (Ising point), an empty circle (hidden π-rotated AF Kitaev point), a filled circle (explicit AF Kitaev point), and empty triangle ("compass" point). For completeness, the true compass point is also shown (a filled triangle). Panel (b)—the deviation $\tilde{\theta}$ from the Z axis, here denoted as ϑ, as a function of the Γ' parameter for line (3.83). $\tilde{\theta}$ monitors the direction of the interaction axis $\mathbf{n}_\eta$ of the Ising-Kitaev-"compass" model. Panel (c)—the phase diagram of the Ising-Kitaev-"compass" model, identical for the positive and negative $\tilde{\theta}$ values. The vertical axis represents the reciprocal space correlation (total spin structure factor) $\mathbf{S}(\mathbf{q})$, plotted for the wavevectors $\mathbf{q} = \Gamma$, M, Γ', X and K, characteristic for the FM, zigzag, Néel, stripy and vortex patterns, respectively. The light-blue color marks the approximately classical Néel phase, the pink color—AF KSL, and the white color—the Néel order approximately in the honeycomb plane as well as the vortex region. Orderings with the maximal probability in the above regions are shown in panel (d), while the 1st-Brillouin-zone maps of $\mathrm{S}^z(\mathbf{q})$ can be found in panel (e). Figure has been published in [29].

selected bond, one has to find the R_k matrices on the subsequent sites forming the other bonds. This step is quite easy for the hidden SU(2) case, since one can rewrite formula (3.98) as

$$\mathcal{R}_k = \mathcal{H}_{kj}\mathcal{R}_j\mathcal{H}'^{-1}_{kj}. \tag{3.99}$$

Then, one has to repeat the procedure until the unit cell of the transformation[80] is complete. For the interaction-axis Hamiltonians, such as Ising, Kitaev or compass, the search is less automatic because $\mathcal{H}'^{-1}_{ij}$ does not exist.[81] In that context, it is very fortunate that the J-K-Γ-Γ' model possesses a self-dual transformation and the hidden Kitaev points could be determined in that way.

[80] Containing at least one site from each sublattice.

[81] Naturally, one can freely transform back and forth between $\mathcal{H}_{ij}$ and $\mathcal{H}'_{ij}$ once all the R_k matrices are known.

Phase diagram of the Ising-Kitaev-"compass" model

So far we have described only the selected values of $|\tilde{\theta}|$ for which model (3.94) becomes Ising, Kitaev or "compass". However, since the evolution of $\tilde{\theta}$ is continuous, one should be able to observe to what extent the corresponding ground states expand beyond these special points. Here we focus on $\tilde{\theta} \leq 0$ for an easier comparison between Fig.3.23 (b) and (c) , but, because of the $\mathcal{T}_1$ connection, the diagram for $\tilde{\theta} \geq 0$ is identical. We mention that an analogical model was analysed in Ref. [102] without the J-K-Γ-Γ' context.

We begin again with Fig. 3.23 (c) and $\tilde{\theta} = 0$ at the Ising point. There, the Néel moments oriented along the Z direction are completely devoid of quantum fluctuations. We deduce it from the 50% probability and the high values of the total pseudospin-pseudospin reciprocal-space correlation $\mathbf{S}(\mathbf{q})$,[82] plotted for the wavevectors $\mathbf{q} = \Gamma$, M, Γ', X and K, characteristic for the FM, zigzag, Néel, stripy and vortex patterns, respectively.[83] Clearly, the Néel signal $\mathbf{S}(\Gamma')$ stays at a fairy high level in the largest region on the diagram. As $|\tilde{\theta}|$ increases, the quantum fluctuations enter due to the rotation of the interaction axes from the vertical direction. Still, their amount is quite reduced, maintaining the approximately classical character of the ground state despite the model not being Ising anymore. Only when the horizontal component of the interaction axis becomes sufficiently large, the fluctuations increase rapidly, inhibiting the Néel probability and $\mathbf{S}(\Gamma')$.

Beyond $|\tilde{\theta}| \approx 49.5°$ the LRO dissolves into the critical case of the Kitaev spin liquid. Analogically to the $K = +1$ point, the hidden π-rotated AF Kitaev point is surrounded by a finite AF KSL region, of great importance for experimentalists. Indeed, the hidden region shows the liquid fingerprints: a wave-like pattern in $\langle \mathrm{S}^z_{\mathbf{q}} \mathrm{S}^z_{-\mathbf{q}} \rangle$ in Fig. 3.23 (e), contributing to the very low and flat $\mathbf{S}(\mathbf{q})$ signal at all the plotted wavevectors, and the maximal probability of any pattern equal or below 0.1% (not shown). The size of this hidden AF KSL region ($|\tilde{\theta}| \in [49.5, 62]°$) should be transferable to the size of the original AF KSL.[84]

For $|\tilde{\theta}| \in (62, 77)°$ stronger signal at the Γ' point emerges, accompanied by the slightly weaker signal at the X point (Fig. 3.23 (e) for the representable 67°) while the Néel pattern tilted by 5° from the honeycomb plane has the highest probability (middle pattern in Fig. 3.23 (d)). The level of the quantum fluctuations seems to be comparable to the AF Heisenberg point.

At $|\tilde{\theta}| \approx 77°$, the Γ' signal ceases while the one at the X point spills and solidifies around the K point, related to the vortex pattern. In this region ($|\tilde{\theta}| \in (77, 90]°$) two patterns are distinguished: vortex-a and vortex-b, with the probabilities 3.16% and 3.05%, correspondingly. Their fairy low values[85] may suggest that the region does not have the LRO, similarly to the neighborhood of the true compass point, where the two zigzag regions as well as the FM and vortex regions meet, but the probabilities are low.[86] Because the presence of the two last phases did not agree with Ref. [102], claiming one dimer phase instead, additional verification was needed. The maximal-overlap calculations on the 32-site clusters confirmed the in-plane Néel and vortex-a preference [29].

Experimental relevance of the hidden KSL regions

Because of the self-duality, not only the AF and FM Kitaev points but also the finite Kitaev spin liquid lakes around them have their hidden siblings of the size dictated by the $\mathcal{T}_1$ transformation.

[82] Total spin structure factor.

[83] Cf. Figs. 2.16 and 3.12.

[84] Here we are at odds with Ref. [102], in which a tensor-network analysis predicted KSL for $[52.7, 57.6]°$, despite the previous compatibility of the tensor-network and ED results for the Kitaev-Heisenberg model [103]. We suspect that the reason may be the difference in processing the level crossings or in the extrapolation of the bond dimension.

[85] Still above 1%.

[86] In that case vortex-b has slightly higher probability than vortex-a. For the neighborhood of the true compass point a disordered finite region was suggested in Refs. [99, 100].

The hidden FM KSL patch lies in the $\Gamma < 0$ part of the parameter space, far away from the positive Γ values estimated for the Kitaev candidate materials synthesised so far. Perhaps in the future the negative Γ will be also utilized, materials-wise. If so, the potential substantial size of the unexplored hidden FM KSL lake,[87] makes the acceptable range of the parameters larger.

The hidden AF KSL region is nowadays a more reachable goal. This is because it neighbors with the lower zigzag region in the parameter range[88] that is not so far from the estimates for Na_2IrO_3 and α-$RuCl_3$. Namely, it has negative K,[89] small positive J and negative Γ'. While the considered materials diverge from the spin-liquid patch because of the presence of J_3 and the much smaller estimate of $|\Gamma'|$, one could think of driving the system there by e.g. enforcing stronger trigonal distortion to increase $|\Gamma'|$. Even more available is the magnetically induced intermediate phase (IP), mentioned in Chapter 2. According to Ref. [38], under the uniform magnetic field perpendicular to the honeycomb plane the IP phase spreads "above" the zigzag region, including the position of α-$RuCl_3$ estimated by *ab initio* methods, up to the hidden AF Kitaev point.

3.5 Comparison with experiment

Finally, we compare the ordered moment results presented in this chapter with the experimental values obtained for Na_2IrO_3 and α-$RuCl_3$. The magnetic properties of materials can be examined e.g. by the resonant elastic X-ray scattering (REXS) and neutron difraction (ND). Although both types of experiments measure the observables related to the pseudospins $\mathbf{S}$, the details of this relation are not simple. Below we follow Ref. [11], describing the road from the experimental magnetic properties of the above materials to the properties of the pseudospins.

Neutron diffraction probes Fourier components of the magnetic moment $\mathbf{M}$, related to the pseudospin by the g-factors

$$\mathbf{M} = \begin{pmatrix} g_{\mathrm{X}} \mathrm{S}^{\mathrm{X}} \\ g_{\mathrm{Y}} \mathrm{S}^{\mathrm{Y}} \\ g_{\mathrm{Z}} \mathrm{S}^{\mathrm{Z}} \end{pmatrix}, \tag{3.100}$$

where XYZ is the orthogonal frame presented in Figs. 2.6 (b) and 3.21 (b), related to the Kitaev cubic frame via rotation (2.23).

In contrast, REXS probes Fourier components of the effective REXS operator R, for the Na_2IrO_3 and α-$RuCl_3$ compounds related to another operator $\mathbf{N}$ by [11, 104]

$$\mathrm{R} \propto i\mathbf{P} \cdot \mathbf{N}, \tag{3.101}$$

where $\mathbf{P} = \epsilon \times \epsilon'$ describes the polarization of the incoming (ϵ) and outgoing (ϵ') photons, while

$$\mathbf{N} = \begin{pmatrix} f_{\mathrm{X}} \mathrm{S}^{\mathrm{X}} \\ f_{\mathrm{Y}} \mathrm{S}^{\mathrm{Y}} \\ f_{\mathrm{Z}} \mathrm{S}^{\mathrm{Z}} \end{pmatrix}. \tag{3.102}$$

Both the f and the g-factors depend on the trigonal crystal field $\delta = 2\Delta/\lambda$ in a nontrivial way. Here Δ is the crystal-field splitting due to the trigonal distortion of the oxygen/chlorine octahedra and λ is the ionic spin-orbit coupling. In particular, the trigonal crystal field in the Z direction differentiates only between this direction and the perpendicular plane, leading to $g_{\mathrm{X}} = g_{\mathrm{Y}} = g_{\mathrm{XY}}$, $f_{\mathrm{X}} = f_{\mathrm{Y}} = f_{\mathrm{XY}}$. Following Ref. [11], we utilize the formulae

$$g_{\mathrm{XY}} = -\left(1 + \sqrt{2} s_{2\vartheta} - c_{2\vartheta}\right), \tag{3.103}$$

[87] Similarly to the FM KSL region around $K = -1$

[88] Of the original J-K-Γ-Γ' model.

[89] While the hidden Kitaev coupling K' is positive.

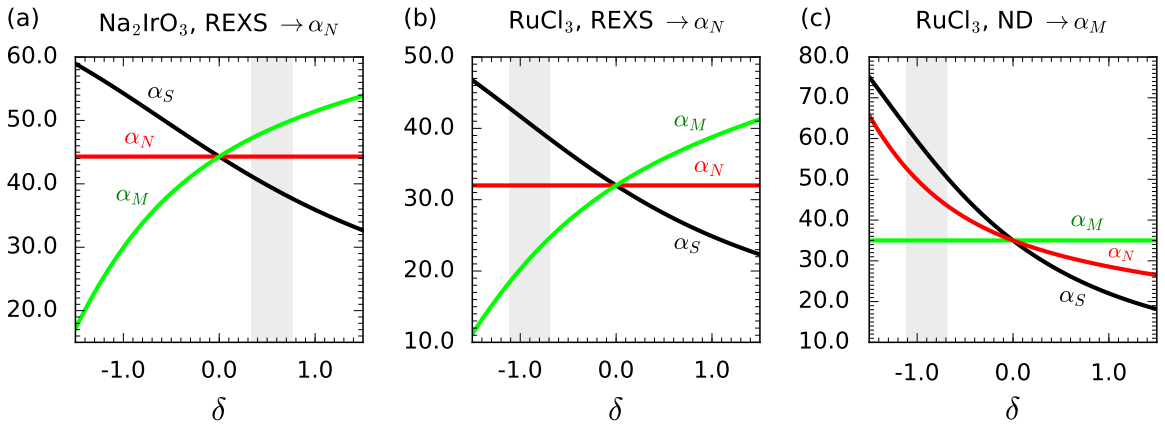

FIGURE 3.24: Mutual relations between the angles to the honeycomb plane for the three moments: pseudospin $\langle \mathbf{S} \rangle$, magnetic moment $\langle \mathbf{M} \rangle$ and REXS vector $\langle \mathbf{N} \rangle$. In each panel we fix the experimentally determined angle and calculate the other two as a function of the trigonal field δ. The grey filled region provides the possible range of δ estimated indepedently [105, 106, 107, 54], see the main text, and enables to determine the approximate α_{S} value. The vertical axis is calibrated in degrees. Panels (a) and (c) are recalculated from Fig. 4 (d) of Ref. [11], panel (b) is established based on the recent α_{N} measurement [58].

$$g_{\mathrm{Z}} = -\left(1 + 3c_{2\vartheta}\right), \tag{3.104}$$

$$f_{\mathrm{XY}} = \frac{1}{2} + \frac{5}{6\sqrt{2}} s_{2\vartheta} - \frac{1}{6} c_{2\vartheta}, \tag{3.105}$$

$$f_{\mathrm{Z}} = 1 + \frac{2}{3} c_{2\vartheta} - \frac{1}{3\sqrt{2}} s_{2\vartheta}, \tag{3.106}$$

where $c_{2\vartheta} = (1+\delta)/r$, $s_{2\vartheta} = 2\sqrt{2}/r$, $r = \sqrt{8 + (1+\delta)^2}$, to estimate the orientation and the absolute value of the pseudospin for the materials in question. An in-depth derivation of the above g and f-factors is provided in Refs. [104, 11].

Pseudospin direction

In the Na_2IrO_3 case, REXS provides the values of the elevation of $\langle \mathbf{N} \rangle$ above the honeycomb plane, $\alpha_{\mathrm{N}} \approx 44.3°$, and the azimuthal angle, $\phi_{\mathrm{N}} = 0°$ [39].[90] Because of this and the relations: $f_{\mathrm{X}} = f_{\mathrm{Y}} = f_{\mathrm{XY}}$, $g_{\mathrm{X}} = g_{\mathrm{Y}} = g_{\mathrm{XY}}$ for both materials, all the moments are fixed to the XZ plane. Therefore, we may treat the problem as 2D. In the XZ plane one can write:

$$\left\langle \mathrm{N}^{\mathrm{X}} \right\rangle = |\langle \mathbf{N} \rangle| \cos \alpha_{\mathrm{N}} = f_{\mathrm{XY}} \left\langle \mathrm{S}^{\mathrm{X}} \right\rangle = f_{\mathrm{XY}} |\langle \mathbf{S} \rangle| \cos \alpha_{\mathrm{S}}, \tag{3.107}$$

$$\left\langle \mathrm{N}^{\mathrm{Z}} \right\rangle = |\langle \mathbf{N} \rangle| \sin \alpha_{\mathrm{N}} = f_{\mathrm{Z}} \left\langle \mathrm{S}^{\mathrm{Z}} \right\rangle = f_{\mathrm{Z}} |\langle \mathbf{S} \rangle| \sin \alpha_{\mathrm{S}}. \tag{3.108}$$

Then, dividing Eq. (3.108) by (3.107) results in

$$\frac{\left\langle \mathrm{N}^{\mathrm{Z}} \right\rangle}{\left\langle \mathrm{N}^{\mathrm{X}} \right\rangle} = \tan \alpha_{\mathrm{N}} = \frac{f_{\mathrm{Z}}}{f_{\mathrm{XY}}} \tan \alpha_{\mathrm{S}}, \tag{3.109}$$

and thus

$$\alpha_{\mathrm{S}} = \arctan\left(\frac{f_{\mathrm{XY}}}{f_{\mathrm{Z}}} \tan \alpha_{\mathrm{N}} \right). \tag{3.110}$$

[90] We count the ϕ_{N}, ϕ_{M} and ϕ_{S} angles from the +X direction, opposite to Refs. [39, 58].

Similarly, we can also obtain

$$\tan\alpha_{\mathrm{M}} = \frac{g_{\mathrm{Z}}}{g_{\mathrm{XY}}}\tan\alpha_{\mathrm{S}}, \tag{3.111}$$

and thus

$$\alpha_{\mathrm{M}} = \arctan\left(\frac{g_{\mathrm{Z}}}{g_{\mathrm{XY}}}\tan\alpha_{\mathrm{S}}\right) \tag{3.112}$$

we complete our set of angles calculated from a given α_{N}. Their evolution in δ is shown in Fig. 3.24 (a), reproduced from Ref. [11] based on the above scheme.

In order to at least roughly estimate the experimental window of the trigonal field δ for Na_2IrO_3, visible in Fig. 3.24 (a) as the grey area, we again followed the recipe from Ref. [11]. Its left border $\delta \approx +0.35$ was set by applying the g-factor anisotropy $g_{\mathrm{Z}}/g_{\mathrm{XY}} \approx 1.4$ [105] to Fig. 4 (b) of Ref. [11]. The right border was estimated in Ref. [9] from the separation of the B and C intensity peaks in the magnetic excitation spectra[91] [106] as $\delta \approx +0.75$. The crossing of the black line and the grey region in Fig. 3.24 (a) estimates the experimental window of α_{S} for Na_2IrO_3 as $\alpha_{\mathrm{S}} \in [37.8, 41.1]^\circ$ from the honeycomb plane.

In the α-$RuCl_3$ case [Fig. 3.24 (b)-(c)], the trigonal field was roughly estimated based on the g-factor anisotropy $g_{\mathrm{Z}}/g_{\mathrm{XY}} \in [0.4, 0.5]$ [107, 54], resulting in $\delta \in [-1.1, -0.7]$ [11]. For the experimentally established $\alpha_{\mathrm{N}} \approx 32^\circ$ [58] this led to $\alpha_{\mathrm{S}} \in [38.6, 42.7]^\circ$ in Fig. 3.24 (b). However, REXS is not the only experiment that can provide the estimate of the pseudospin orientation. Neutron diffraction performed on α-$RuCl_3$ measured the elevation of the magnetic moment $\langle\mathbf{M}\rangle$ as $\alpha_{\mathrm{M}} \approx 35^\circ$ [57]. Proceeding in an analogous way as with formulae (3.107)-(3.112) but with the fixed α_{M} this time, one obtains:

$$\alpha_{\mathrm{S}} = \arctan\left(\frac{g_{\mathrm{XY}}}{g_{\mathrm{Z}}}\tan\alpha_{\mathrm{M}}\right), \tag{3.113}$$

and

$$\alpha_{\mathrm{N}} = \arctan\left(\frac{f_{\mathrm{Z}}}{f_{\mathrm{XY}}}\tan\alpha_{\mathrm{S}}\right). \tag{3.114}$$

This leads to Fig. 3.24 (c), which presents the evolution of both angles reproduced from Ref. [11] based on the above formulae. By applying the estimated borders of the trigonal field δ we obtain the experimental α_{S} window for α-$RuCl_3$ from the neutron diffraction: $\alpha_{\mathrm{S}} \in [50.7, 62.5]^\circ$. Note, that the above estimates are rather rough, meant as a suggestion rather than a definite verification. For example, they lack the assessment of how the measurement uncertainties may influence the uncertainties of α_{S}.

Having estimated α_{S} windows, we may search for the values they contain on the slices of the J-K-Γ-Γ' -J_3 phase diagram [explicitely—on the maps of α_{S}]. To this end, Fig. 3.25 presents the evolution of α_{S} in the zigzag phase predicted by the CMFT [Fig. 3.25 (a)] and the maximal-overlap [Fig. 3.25(b) and (c)] methods.

As already mentioned, REXS fixes also the azimuthal angle $\phi_{\mathrm{N}} = 0^\circ$, and hence $\phi_{\mathrm{S}} = 0^\circ$ for both materials [39, 58], which means that the projection of the pseudospin moment to the honeycomb plane lies along the X axis, between the projections of the x and y Kitaev cubic axes. The simulated zigzag moment has such an orientation mostly when the K parameter is negative

[91] Following Appendix C of Ref. [11], when both the spin-orbit coupling and the trigonal distortion effects are taken into account, the t_{2g} subshell splits into the doubly degenerate A, B, C Kramers levels. The A level represents the ground state in pseudospins $\tilde{\mathrm{J}} = 1/2$. The B and C levels simplify to the ionic $\mathrm{J} = 3/2$ when the trigonal distortion is absent. The transitions from A to B and C provide the anisotropic intensities in the magnetic response in the trigonal Z vs X and Y direction. This results in the separation of the peaks corresponding to the A$\rightarrow$ B and A$\rightarrow$C transitions by $\Delta_{\mathrm{BC}} = \lambda\left(\sqrt{8+(1+\delta)^2} - 3 + \delta\right)/4$. Such an anisotropy can be obtained when utilizing single crystals. Working with powders provides the averaged, more isotropic intensities which may not be enough for a reliable determination of δ.

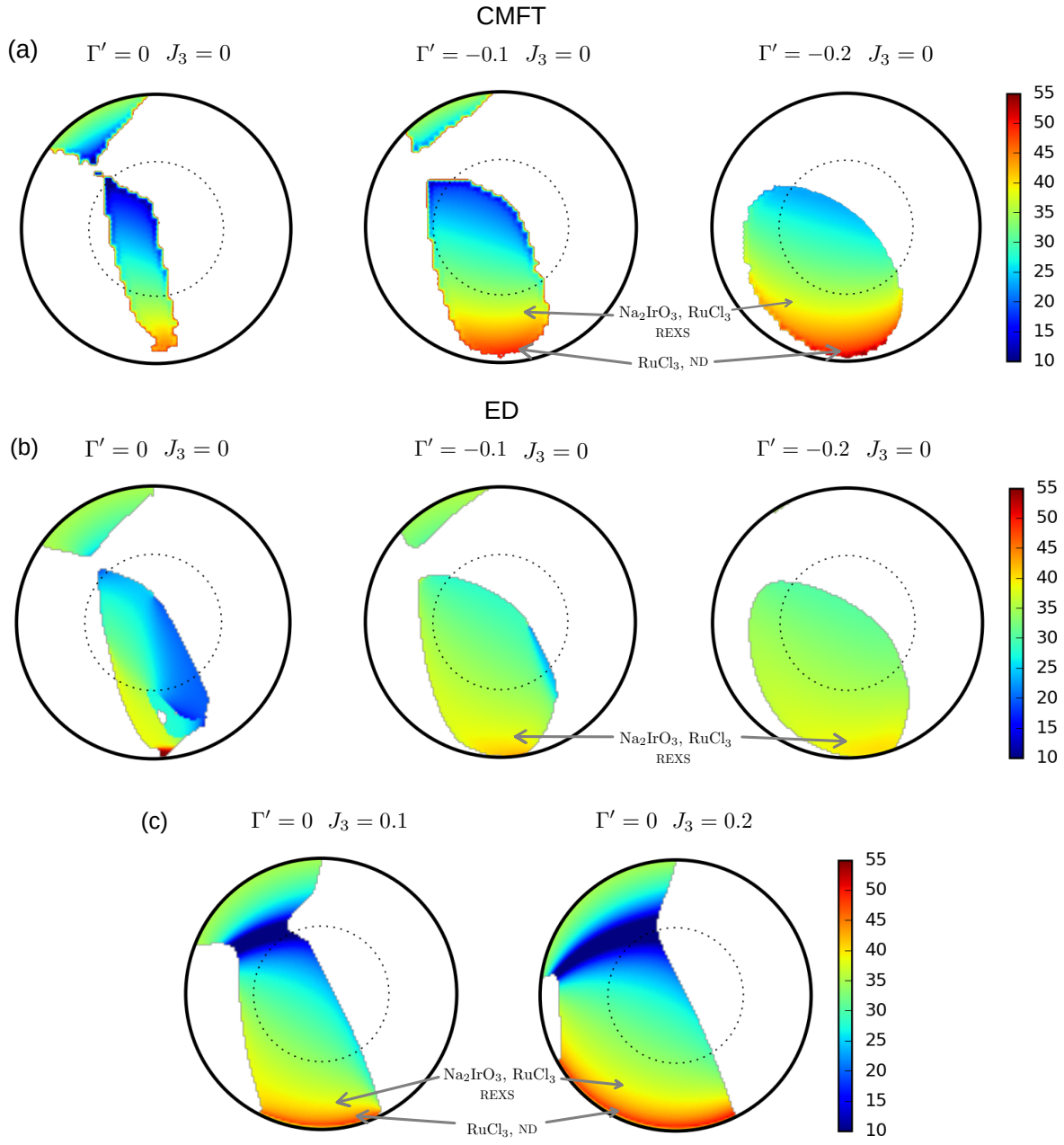

FIGURE 3.25: The maps of α_S—the elevation of the pseudospin from the honeycomb plane for the zigzag phase of the J-K-Γ-Γ'-J_3 model. Panel (a)—the maps calculated using the CMFT method for the relevant $J_3 = 0$ slices; panels (b)-(c)—the maps calculated utilizing the maximal-overlap (ED based) method for the $J_3 = 0$ and $\Gamma' = 0$ slices, respectively. All the maps are adjusted to the same color scale $\alpha_S \in [10, 55]°$, which is a compromise between encompassing the whole range in both methods and showing the evolution with a good resolution. The dark-blue values on panels (b) and (c) exceed this scale and reach the $\alpha_S = 0°$ in the honeycomb plane, as discussed in Sec. 3.4.4. The arrows indicate the color intervals corresponding to α_S estimated from the resonant elastic X-ray scattering measurements on Na_2IrO_3 and α-$RuCl_3$ and the neutron diffraction measurements on α-$RuCl_3$.

(ferromagnetic). This conclusion is based on the classical-energy and the order-from-disorder analysis in Ref. [11], sketched in Fig. 2.14, the maps of ϕ_S provided by the maximal-overlap method in Figs. 3.15 (e), 3.18 (e), 3.19 (e) as well as the J_3 maximal-overlap data. The FM K parameter rules out the upper zigzag region with AF K and points towards the lower zigzag region with (mostly) FM K.

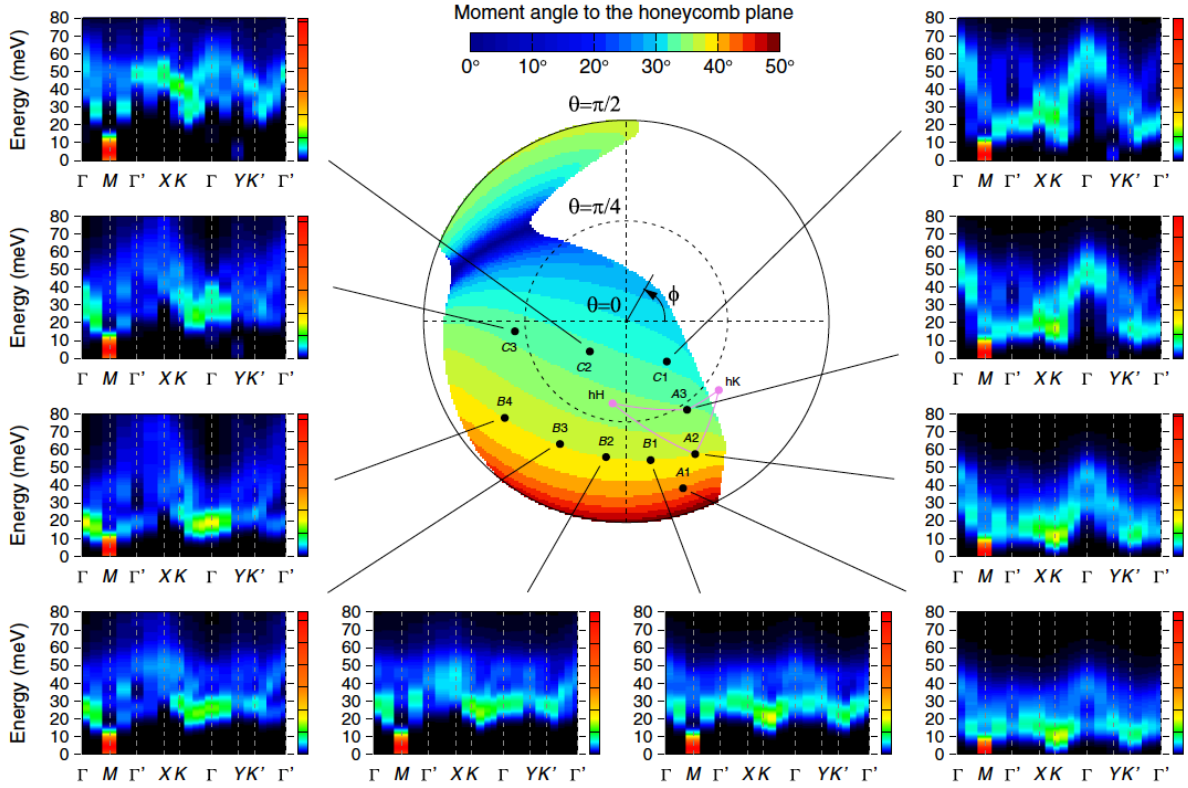

FIGURE 3.26: The map of the α_S angle calculated using the maximal-overlap method for the J-K-Γ-Γ'-J_2-J_3 model with the fixed parameters: $\Gamma' = -0.1$, $J_2 = 0.05$, $J_3 = 0.1$. For the selected points the resonant inelastic X-ray scattering (RIXS) intensities along the high symmetry paths of the 1st BZ are calculated using ED. hH and hK denote the projections of the zigzag SU(2) and hidden AF Kitaev points, respectively. Figure taken from Ref. [108].

When searching for the experimental windows of α_S we excluded also the $\Gamma' = J_3 = 0$ slices, because the REXS-based estimates appear there in a part of the lower zigzag region where the collinear order is unstable to the non-collinear tendencies, see Fig. 3.15 (f) for a reminder. In the rest of Fig. 3.25 the arrows do *not* indicate a specific point on a particular slice but rather an extended region, marked by the suitable color range.

In fact, in the Na_2IrO_3 case, the REXS-based window ($\alpha_S \in [37.8, 41.1]^\circ$) can be identified as a yellow stripe appearing at moderate Γ values[92] in the $J_3 = 0$, $\Gamma' < 0$ CMFT-based slices and at small Γ values in both J_3 and Γ'-active maximal-overlap-based slices. The REXS-based window for α-$RuCl_3$ ($\alpha_S \in [38.6, 42.7]^\circ$) practically overlaps with the above locations. However, the neutron-diffraction estimate ($\alpha_S \in [50.7, 62.5]^\circ$) points to a much weaker Γ. While the faster angular evolution in the CMFT case leads to $\alpha_S > 50^\circ$ at the very bottom of the lower zigzag regions in the $\Gamma' < 0$ slices, the slower evolving angle in the more quantum ED-based ground state does not reach those estimates for $\Gamma' < 0$ not only in the chosen here $\Gamma' = -0.1$ and -0.2 slices, but even for much higher $|\Gamma'|$, see Fig. A.4 (g)-(l). However, when the AF value of the J_3 parameter is considered, one can find the α_S window estimated form the neutron diffraction at a wide red stripe on both slices of Fig. 3.25 (c).

We stress, that in the above analysis Γ' and J_3 are probed separately, to better understand the influence of both parameters on the α_S evolution. The next logical step would be to calculate such maps, preferably with the less biased maximal-overlap method, for both parameters included, and then search for the experimental α_S windows on such maps. First such verification has been

[92] See a quick guide to the circular maps in Sec.2.5.1 for a reminder.

recently published in Ref. [108], where the maximal-overlap-based slice of the J-K-Γ-Γ'-J_2-J_3 model for $\Gamma' = -0.1$, $J_2 = 0.05$, $J_3 = 0.1$ was presented, along with the ED-based maps of the resonant inealastic X-ray scattering (RIXS) intensity for several selected points in the slice (Fig. 3.26). This theoretical result was compared to the experimental RIXS intensity for Na_2IrO_3 (cf. Fig 4. in Ref. [108]). Based on this and the experimental $\alpha_S \in [37.8, 41.1]^\circ$ window, the points 2A ($\alpha_S \approx 38^\circ$) and 3A ($\alpha_S \approx 34^\circ$) were selected. While at the point 3A the experimental and theoretical RIXS intensities match better, point 2A fits better with the experimental α_S window.

This is an example of a more general problem with Na_2IrO_3 and α-$RuCl_3$. Various experimental and *ab-initio* results for these materials indicate slightly different points or regions of the parameter space. In general, there seem to be a recently established consensus that both materials have the $K < 0$ and non-negligible $J_3 > 0$ contributions in the effective model, but beyond that, each experiment and calculation seem to bring a new estimate. One should note however, that each method feasible for those systems makes some sort of approximation, so this may be the price for the compromise.

Pseudospin value

In this section we will express the experimental magnetic moment value (per magnetic ion), described in Sec. 2.3.4, to the pseudospin $\langle \mathbf{S} \rangle$ value and compare it to the CMFT estimates.

Before we dive into this analysis, let us first state an important technical note:
In this thesis we are utilizing the dimensionless versions of various angular momentum operators —$\hbar$ was removed from their definitions for convenience. The magnetic moment definitions: (3.2), (3.8), (3.12), (3.13), (3.14) and (3.100) incorporated these dimensionless momentum operators and were dimensionless themselves. It is a convenient convention for calculations, however, for the comparison with the experiment one has to make sure to compare the quantities of the same dimension.

The full definition of the reduced magnetic moment for iridates and ruthenates takes the form

$$\mathbf{M}_{exp} = 2\mu_B \mathbf{S}, \tag{3.115}$$

where μ_B is the Bohr magneton, equal to $e\hbar/(2m_e)$ in the SI units, and the minus sign before μ_B was neutralised by the minus sign before the pseudospin $\mathbf{S}$, see eq. (3.14) for a reminder.

Consequently, formula (3.100) changes into

$$\mathbf{M}_{exp} = -\mu_B \begin{pmatrix} g_X S^X \\ g_Y S^Y \\ g_Z S^Z \end{pmatrix}. \tag{3.116}$$

Note that the magnetic moment lies in fact in the XZ plane, as explained in the previous section.

Now we will be deriving the formula connecting the value of the magnetic moment with the value of the pseudospin. From the definition of the norm of the dimensionless magnetic moment we may write

$$\begin{aligned} |\langle \mathbf{M} \rangle| &= \sqrt{\langle \mathbf{M} \rangle \cdot \langle \mathbf{M} \rangle} = \sqrt{g_X^2 \langle S^X \rangle^2 + g_Z^2 \langle S^Z \rangle^2} = \sqrt{g_X^2 |\langle \mathbf{S} \rangle|^2 \cos^2 \alpha_S + g_Z^2 |\langle \mathbf{S} \rangle|^2 \sin^2 \alpha_S} \\ &= |\langle \mathbf{S} \rangle| \sqrt{g_X^2 \cos^2 \alpha_S + g_Z^2 \sin^2 \alpha_S}. \end{aligned} \tag{3.117}$$

Then, the value of the pseudospin $|\langle \mathbf{S} \rangle|$ is related to the value of the dimensionless magnetic moment by

$$|\langle \mathbf{S} \rangle| = \frac{|\langle \mathbf{M} \rangle|}{\sqrt{g_X^2 \cos^2 \alpha_S + g_Z^2 \sin^2 \alpha_S}}. \tag{3.118}$$

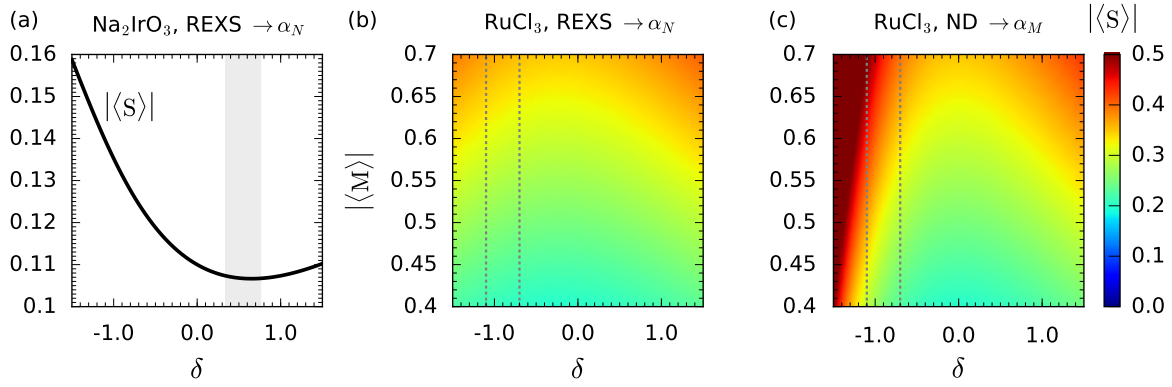

FIGURE 3.27: The translation of the experimental values of the ordered magnetic moments for Na_2IrO_3 and α-$RuCl_3$ to the length of the dimensionless pseudospin average $\langle \mathbf{S} \rangle$. Panel (a)—$|\langle \mathbf{S} \rangle|$ as a function of the trigonal field δ, calculated for the magnetic moment value and the α_{N} value for Na_2IrO_3 provided by ND and REXS, respectively. The estimated window for the trigonal field in Na_2IrO_3 is marked as a grey region. Panel (b)—similarly obtained experimental estimate of $|\langle \mathbf{S} \rangle|$ for α-$RuCl_3$, consisting of a map in $\{\delta, |\langle \mathbf{M} \rangle|\}$, where $|\langle \mathbf{M} \rangle| = |\langle \mathbf{M}_{exp} \rangle|/\mu_{\mathrm{B}}$, see the main text. Panel (c)— the map of of $|\langle \mathbf{S} \rangle|$ for α-$RuCl_3$, based on the experimental interval of the magnetic moment value and the α_{M} value from ND. In panels (b)-(c), for transparency, the estimated trigonal field window is marked by the two grey dashed lines.

Taking into account that $|\langle \mathbf{M} \rangle| = |\langle \mathbf{M}_{exp} \rangle|/\mu_{\mathrm{B}}$, the relation to the experimental magnetic moment takes the form

$$|\langle \mathbf{S} \rangle| = \frac{|\langle \mathbf{M}_{exp} \rangle|}{\mu_{\mathrm{B}}} \frac{1}{\sqrt{g_{\mathrm{X}}^2 \cos^2 \alpha_{\mathrm{S}} + g_{\mathrm{Z}}^2 \sin^2 \alpha_{\mathrm{S}}}}. \tag{3.119}$$

Hence, we have obtained the relation between the value of the dimensionless pseudospin, and the magnetic moment value provided by the neutron diffraction experiments, described in Sec. 2.3.4. Note, that formula (3.119) contains also α_{S}. We will utilize formulae (3.110) and (3.113) in order to relate this angle to the experimental estimates of α_{N} and α_{M}, respectively.

Fig. 3.27 presents the pseudospin value generated from the experimental magnetic moment value for Na_2IrO_3 and α-$RuCl_3$ (0.22 μ_{B}/Ir [52] and 0.4-0.7 μ_{B}/Ru [54], respectively) utilizing formula (3.119) as well as formulae (3.110), (3.113) for α_{S}. While in the Na_2IrO_3 case the only possible access to α_{S} was through the experimental α_{N} value, in the α-$RuCl_3$ case we could utilize the experimental α_{N} and α_{M} values, as discussed in the previous section. Both formulae (3.110), (3.113) are the functions of the trigonal field δ through the f and g-factors (3.105)-(3.104). Therefore, Fig. 3.27 (a) shows a 1D $|\langle \mathbf{S} \rangle|(\delta)$ dependence, with the δ interval estimated for Na_2IrO_3 indicated as the grey region similarly to Sec. 3.5.

Figs. 3.27 (b) and (c) present the results for α-$RuCl_3$. Because in the α-$RuCl_3$ case an interval of the value of the experimental magnetic moment was available, we prepared the maps of $|\langle \mathbf{S} \rangle|$ in $\{\delta, |\langle \mathbf{M} \rangle|\}$, where $|\langle \mathbf{M} \rangle| = |\langle \mathbf{M}_{exp} \rangle|/\mu_{\mathrm{B}}$ was restricted to the experimental 0.4-0.7. Fig. 3.27 (b) presents a variant of such a map, for which α_{S} was included through formula (3.110), connecting it to the experimental value of α_{N} provided by REXS on α-$RuCl_3$. Fig. 3.27 (c) on the other hand utilizes the experimental α_{M} value for the material, provided by neutron diffraction.

Having translated the the experimental magnetic moment value to the value of the pseudospin, we may now compared these estimates for Na_2IrO_3 and α-$RuCl_3$ with the ordered (pseudospin) moment value obtained by CMFT. As can be seen in Fig. 3.27 (a), in the Na_2IrO_3 case the experimental $|\langle \mathbf{S} \rangle|$ estimate, located within the grey region is below 0.11. A comparison of

this number with the CMFT-based maps of the ordered moment value (Figs. 3.15, 3.18, 3.19 (b)) leads to the conclusion, that $|\langle \mathbf{S} \rangle| = 0.11$ cannot be found in the zigzag regions of any of the so-far considered $\Gamma' \leq 0$, $J_3 = 0$ slices.

In the α-$RuCl_3$ case Fig. 3.27 (b) suggests the range of the pseudospin value between 0.2 and 0.35, depending on the $|\langle \mathbf{M} \rangle|$ interval. Similarly, Fig. 3.27 (c) estimates the pseudospin value between 0.2 to even 0.5. The values from both (b) and (c) cases can be easily found on the CMFT-based maps (Figs. 3.15, 3.18, 3.19 (b)).[93] Such broad ordered moment value intervals, however, do not bring information allowing to pinpoint the material's position on the phase diagram more precisely than it is already done in the previous section.

Summing up, it seems that the pseudospin value for Na_2IrO_3 is completely off the CMFT-based maps, while the predictions for α-$RuCl_3$ fit *all* of them, with the caveat that the classical part of the estimate from Fig. 3.27 (c) lies in the region considered as an artifact of the CMFT method. Therefore, the CMFT-based maps turned out not to be very helpful in narrowing down the position of α-$RuCl_3$ in the parameter space of the J-K-Γ-Γ' model, at least not with the current stage of knowledge about the trigonal distortion value and the magnetic moment value in the material. Based on the analysis of the ordered moment value provided by different methods for the Kitaev-Heisenberg model (cf. table 3.1) we suspect, that the CMFT result is also overestimated for the J-K-Γ-Γ' model and the zigzag ordered moment values should be lower. Therefore, similar systematic calculations by other methods would be highly appreciated.

[93] We note that the classical values ≈ 0.5 can be found in the bridge between the upper and lower zigzag region of the $\Gamma' = 0$, $J_3 = 0$ on Fig. 3.15 (b). As already discussed though, we consider this bridge an artifact of the method. Also, the completely classical experimental value seems rather overestimated, from our (limited) knowledge of the material.

3.6 Summary and conclusions

The magnetic properties of the $4d$ and $5d$ transition-metal oxides are highly non-trivial. The magnetism of Na_2IrO_3 and α-$RuCl_3$, exibiting both the features of the strong frustration and the long-range magnetic order, is in particular difficult to grasp, requiring the extensive experimental and theoretical self-consistent effort. Because of the strong influence of the relativistic spin-orbit coupling on the exchange processes in these correlated materials, it is convenient to approximate their low-energy behaviour by the effective Kitaev-like models.

In this chapter, we have presented our multi-method theoretical analysis of the Kitaev-Heisenberg model and the J-K-Γ-Γ' model, with some insight about the third-neighbor Heisenberg term J_3.

Various approaches:

- exact diagonalization (ED), self-consistent cluster mean –field theory (CMFT), linearized CMFT, classical energy analysis, linear spin-wave theory (LSWT) and second-order perturbation theory (SOPT) in the Kitaev-Heisenberg case,
- the maximal overlap method, CMFT, linearized CMFT, classical energy analysis as well as the analytical analysis of the special manifolds and the emergent effective models in the J-K-Γ-Γ' case

contributed to the corresponding composite phase diagrams, revealing the internal structure of the phases. We provided the qualitative explanation of the observed trends by the analysis of the classical energy and the distance to the "sources": the explicit and hidden SU(2) points, the hidden Ising, Kitaev and compass points and the classical manifolds. Since the Kitaev-Heisenberg model constitutes a special case of the J-K-Γ-Γ' model, the resulting composite phase diagram can serve as a set of detailed maps, that may be useful when investigating the observed or predicting the new material features.

Main feature: classical vs quantum character

The most outstanding feature in our data is the quantum vs classical character of the various nontrivial regions on the phase diagram. We can view the phase diagram as a landscape shaped by the amount of the quantum fluctuations: from the classical, rigidly ordered high "mountain ranges", through the very fluctuating but still ordered "lowlands", up to the Kitaev-spin-liquid "lakes". These "topographic" features were corroborated by various quantities: the value of the ordered moment from the LSWT and CMFT, the maximal eigenvalue λ_{max} from the linearized CMFT and the maximal overlap between the classical pattern and the quantum (ED) ground state.

On the phase diagram of the Kitaev-Heisenberg model the classical vs quantum behaviour of the LRO phases [FM and stripy vs Néel and zigzag], was explained utilizing the $\mathcal{T}_4$ analytical mapping connecting the points within the self-dual pairs. The ordered moment value obtained from the full CMFT procedure as well as λ from the linearized CMFT obeyed the $\mathcal{T}_4$ connection, displaying the saturated values for the FM and stripy phases and the reduced values for the Néel and zigzag phases.

On the phase diagram of the J-K-Γ-Γ' model the above collinear phases expand in Γ and Γ'. Moreover, the strong non-collinear tendencies appear, producing the vortex phase, characterized by the 6-sublattice magnetic ordering. Interestingly, all of the above phases, except zigzag, loose significant amount of the quantum fluctuations for $\Gamma > 0$. Even the Néel phase displays more classical λ_{max}, ordered moment and probability values. In contrast, the zigzag regions remain strongly quantum, with the probability of the zigzag pattern below 3%, the ordered moment value 0.34-0.35 and λ_{max} below 10. Independent evolution of the Néel and zigzag phases is possible because these phases are no longer connected via a self-dual transformation.

Highlight: the Ising-Kitaev-compass model

Among the many symmetry features discussed in Chapters 2-3, we would like to highlight the derivation of the Ising-Kitaev-compass model (IKc) from the J-K-Γ-Γ' model. This simpler Hamiltonian consists of an anisotropic interaction, understood as the interaction axis. The orientation of such axis is in general bond-dependent. As described in Sec. 3.4.6, through the umbrella effect, the interaction axes from the three bonds meeting at each site evolve from the direction perpendicular to the honeycomb plane, where all of them are parallel, producing the AF Ising model with the classical Néel ground state, through the umbrella opened by ca. 54.74°, resulting in the orthogonal arrangement of the axes and the Kitaev model with its Kitaev spin-liquid ground state, up to the fully opened umbrella with the interaction axes in the honeycomb plane, creating the compass model with its non-trivial ground state. The compass model is found not only within the Ising-Kitaev-compass line, but also at another, separate compass point. The phase diagram of the IKc model contains both the explicit AF Kitaev spin-liquid region and its self-dual copy located at the experimentally suggested $K < 0$ part of the parameter space.

Explicit and hidden KSL windows

The explicit Kitaev spin-liquid windows were investigated mostly using the ED-based methods, with some limited linearized and full CMFT contribution. For the Kitaev-Heisenberg model, the smaller size of the AF KSL vs the larger size of the FM KSL and the distinct character of the KSL/LRO transitions in both cases were confirmed by the ED -based pseudospin correlations and the dynamical spin susceptibility χ''. Although the CMFT-based correlations confirmed the size of the spin-liquid "lakes", a softer character of the FM KSL/LRO transiton was not well captured. The different size of the KSL regions was explained by the amount of the quantum fluctuations in the competing KSL and LRO states.

The limited expanse of the spin-liquid ground state for non-zero Γ and Γ' as well as the spin-liquid background even in the potentially magnetically ordered parts of the $K < 0$, $J = \Gamma' = 0$ line were confirmed by the ED-based methods.

The hidden AF KSL region, investigated as a part of the IKc model, is currently of great interest, because of its position in the $K < 0$ part of the phase diagram of the J-K-Γ-Γ' model, relatively close to the experimental [108] and *ab-initio* estimates [60] of the positions of Na_2IrO_3 and α-$RuCl_3$. The hidden FM KSL region is currently less attractive because of its position in the $\Gamma < 0$ part of the parameter space. However, if it was possible to design a crystal with $\Gamma < 0$, then tuning the material so that its effective-model parameters fit into the hidden FM KSL "lake" may be easier because of the potentially larger size of this "lake".

Highlight: the new classical manifolds

Both the maximal overlap and CMFT methods show also a rather consistent picture in terms of the pseudospin ordered moment direction. In the Kitaev-Heisenberg model the pseudospins orient themselves along one of the Kitaev cubic axes (xyz), elevated from the honeycomb plane by ca. 35.26°.

Adding the Γ and Γ' terms tilts the moment in various directions, depending on the ratio of the J, K, Γ, and Γ' parameters. In particular, it creates the approximately classical subphases within the Néel and FM regions. Their classical character is related with the out-of-(the honeycomb)-plane orientation of the moments in the ground state. It turns out that the quantum fluctuations potentially flipping the pseudospins along this direction vanish within the two classical manifolds. These special manifolds can be imagined as the "ridges" of the "mountain ranges" seen on the suitable maps, and are the source of the approximately classical behaviour in the out-of-plane subphases.

Ordered moment direction: fast vs slow evolution

The elevation of the pseudospin moment above the honeycomb plane α_S can experience "fast" or "slow" evolution in Γ, in the FM and Néel or zigzag and stripy regions, respectively. Both the CMFT and the maximal overlap methods reveal almost immediate response of α_S in the FM and Néel regions to the change in Γ and Γ'. In these cases, the quantum effects make only a small correction over the conclusions drawn from the classical energy analysis. Moreover, when introducing $\Gamma' < 0$, new subphases develop first near the outer rim of the phase diagram, with the moment direction perpendicular to the so-far-observed direction. The changes in the in-plane component of the direction are more subtle in the above phases as several energetically equivalent options are possible.

Ordered moment value in the FM and Néel phases

The pseudospin ordered moment value estimated by the CMFT method is strongly classical in the FM phase, reaching exactly the value of 0.5 for the FM SU(2) point as well as for the classical FM manifold. In the Néel phase of the J-K-Γ-Γ' model the moment value is reduced by the quantum fluctuations around the outer rim of the ordered moment maps. With increasing Γ the latter value becomes more classical, reaching the 0.5 limit for the AF classical manifold, including the hidden AF Ising point.

Ordered moment in the vortex phase

In the vortex phase the pseudospin moments lie mostly in the honeycomb plane, arranged either perpendicularly to (vortex-a) or along the bonds (vortex-b). Here the most probable direction depends on the distance to the SU(2) and compass points. Although both the maximal overlap and the CMFT methods consistently estimate the overall vortex boundaries, CMFT struggles with the reliable distribution of the vortex-a and vortex-b types. We suspect that the current CMFT result is not a definite verification, since the Anzaetze allowing for the out of plane component of the pattern were not included and the 6-sublattice site-averaging did not allow for such component to develop from the utilized in-plane Anzaetze. We realize, however, that the full verification of the vortex phase via the CMFT method is probably too computationally expensive. Finally, note that the ordered moment value in the vortex phase lies in the classical regime as well, reaching the 0.5 value at the SU(2) vortex point.

Ordered moment in the zigzag phase

Under the influence of $\Gamma > 0$, the original zigzag region of the Kitaev-Heisenberg model slightly expands, forming the upper zigzag region. Interestingly, another zigzag region appears in the lower part of the J-K-Γ maps. Notably, $\Gamma' < 0$ both supresses the upper zigzag and strengthens the lower zigzag region, while $J_3 > 0$ supports both regions, to the point of merging them together. In the upper zigzag region, in the case with the zigzag FM chains along a and b bonds, the moments are oriented close to the Kitaev cubic z axis, with a gentle decreasing tendency of α_S. When $J_3 > 0$ is included, the moments have the chance to reach the honeycomb plane, where they can change the in-plane component without the energy loss.

In the lower zigzag region the moments are oriented in between the x and y Kitaev cubic axes, so that the in-plane component differs by 180° between the two regions. Here α_S also gently decreases with the increasing Γ. We note that the evolution of α_S is faster for the CMFT results due to the smaller amount of the quantum fluctuations in the ground state. Nevertheless, the trend for the maximal overlap and CMFT result is similar and this kind of bias—manageable.

The CMFT-based value of the ordered moment in the zigzag regions is mostly reduced by the quantum fluctuations, although we suspect that alternative methods could provide an even more

reduced result, perhaps fitting better with the measurements. Nevertheless the CMFT-based value still allows for the distinction between the quantum vs classical character of each phase, suggesting the quantum character of the zigzag case.

Comparison with experiment

We have expressed the direction of the magnetic-moment related observables: $\langle \mathbf{N} \rangle$ and $\langle \mathbf{M} \rangle$, provided respectively by the resonant elastic X-ray scattering (REXS) and the neutron diffraction (ND), in terms of the direction of the pseudospin $\langle \mathbf{S} \rangle$, utilized by the maximal overlap and CMFT methods. The resulting experimental α_{S} windows: $\alpha_{\mathrm{S}} \in [37.8, 41.1]^\circ$ for Na_2IrO_3, $\alpha_{\mathrm{S}} \in [38.6, 42.7]^\circ$ ($\alpha_{\mathrm{S}} \in [50.7, 62.5]^\circ$), obtained from α_{N} (α_{M}), for α-$RuCl_3$, are discussed on the maps where Γ' and J_3 are considered separately [Fig. 3.25]. As a result, we obtain quite reliable conclusions that Γ' is enough to reproduce the orientation of the REXS-based moments for both Na_2IrO_3 and α-$RuCl_3$, while to obtain the ND-based estimation J_3 is needed in the effective Hamiltonian. We also comment on the recent results [108], where both Γ' and J_3 were included in the α_{S} map and a comparison with the REXS-based result was provided.

We have also expressed the experimental value of the magnetic moment for both materials in terms of the value of the pseudospin, that can be compared with the ordered (pseudospin) moment value obtained from CMFT. In the Na_2IrO_3 case, the translated experimental pseudospin estimate is below 0.11. Such a low value cannot be found in the zigzag regions of any of the so-far considered $\Gamma' \leq 0$, $J_3 = 0$ maps of the ordered moment value obtained from CMFT.

The more complex α-$RuCl_3$ case bears two estimated intervals of the pseudospin value: one interval, derived from the magnetic moment value $|\langle \mathbf{M} \rangle|$ (estimated by ND) and α_{N} value (estimated by REXS), ranges between 0.2 and 0.35, depending on the $|\langle \mathbf{M} \rangle|$ interval. Alternative estimate of the pseudospin value, derived from the magnetic moment value $|\langle \mathbf{M} \rangle|$ and α_{M} (both estimated by ND) ranges between 0.2 to even 0.5. These values can be easily found on the CMFT-based maps. Such broad intervals of the pseudospin value, however, do not allow to locate the position of α-$RuCl_3$ coupling parameters on the ordered moment value maps more precisely than it is already done by the pseudospin direction, at least not with the current stage of knowledge about the material. Based on the analysis of the ordered moment value provided by different methods for the Kitaev-Heisenberg model we suspect that the CMFT result is also overestimated for the J-K-Γ-Γ' model and the zigzag ordered moment values should be lower. Therefore, calculations of the ordered moment value using alternative methods are highly needed.

Pros and *cons* of the considered methods

In summary, it turns out that the Kitaev-like models require as much quantum fluctuations preserved in the numerical ground state as possible in order not to destroy all the nuances of the zero-temperature phase diagrams. The inclusion of the mean-field term, even just on the boundary, affects these delicate effects too much. While CMFT can reproduce the general trends visible in the ED results and supplement the pool of results with qualitatively reliable value of the ordered moment obtained in a direct way, the fine beauty of the strongly quantum phases is lost. The reason can be boiled down to the nature of the method: we have effectively filtered out the parts of the ground state to achieve the effect observed in the real materials: the non-zero magnetic ordered moment for the LRO phases. Since in CMFT the filtration was done in a rather crude way, by the partial initial polarization, many effects for which the quantum fluctuations were important were hindered as a consequence. The maximal overlap method achieves some of the considered goals in a more sophisticated way—it provides the classical patterns which have maximal overlap with the ground state while not compromising on the ground state quality.

We have gathered quite an amount of evidence that CMFT is not well suited for the systems in which frustration is an effect of the bond-anisotropy. The mean field applied to the periodic

boundary conditions deals with that frustration in a different way than the pure exact diagonalization, for the latter tends to lift the frustration by creating a superposition of the magnetic patterns in the ground state. As a result, CMFT creates artificial non-colinear tendencies in the ground state of the bond-anisotropic Hamiltonians. The only exceptions are the explicit and hidden SU(2) points, where the ultimate interaction is bond-isotropic.

We have partially corrected this effect by applying the $\mathrm{S}_i^z\langle\mathrm{S}_j^z\rangle$ decoupling for the Kitaev-Heisenberg model, where it is fully justified because of the easy axis being always one of the Kitaev cubic xyz axes, and by applying the site-averaging at the boundary after every iteration of the CMFT loop for the J-K-Γ-Γ' model. These means promoted collinearity, but at a cost of some side effects. Nevertheless, we think that the potential CMFT calculations for the J-K-Γ-J_3 model have some chance of being successful, because the J_3 term is bond-isotropic. This is also supported by the maximal-overlap slices showing less quantum fluctuations there. Therefore, in Appendix A.3 we propose a CMFT setup for the J_3 term.

Chapter 4

Introduction to spin-orbital entanglement

Quantum entanglement is an intriguing property of matter, absent in our everyday classical experience. Namely, the result of the measurement in one part of the entangled system influences the result of the subsequent measurement in the other part of the system. This phenomenon inspired physicists for many years, leading to both thought and real experiments testing, e.g., how two particles prepared in the entangled state and then spatially separated can "know" about each other's behaviour [109]. Quantum entanglement famously inspired the idea of qubits and quantum computing, promising the computers much faster than the classical machines [109].

The goal of this chapter is to first introduce the reader to the quantum entanglement in general and then to discuss a very specific case of entanglement involving both spin and orbital degrees of freedom. We will explain the basic features of the phenomenon, starting from the small systems and following with the analysis how it can be estimated for the larger systems. However, we stress that we merely scratch the surface of the quantum entanglement, focusing on an intuitive understanding, while much more advanced matematical tools have been discussed in detail in the literature [110, 109].

4.1 Quantum entanglement

Let us explore the topic of quantum entanglement starting from a simple example. Imagine a two-site system, for which each site is described by a spin S = 1/2 degree of freedom, bound together by the Heisenberg interaction

$$\mathcal{H} = J\mathbf{S}_1 \cdot \mathbf{S}_2. \tag{4.1}$$

If we set $J = +1$, the singlet ground state, corresponding to the non-degenerate E = −3/4 level can be written as

$$|\mathrm{S}_{tot} = 0, \mathrm{S}^z_{tot} = 0\rangle = \frac{1}{\sqrt{2}} \left(|\uparrow_1\downarrow_2\rangle - |\downarrow_1\uparrow_2\rangle \right), \tag{4.2}$$

while the three-fold degenerate excited level E = +1/4 corresponds to the triplet state

$$|\mathrm{S}_{tot} = 1, \mathrm{S}^z_{tot} = -1\rangle = |\downarrow_1\downarrow_2\rangle, \tag{4.3}$$

$$|\mathrm{S}_{tot} = 1, \mathrm{S}^z_{tot} = 0\rangle = \frac{1}{\sqrt{2}} \left(|\uparrow_1\downarrow_2\rangle + |\downarrow_1\uparrow_2\rangle \right), \tag{4.4}$$

$$|\mathrm{S}_{tot} = 1, \mathrm{S}^z_{tot} = +1\rangle = |\uparrow_1\uparrow_2\rangle. \tag{4.5}$$

Focusing first on the singlet state (4.2), let us attempt to express it as a generic product state for the two-site system

$$\begin{aligned} \frac{1}{\sqrt{2}} \left(|\uparrow_1\downarrow_2\rangle - |\downarrow_1\uparrow_2\rangle \right) &= \left(\alpha|\uparrow_1\rangle + \beta|\downarrow_1\rangle \right) \otimes \left(\gamma|\uparrow_2\rangle + \delta|\downarrow_2\rangle \right), \\ &= \alpha\gamma|\uparrow_1\uparrow_2\rangle + \beta\gamma|\downarrow_1\uparrow_2\rangle + \alpha\delta|\uparrow_1\downarrow_2\rangle + \beta\delta|\downarrow_1\downarrow_2\rangle, \end{aligned} \tag{4.6}$$

where α, β, γ and δ are in general complex coefficients, which should fulfill the following equations:

$$\alpha\gamma = 0, \tag{4.7}$$
$$\beta\delta = 0, \tag{4.8}$$
$$\beta\gamma = -\frac{1}{\sqrt{2}}, \tag{4.9}$$
$$\alpha\delta = \frac{1}{\sqrt{2}}. \tag{4.10}$$

However, the above set of equations cannot be fulfilled [111]. In other words, it is impossible to rearrange the singlet state into a direct product between sites

$$\frac{1}{\sqrt{2}}\left(|\uparrow_1\downarrow_2\rangle - |\downarrow_1\uparrow_2\rangle\right) \neq \left(\alpha|\uparrow_1\rangle + \beta|\downarrow_1\rangle\right) \otimes \left(\gamma|\uparrow_2\rangle + \delta|\downarrow_2\rangle\right), \tag{4.11}$$

therefore it is called an *entangled* state.

4.1.1 Subtleties: choice of basis and degenerate states

Singlet state

When diagonalizing Hamiltonian (4.1) we described the eigenstates in the eigenbasis of the S^z operator $\{|\uparrow\rangle = |\uparrow_z\rangle, |\downarrow\rangle = |\downarrow_z\rangle\}$. Let us now transform the singlet state to the eigenbases of the remaining orthogonal projections of $\mathbf{S}$ at each site—either

$$|\uparrow_x\rangle = \frac{1}{\sqrt{2}}\left(|\uparrow_z\rangle + |\downarrow_z\rangle\right), \tag{4.12}$$
$$|\downarrow_x\rangle = \frac{1}{\sqrt{2}}\left(|\uparrow_z\rangle - |\downarrow_z\rangle\right) \tag{4.13}$$

or

$$|\uparrow_y\rangle = \frac{1}{\sqrt{2}}\left(|\uparrow_z\rangle + i|\downarrow_z\rangle\right), \tag{4.14}$$
$$|\downarrow_y\rangle = \frac{1}{\sqrt{2}}\left(|\uparrow_z\rangle - i|\downarrow_z\rangle\right). \tag{4.15}$$

By rewriting

$$\frac{1}{\sqrt{2}}\left(|\uparrow_{z1}\downarrow_{z2}\rangle - |\downarrow_{z1}\uparrow_{z2}\rangle\right) = -\frac{1}{\sqrt{2}}\left(|\uparrow_{x1}\downarrow_{x2}\rangle - |\downarrow_{x1}\uparrow_{x2}\rangle\right) = \frac{i}{\sqrt{2}}\left(|\uparrow_{y1}\downarrow_{y2}\rangle - |\downarrow_{y1}\uparrow_{y2}\rangle\right), \tag{4.16}$$

one sees that the singlet state remains entangled independently of the choice of basis.

Triplet state

Moving to a more complex case of the triplet state, one immediately notices that in the S^z eigenbasis states (4.3) and (4.5) have the product form, while state (4.4) with $S^z_{tot} = 0$ is entangled. Translation to the S^x and S^y eigenbases results in

$$\begin{aligned}|S_{tot} = 1, S^z_{tot} = 0\rangle &= \frac{1}{\sqrt{2}}\left(|\uparrow_{z1}\downarrow_{z2}\rangle + |\downarrow_{z1}\uparrow_{z2}\rangle\right) = \frac{1}{\sqrt{2}}\left(|\uparrow_{x1}\uparrow_{x2}\rangle - |\downarrow_{x1}\downarrow_{x2}\rangle\right) \\ &= \frac{-i}{\sqrt{2}}\left(|\uparrow_{y1}\uparrow_{y2}\rangle - |\downarrow_{y1}\downarrow_{y2}\rangle\right).\end{aligned} \tag{4.17}$$

Thus, by recalling the simple examples of $|\mathrm{S}_{tot}=0,\mathrm{S}^z_{tot}=0\rangle$ and $|\mathrm{S}_{tot}=1,\mathrm{S}^z_{tot}=0\rangle$ states we have shown how quantum entanglement can be regarded as a real physical feature, independent of the choice of basis. For completeness we evaluate also a product state, e.g.

$$\begin{aligned}|\mathrm{S}_{tot}=1,\mathrm{S}^z_{tot}=-1\rangle = |\downarrow_{z1}\downarrow_{z2}\rangle &= \frac{1}{2}\left(|\uparrow_{x1}\rangle - |\downarrow_{x1}\right)\otimes\left(|\uparrow_{x2}\rangle - |\downarrow_{x2}\rangle\right)\\ &= -\frac{1}{2}\left(|\uparrow_{y1}\rangle - |\downarrow_{y1}\rangle\right)\otimes\left(|\uparrow_{y2}\rangle - |\downarrow_{y2}\rangle\right),\end{aligned} \tag{4.18}$$

reducing it to a product form in all bases.

At first one could hesitate how to treat the $+1/4$ level, for it corresponds to both entangled and product states. To have a more comprehensive picture one may interpolate between the two-site Ising and Heisenberg models. Indeed, the Ising lower doublet level[1] splits due to the lowering of the ground state energy from $-1/4$ to $-3/4$ and raising the energy from $-1/4$ to $+1/4$ by the quantum fluctuations. In this way a time-reversal invariant, quadrupolar state $|\mathrm{S}_{tot}=1,\mathrm{S}^z_{tot}=0\rangle$ is formed, for which the dipolar[2] $\langle\mathbf{S}_{tot}\rangle$ average vanishes while the quantum fluctuations are restricted to the xy plane [112]. Summing up, $|\mathrm{S}_{tot}=1,\mathrm{S}^z_{tot}=0\rangle$ is a quadrupolar state, but when composed of spins 1/2 on each site, it fulfils all the requirements for the entangled state.

Nevertheless, in the case of degenerate level it seems justified to take the dipolar states $|\mathrm{S}_{tot}=1,\mathrm{S}^z_{tot}=\pm1\rangle$ corresponding to the simplest, not entangled case as representative. However, if the triplet level is split due to some additional interaction involved, the entanglement properties of the quadrupolar state may be the only available option. Thus, below we will be considering the least-entangled state as a representative of a phase.

Although such a straight forward procedure is feasible for certain small systems, more refined concepts are needed to describe the entanglement more generally. Below we describe the simplest of such general approaches.

4.1.2 Reduced density matrix

In quantum entanglement literature one often encounters the formula for the entanglement entropy which contains the so-called reduced density matrix. In order to explain how this matrix estimates the entanglement we need to take a broader view. We will however avoid some details, which are still under discussion in the context of foundations of quantum mechanics [113], while not being essential for the understanding of this and the following chapter.

Let us start with introducing the concept of pure vs mixed states, a pure state is a quantum state of an isolated system. We can write the Hamiltonian for such a system and assume its eigenstates describe the system in the maximal available way. In contrast, a mixed state may describe a system, in which there is another level of uncertainty because it is in some way connected to another system. However, the details about this other part are either unavailable or inconvenient for us to explore.[3] We would like to focus on the first part only, but this is problematic—because of its openness[4] the system can no longer be described by the unique state vector. Instead, one utilizes the concept of the density matrix ρ which can be decomposed into $\sum_i p_i|\psi_i\rangle\langle\psi_i|$, where $|\psi_i\rangle$ are pure states and p_i are probabilities. This decomposition[5] is called a proper mixture [114]. Below we will focus on a different way of obtaining the mixed states,

[1] Represented by $\{|\uparrow_{z1}\downarrow_{z2}\rangle, |\downarrow_{z1}\uparrow_{z2}\rangle\}$ states.
[2] Vector-type.
[3] E.g. because of its size, as in the case of a reservoir.
[4] I.e. connection to reservoir.
[5] It is not unique.

via tracing out parts of the density matrices of pure states, leading to the so-called improper mixtures [114].[6]

For a pure composite state $|\psi\rangle$ we define a density matrix as simply $\rho = |\psi\rangle\langle\psi|$. Then, we divide the system into two subsystems A and B.[7] To examine the entanglement between subsystems A and B one constructs the reduced density matrices

$$\rho_{\mathrm{A}} = Tr_{\mathrm{B}}\rho, \tag{4.19}$$

$$\rho_{\mathrm{B}} = Tr_{\mathrm{A}}\rho, \tag{4.20}$$

where $Tr_{\mathrm{B}}/Tr_{\mathrm{A}}$ are partial traces over the diagonal elements in subspace B/A. Similarly to Ref. [111], we illustrate the idea of the reduced density matrix on our singlet example, with A=1, B=2:

$$\begin{aligned}
\rho_1 =& Tr_2\left[\frac{1}{2}\left(|\uparrow_1\downarrow_2\rangle - |\downarrow_1\uparrow_2\rangle\right)\left(\langle\uparrow_1\downarrow_2| - \langle\downarrow_1\uparrow_2|\right)\right] = \frac{1}{2}Tr_2(|\uparrow_1\rangle\langle\uparrow_1| \otimes |\downarrow_2\rangle\langle\downarrow_2| \\
&- |\downarrow_1\rangle\langle\uparrow_1| \otimes |\uparrow_2\rangle\langle\downarrow_2| - |\uparrow_1\rangle\langle\downarrow_1| \otimes |\downarrow_2\rangle\langle\uparrow_2| + |\downarrow_1\rangle\langle\downarrow_1| \otimes |\uparrow_2\rangle\langle\uparrow_2| \\
&= \frac{1}{2}(|\uparrow_1\rangle\langle\uparrow_1| \otimes \underbrace{(\sum_i \langle i|\downarrow_2\rangle\langle\downarrow_2|i\rangle)}_{\text{sum over diagonal}} - |\downarrow_1\rangle\langle\uparrow_1| \otimes (\sum_i \langle i|\uparrow_2\rangle\langle\downarrow_2|i\rangle) \\
&- |\uparrow_1\rangle\langle\downarrow_1| \otimes (\sum_i \langle i|\downarrow_2\rangle\langle\uparrow_2|i\rangle) + |\downarrow_1\rangle\langle\downarrow_1| \otimes (\sum_i \langle i|\uparrow_2\rangle\langle\uparrow_2|i\rangle)) \\
&= \frac{1}{2}(|\uparrow_1\rangle\langle\uparrow_1| \otimes (\sum_i \langle\downarrow_2|i\rangle\langle i|\downarrow_2\rangle) - |\downarrow_1\rangle\langle\uparrow_1| \otimes (\sum_i \underbrace{\langle\downarrow_2|i\rangle}_{\text{number}}\underbrace{\langle i|\uparrow_2\rangle}_{\text{number}}) \\
&- |\uparrow_1\rangle\langle\downarrow_1| \otimes (\sum_i \langle\uparrow_2|i\rangle\langle i|\downarrow_2\rangle) + |\downarrow_1\rangle\langle\downarrow_1| \otimes (\sum_i \langle\uparrow_2|i\rangle\langle i|\uparrow_2\rangle)) \qquad (4.21) \\
&= \frac{1}{2}\left(|\uparrow_1\rangle\langle\uparrow_1|\langle\downarrow_2|\downarrow_2\rangle - |\downarrow_1\rangle\langle\uparrow_1|\langle\downarrow_2|\uparrow_2\rangle - |\uparrow_1\rangle\langle\downarrow_1|\langle\uparrow_2|\downarrow_2\rangle + |\downarrow_1\rangle\langle\downarrow_1|\langle\uparrow_2|\uparrow_2\rangle\right) \qquad (4.22) \\
&= \frac{1}{2}\underbrace{\left(|\uparrow_1\rangle\langle\uparrow_1| + |\downarrow_1\rangle\langle\downarrow_1|\right)}_{\mathrm{id}} = \frac{1}{2}\mathrm{id} \qquad (4.23)
\end{aligned}$$

where in steps (4.21) and (4.22) we decomposed the identity matrix $\sum_i |i\rangle\langle i|$ in the basis $\{|i\rangle = |\uparrow_2\rangle, |\downarrow_2\rangle\}$.

In general, the density matrix represents a pure state if it has only one nonzero eigenvalue [115, 111].[8] In that context, we observe that while the full density matrix ρ of the singlet state has eigenvalues: 3-fold degenerate 0 and non-degenerate 1, the diagonal form (4.23) has two nonzero eigenvalues [doubly-degenerate 1/2], therefore it represents a mixed state in the subspace 1. Thus, we have obtained a consistent picture describing an entangled state as a pure state for which partial traces produce mixed states reduced to the suitable subspaces. In other words, an entangled state cannot be separated into pure states in the corresponding subspaces.

4.1.3 Entropy

Why can we estimate the entanglement utilizing entropy? Let us again present a broader view. In classical physics the thermodynamic entropy can be interpreted statistically as a measure of

[6] We note, that the subtleties between the proper and improper mixture are still discussed in the context of quantum measurement. Here our goal is to provide the most intuitive introduction, hence the omission.

[7] Note, that although for small systems it may be trivial, like in the above singlet-triplet example, where there was only one selection possible, for larger systems and spatial entanglement more choices are available.

[8] This is equivalent to the condition $Tr\left(\rho^2\right) = 1$. Since the eigenvalues represent probabilities it should be +1 for a (normalized) pure state.

disorder in a microscopic scale [116]. To put it simply, for some macrostates described by extensive properties such as volume or temperature, there is only few microstate configurations that could reproduce macroscopic description, while for some others there are many such microstates. If we can only measure temperature, volume and pressure, then, even from the classical point of view we cannot say for certain in what microstate the system is in, since there are many configurations that build the same macroscopic picture [117].

Entropy estimates this uncertainty—for a highly "organized" system the entropy will be small or even zero if there is only one possible microstate, while for a "disorganized", almost randomly arranged system the entropy will be high.[9] Formally, this is encoded in the formulae for the Boltzmann and Gibss entropies, $\mathcal{S}_{\mathrm{B}} = k_{\mathrm{B}} \ln \Omega$ and $\mathcal{S}_{\mathrm{G}} = -k_{\mathrm{B}} \sum_i p_i \ln p_i$, correspondingly, where k_{B} is the Boltzmann constant, Ω is the number of microstates and p_i are the probabilities of the microstates. If we consider an isolated system in the thermodynamic equilibrium, then we can write $p_i = 1/\Omega$ and the $\pm$ sign in the definition can be easily related to the properties of the logarithm as a function.

Entropy as an estimate of uncertainty is also utilized in the classical information theory, where it is known as the Shannon entropy $\mathcal{S}_{\mathrm{S}} = -\sum_i p_i \log_2 p_i$ [118, 119]. Usually written in bits—basic unit of information in binary basis —it estimates by how much a piece of informaton reduced our uncertainty. In other words, it tells us how many new bits of information we gain on average by learning a particular information. Currently, the classical statistical entropy $\mathcal{S}_{\mathrm{G}}/k_{\mathrm{B}}$ is interpreted as Shannon entropy corresponding to the average amount of information that would have to be supplemented to the macroscopic description to verify a microstate of a system.

Role of the logarithm

No matter whether we start form the information theory or statistical mechanics, we want the entropies of two independent events/ensembles to sum up into the entropy of the joint sequence/ensemble [117]. We want entropy to be additive and thus an extensive property, such as volume, pressure or temperature. The information we search for is already held by the number of (micro)states, it becomes however quite inconvenient for large systems [117]. For example, for 2, 4, 8 and 16-site systems with one classical Ising spin[10] per site there will be $2^2 = 4$, $2^4 = 16$, $2^8 = 256$ and $2^{16} = 65536$ possible states of the system,[11] so the number of states increases as 2^{N} for an N-element system, providing extremely large numbers for a relatively small extension of the system, which is quite impractical. Taking the logarithm of the number of states transforms those numbers into much smaller ones and the multiplicative behaviour of the number of states into the additive behaviour of the logarithm [117].

Von Neumann entropy

In order to be able to consider quantum systems in the statistical framework, the von Neumann entropy was defined [120], for which, instead of the classical probabilities/probability density, one utilizes their quantum equivalent. Such entropy is defined by the formula

$$\mathcal{S}_{\mathrm{vN}} = -Tr\left(\rho \ln \rho\right), \tag{4.24}$$

where ρ is the density matrix described in the previous section. We replace the ordinary sum with the sum over diagonal—the trace, convenient because of its invariant character, independent of the chosen basis. The von Neumann entropy estimates how much information we miss in order to properly define a quantum state, i.e. to what degree the system is in a mixed state. The von

[9] In thermodynamics it makes more sense to analyse the entropy change $\Delta\mathcal{S}$ rather than the absolute values of $\mathcal{S}$, since one observes e.g. how gas fills the empty part of the container after removing a blocade [116, 117].

[10] For now we restrict ourselves to the classical case.

[11] Each site can be easily interpreted as containing one bit of information.

Neumann entropy of a composite system has an interesting property that would be impossible for the classical case: in case of the state that is pure but entangled, the von Neumann entropies of the state reduced to the suitable subspaces via a partial trace (entanglement entropies) are non-zero, but the von Neumann entropy of the whole system can vanish [110, 121].

Entanglement entropy

Entanglement entropy is the von Neumann entropy of the state created by the partial trace [122]. Namely,

$$\mathcal{S}_{\text{vN}} = -Tr_{\text{A}} \left(\rho_{\text{A}} \ln \rho_{\text{A}} \right), \tag{4.25}$$

where ρ_{A} is the reduced density matrix of system A, obtained via a partial trace over system B. It still measures the degree of "mixing" in subspace A, while being more practical than the reduced density matrix itself for certain applications. Thus, by estimating how mixed the reduced state is, the entropy provides the measure of quantum entanglement as well.

Finally, we add two technical remarks: (i) because in the following chapter we will be comparing different system sizes, we prefer a normalized version of the above formula

$$\mathcal{S}_{\text{vN}} = -\frac{1}{\text{L}} Tr_{\text{A}} \left(\rho_{\text{A}} \ln \rho_{\text{A}} \right), \tag{4.26}$$

where L is the system size; (ii) in the degenerate case, similarly to Sec. 4.1.1, we will search for the least-entangled state corresponding to the degenerate energy by calculating the entanglement entropy for each state and selecting the minimal value.

4.2 Spin-orbital entanglement

In principle, the entanglement may concern any two kinds of degrees of freedom the system can be divided into, it does not have to be strictly the spatial entanglement. In particular, in some circumstances the entanglement between spins and orbitals may appear, as in the ground states of $LaTiO_3$, $LaVO_3$, YVO_3 and $Ba_3CuSb_2O_9$ [123, 124, 125, 126, 127, 59]. More precisely, for compounds weak or negligible Jahn-Teller interaction, there will be still some degeneracy left in the orbital sector [28]. Partial filling of the degenerate orbitals allows for quantum fluctuations of orbitals, shown experimentally for $LaTiO_3$ [128], $YTiO_3$[129] and YVO_3[130].

As a result, in the absence of Hund's coupling, the spin-orbital Hamiltonians of the Kugel-Khomskii type for the t_{2g} –restricted cubic titanates and vanadates contain the $(\mathbf{S}_i \cdot \mathbf{S}_j)(\mathbf{T}_i \cdot \mathbf{T}_j)$ term, where $\mathbf{S}$ and $\mathbf{T}$ are spin and orbital (pseudospin) operators. This four-operator term allows for the spin orbital entanglement [28].

In what follows we will describe in detail an idealized case where the spin-orbital Hamiltonian is SU(2)⊗SU(2) symmetric and the system is one-dimensional. While, as the reader will see, such a symmetric setup serves as a good starting point for investigating the spin-orbital entanglement, offering non-trivial phase diagram, there actually exist materials for which such symmetric model was considered: NaV_2O_5 and $Na_2Ti_2Sb_2O$— the quasi-one dimensional materials described by the 1/4-filled two-band Hubbard model [131, 132]. Below we discuss in detail the phase diagram of the SU(2)⊗SU(2) symmetric spin-orbital model for a chain with periodic boundary conditions (PBC), with the goal to describe the spin-orbital entanglement for this case.

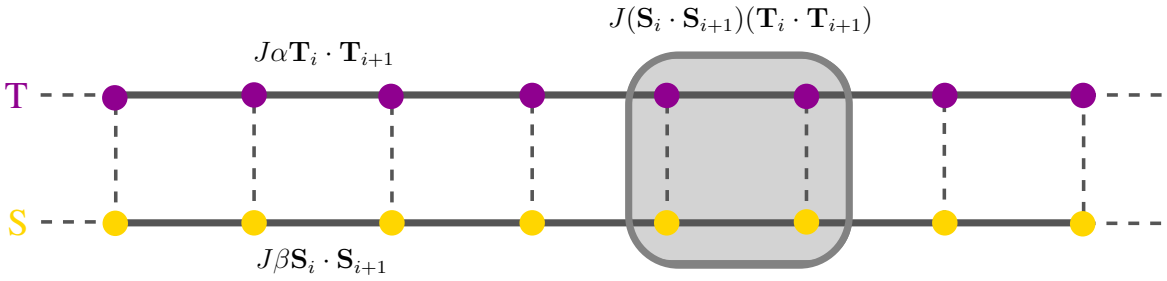

FIGURE 4.1: The spin-orbital chain with periodic boundary conditions can also be viewed as a ladder with one leg built from pseudospins T and the other from spins S. $J\alpha$, $J\beta$ and J are the coupling parameters of the Kugel-Khomski model (4.27), standing before the indicated terms.

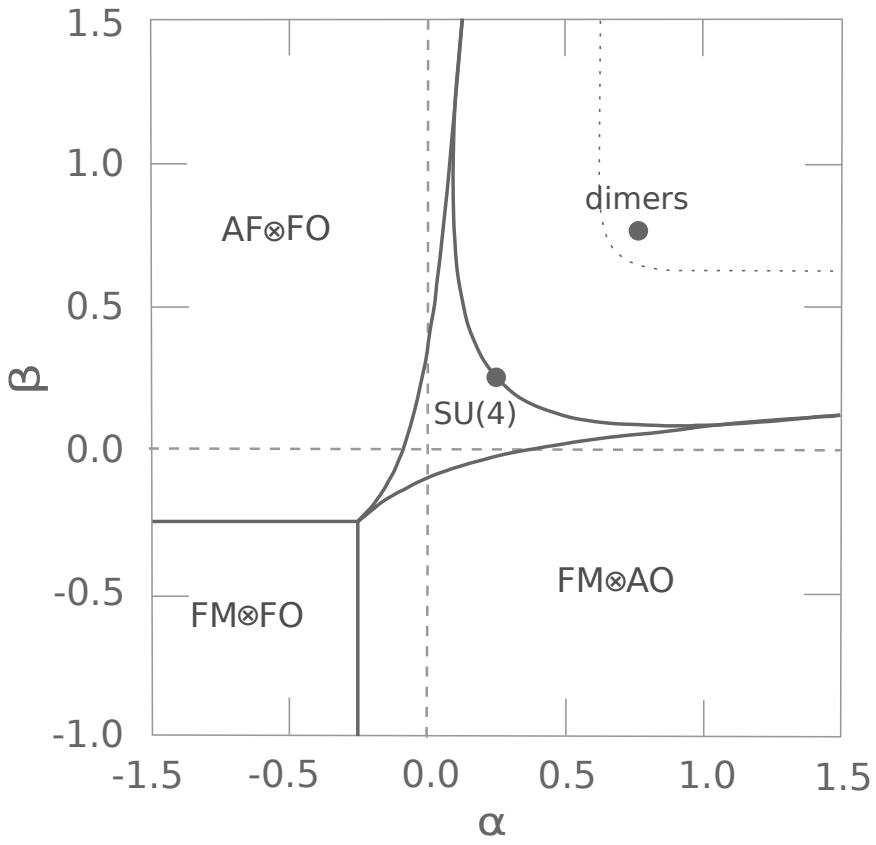

FIGURE 4.2: Phase diagram of the SU(2)⊗ SU(2) symmetric spin-orbital model, redrawn from Ref. [133] with modified names. The diagram consists of three product phases: FM⊗FO (ferromanetic ⊗ ferroorbital), AF⊗FO (antiferromagnetic ⊗ ferroorbital), FM⊗AO (ferromagnetic ⊗ alternating orbital), as well as spin-orbitally entangled phases: (i) the critical phase in the middle with qualitatively the same singlet ground state as in the exact SU(4) point (grey circle at $\alpha = \beta = +0.25$), and (ii) the gapped phase with the translational symmetry broken due to dimerization [labeled as "dimers"]. The faint dotted line reveals an internal structure of the latter phase, where the excitation spectra differ (stable magnons vs continuum), while the ground state is qualitatively the same. The Kolezhuk-Mikeska (KM) point, with exact, doubly-degenerate dimerized ground state is marked by the grey circle at $\alpha = \beta = +0.75$. Note, that the presented boundary between the SU(4) singlet and the dimerized phase is partly analytical, partly Density-Matrix-Renormalization-Group (DMRG)-based. For ED on small to medium-size finite chains this boundary will be moved to the right due to the finite-size effects.

4.2.1 Phase diagram of the SU(2)⊗ SU(2) symmetric spin-orbital model

The SU(2)⊗ SU(2) symmetric spin-orbital Hamiltonian of the Kugel-Khomskii type has the form

$$\mathcal{H}_{\mathrm{SE}} = J \sum_i \left[(\mathbf{S}_i \cdot \mathbf{S}_{i+1} + \alpha)(\mathbf{T}_i \cdot \mathbf{T}_{i+1} + \beta) - \alpha\beta \right], \tag{4.27}$$

where we assume $J = +1$. The spin S and effective orbital (pseudospin) T quantum numbers on every site are equal 1/2, both represented by the spin 1/2 algebra of the Pauli matrices. Hence, such spin-orbital chain is mathematically equivalent to a ladder with one leg represented by spins and the other by pseudospins [134], see Fig. 4.1.

An increase of interest in the model twenty years ago led to a progressively more refined phase diagram, published subsequently in references [131, 135, 136, 137, 138, 132, 133]. Here we discuss its most up-to-date version from Ref. [133], presented in Fig. 4.2. The referred phase diagram encompasses simple product phases: FM⊗FO—displaying ferromagnetic and ferroorbital correlations, AF⊗FO—antiferromagnetic and ferroorbital correlations, FM⊗AO— ferromagnetic and alternating-orbital correlations, as well as spin-orbitally entangled phases in the central and upper-right part of the phase diagram. Here we note that, because of the low dimensionality, all the "antiferro" sectors do not have long range order and only short-range correlations exist.

Product phases

The origin of the product phases can be easily understood when one rewrites Hamiltonian (4.27) as

$$\mathcal{H}_{\mathrm{SE}} = J \sum_i \left((\mathbf{S}_i \cdot \mathbf{S}_{i+1}) (\mathbf{T}_i \cdot \mathbf{T}_{i+1}) + \alpha \mathbf{T}_i \cdot \mathbf{T}_{i+1} + \beta \mathbf{S}_i \cdot \mathbf{S}_{i+1} \right). \tag{4.28}$$

When the $(\mathbf{S}_i \cdot \mathbf{S}_{i+1})(\mathbf{T}_i \cdot \mathbf{T}_{i+1})$ term, generating the spin-orbital entanglement, is small compared to the $\alpha \mathbf{T}_i \cdot \mathbf{T}_{i+1}$ and $\beta \mathbf{S}_i \cdot \mathbf{S}_{i+1}$ terms and at least one sector has a ferro(magnetic) coupling parameter, α and/or $\beta < 0$, there is no spin-orbital entanglement in the ground state.

Instead, the ground state is a product of the spin and orbital states. These states are described by the total spin/orbital quantum number $[\mathrm{S}_{tot}/\mathrm{T}_{tot}]$ of the whole chain and the projection of the total spin/pseudospin to the z axis $[\mathrm{S}^z_{tot}/\mathrm{T}^z_{tot}]$. For convenience, we can utilize a generalized notation $[\mathrm{O}_{tot}, \mathrm{O}^z_{tot}]$, representing the total spin or the total pseudospin and its z projection. Note, that since we are considering the spin-orbital chains with an even number of sites and the spin/pseudospin 1/2 degree of freedom on each of them, the values of O_{tot}, O^z_{tot} will be always integer.

Hence, in the product phases of the model (4.28) the ground state is a product of states taken from the set:

$$\{\text{singlet } |\mathrm{O}_{tot} = 0, \mathrm{O}^z_{tot} = 0\rangle,\ n\text{th multiplet } |\mathrm{O}_{tot} = \mathrm{O}^{max}_{tot}, \mathrm{O}^z_{tot} = n\rangle\}, \tag{4.29}$$

where O^{max}_{tot} is the maximal possible value of the total spin/pseudospin quantum number for a given chain of spins/pseudospins 1/2 and even number of sites, $n \in \{-\mathrm{O}^{max}_{tot}, -(\mathrm{O}^{max}_{tot} - 1), ..., +(\mathrm{O}^{max}_{tot} - 1), +\mathrm{O}^{max}_{tot}\}$, singlet represents the antiferro sector while multiplet—ferro sector of the product state. For simplicity, the ferro sectors in the product phases can be represented by the fully polarized states[12]. In contrast, the antiferromagnetic sectors are disordered and non-degenerate (only short-range order, as in the S = 1/2 Heisenberg chain). Both sectors can be solved analytically by the Bethe-Ansatz technique [131].

[12] i.e. $|\mathrm{O}_{tot} = \mathrm{O}^{max}_{tot}, \mathrm{O}^z_{tot} = \pm \mathrm{O}^{max}_{tot}\rangle$

The phases considered so far were simple product phases, where there was no quantum entanglement between the spin and orbital degrees of freedom. Now we move to the highly-nontrivial central phase, bearing the largest values of the spin-orbital entanglement in the whole phase diagram.

SU(4) singlet phase

We start the description of the central SU(4) singlet phase from the exactly solvable point $\alpha = \beta = 1/4$, lying on the analytical boundary with the dimerized phase (grey circle in Fig. 4.2). This is the point where the SU(2)$\otimes$ SU(2) Hamiltonian symmetry is upgraded to SU(4). In other words, the Hamiltonian at this point is invariant under any of the transformations generated by the operators $\mathrm{S}^{\epsilon}_{tot} = \sum_i \mathrm{S}^{\epsilon}_i$, $\mathrm{T}^{\epsilon}_{tot} = \sum_i \mathrm{T}^{\epsilon}_i$ and $\mathrm{Y}^{\epsilon\zeta} = \sum_i \mathrm{S}^{\epsilon}_i \mathrm{T}^{\zeta}_i$, $\epsilon, \zeta = x, y, z$, and their combinations [136].

At the SU(4) point one can solve the Hamiltonian analytically, e.g. by applying the Bethe Ansatz [139, 136], utilizing the approximation for low energies[13] or even applying the Majorana fermions [141]. We will now briefly summarize the ground state at the SU(4) point and then explain how the ground state in the whole phase is related to the emerging picture.

For chains of $4n$ sites the ground state is the SU(4) invariant singlet,[14] for which not only the total spin and total orbital quantum numbers are zero, but also the sum of the effective SU(4) pseudospins, to which the Hamiltonian can be reduced, vanishes. From a practical point of view this means that the correlations built out of the operators S^z_{tot},T^z_{tot}, and $\sum_i \mathrm{S}^z_i \mathrm{T}^z_i$ should disappear in this state [136].

Now it is time to move away from the SU(4) point. Obviously, by doing so we reduce the SU(4) symmetry to the SU(2)$\otimes$SU(2) one, but analytical and numerical (Density Matrix Renormalization Group, DMRG) inspection [140] suggests, that the ground state behaves as if the SU(4) symmetry was still intact, representing critical case of the state at the exact point [134]. The whole central region has the SU(4)-symmetric singlet ground state and gapless excitations. Importantly, the SU(4) singlet ground state has even stronger quantum fluctuations than the ones appearing in the SU(2) AF Heisenberg chain [142], because of the significant spin-orbital entanglement.

Dimerized phase

Again, we start the description from a special point, located at $\beta = \alpha = 3/4$ in Fig. 4.2. The Kolezhuk-Mikeska (KM) point has an exact, doubly-degenerate, gapped ground state [137], where each of the states has the spin-spin and orbital-orbital singlets arranged in a staggered way.

The KM state is an example of a broader class of states called the non-Haldane spin liquids [143], for which the magnon excitations are unstable [134], and which display the non-zero values of the dimer correlation, in contrast to the Haldane spin liquid of the spin S = 1 chain [133]. We can qualitatively imagine such staggered dimers when thinking of the whole dimerized phase, there are however few caveats one should be aware of: (i) although for $\alpha = \beta \gg J$ the magnons are unstable, they tend to stabilize for the region closer to the analytical boundary with the SU(4) singlet [134]; (ii) away from the KM point the spin-orbital entanglement appears, of the strenght depending on the ratio of α, β and J parameters.

The 1D case described above will serve as a starting point for our calculations, exploring the situation when the spin-orbital Kugel-Khomskii Hamiltonian is supplemented with the on-site spin-orbit coupling term. Chapter 5 explores this situation in detail.

[13] The so-called SU(4) Weiss-Zumino-Witten (WZW) theory [140]

[14] Table 1. in Ref. [138] contains the representations available for $4n$ and $4n + 2$ chains.

Chapter 5

Spin-orbital entanglement evolution with the on-site spin-orbit coupling

Part of the results presented in this chapter was published in two papers:

- [144] Dorota Gotfryd, Ekaterina M. Pärschke, Jiří Chaloupka, Andrzej M. Oleś, and Krzysztof Wohlfeld, *How spin-orbital entanglement depends on the spin-orbit coupling in a Mott insulator*, Phys. Rev. Research **2**, 013353 (2020).
- [145] Dorota Gotfryd, Ekaterina M. Pärschke, Krzysztof Wohlfeld, and Andrzej M. Oleś, *Evolution of Spin-Orbital Entanglement for Increasing Ising Spin-Orbit Coupling*, Condens. Matter **5**, 53 (2020).

5.1 Motivation

Spin-orbital entanglement in the strong SOC limit

The spin-orbital entanglement story described in Chapter 4, in which partially filled t_{2g} orbitals with weak Jahn-Teller orbital-lattice coupling [146, 124, 28, 147] provide the most optimal conditions for the entanglement to emerge, is far from being complete. In particular, the on-site spin-orbit coupling (SOC) of relativistic origin may influence the spin-orbital entanglement.

As already pointed out in Sec. 2.1.1, in heavier 4d and 5d transition-metal compounds the effective ionic spin-orbit coupling $\propto \lambda \mathbf{S}_i \cdot \mathbf{L}_{t_{2g}i}$, where $\mathbf{L}_{t_{2g}}$ is the orbital angular momentum operator projected to the t_{2g} subshell, can be quite strong, leading to the formation of the new local quantum numbers $\tilde{\mathrm{J}}_i$. Although in case of the iridates strong spin-orbit coupling lifts the orbital degeneracy[1] completely, making the Kramers doublet a ground-state level [4, 148], the effective Hamiltonian in $\tilde{\mathrm{J}}$ pseudospins may introduce the quantum-entangled phases depending on the bond geometry. Namely, for the case of 180° Ir-O-Ir angle of the corner-sharing octahedra in Sr_2IrO_4, the effective Hamiltonian has a dominant Heisenberg term [4], which may lead to quantum effects in certain parameter regimes. In contrast, the 90° Ir-O-Ir angle in Na_2IrO_3 leads to an effective Ising bond Hamiltonian. However, the honeycomb arrangement of the Ir-Ir bonds in the compound, results in a bond-anisotropic selection of those Ising terms, creating an effective Kitaev term with the highly entangled quantum spin-liquid ground state. The potential connection between this spatial entanglement in the effective pseudospins $\tilde{\mathrm{J}}$ and the spin-orbital entanglement requires further verification though. Our results on a much simpler, one-dimensional model [144, 145] may provide some hints on the above issue.

Key idea

Somewhat surprisingly, a systematic examination of the spin-orbital entanglement has focused so far on the negligible SOC limit, concerning mainly the 3d transition-metal oxides [28, 146], presented in detail in the previous chapter. Very few studies have explored the perturbation

[1] Important for spin-orbital entanglement.

by the SOC term in the context of the spin-orbital entanglement [133]. On the other hand, the dominant SOC limit,[2] discussed in the first two chapters of this thesis, seems to be also barely explored in this context.[3] Finally, the interpolation between the weak and the dominant spin-orbit coupling limit appears only in few studies [149, 150, 151, 152].

Our purpose is to interpolate between the weak and dominant SOC limits specifically to study the evolution of the spin-orbital entanglement in the ground state, and thus bring a deeper understanding of its aspects described above. We describe the problem in terms of the three questions [144]:

1. What kind of evolution does the spin-orbital entanglement develop with increasing spin-orbit coupling?

2. Can one always assume that in the limit of strong spin-orbit coupling the spin-orbital entanglement is indeed non-zero?

3. How does the spin-orbital entanglement arise in the limit of strong spin-orbit coupling?

We formulate a minimal model to address the above questions, hoping that our analysis will inspire more studies exploring all the above aspects, including the real materials.

5.2 Minimal low-energy model

Since we focus on the interpolation between the weak and dominant SOC limits, our minimal model is of composite form:

$$\mathcal{H} = \mathcal{H}_{\mathrm{SE}} + \mathcal{H}_{\mathrm{SOC}}, \tag{5.1}$$

where $\mathcal{H}_{\mathrm{SE}}$ represents a spin-orbital term of the Kugel-Khomskii type, typically derived from the superexchange virtual processes [146], while $\mathcal{H}_{\mathrm{SOC}}$ stands for the on-site spin-orbit coupling term. Such a straight forward approach in principle allows for a systematic examination of the evolution of the spin-orbital entanglement with the on-site SOC. However, with the spin and orbital degrees of freedom explicitly present in the Hamiltonian, the size of the Hilbert space can grow rapidly. Therefore, one has to carefully choose $\mathcal{H}_{\mathrm{SE}}$ and $\mathcal{H}_{\mathrm{SOC}}$ terms to balance the relevance for real materials with the computational availability.

For the S = T = 1/2 spin and pseudospin (orbital) quantum numbers on every site, we selected the SU(2)⊗SU(2) symmetric Kugel-Khomskii term

$$\mathcal{H}_{\mathrm{SE}} = J \sum_i \left[(\mathbf{S}_i \cdot \mathbf{S}_{i+1} + \alpha)(\mathbf{T}_i \cdot \mathbf{T}_{i+1} + \beta) - \alpha\beta \right], \tag{5.2}$$

described in detail in Sec. 4.2.1, and the on-site spin-orbit coupling term of the Ising type

$$\mathcal{H}_{\mathrm{SOC}} = 2\lambda \sum_i \mathrm{S}_i^z \mathrm{T}_i^z. \tag{5.3}$$

The choice of the SU(2) symmetry in the orbital sector of the $\mathcal{H}_{\mathrm{SE}}$ term was motivated by the existence of the robust spin-orbitally entangled region, guaranteed by the $J\,(\mathbf{S}_i \cdot \mathbf{S}_{i+1})\,(\mathbf{T}_i \cdot \mathbf{T}_{i+1})$ term when the positive superexchange coupling J dominates over $|\alpha|$ and $|\beta|$, as well as a very good understanding of the model phase diagram (cf. Sec. 4.2.1). The above features make the SU(2)⊗SU(2) symmetric $\mathcal{H}_{\mathrm{SE}}$ an interesting starting point for further extensions.

[2] Over the Kugel-Khomskii superexchange J.

[3] The only related case we are aware of discusses the spatial entanglement of the spin 1/2 ladder with the Heisenberg interaction on legs and rungs as well as the four-spin interaction mathematically equivalent to $(\mathbf{S}_i \cdot \mathbf{S}_j)\,(\mathbf{T}_i \cdot \mathbf{T}_j)$. As we will show in a moment, we are considering a case with a different type of spin-orbit coupling.

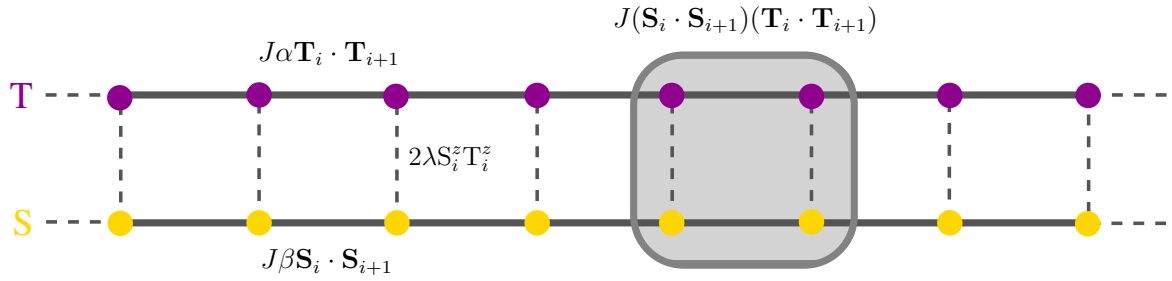

FIGURE 5.1: The spin-orbital chain with periodic boundary conditions. Compared with Fig. 4.1, the spin-orbit coupling interaction has been added on the rungs.

The Ising spin-orbit coupling may seem an unintuitive choice, yet such anisotropic spin-orbit coupling terms have appeared in literature for certain systems [147, 153]. Namely, they may arise if the bond geometry and other conditions allow to reduce the SOC term, by removing the inactive orbitals. This results in the reduced $\mathcal{H}_{\mathrm{SOC}}$ forms: $2\lambda \sum_i \mathrm{S}_i^x \mathrm{T}_i^y$ for YVO_3 [147][4] and $2\lambda \sum_i \mathrm{S}_i^z \mathrm{T}_i^y$ for KO_2 [153].[5] Local mixing of two out of three orbitals can be also shown by a special type of the zigzag optical chains emulating the spin-orbital interactions, including the mixing of p^x and p^y or xy and yz orbitals [156].

Because the Kugel-Khomskii term (5.2) is SU(2)⊗SU(2) symmetric, replacing formula (5.3) by any term of the type $2\lambda \sum_i \mathrm{S}_i^\gamma \mathrm{T}_i^\delta$ in formula (5.1) would produce results equivalent to the ones we will be presenting, up to the suitable rotations in the the spin/orbital subspaces. Formula (5.3) looks the most elegant of them all. Although this anisotropic spin-orbit coupling is the simplest possible, we will show that it brings highly non-trivial effects.

Some details concerning the geometry

In order to accommodate both spin S and effective orbital momentum (pseudospin) T in the numerical studies, Hamiltonian (5.1) is applied to the simplest system: the spin-orbital chain with periodic boundary conditions (PBC). Interestingly, the chain, shown in Fig. 5.1, which has $\mathrm{S} = \mathrm{T} = 1/2$ quantum numbers on every site, is also mathematically equivalent to a spin-1/2 ladder with properly chosen interactions.

5.3 Methods

When considering various approaches to the quantum entanglement it is essential to chose a method which does not compromise the possible quantum fluctuations in the system. Naturally, the best option would be to solve the problem analytically. However, for example Bethe anzatz is applicable only in selected manifolds of the phase diagram in Fig. 4.2. Among the considered numerical methods, exact diagonalization (ED, see Sec. 3.2.1) is both easy to apply in the whole parameter range and relatively unbiased, compromising only the long-range quantum effects through the periodic boundary conditions (PBC). However, intuitively in the *ground state* we

[4] Specifically, for this partially filled t_{2g} system the already reduced form $2\lambda \sum_i (\mathrm{S}_i^x \cos\phi_i + \mathrm{S}_i^z \sin\phi_i)\, \mathrm{T}_i^y$ further reduces to $2\lambda \sum_i \mathrm{S}_i^x \mathrm{T}_i^y$ in an idealized case for the tilting of the VO_6 octahedron at site i, $\phi_i = 0$ [147].

[5] The material belongs to the so-called alkali hyperoxides, for which virtual hoppings building the effective Hamiltonians concern O_2-AM-O_2 bonds [154, 155], where O_2 is a moloecular oxygen ion and AM is an alkali metal. The local SOC matrix presented in Ref. [153] has the form $i\lambda \sum_i \mathrm{S}_i^z (|p_i^y\rangle\langle p_i^x| - |p_i^x\rangle\langle p_i^y|) = i\lambda \sum_i \mathrm{S}_i^z (\mathrm{T}_i^- - \mathrm{T}_i^+)$ in the basis of the p^x and p^y orbitals building the antibonding configuration of O_2. This can be rewritten as $2\lambda \sum_i \mathrm{S}_i^z \mathrm{T}_i^y$.

generally expect rather local entanglement effects, following from the interplay of the nearest-neighbor $\mathcal{H}_{\rm SE}$ and the on-site $\mathcal{H}_{\rm SOC}$ terms as well as reduced dimensionality.

In order to properly capture the entanglement in the critical SU(4)-singlet state for model (5.1) we restrict ourselves to the $\mathrm{L} = 4n$-site chains.[6] ED enabled numerical studies from $\mathrm{L} = 4$ up to $\mathrm{L} = 20$ sites for the selected points. While 4 sites were easily accessible for the full ED procedure, we opted for the Lanczos method [82] for the larger systems. Such versatility made the method a good choice for first (to our best knowledge) such a thorough study of the spin-orbital entanglement.

5.3.1 Entanglement-related observables

In the ED-based ground state we evaluate several observables relevant for the model, out of which two estimate the spin-orbital entanglement. Namely, we accommodate the entanglement entropy of the von Neumann type, described in detail in Sec. 4.1.3,

$$\mathcal{S}_{\rm vN} = -\frac{1}{\mathrm{L}} Tr_{\rm S} \left(\rho_{\rm S} \ln \rho_{\rm S}\right), \tag{5.4}$$

to the spin and orbital subspaces. In a nutshell, the reduced density matrix

$$\rho_{\rm S} = Tr_{\rm T}\rho, \tag{5.5}$$

describes a mixed state in the spin subspace if the original state in the full Hilbert space is entangled, ensuring a non-zero, positive value of the entanglement entropy.

Independently, we utilize the intersite spin-orbital correlation,

$$\mathcal{C}_{\rm SO} = \frac{1}{\mathrm{L}} \sum_i \left[\langle (\mathbf{S}_i \cdot \mathbf{S}_{i+1}) (\mathbf{T}_i \cdot \mathbf{T}_{i+1})\rangle - \langle \mathbf{S}_i \cdot \mathbf{S}_{i+1}\rangle \langle \mathbf{T}_i \cdot \mathbf{T}_{i+1}\rangle\right], \tag{5.6}$$

which literally estimates the difference between a fully quantum $(\mathbf{S}_i \cdot \mathbf{S}_{i+1})(\mathbf{T}_i \cdot \mathbf{T}_{i+1})$ term and its mean-field decoupling into the spin and orbital sectors [28]. Hence, it is sensitive to the spin-orbital entanglement within nearest neighbors. Several examples in the literature, see Refs. [157, 158], have already proven its usefulness in exploring the spin-orbital entanglement for the superexchange-related systems.

5.3.2 Other observables

To capture other aspects of the evolution in the spin-orbit coupling λ we utilize the full intersite spin-spin and orbital-orbital nearest-neighbor correlation functions

$$S = \frac{1}{\mathrm{L}} \sum_i \langle \mathbf{S}_i \cdot \mathbf{S}_{i+1}\rangle, \tag{5.7}$$

$$T = \frac{1}{\mathrm{L}} \sum_i \langle \mathbf{T}_i \cdot \mathbf{T}_{i+1}\rangle. \tag{5.8}$$

Since the SU(2)⊗SU(2) symmmetric $\mathcal{H}_{\rm SE}$ term treats the spin and orbital degrees of freedom equally, we expect the complementary behaviour of the above functions.

[6] For a $4n$ site chain the ground state is not degenerate, highly simplifying the numerical efforts, for a $4n+2$ chain the ground state is degenerate, see Sec. 4.2.1.

We also thoroughly monitor the anisotropic effects possibly introduced by the Ising SOC via the partial nearest-neighbor correlation functions

$$S^{\gamma\gamma} = \frac{1}{\mathrm{L}} \sum_i \langle \mathrm{S}_i^\gamma \mathrm{S}_{i+1}^\gamma \rangle \tag{5.9}$$

and

$$T^{\gamma\gamma} = \frac{1}{\mathrm{L}} \sum_i \langle \mathrm{T}_i^\gamma \mathrm{T}_{i+1}^\gamma \rangle, \tag{5.10}$$

where $\gamma \in \{x, y, z\}$, as well as the partial on-site correlation functions

$$\mathcal{O}_{\mathrm{SO}}^{\eta\zeta} = \frac{1}{\mathrm{L}} \sum_i \langle \mathrm{S}_i^\eta \mathrm{T}_i^\zeta \rangle, \tag{5.11}$$

where $\eta, \zeta \in \{x, y, z\}$. As already mentioned in Sec. 4.2.1, the operators in the latter functions belong to the set of generators of the SU(4) group. Among them, $\mathcal{O}_{\mathrm{SO}}^{zz}$ function, which we will from now on call $\mathcal{O}_{\mathrm{SO}}$ for simplicity,

$$\mathcal{O}_{\mathrm{SO}} = \frac{1}{\mathrm{L}} \sum_i \langle \mathrm{S}_i^z \mathrm{T}_i^z \rangle, \tag{5.12}$$

conveniently monitors the response of the system to the Ising SOC (5.3).

5.4 Global results

First, we explore the global evolution of the spin-orbital entanglement, examining the entanglement entropy calculated in the ground state of Hamiltonian (5.1) in a broad parameter range. Fig. 5.2 (a) reproduces the spin-orbital entanglement for $\lambda = 0$ for 4 sites. As expected, the spin-orbital entanglement is absent in the product AF⊗FO, FM⊗FO and FM⊗AO phases (as evidenced by the zero entropy values represented by the darkest blue in the second, third and fourth quadrant of the Fig. 5.2 (a))[7] and is finite, although strongly decreasing, in the dimerized phase in the first quadrant. Entropy reaches significant values only in the central part of the map, due to the dominance of the $(\mathbf{S}_i \cdot \mathbf{S}_{i+1})\,(\mathbf{T}_i \cdot \mathbf{T}_{i+1})$ term when $|\alpha|$ and $|\beta|$ are sufficiently small. Such conditions allow the critical SU(4) singlet state to occupy a finite region beyond the exact SU(4) point at $\alpha = \beta = 1/4$. For completeness, we note that the entropy slope and the border between the critical SU(4) singlet and dimerized phases is system-size dependent [see Fig. B.1 (a) for a comparison with the 12-site case], in agreement with the literature [132, 133] and seemingly approaching analytical boundary visible in Fig. 4.2. The situation does not change much for small λ values illustrated in Fig. 5.2 (b).

A completely different picture emerges in the limit of $\lambda \to \infty$ [Figs. 5.2 and B.1 (c)], where the significant values of entropy, larger than in the $\lambda = 0$ case, occupy an entire "stripe" approximately defined by $-\frac{1}{2} \leq \alpha + \beta \leq 2$. While the lower boundary of the stripe is sharp and system-size dependent, the upper boundary shrinks with the system size.[8] In Sec. 5.7 we will present the analytical and numerical justification of this behaviour. Above this "quantum stripe", for the examined 4, 8 and 12 sites the spin-orbital entanglement is still non-zero, but uniform and decreasing with the system size. Interestingly, the entanglement value is approximately stable along the lines of constant $\alpha + \beta$.

[7] The convention for the quadrants is identical to the quadrant convention for the Cartesian coordinate system known from basic mathematics, i.e. the first quadrant has both coordinates positive.

[8] Verified for 4, 8 and 12-site chains.

A natural question arising from the analysis of Figs. 5.2 (a)-(c) is how the system evolves from Fig. 5.2 (a)-(b) to Fig. 5.2 (c). Figs. 5.2 (d)-(i) interpolate between the above contrasting cases, supplementing them with the intermediate stages of the entanglement evolution. They reveal that significant entropy values, originally restricted to the central region, increase even further and gradually spread out with the growing λ, eventually forming the "quantum stripe" for sufficiently large spin-orbit coupling. In particular, infinitesimal entropy values appear on the boundaries of the previously strictly AF$\otimes$FO and FM$\otimes$AO phases as soon as $\lambda > 0$, clearly visible from Fig. 5.2 (e) on.

In contrast, the FM$\otimes$FO phase does not dress in the spin-orbital entanglement, for the latter cannot be easily induced in this classical[9] state by the also classical SOC. A sharp boundary, at first restricting the classical state to the third quadrant of Fig. 5.2 (b), gradually moves, enabling a much wider classical region in Fig. 5.2 (i), already quite close to the classical triangle visible in Fig. 5.2 (c).

Summing up, Fig. 5.2 reveals that the *global* evolution of the spin-orbital entanglement is gradual but highly nontrivial. The entanglement is spreading in some regions of $\{\alpha, \beta\}$ while disappearing from others with increasing spin-orbit coupling. Thus, the road the state shown in Fig. 5.2 (c), where the spin orbital entanglement emerges and even becomes substantial in regions not affected by this type of entanglement for $\lambda = 0$, is not straight forward. Moreover, the intermediate slices of the global evolution show that while in some regions of $\{\alpha, \beta, \lambda\}$ the entanglement evolves in a continuous way, in some parts sharp boundaries are visible as well.

A question whether one can reasonably define a boundary λ_{CRIT} separating phases of different physical properties seems worth considering. To this end, we selected two representative cuts in $\{\alpha, \beta, \lambda\}$ parameter space, along the lines $\alpha + \beta = 0$ and $\alpha + \beta = -1$, marked as the diagonal white dashed and red dashed lines in Fig. 5.2, correspondingly. In the upcoming sections, we analyse in great detail the evolution in λ along the above lines, searching for the answers why the spin-orbital entanglement can spread, but also be suppressed for $\lambda \to \infty$. On each line we attempt to set λ_{CRIT}, defining it as a single value or an entire interval when necessary. Then, we discuss the global evolution again, inspecting Fig. 5.2 with more insight.

5.5 Evolution along the $\alpha + \beta = 0$ line

When $\lambda = 0$ the selected $\alpha + \beta = 0$ line crosses both the FM$\otimes$AO/AF$\otimes$FO product phases and the spin-orbitally entangled critical SU(4)-singlet phase. As shown in Fig. 5.2, the spin-orbital entanglement increases and spreads significantly along the line with the growing λ. As a result, in Fig. 5.2 (c) the line lies within the "quantum stripe" of the high entanglement values in the limit of $\lambda \to \infty$. To better understand this trend, in Fig. 5.3 we directly analyse the entanglement evolution in λ, utilizing the logarithmic scale to display several orders of magnitude in a compact way. We monitor the entanglement entropy $\mathcal{S}_{\mathrm{vN}}$, sensitive to the total spin-orbital entanglement, as well as the $\mathcal{C}_{\mathrm{SO}}$ correlation function (formula (5.6)) for the spin-orbital entanglement restricted to the nearest neighbors. We also monitor the response of the system to the Ising spin-orbit coupling via the $\mathcal{O}_{\mathrm{SO}}$ correlation (formula (5.12)). [Note, that we base the observations below on results for L = 4, 8 and 12-site chains presented in Figs.B.3, 5.3, and B.4, respectively.]

Already from the $\{\alpha, \lambda\}$ maps in the representative $\alpha \in [-1, 1]$ interval, presented in Fig. 5.3 (a)-(b), one can draw quite general conclusions, distinguishing three regimes of the spin-orbital entanglement:

1. Two regions in the $\{\alpha, \lambda\}$ parameter space for which the entanglement entropy and the $\mathcal{C}_{\mathrm{SO}}$ correlation function are vanishingly small, located symmetrically at $|\alpha| \gtrsim 0.1$ and $\lambda/J \lesssim 10^{-1}$-$10^{0}$, characterized by the dark-blue color in Fig. 5.3 (a)-(b).

[9] If one considers polarized states as the simplest.

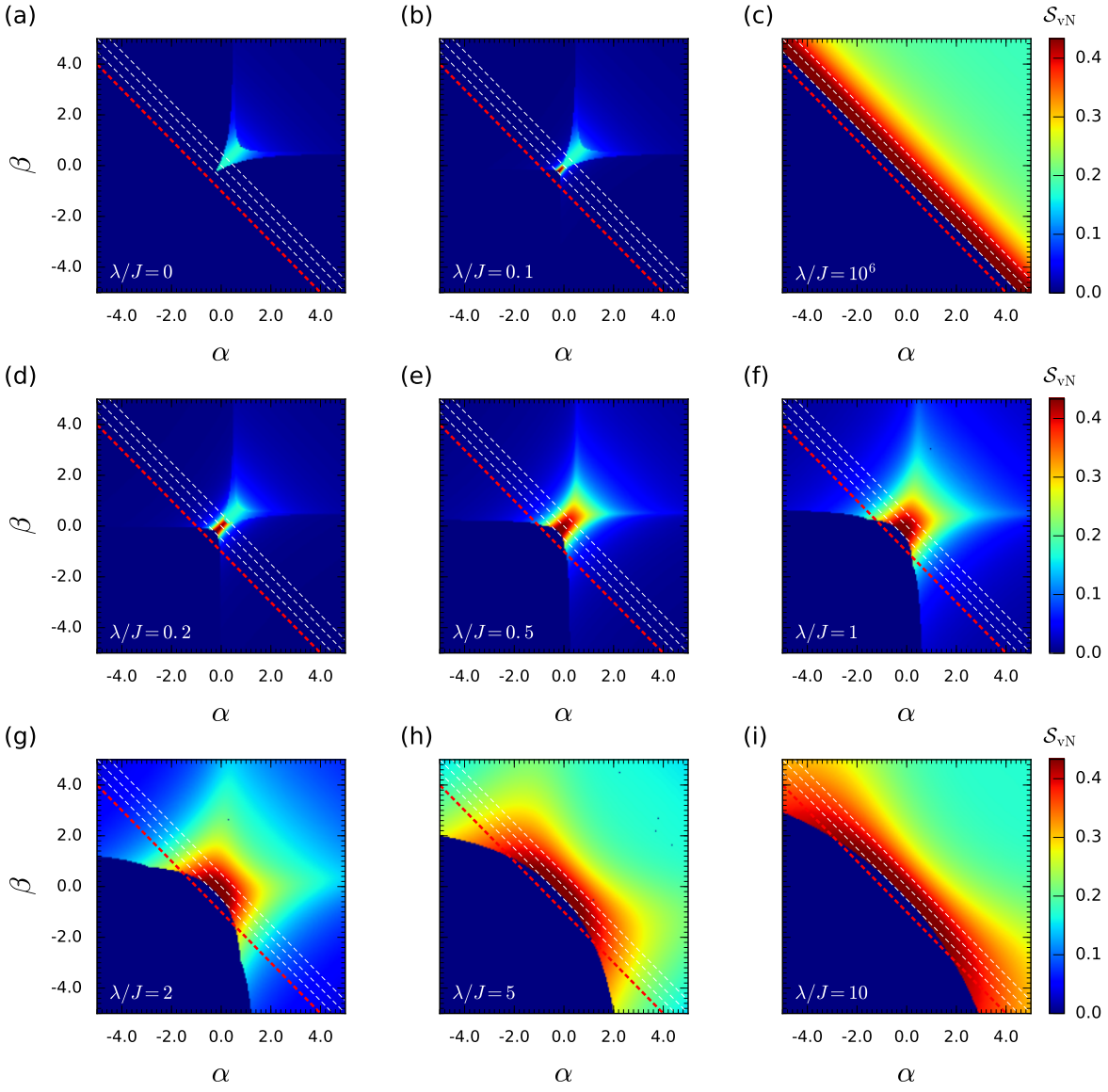

FIGURE 5.2: Evolution of the spin-orbital entanglement entropy of the von Neumann type (5.4) as a function of the on-site spin-orbit coupling parameter λ, calculated in the ground state of the 4-site chain. Panels depict the $\{\alpha, \beta\}$ slices for the representative values of λ/J. Panels (a) and (b) capture the spin-orbital entanglement for the negligible λ values, in contrast to panel (c), where the dominant λ limit is shown. Panels (d)-(i) show intermediate stages between (b) and (c). The white dashed lines represent (from the left to the right) the hidden FM Heisenberg, XY, AF Heisenberg models emerging in the dominant λ limit for $\alpha + \beta = -1/2$, $\alpha + \beta = 0$ and $\alpha + \beta = 1/2$, respectively. Finite uniform entanglement (light green) above the dashed lines appears on panel (c) due to the finite-size effects. Similarly, for longer chains the "quantum stripe" (red region around the diagonal $\alpha + \beta = 0$ line) would better fit within the two outer white dashed lines, see Fig. B.1 for a comparison with the 12-site case. The red dashed $\alpha + \beta = -1$ line is representative for the disappearing spin-orbital entanglement in the lower-left part of the slices for the dominant λ parameter. Figure has been published in Ref. [145].

2. The dark-red region with the maximal entropy values, dominating the top part of the map, restricted by $\lambda/J \gtrsim 10^{-1}$-$10^{1}$ for all α values visible in the figure.

3. The "T-shaped" region for which the entropy is neither negligible nor maximal, situated in between cases 1. and 2.

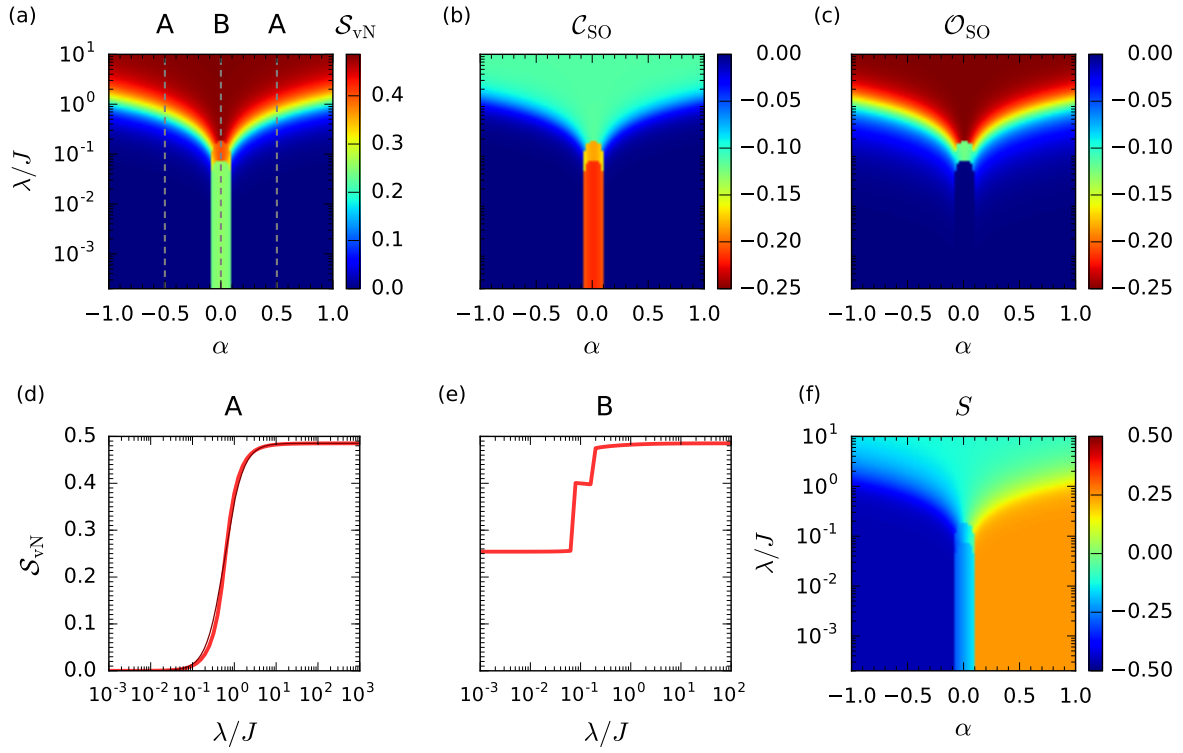

FIGURE 5.3: The evolution of the spin-orbital entanglement with increasing spin-orbit coupling parameter λ along the $\alpha + \beta = 0$ line. The entanglement entropy and selected correlation functions were calculated in the ground state of Hamiltonian (5.1) for the 8-site chain: (a)—the entanglement entropy ($\mathcal{S}_{\mathrm{vN}}$) map in $\{\alpha, \lambda\}$; (b), (c)—analogical maps of the nearest-neighbor spin-orbital correlation ($\mathcal{C}_{\mathrm{SO}}$) and the on-site spin-orbital correlation ($\mathcal{O}_{\mathrm{SO}}$); (d)—the evolution of the entanglement entropy along cut A through the map shown on panel (a) at $|\alpha| = 0.5$, fitted with the logistic function (black thin line); (e)—the evolution of the entanglement entropy along cut B at $|\alpha| = 0$; (f) the map of the spin nearest-neighbor correlation function S in $\{\alpha, \lambda\}$. All the maps are restricted to the representative $\alpha \in [-1, 1]$ interval. The shape of the phase boundaries is dependent on the logarithmic scale of λ. Analogous evolution for the 4 and 12-site chains can be found in Figs. B.3 and B.4, respectively.

Noticeably, the region no 3. is not uniform. It consists of a subregion with the non-zero entropy values for $|\alpha| \lesssim 0.1$ increasing in discrete steps, see also Figs. B.3, B.4, and two "rainbow" subregions of continuous entropy growth. The different character of these intermediate stages calls for a more detailed examination.

To understand the onset of this complex behaviour we inspect two representative cuts through these qualitatively different cases of the entanglement evolution in λ: cut A for $|\alpha| = 0.5$ and cut B for $\alpha = 0$, indicated with the dashed lines in Fig. 5.3 (a).

5.5.1 From AF $\otimes$ FO/FM $\otimes$ AO to the highly entangled state

Spin-orbital entanglement evolution

First, we analyse the evolution of the entanglement along cut A of Fig. 5.3 (a) when $|\alpha|$ is fixed to 0.5 and only the spin-orbit coupling is being tuned. Fig. 5.3 (d) presents a continuous increase of the spin-orbital entanglement entropy along the cut, which can be described by a logistic function in the logarithmically scaled λ/J.[10]

[10]The sigmoid curve $f = A\frac{1}{1+exp(-k(x-x_0))}$, $x = log_{10}\lambda$ has been fitted with parameters: $A \approx 0.485$—the maximal entropy for 8 sites for $\{\lambda = 10^6, \alpha = \beta = 0\}$; $k = 4.56$; $x_0 = -0.23$.

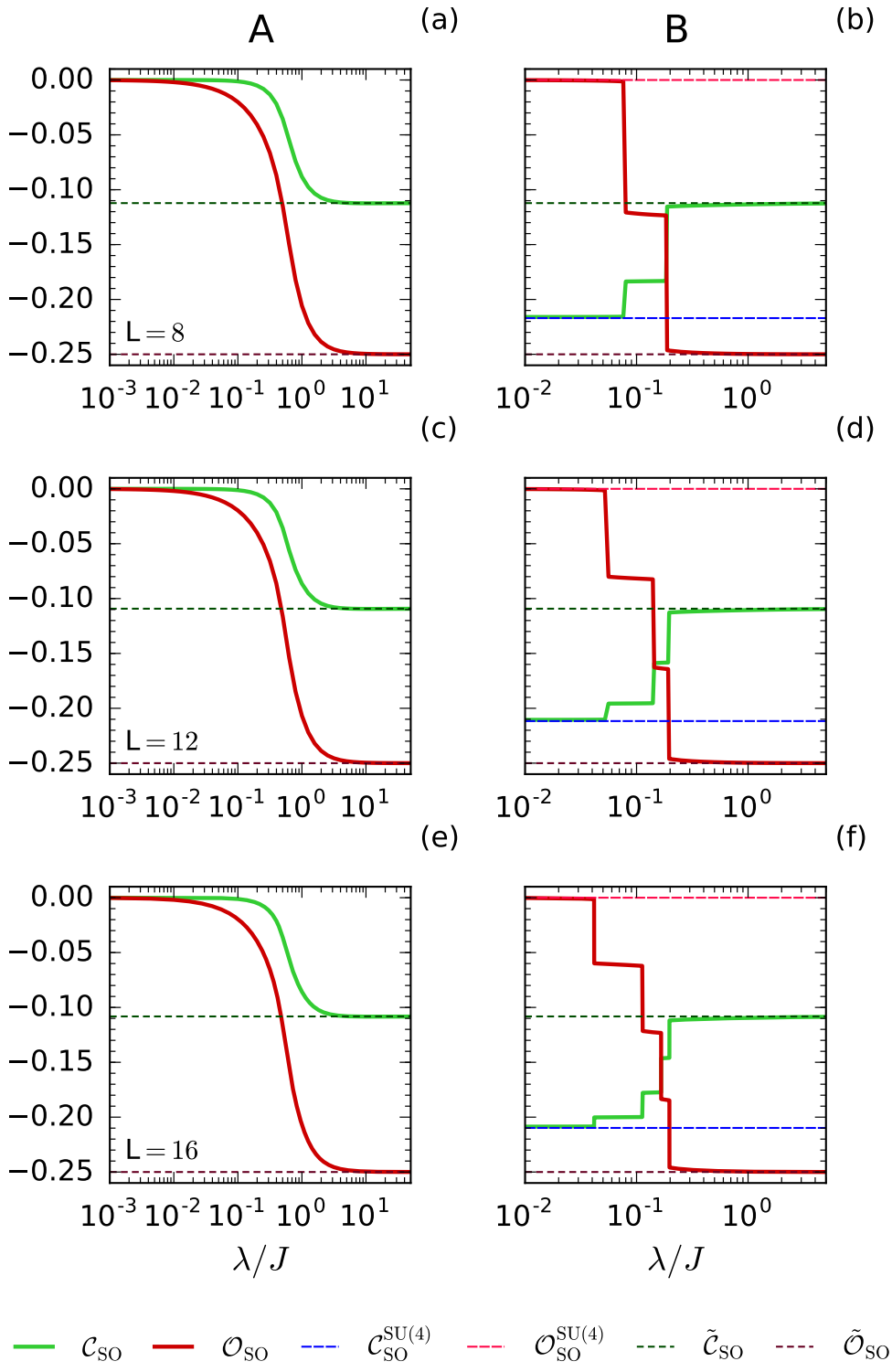

FIGURE 5.4: Trends in the nearest-neighbor spin-orbital correlation $\mathcal{C}_{\rm SO}$ (thick light-green line) and the on-site spin-orbit correlation $\mathcal{O}_{\rm SO}$ (thick red line) along cuts A at $\alpha = +0.5$, $\beta = -0.5$ [panels (a), (c), (e)] and B at $\alpha = \beta = 0$ [panels (b), (d), (f)], where rows represent progresively larger periodic chains of length L $= 4n$ sites. Top row yields results for $L = 8$, middle for $L = 12$, and bottom for $L = 16$ sites. Not shown results for 4 sites fit into the presented tendencies. The dashed lines represent the asymptotic values of the above functions in: (i) the exact SU(4)–point limit $\lambda = 0$, $\alpha = \beta = +0.25$, denoted by $\mathcal{C}_{\rm SO}^{\rm SU(4)}$ and $\mathcal{O}_{\rm SO}^{\rm SU(4)}$ (blue and light–red dashed lines, respectively); (ii) the $\lambda = \infty$, $\beta + \alpha = 0$ XY limit denoted by $\tilde{\mathcal{C}}_{\rm SO}$ and $\tilde{\mathcal{O}}_{\rm SO}$ (dark-green and dark-red dashed lines, respectively). Figure has been published in Ref. [144].

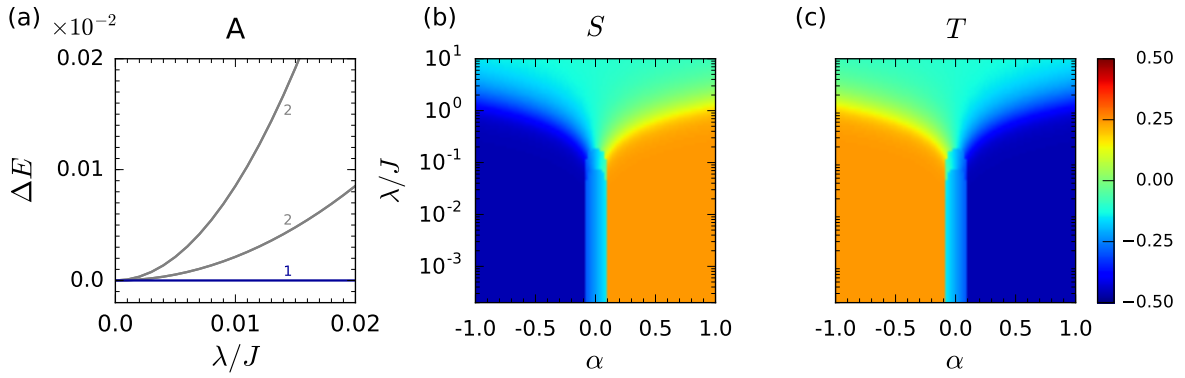

FIGURE 5.5: Energetics and magnetic properties of the ground state along the $\alpha + \beta = 0$ line. Panel (a)—splitting of the 5-fold degenerate ground-state energy level of the 4-site chain for $\lambda > 0$ on cut A, shown via energy differences $\Delta \mathrm{E} = \mathrm{E}_i - \mathrm{E}_0$, with degeneracy of each level denoted by a number. Panels (b)-(c)—$\{\alpha, \lambda\}$ maps of S 5.7 and T 5.8 nearest-neighbor correlation functions for 8-site chain on the $\alpha + \beta = 0$ line restricted to the representative $\alpha \in [-1, 1]$ interval. The shape of the phase boundaries is dependent on the logarithmic scale of λ.

Such logistic growth of the spin-orbital entanglement can be divided into three stages: the infinitesimally small entropy values up to $\lambda/J \lesssim 10^{-1}$, the rapid[11] growth for $\lambda/J \in (10^{-1}, 10^{1})$, and the saturated values for $\lambda/J \gtrsim 10^{1}$. $\mathcal{C}_{\mathrm{SO}}$ correlation, indicated as a thick green line in Fig. 5.4, also experiences continuous change, similar for different system sizes [panels (a), (c), (e) for 8, 12, 16 sites, correspondingly].[12] In particular, the comparison of Figs. B.3, 5.3, B.4 (d) and 5.4 (a), (c), (e) shows that the extent of the three stages of logistic evolution is system-size independent for both the entropy and $\mathcal{C}_{\mathrm{SO}}$ with a good approximation, thus we may expect such behaviour also in the thermodynamic limit. Moreover, it allows us to approximately define λ_{CRIT} for cut A as an interval of rapid growth of the spin-orbital entanglement: $\lambda_{\mathrm{CRIT}}/J \in (10^{-1}, 10^{1})$.[13]

Focusing on the ground state properties for $\lambda < \lambda_{\mathrm{CRIT}}$, we observe that in this interval the system is quite resistent to the on-site spin-orbit coupling, returning only negligible values of $\mathcal{O}_{\mathrm{SO}}$ correlation [dark blue color in Fig. 5.3 (c) as well as the infinitesimal values of the thick red curve in Figs. 5.4 (a), (c), (e)]. The weak response to the spin-orbit coupling for small λ coincides with the negligible spin-orbital entanglement, not present in the ground state for $\lambda = 0$. In order to understand how even an infinitesimal spin-orbital entanglement could appear below λ_{CRIT} due to the classical SOC we inspect the magnetic properties and energetics along cut A.

Magnetic evolution

Crucially, the *overall* magnetic properties of the system, monitored by the full nearest-neighbor spin S and orbital T correlation functions (5.7)-(5.8), reveal strong similarity to the $\lambda = 0$ case. By following Figs. B.3, 5.3, B.4 (f) and 5.5 (b) at $\{\alpha = +0.5, \beta = -0.5\}$, one notices that $S \simeq +0.25$ for $\lambda \lesssim \lambda_{\mathrm{CRIT}}$ independently of the system size, indicating that the system still behaves like a ferromagnetic chain in the spin sector. In contrast, the values of the T correlation reach $\simeq -0.5$, -0.46 and -0.45 for the L = 4, 8 and 12-site chains, correspondingly, which is quite close to the analytical value -0.44 provided by the AF Bethe Ansatz. A map of the T correlation for 8 sites is shown in Fig. 5.5 (c). For the complementary case of $\{\alpha = -0.5, \beta = +0.5\}$

[11] In logarithmic scale.

[12] The unshown result for 4 sites also agrees with this tendency.

[13] We note though that the interval boundaries will shift up for higher values of $|\alpha|$ exceeding the borders shown in Fig. 5.3.

TABLE 5.1: Spin correlations in the eigenstates of the two-site Heisenberg model.

	$\|S_{tot}=0, S^z_{tot}=0\rangle$	$\|S_{tot}=1, S^z_{tot}=-1\rangle$	$\|S_{tot}=1, S^z_{tot}=0\rangle$	$\|S_{tot}=1, S^z_{tot}=+1\rangle$
$\langle S^x_1 S^x_2\rangle$	-0.25	0	+0.25	0
$\langle S^y_1 S^y_2\rangle$	-0.25	0	+0.25	0
$\langle S^z_1 S^z_2\rangle$	-0.25	+0.25	-0.25	+0.25
$\langle \mathbf{S}_1 \cdot \mathbf{S}_2\rangle$	-0.75	+0.25	+0.25	+0.25

the full spin and orbital correlations exchange values, so that the spin sector behaves like an antiferromagnetic and orbital sector—like a ferro-orbital chain. The above behaviour indicates that the regions below λ_{CRIT} qualitatively resemble the phases obtained in the limit of $\lambda = 0$: FM⊗AO/AF⊗FO for $\alpha = 0.5$ /-0.5, respectively.

However, the partial nearest-neighbor correlation functions $S^{\gamma\gamma}$ and $T^{\gamma\gamma}$ [formulae (5.9)-(5.10)] display an anisotropic behaviour, visible in Figs. 5.6(a), (c), (e) for $\lambda > 0$ for the $\alpha = +0.5$ case. In particular, for $\lambda/J \lesssim 3 \cdot 10^{-1}$ a partial anisotropy exists, concerning the ferromagnetic spin sector, whereas the strongly antiferro $T^{\gamma\gamma}$ correlations are isotropic. The anisotropy distinguishes the ferromagnetic values of the planar $S^{\delta\delta}$ correlations (where $\delta = x, y$) from the antiferromagnetic values of S^{zz}.

2-site toy model

To understand what happens, it is instructive to recall the 2-site case of the Heisenberg model. The eigenstates of the model consist of an antisymmetric, non-degenerate singlet state

$$|S_{tot}=0, S^z_{tot}=0\rangle = \frac{1}{\sqrt{2}}\left(|\uparrow_1\downarrow_2\rangle - |\downarrow_1\uparrow_2\rangle\right), \tag{5.13}$$

characterized by $S_{tot} = 0$, and three states representing the $S_{tot} = 1$ level

$$|S_{tot}=1, S^z_{tot}=-1\rangle = |\downarrow_1\downarrow_2\rangle, \tag{5.14}$$

$$|S_{tot}=1, S^z_{tot}=0\rangle = \frac{1}{\sqrt{2}}\left(|\uparrow_1\downarrow_2\rangle + |\downarrow_1\uparrow_2\rangle\right), \tag{5.15}$$

$$|S_{tot}=1, S^z_{tot}=+1\rangle = |\uparrow_1\uparrow_2\rangle. \tag{5.16}$$

While the $|S_{tot}=1, S^z_{tot}=\pm1\rangle$ states are of the purely product type, both the $|S_{tot}=0, S^z_{tot}=0\rangle$ and $|S_{tot}=1, S^z_{tot}=0\rangle$ states are legitimately entangled the latter called a *quadrupolar* state.[14]

Table 5.1 provides the values of the spin correlations in the above states. While in the singlet state the total spin correlation $S = \langle \mathbf{S}_1 \cdot \mathbf{S}_2\rangle = -0.75$[15] can be evenly decomposed into $\langle S^\gamma_1 S^\gamma_2\rangle = -0.25$, $\gamma = x, y, z$, for the triplet state the situation is more complex. In the product states the only non-zero correlation follows the polarization along the z axis. Contrastingly, in the quadrupolar state the planar correlations are ferromagnetic while $\langle S^z_1 S^z_2\rangle$ is antiferromagnetic. Nevertheless, the quadrupolar case still sums up to $\langle \mathbf{S}_1 \cdot \mathbf{S}_2\rangle = +0.25$.[16]

[14] See Sec. 4.1.1.

[15] In the case of the AF Heisenberg interaction, the $\langle \mathbf{S}_1 \cdot \mathbf{S}_2\rangle = -0.75$ value in a singlet ground state fits into the pattern converging to the Bethe Ansatz with the growing chain size. The FM case is size-independent for the correlations per bond.

[16] If we average $\langle S^\gamma_1 S^\gamma_2\rangle$ over the whole triplet level, we would loose this internal structure, obtaining isotropic $\langle S^\gamma_1 S^\gamma_2\rangle = +0.25$. This is what we refer to in Ref. [144].

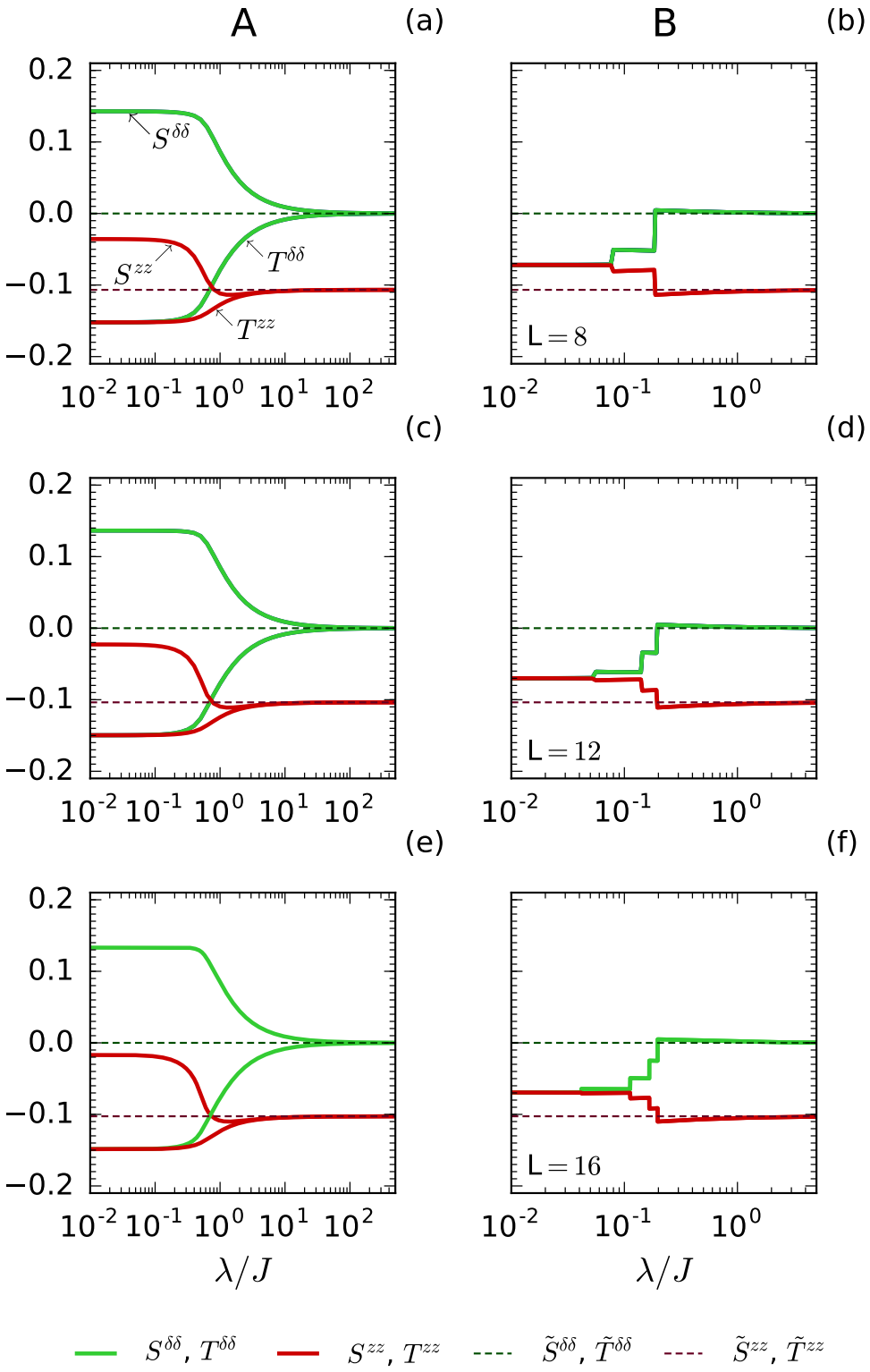

FIGURE 5.6: The evolution of the partial spin $S^{\gamma\gamma}$ 5.9 and orbital $T^{\gamma\gamma}$ 5.10 correlation functions in λ, where $\gamma = x, y, z$. The results for the representative cut A at $\{\alpha = +0.5, \beta = -0.5\}$ are shown on panels (a), (c), (e) for the progressively larger chains of L = 8, 12 and 16 sites. The results for cut B at $\alpha = \beta = 0$ are displayed on panels (b), (d), (f) in an identical manner. The planar $S^{\delta\delta}$ and $T^{\delta\delta}$ components, where $\delta = x, y$, are marked by the green color, while the S^{zz} and T^{zz} components are denoted in red, see also panel (a). Asymptotic values of the functions in the limit $\lambda = \infty$ are indicated by the dark-green dashed lines for $\tilde{S}^{\delta\delta}$, $\tilde{T}^{\delta\delta}$ and the dark-red dashed lines for $\tilde{S}^{zz}$, $\tilde{T}^{zz}$. Figure has been published in Ref. [144].

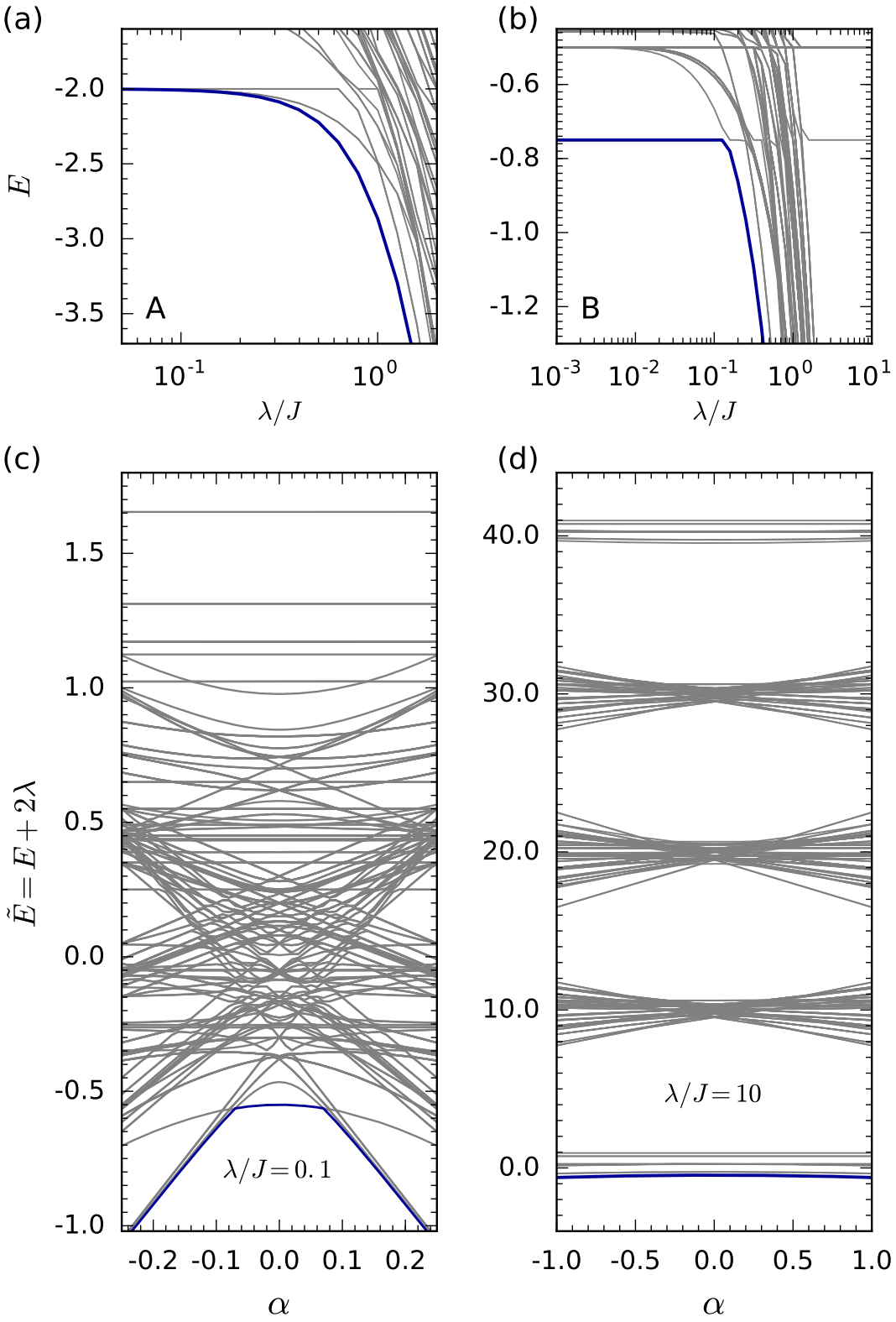

FIGURE 5.7: Exact energy spectra along the $\alpha + \beta = 0$ line for increasing λ obtained for the 4-site chain. Panels (a)-(b)—the ground state energy (in blue) and the low-lying excited levels (in grey) for cuts A and B, correspondingly. Panels (c)-(d)—the full spectra for the representative λ cuts, where the vertical axis yields the shifted energy $\tilde{\mathrm{E}} = \mathrm{E} + 2\lambda$. Figure has been published in Ref. [144].

Let us now consider the 2-site case for the spin-orbital model (5.1) with $\alpha = +0.5$, $\beta = -0.5$. In the absence of the on-site spin-orbit coupling, the FM $\otimes$ AO ground state has the form

$$|\mathrm{S}^z_{tot} = -1, \mathrm{T}^z_{tot} = 0\rangle = \frac{1}{\sqrt{2}}|\downarrow_1\downarrow_2\rangle \otimes (|-_1 +_2\rangle - |+_1 -_2\rangle)\,, \tag{5.17}$$

$$|\mathrm{S}^z_{tot} = 0, \mathrm{T}^z_{tot} = 0\rangle = \frac{1}{2}\underbrace{(|\uparrow_1\downarrow_2\rangle + |\downarrow_1\uparrow_2\rangle)}_{\text{quadrupolar}} \otimes \underbrace{(|-_1 +_2\rangle - |+_1 -_2\rangle)}_{\text{singlet}}, \tag{5.18}$$

$$|\mathrm{S}^z_{tot} = +1, \mathrm{T}^z_{tot} = 0\rangle = \frac{1}{\sqrt{2}}|\uparrow_1\uparrow_2\rangle \otimes (|-_1 +_2\rangle - |+_1 -_2\rangle)\,, \tag{5.19}$$

where $|+\rangle$, $|-\rangle$ are the eigenstates of the orbital operator T^z. The three-fold degeneracy appears due to the $\mathrm{S}_{tot} = 1$ states in the spin sector, whereas the orbital sector is represented by a singlet $|\mathrm{T}_{tot} = 0, \mathrm{T}^z_{tot} = 0\rangle$. Note, that while partial correlations averaged over the whole $\mathrm{S}_{tot} = 1$ subspace will be isotropic, Table 5.1 provides their internal structure in particular states. Interestingly, the quadrupolar state in the spin sector is responsible for the anisotropic behaviour qualitatively equivalent to the one in Fig. 5.6(a), (c), (e) with the planar functions being ferro and $\langle \mathrm{S}^z_1 \mathrm{S}^z_2\rangle$—antiferromagnetic.

We have verified that for $\lambda \approx 10^{-2}$ the no longer degenerate ground state has the form

$$|\mathrm{GS}(\lambda \approx 10^{-2})\rangle = \Delta_1 \underbrace{(|\uparrow_1\downarrow_2\rangle + |\downarrow_1\uparrow_2\rangle)}_{\text{quadrupolar}} \otimes \underbrace{(|-_1 +_2\rangle - |+_1 -_2\rangle)}_{\text{singlet}} \tag{5.20}$$

$$+ \underbrace{\Delta_2\,(|\uparrow_1\downarrow_2\, -_1 +_2\rangle - |\downarrow_1\uparrow_2\, +_1 -_2\rangle)}_{\text{spin-orbitally entangled}}, \tag{5.21}$$

where $\Delta_1 \approx 0.495$, $\Delta_2 \approx 10^{-2}$. Besides the quadrupolar $\otimes$ singlet term (5.20) present for $\lambda = 0$, it consist of a spin-orbitally entangled term (5.21), smaller by one order of magnitude. Notably, both of the terms (5.20)-(5.21) produce vanishing on-site averages $\langle \mathrm{S}^z_i\rangle = 0$, $\langle \mathrm{T}^z_i\rangle = 0$, summing up to $\langle \mathrm{S}^z_{tot}\rangle = 0$, $\langle \mathrm{T}^z_{tot}\rangle = 0$.

4-site chain

Following this trend, an inspection of $\langle \mathrm{S}^z_i\rangle$, $\langle \mathrm{S}^z_{tot}\rangle$ for the 4-site case revealed that the five-fold degeneracy at $\lambda = 0$ [due to the ferromagnetic $\mathrm{S}_{tot} = 2$ sector] is split into a singlet level and two doublet levels by the infinitesimal λ, as illustrated in Fig. 5.5 (a). The non-degenerate ground state is characterized by $\langle \mathrm{S}^z_i\rangle = 0$, $\langle \mathrm{T}^z_i\rangle = 0$, $\langle \mathrm{S}^z_{tot}\rangle = 0$, $\langle \mathrm{T}^z_{tot}\rangle = 0$. Hence, we conclude that for $\lambda \lesssim \lambda_{\mathrm{CRIT}}$ the quantum fluctuations within the spin and orbital sectors lower the energy of the ($\mathrm{S}^z_{tot} = 0$, $\mathrm{T}^z_{tot} = 0$) state, selecting it as the ground state of the approximately product nature *between* spin and orbitals, but entangled within those sectors, similarly to the 2-site case. Therefore, we view the anisotropic behaviour of the $S^{\gamma\gamma}$ and the isotropic behaviour of the $T^{\gamma\gamma}$ correlations as a signature of a ground state where quantum entanglement does exist, but the majority of it is kept inside the spin and orbital sectors for $\lambda \lesssim \lambda_{\mathrm{CRIT}}$. We expect an analogous effect at ($\alpha = -0.5$, $\beta = +0.5$), with the ground state being dominated by the maximal T_{tot} and $T^z_{tot} = 0$ entangled state in the orbital sector and the singlet state ($\mathrm{S}_{tot} = 0$, $\mathrm{S}^z_{tot} = 0$) in the spin sector.

Perturbed FM⊗AO/AF⊗FO states

Although technically there is a level crossing at $\lambda = 0$, in which the ground state degeneracy is lifted and the polarized states of the ferro sector become excited, overall the physics between the spin and orbital sectors in the small λ regime is still product-like, because there is not enough spin-orbital entanglement to qualitatively change it. Spin-orbital entanglement is still

"silent", being dominated by the larger product terms, but could grow for larger λ values. Thus *qualitatively* these are still the FM $\otimes$ AO and AF $\otimes$ FO phases, therefore in what follows we call them the *perturbed* FM $\otimes$ AO/AF $\otimes$ FO states.

Crossover from the perturbed FM⊗AO/AF⊗FO to the highly entangled state

The evolution of the spin-orbital entanglement along cut A is continuous because there is no level crossing for $\lambda > 0$, see Fig. 5.7 (a). Increasing λ beyond the perturbed product interval leads, through the logistic growth, to the saturation of the entanglement entropy.[17] Therefore, despite the analytical changes in the observables discussed above, we divided the evolution to three stages: the perturbed FM⊗AO and AF⊗FO states, the intermediate region λ_{CRIT} and the *highly entangled state*. Although there is no abrupt phase transition, the state for $\lambda \lesssim \lambda_{\mathrm{CRIT}}$ has fundamentally different properties from the one for $\lambda \gtrsim \lambda_{\mathrm{CRIT}}$. We will focus on the latter region in Sec. 5.7.

5.5.2 From the SU(4) singlet to the highly entangled state

Divergence from the SU(4) singlet

We will now analyse the evolution of the ground state properties with increasing λ along cut B [$\alpha = \beta = 0$]. At $\lambda = 0$ the system already is in a spin-orbitally entangled state—a singlet for which not only $\mathrm{S}_{tot} = 0$, $\mathrm{T}_{tot} = 0$, as would be for the singlet states in the spin and orbital sectors, but also the sum of the SU(4)-pseudospins[18] vanishes. We verify whether the system is in the critical SU(4)-singlet ground state in two ways:

1. By calculating averages of all nontrivial generators of the SU(4) group. Indeed, $\langle \mathrm{S}^{\gamma}_{tot} \rangle = 0$, $\langle \mathrm{T}^{\gamma}_{tot} \rangle = 0$, $\langle \sum_i \mathrm{S}^{\gamma}_i \mathrm{T}^{\epsilon}_i \rangle = 0$, where $\gamma, \epsilon \in \{x, y, z\}$.
2. By comparing the $\mathcal{O}_{\mathrm{SO}}$ and $\mathcal{C}_{\mathrm{SO}}$ values to their asymptotes at the exact SU(4) point ($\alpha = \beta = 1/4, \lambda = 0$). While the convergence of the $\mathcal{O}_{\mathrm{SO}}$ correlation to zero is a natural consequence of point 1., since the function is just $\langle \sum_i \mathrm{S}^{z}_i \mathrm{T}^{z}_i \rangle$ per site, the $\mathcal{C}_{\mathrm{SO}}$ comparison is truly independent and involves the spin-orbital entanglement directly.

Remarkably, the $\mathcal{O}_{\mathrm{SO}}$ and $\mathcal{C}_{\mathrm{SO}}$ functions still converge to the SU(4) point asymptotes, denoted by the blue and light-red dashed lines in Figs. 5.4 (b), (d), (f), for a finite λ interval. However, for large enough λ the correlations diverge from the asymptotes in a discontinuous way, through 1, 2, 3 and 4 kinks for 4, 8, 12, and 16 sites, respectively. This suggests n kinks for $\mathrm{L} = 4n$ sites. In particular, the vanishing values of the $\mathcal{O}_{\mathrm{SO}}$ correlation before the first kink indicate that the system is strongly resistant to the matching Ising SOC, remaining within the critical SU(4)-singlet regime. For completeness we note that a closer inspection of the SU(4) generators for $\lambda > 0$ revealed that only the generator proportional to $\mathcal{O}_{\mathrm{SO}}$ becomes finite after the first kink.

The behaviour of the $\mathcal{C}_{\mathrm{SO}}$ function has already indicated that the spin-orbital entanglement changes in a discontinuous way along cut B. Below we inspect this evolution more thoroughly, via the entanglement entropy.

Spin-orbital entanglement evolution

As shown in Figs. B.3, 5.3 and B.4 (a), (e), without the on-site spin-orbit coupling the value of the spin-orbital entanglement entropy is already quite substantial in the SU(4)-singlet ground state. Turning on λ initiates an effect similar to the one observed in the $\mathcal{O}_{\mathrm{SO}}$ and $\mathcal{C}_{\mathrm{SO}}$ correlations:

[17] 0.504 for the $L = 12$ site chain.

[18] Natural degrees of freedom for the phase, see Sec. 4.2.1 for more references.

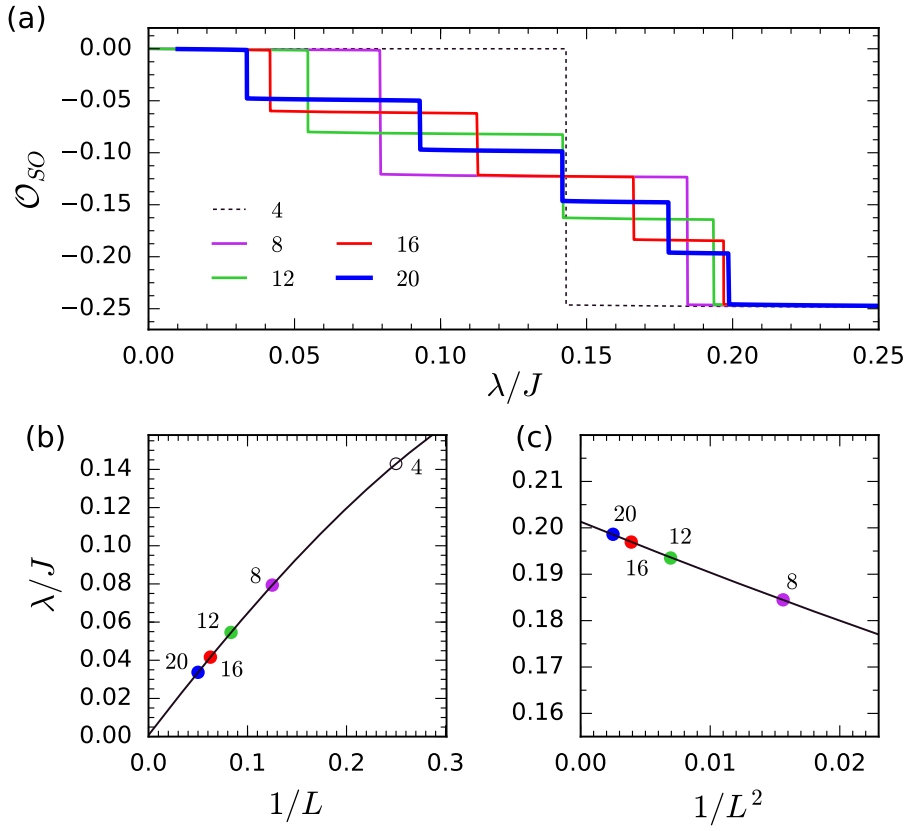

FIGURE 5.8: Finite size scaling of the range of the intermediate entangled state along cut B at $\alpha = \beta = 0$. Panel (a)—the discontinuous evolution in λ exemplified by the $\mathcal{O}_{\mathrm{SO}}$ correlation function, where n kinks appear for $\mathrm{L} = 4n = 4$, 8, 12, 16 and 20 sites. Panel (b)—the position of the first kink decreases linearly in 1/L. Panel (c)—the position of the last kink increases linearly in $1/(\mathrm{L}^2)$. Both fits, with coefficients provided in the main text, utilize the ED results for L = 4, 8, 12, 16 and 20 sites presented as the colorful dots. Figure has been published in Ref. [144].

the entropy is resistant to the spin-orbit coupling for a finite λ interval, only to abruptly increase for large enough λ value. In case of the 4-site chain the new value is almost saturated [Fig. B.3 (e)], while for 8 and 12 sites more intermediate stages are needed to reach the highly entangled state. Again, we cautiously expect n kinks for $\mathrm{L} = 4n$ sites.

Magnetic evolution

The discontinuities concern also the magnetic properties, appearing in the S and T correlations in Figs. B.3, 5.3, B.4 (f) and 5.5 (b)-(c), as well as in partial correlation functions $S^{\gamma\gamma}$, $T^{\gamma\gamma}$ in Figs. 5.6 (b), (d), (f). Note, that while the S and T evolution is identical along the whole cut B, $S^{\gamma\gamma}$ and $T^{\gamma\gamma}$ are also isotropic and antiferromagnetic before the first kink, suggesting the presence of the SU(4)-singlet state. The planar correlations [$S^{\delta\delta}$ and $T^{\delta\delta}$, where $\delta = x$, y] and the S^{zz} and T^{zz} correlations separate in the subsequent kinks, so that after the final kink the planar correlations converge to zero while the zz correlations stabilize at a finite antiferro value. This will be discussed in more detail in Sec. 5.7.

Exact spectra for the 4-site chain

In order to verify the cause of the discontinuous change in all the above ground state properties, we investigate the full energy spectrum of the 4-site chain. As expected along cut B, Fig. 5.7

TABLE 5.2: First 9 energy levels of Hamiltonian (5.1) on a 4-site chain at $\alpha = \beta = 0$ and for representative values of λ. $\tilde{\mathrm{E}}$ represents the shifted energies [cf. eq. (5.22)] while d stands for the degeneracy of each level. Table published in Ref. [144].

$\lambda = 0$		$\lambda/J = 0.1$		$\lambda/J = 10$	
$\tilde{\mathrm{E}}$	d	$\tilde{\mathrm{E}}$	d	$\tilde{\mathrm{E}}$	d
−0.75	1	−0.55	1	−0.45736	1
−0.50	28	−0.46570	1	−0.25	2
−0.45711	9	−0.37965	4	0.24367	1
−0.43301	12	−0.36944	8	0.24684	2
−0.40139	1	−0.30	15	0.24688	4
−0.25	48	−0.26229	2	0.24691	1
0.0	76	−0.25345	2	0.25	2
0.25	34	−0.25	2	0.74369	2
0.43301	12	−0.24561	2	0.94779	1

(b) reveals a level crossing between the non-degenerate ground state and the first excited state at $\lambda \approx 0.14219J$, exactly at the position of the only kink of the 4-site system.

Furthermore, the whole spectrum evolves with λ, see the progressively zoomed levels in Figs. B.5 (b), (d), (f). Table 5.2 presents the nine lowest energy levels of Hamiltonian (5.1) for $\alpha = \beta = 0$ and representable values of λ. In order to compare the small and large spin-orbit coupling cases more easily, we eliminated the λ energy scale by introducing

$$\tilde{\mathrm{E}} = \mathrm{E} + 2\lambda. \tag{5.22}$$

Even though the ground state energy $\mathrm{E} = -0.75$ is non-degenerate at $\lambda = 0$, the excited levels may be massively degenerate,as shown in the second column of Table 5.2 A weak spin-orbit coupling $\lambda/J = 0.1$ largely reduces the above degeneracy, as illustrated in the third and fourth column of Table 5.2. The multiple level splittings contribute to relatively a dense spectrum even at $\alpha = \beta = 0$, see the central part of Fig. 5.7 (c). However, such amount of the spin-orbit coupling does not modify the ground state, which is still of the critical SU(4)-singlet character, as discussed in previous sections.

Although through a unique level crossing at $\lambda/J = 0.14219$ the character of the ground state changes to the highly entangled state, the excited levels may still cross for higher λ values [Fig. 5.7 (b)]. The general trend is to sort the energies into 5 bands, separated by the gaps $\sim \lambda$ [the so called λ energy scale]. In this way, in Fig. 5.7 (d), already for $\lambda/J = 10$ the bands are well isolated by gaps $\sim \lambda$ not only at $\alpha = \beta = 0$,[19] but also for the whole $\alpha \in [-1, 1]$ interval along the $\alpha + \beta = 0$ line. The internal structure of the lowest band for $\lambda/J = 10$ and $\alpha = \beta = 0$ is exhibited in the fifth and sixth column of Table 5.2. For $\lambda \to \infty$ these overall 16 energies converge to the spectrum of the effective model in $\tilde{\mathrm{J}}$ pseudospins with degeneracies 1, 2, 10, 2, 1, discussed in more detail in Sec. 5.7

Finite-size scaling

For both entropy and all the discussed correlation functions the number of kinks increases and their position changes coherently with the system size, keeping n kinks for $\mathrm{L} = 4n$ sites relation.

[19] Which happens earlier.

Below we perform the finite-size scaling procedure based on even larger set of chains and discuss the predicted behaviour in thermodynamic limit.

Fig. 5.8 (a) presents the evolution along cut B for all the systems currently available to us: L = 4, 8, 12, 16 and 20 sites, exemplified by the $\mathcal{O}_{\mathrm{SO}}$ correlation function. Notably, n kinks for L = $4n$-site chains are still supported for larger systems. In order to discuss the extent of the SU(4) singlet in the phase diagram and the behaviour of a macroscopic system we have utilized polynomial fits to the accumulated data for the first and the final kink. The fits, presented in Figs. 5.8 (b) and (c), respectively, confirmed that the first and the final kink scale differently with the system size.

Namely, the position of the first kink k_1

$$k_1 = 0.00004 + 0.69712\,x \ - 0.50147\,x^2 \tag{5.23}$$

decreases almost linearly with $x = 1/\mathrm{L}$ in Fig. 5.8 (b), converging to $\lambda/J = 0$ when $\mathrm{L} \to \infty$. Thus, we expect that in thermodynamic limit the SU(4) singlet will be immediately altered for $\lambda > 0$.

In contrast, the final kink k_f

$$k_f = 0.20132 - 1.13007\,x^2 + 3.14415\,x^4, \tag{5.24}$$

scales approximately quadratically with 1/L, hence—almost linearly with $1/(\mathrm{L}^2)$, as visible in Fig. 5.8 (c). Crucially, its position in the thermodynamic limit *stops* at $\lambda/J \simeq 0.2$, guaranteeing stability of the phase below it. Therefore, for cut B we define λ_{CRIT} as a single number: $\lambda_{\mathrm{CRIT}}/J \simeq 0.2$.

Summing up, in the thermodynamic limit we expect the spin-orbital entanglement to continuously grow from the value in the SU(4) singlet to $\lambda_{\mathrm{CRIT}}/J \simeq 0.2$, after which it will start to saturate in the highly entangled state. We call the state stabilized for $0 < \lambda < \lambda_{\mathrm{CRIT}}$ an *intermediate entangled state* (IES).

5.5.3 Phase diagram

In this section we investigate the evolution of the system with the increasing on-site spin-orbit coupling along the $\alpha + \beta = 0$ line. While we mainly focus on the spin-orbital entanglement [in the ground state], we have also monitored the magnetic properties and energetics of the system. After the detailed inspection along the representative cuts A and B, complemented by the details about the energy spectra and $\{\alpha, \lambda\}$ maps along the line, we may now formulate more precise conclusions supporting the first observations made at the beginning of this section.

Namely, the two regions with vanishing spin-orbital entanglement, restricted by $|\alpha| \gtrsim 0.08$ and $\lambda/J \lesssim \lambda_{\mathrm{CRIT}}$, can now be recognised as the perturbed FM $\otimes$ AO/AF $\otimes$ FO states, marked on the phase diagram 5.9 with a semi-transparent blue to indicate the almost non-existent spin-orbital entanglement in the ground state.

The central, less transparent, green region in Fig. 5.9 symbolizes the intermediate entangled state, restricted by $|\alpha| \lesssim 0.08$ and $\lambda/J \lesssim \lambda_{\mathrm{CRIT}}$. In this case the ground state evolves through n kinks for the $4n$-site system, which results in the continuous evolution from the SU(4) singlet up to λ_{CRIT}. In particular, the fact that the position of the nth kink stabilized at $\lambda/J \simeq 0.2$ in the thermodynamic limit may suggest a change of slope in the growth of the spin-orbital entanglement, justifying the distinction of the intermediate entangled state.[20]

[20] Here we would like to remark that away from the $\alpha + \beta = 0$ line but still within the boundaries marked by the white dashed lines in Fig. 5.2 the kinks may appear sooner or later in λ, depending on the proximity to the exact SU(4) point. Namely, the closer to the SU(4) point, the more resistant the ground state should be to the Ising spin-orbit coupling. Inspecting the central region in Figs. 5.2 and B.1 confirms this intuition.

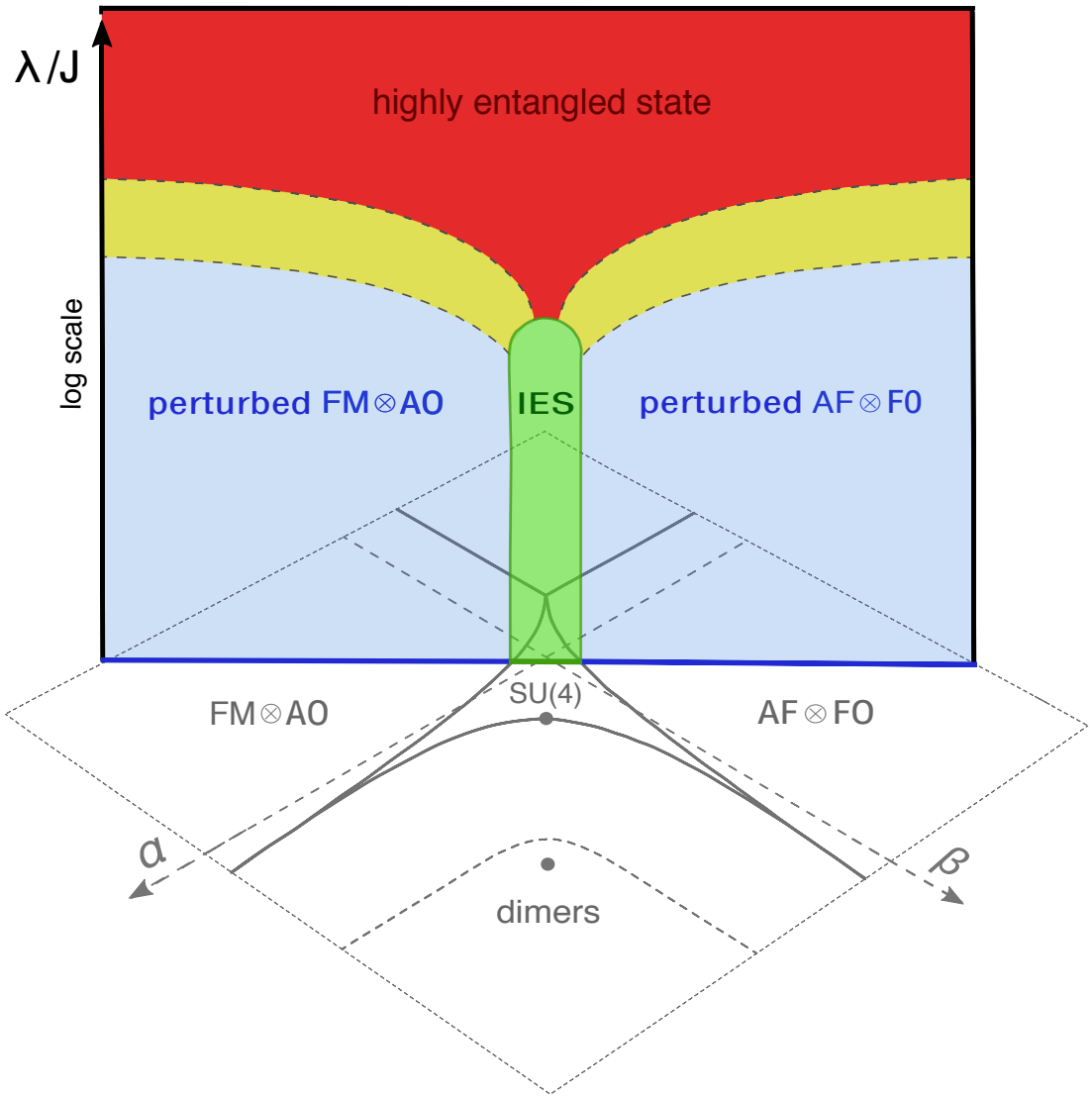

FIGURE 5.9: Ground-state phase diagram of model (5.1) along the $\alpha + \beta = 0$ line. The phases were distinguished based on the spin-orbital entanglement, the magnetic properties as well as the energetics, see the main text. The considered evolution starts at $\lambda = 0$, where the diagram is redrawn in grey based on Ref. [133], see also Fig. 4.2. The shape of the phase boundaries depends on the logarithmic scale of λ. The diagram is based on the ED results on small to moderate-size clusters. We discuss the validity of this picture in the thermodynamic limit in the main text. Figure has been published in Ref. [144].

With the denser scans along the $\alpha + \beta = 0$ line for $\lambda/J = 0.1$ we were able to pinpoint the "horizontal" phase transition from the intermediate entangled state to the FM $\otimes$ AO/AF $\otimes$ FO state, observed as the discontinuities in the entropy and correlation functions as well as in the level crossing [Fig. 5.7 (c)], to $|\alpha| \approx 0.08$.

As exemplified by cut A, the ground state evolution in λ from the FM$\otimes$AO/AF$\otimes$FO phases to the highly entangled state is of a crossover type. The degenerate ground-state level is split as soon as $\lambda > 0$, selecting $S^z_{tot} = T^z_{tot} = 0$ state as the ground state, allowing however for a tiny amount of the spin-orbital entanglement. As the energy gap increases due to the growing spin-orbit coupling, the ground state properties evolve smoothly, gaining more and more spin-orbital entanglement, until the saturation for high enough λ values. This logistic growth of the

entanglement results in the ground state in the large λ limit in many ways much different from the one at small λ, despite the lack of a level crossing for $\lambda > 0$. Therefore, we have distinguished λ_{CRIT} as a region of a dynamical change of the ground-state properties, marked in Fig. 5.9 as a yellow stripe with dashed boundaries, emphasising the crossover character.

Regardless of the starting point along the $\alpha + \beta = 0$ line, increasing the spin-orbit coupling will eventually lead to the region of the saturated spin-orbital entanglement and the weakly antiferro nearest-neighbor corelations S and T. This highly entangled state is marked in opaque red in Fig. 5.9 (c).

5.6 Evolution along the $\beta + \alpha = -1$ line

Fig. 5.2 and the data behind it revealed that the classical region, at $\lambda = 0$ consisting of the Heisenberg ferro states in both the spin and orbital sector (FM $\otimes$ FO), gradually spreads out for increasing λ, occupying the whole half-plane below the "quantum stripe" in Fig. 5.2 (c). While the evolution of the FM $\otimes$ FO phase in the Ising SOC seems rather trivial, it is particularly interesting how exactly the lower parts of the AF$\otimes$FO/FM$\otimes$AO phases evolve into a completely classical state once the spin-orbit coupling is dominant below the $\alpha + \beta = -1/2$ line.

Here we concentrate on the evolution in λ along the representative $\alpha+\beta = -1$ line, indicated by the red dashes in Fig. 5.2. We have selected this particular line because it crosses all the product phases at $\lambda = 0$: AF $\otimes$ FO, FM $\otimes$ FO, and FM $\otimes$ AO, and lies below the "quantum stripe" in the $\lambda \to \infty$ limit. Moreover, the line runs close enough to the center of the $\{\alpha, \beta\}$ maps for the evolution to be rather compact.

Similarly to Fig. 5.3, we calculated the dense scans in $\{\alpha, \lambda\}$ of the entanglement entropy and the correlation functions, which are displayed in Fig. 5.10. On one hand, the central part of the entropy and $\mathcal{C}_{\mathrm{SO}}$ maps [Fig. 5.10 (a) and (b), correspondingly] does not contain any spin-orbital entanglement. The FM$\otimes$FO phase immediately responds to the Ising spin-orbit coupling, resulting in the maximal value of $\mathcal{O}_{\mathrm{SO}}$ correlation as soon as $\lambda > 0$ [Fig. 5.10 (c)]. On the other hand, the AF $\otimes$ FO and FM $\otimes$ AO phases do gain spin-orbital entanglement, similarly as along the $\beta + \alpha = 0$ line. However, in contrast to the case described in Sec. 5.5.1, the high entropy sharply drops to zero for a certain value of λ. Similarly to the previous section, we have selected representative cuts in order to investigate the details of the above processes: cut C at ($\alpha = 1.5$, $\beta = -2.5$) and symmetrically at ($\alpha = -2.5$, $\beta = 1.5$), starting with the FM $\otimes$ AO/AF $\otimes$ FO phases, and cut D at $\alpha = \beta = -0.5$, starting with the FM $\otimes$ FO phase at $\lambda = 0$.

From AF $\otimes$ FO/FM $\otimes$ AO to the fluctuation-free state

Here we follow cut C at ($\alpha = 1.5$, $\beta = -2.5$), starting with the FM $\otimes$ AO phase for $\lambda = 0$ and then discuss an analogous case for the starting point in the AF $\otimes$ FO phase. Similarly to cut A discussed in Sec. 5.5.1, as soon as $\lambda > 0$, the degenerate ground state level, spanned by the multiplet

$$\{|\mathrm{S}_{tot} = \mathrm{S}_{tot}^{max}, \mathrm{S}_{tot}^{z} = n\rangle\}, \tag{5.25}$$

where S_{tot}^{max} is the maximal possible value of the total spin and $n \in \{-\mathrm{S}_{tot}^{max}, -(\mathrm{S}_{tot}^{max} - 1), ..., +(\mathrm{S}_{tot}^{max} - 1), +\mathrm{S}_{tot}^{max}\}$,[21] is split and only the product of internally entangled states

$$|\mathrm{S}_{tot} = \mathrm{S}_{tot}^{max}, \mathrm{S}_{tot}^{z} = 0\rangle \otimes |\mathrm{T}_{tot} = 0, \mathrm{T}_{tot}^{z} = 0\rangle, \tag{5.26}$$

supplemented by a small spin-orbitally entangled term is left as the ground state, cf. Sec. 5.5.1 for the 2-site formula. Along cut C, the spin-orbital entanglement is still infinitesimal and the magnetic properties of the system, presented in Fig. 5.10 (f), are that of the perturbed

[21] Cf. Sec. 4.2.1.

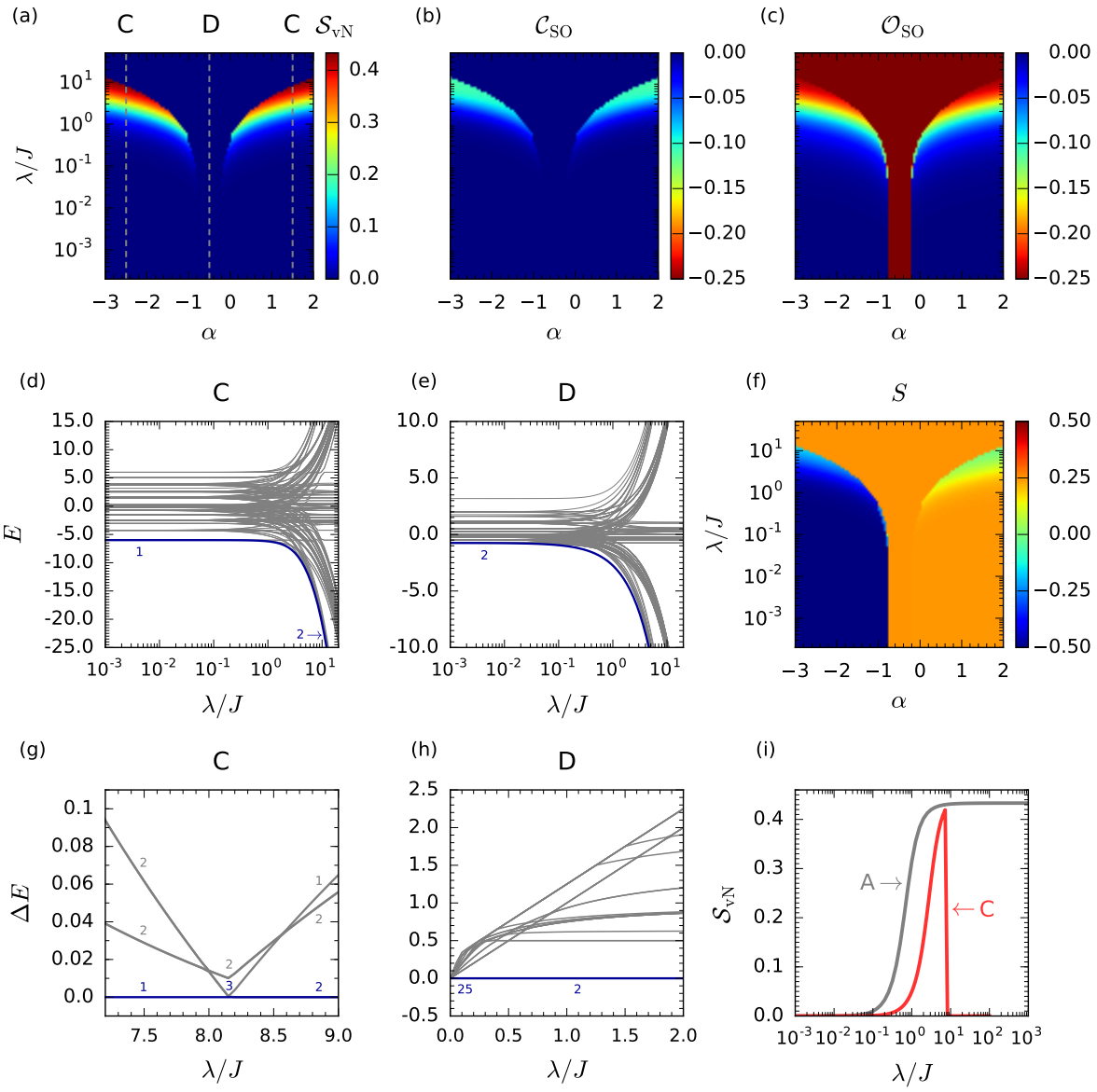

FIGURE 5.10: Spin-orbital entanglement evolution in λ along the $\alpha + \beta = -1$ line. The entanglement entropy and selected correlation functions were calculated in the ground state of Hamiltonian (5.1) on the 4-site chain. Panel (a)—the map in $\{\alpha, \lambda\}$ of the entanglement entropy $\mathcal{S}_{\mathrm{vN}}$. Panels (b), (c)—analogous maps of the nearest-neighbor spin-orbital correlation $\mathcal{C}_{\mathrm{SO}}$ and the on-site spin-orbital correlation $\mathcal{O}_{\mathrm{SO}}$. Full energy spectrum along cuts C and D is presented on panels (d)-(e), with the ground state marked in blue and its degeneracy marked by a number. Panel (f)—the map in $\{\alpha, \lambda\}$ of the spin nearest-neighbor correlation function S. Panel (g) presents the energy differences $\Delta \mathrm{E} = \mathrm{E}_i - \mathrm{E}_0$ between the first four excited states and the ground state around the sharp transition on cut C. Panel (h) illustrates the splitting of the 25-fold degenerate FM $\otimes$ FO ground state level for $\lambda > 0$. Panel (i) presents a comparison of the entanglement entropy curves along cuts A and C. All maps are restricted to the representative $\alpha \in [-3, 2]$ interval, symmetric in relation to cut D at $\alpha = \beta = -0.5$. The shape of the phase boundaries is dependent on the logarithmic scale of λ. Figure has been published in Ref. [145].

FM $\otimes$ AO phase for $\lambda/J \lesssim 10^0$. For higher λ values the continuously accumulating spin-orbital entanglement becomes clearly visible as a "rainbow" in Fig. 5.10 (a), forming the intermediate dynamical region. However, in contrast to cut A, the entropy sharply drops to zero for $\lambda/J \approx 8.175 \pm 0.025$. Fig. 5.10 (i) compares the entropy evolution along cuts A and C.[22]

Inspection of the energy spectrum for the 4-site chain reveals the origin of such behaviour. Since in Fig. 5.10 (d) it is quite difficult to spot the level crossing suggested by the sharp drop in entropy, in Fig. 5.10 (g) we plotted the differences between the excited and the ground-state energies $\Delta \mathrm{E} = \mathrm{E}_i - \mathrm{E}_0$ in grey and the renormalized ground state energy at zero in blue. Indeed, at $\lambda/J \approx 8.175 \pm 0.025$ a level crossing between the non-degenerate ground state level and the doubly degenerate excited level happens. In this way the perturbed FM $\otimes$ AO state becomes an excited state, perhaps gradually gaining further entanglement and crossing another excited 2-fold degenerate state for larger λ. The new doubly-degenerate ground state, consisting of

$$|... \uparrow_i \uparrow_{i+1} ...\rangle |... -_i -_{i+1} ...\rangle, \tag{5.27}$$

and

$$|... \downarrow_i \downarrow_{i+1} ...\rangle |... +_i +_{i+1} ...\rangle, \tag{5.28}$$

is devoid from any quantum entanglement. This state will be justified by the analysis along cut D in the next section.

Summing up the evolution along cut C, we will again try to provide λ_{CRIT} separating different stages of the evolution. As the reader might have already guessed, there will be two λ_{CRIT} in this interesting case:

1. $\lambda_{\mathrm{CRIT1}}/J \in (10^0, 8.175)$—an interval of rapidly but continuously growing spin-orbital entanglement, "a crossover in the making".

2. $\lambda_{\mathrm{CRIT2}}/J = 8.175$—a level crossing interrupting the above crossover process.

Thus, the system evolves from the FM $\otimes$ AO phase, through the perturbed FM $\otimes$ AO phase for $\lambda \lesssim \lambda_{\mathrm{CRIT1}}$, and is rapidly accumulating spin-orbital entanglement during the λ_{CRIT1} stage, but the crossover is interrupted by a level crossing at λ_{CRIT2}. For $\lambda > \lambda_{\mathrm{CRIT2}}$ the system is in a completely classical, doubly-degenerate state (5.27)-(5.28). Due to the symmetric form of Hamiltonian (5.1) analogous behaviour appears at ($\alpha = -2.5$, $\beta = 1.5$), with the spin and orbital characteristics exchanged.

From FM $\otimes$ FO to the fluctuation-free state

Along cut D at $\alpha = \beta = -0.5$, the evolution starts in the FM $\otimes$ FO phase, for which the ground state is 25-fold degenerate for the 4-site chain, due to the degenerate ferro subspaces in both spin and orbital sectors. The ferro subspace of the Heisenberg model can be described by the set of states

$$\left\{ |\mathrm{O}_{tot} = \mathrm{O}_{tot}^{max}, \mathrm{O}_{tot}^{z} = n\rangle \right\}, \tag{5.29}$$

where O_{tot}^{max} stands for the maximal possible value of the total spin/pseudospin quantum number and $n \in \{-\mathrm{O}_{tot}^{max}, -(\mathrm{O}_{tot}^{max} - 1), ..., +(\mathrm{O}_{tot}^{max} - 1), +\mathrm{O}_{tot}^{max}\}$.[23] While the states with the maximal O_{tot}^{z} projection are fully classical, the states with $n > 0$ will be entangled, similarly to the simple example of the quadrupolar state given in Sec. 5.5.1. Thus, when $\lambda = 0$ in Hamiltonian (5.1), due

[22] Here we argue in a handwaving manner that from the slope of the "C" curve it seems that there may exist a continuation of the rising entropy shape in the excited state, still rapidly growing for a certain λ interval before the saturation. Namely, the highest part of the red curve, despite surpassing 0.4 value, does not seem to be in the decelerating regime, contrastingly to the cut A for the same value.

[23] Cf. Sec. 4.2.1 and 5.5.1.

to the degeneracy, it is possible to choose a completely classical state as representing the ground state sector as well as the internally entangled one. Either way, the spin and orbital sectors are independent in such a ground state, resulting in zero value of the spin-orbital entanglement entropy.

Returning to the 2-site toy model, this time on cut D, one notices that at λ=0 the 9-fold degenerate ground-state energy level is described by: 4 fully polarized states, 4 states polarized in one sector and quadrupolar in the other and, finally, a unique quadrupolar $\otimes$ quadrupolar state. Out of them, the Ising spin-orbit coupling of the antiferro character selects a doublet of completely classical states

$$\{|\uparrow_1\uparrow_2 -_1-_2\rangle, |\downarrow_1\downarrow_2 +_1+_2\rangle\} \tag{5.30}$$

as the ground state. Notably, each of the states (5.30) is arranged in an antiferro-way on each site (between spin and pseudospin) but ferro on the bond, both in the spin and orbital sectors. This results in the maximally-ferro Ising bond correlations ($\langle S_1^z S_2^z\rangle = \langle T_1^z T_2^z\rangle = +0.25$, $\langle S_1^\delta S_2^\delta\rangle = \langle T_1^\delta T_2^\delta\rangle = 0$, $\delta = x$, y) and antiferro Ising values of the on-site correlations ($\langle S_i^z T_i^z\rangle = -0.25$, $\langle S_i^\delta T_i^\delta\rangle = 0$).

An analogous splitting occurs for the 4-site chain in Fig. 5.10 (e), (h), where the 25-fold degenerate level is reduced to the 2-fold degenerate classical groundstate extrapolated from the 2-site case described by formula (5.30):

$$|\uparrow_1\uparrow_2\uparrow_3\uparrow_4\rangle|-_1-_2-_3-_4\rangle, \tag{5.31}$$

and

$$|\downarrow_1\downarrow_2\downarrow_3\downarrow_4\rangle|+_1+_2+_3+_4\rangle. \tag{5.32}$$

Remarkably, such an immediate reaction to the spin-orbit coupling is possible because in this α and β parameter regime the states (5.31)-(5.32) describe the ground state level of not only the Kugel-Khomskii term on its own,[24] but also the ground state level of the SOC term.

The classical ground state cannot produce any kind of entanglement [Fig. 5.10 (a)-(b)]. The lack of quantum fluctuations results in the ferro values of the nearest-neighbor spin correlation $S = +0.25$ [Fig. 5.10 (f)] and $T = +0.25$ (not shown), to which only S^{zz}/T^{zz} contributed with a non-zero value, and the antiferro $\mathcal{O}_{\rm SO} = -0.25$ value [Fig. 5.10 (c)], while the other on-site correlations vanish. This is consistent with the 2-site case. For completeness we add, that along cut D $\lambda_{\rm CRIT} = 0$ due to the massive ground-state level splitting, removing all quantum entanglement from the ground state.

Beyond the $\alpha + \beta = -1$ line

From the trends in Fig. 5.2 one can deduce that for the parallel lines lying further below the $\beta + \alpha = -1/2$ line the above effects will appear for higher values of λ and shifted values of α and β.

Finally, we comment that the $\mathcal{O}_{\rm SO}$ correlation proved to be a good indicator on whether the system is already in a state that would appear for $\lambda \to \infty$. Namely, the saturation of $\mathcal{O}_{\rm SO}$ signals reaching the above limit, discussed in detail below.

5.7 Limit of large spin-orbit coupling

The detailed analysis of the $\alpha + \beta = 0$ and $\alpha + \beta = -1$ lines revealed that in the $\lambda \to \infty$ limit the system may or may not be spin-orbitally entangled, depending on the values of α and β parameters. Along the $\alpha + \beta = -1$ line the ground state in $\lambda > \lambda_{\rm CRIT}$ is completely classical, built out of the spin and orbital configuration, in which the bond correlations are ferromagnetic

[24] More precisely: belong to the ground state subspace.

while the on-site correlations are antiferromagnetic. In contrast, along the $\alpha + \beta = 0$ line the $\lambda \to \infty$ ground state is highly spin-orbitally entangled, while the magnetic properties of the phase are weakly antiferro in both spin and orbital sectors.

Figs. 5.2 and B.1 (c) demonstrate that both the classical and the highly entangled states occupy finite regions of the entropy map in large λ, the latter being confined to the "quantum stripe" around the $\alpha+\beta = 0$ diagonal. A similar picture emerges from the $\mathcal{C}_{\rm SO}$ maps in Fig. B.2. In order to better understand the mechanisms leading to such a variety of possibilities, inspired by Ref. [4], we have derived an effective low-energy Hamiltonian in the $\lambda \to \infty$ limit.

5.7.1 Effective model

For any Hamiltonian of the type $\mathcal{H} = \mathcal{H}_{\rm SE} + \mathcal{H}_{\rm SOC}$, in the strong on-site spin-orbit coupling limit, where the λ energy scale dominates over the superexchange energy scale J, the spectrum of the full Hamiltonian groups into bands separated by the gaps of the order of λ. The low energy physics, confined into the lowest band, can be described by treating the Kugel-Khomskii Hamiltonian $\mathcal{H}_{\rm SE}$ as a perturbation to the dominant spin-orbit coupling $\mathcal{H}_{\rm SOC}$ and projecting the former to the ground state of the latter [4]. We have already mentioned this approach in Sec. 2.1.2, for the case of the quasi-two dimensional iridates. Let us now explain this process step by step.

Let us start with recalling the more general form of the anisotropic on-site spin-orbit coupling

$$\mathcal{H}_{\rm SOC} = 2\lambda \mathrm{S}^{\gamma}\mathrm{T}^{\epsilon}, \tag{5.33}$$

where γ, $\epsilon \in \{x, y, z\}$, resulting from the elimination of inactive orbitals on a particular bond [cf. Sec. 5.2 for a reminder]. Any term of the type (5.33) has a spectrum consisting of two doubly degenerate levels $\pm\lambda/2$, spanned by the eigenvectors

$$\{|\mathrm{ld}_1\rangle, |\mathrm{ld}_2\rangle\} \qquad \text{for the eigenvalue} -\frac{\lambda}{2}, \tag{5.34}$$

$$\{|\mathrm{hd}_1\rangle, |\mathrm{hd}_2\rangle\} \qquad \text{for the eigenvalue} +\frac{\lambda}{2}, \tag{5.35}$$

where $|\mathrm{ld}_i\rangle$, $i = 1, 2$, are the two eigenvectors labeled together as the "lower doublet" while $|\mathrm{hd}_i\rangle$ stand for the eigenvectors of the "higher doublet".

In the general case (5.33), the decomposition of states (5.34)-(5.35) in the spin-orbital basis

$$\{|\mathrm{T}^z, \mathrm{S}^z\rangle\} = \{|+\uparrow\rangle, |+\downarrow\rangle, |-\uparrow\rangle, |-\downarrow\rangle\} \tag{5.36}$$

may appear complicated. However, as already mentioned in Sec. 5.2, general form (5.33) can be reduced to the Ising form

$$\mathcal{H}_{\rm SOC} = 2\lambda \mathrm{S}^{z}\mathrm{T}^{z}, \tag{5.37}$$

via the suitable rotations in the spin and/or orbital subspaces. The spectrum of the form (5.37) written in basis (5.36) is reduced to

$$|\mathrm{ld}_1\rangle = |+\downarrow\rangle, \tag{5.38}$$

$$|\mathrm{ld}_2\rangle = |-\uparrow\rangle, \tag{5.39}$$

$$|\mathrm{hd}_1\rangle = |+\uparrow\rangle, \tag{5.40}$$

$$|\mathrm{hd}_2\rangle = |-\downarrow\rangle. \tag{5.41}$$

In any case, a doubly degenerate ground state allows us to introduce the effective pseudospins $\tilde{\mathrm{J}} = 1/2$, onto which we will be projecting the symmetric Kugel-Khomskii Hamiltonian (5.2).

For clarity, let us note that now we are temporarily changing the notation: in this section $\mathcal{H}_{\mathrm{SE}}$ as well as $\mathcal{H}_{\mathrm{SE}}^{\mathrm{SOC}}$ denote the matrices of the Kugel-Khomskii Hamiltonian (5.2) in the spin-orbital basis (5.36) and in the SOC basis (5.38)-(5.41), respectively. Moreover, we will be utilizing the matrices of the on-site operators $\{\mathrm{T}_i^{\epsilon}\mathrm{S}_i^{\gamma}, \mathrm{T}_i^{\epsilon}\mathrm{id}_i, \mathrm{id}_i\mathrm{S}_i^{\gamma}\}$, where id_i is an identity operator in the suitable subspace, appearing when rewriting Hamiltonian (5.2) with attention to detail. We will be denoting these matrices as $\mathcal{O}_i$ in basis (5.36) and as $\mathcal{O}_i^{\mathrm{SOC}}$ in basis (5.38)-(5.41).[25]

Let us start the downfolding [159] by first transforming $\mathcal{O}_i$ into $\mathcal{O}_i^{\mathrm{SOC}}$:

$$\mathcal{O}_i^{\mathrm{SOC}} = \mathrm{U}_i^{\dagger}\mathcal{O}_i\mathrm{U}_i, \tag{5.42}$$

where U_i is the unitary matrix transforming between the two local bases on each site. In our case U_i is reduced to the permutation of the basis elements:

$$\mathrm{U}_i = \begin{pmatrix} 0 & 0 & 1 & 0 \\ 1 & 0 & 0 & 0 \\ 0 & 1 & 0 & 0 \\ 0 & 0 & 0 & 1 \end{pmatrix} \tag{5.43}$$

Because

$$\mathcal{H}_{\mathrm{SE}}^{\mathrm{SOC}} = \mathrm{U}^{\dagger}\mathcal{H}_{\mathrm{SE}}\mathrm{U}, \tag{5.44}$$

where $\mathrm{U} = \mathrm{U}_i \otimes \mathrm{U}_j$ is the bond unitary matrix, we may now insert the translated matrices $\mathcal{O}_i^{\mathrm{SOC}}$ into the structure dictated by Hamiltonian (5.2).

The second step is the actual downfolding. Namely, utilizing the assumption $\lambda \to \infty$, we project out all the non-zero elements of the $\mathcal{H}_{\mathrm{SE}}^{\mathrm{SOC}}$ matrix connected to the "higher doublet" on at least one of the sites. The resulting matrix has non-zero elements only in the "lower doublet" sectors. For convenience, we remove the remaining zero rows and columns, obtaining the truncated 4×4 matrices. Below we include the explicit form of the truncated $\mathcal{H}_{\mathrm{SE}}^{\mathrm{SOC}}$ matrix, ordered according to $\{|\mathrm{ld}_{1,i}\rangle \otimes |\mathrm{ld}_{1,j}\rangle, |\mathrm{ld}_{1,i}\rangle \otimes |\mathrm{ld}_{2,j}\rangle, |\mathrm{ld}_{2,i}\rangle \otimes |\mathrm{ld}_{1,j}\rangle, |\mathrm{ld}_{2,i}\rangle \otimes |\mathrm{ld}_{2,j}\rangle\}$:

$$\begin{pmatrix} \frac{1}{16}(1+4(\alpha+\beta)) & 0 & 0 & 0 \\ 0 & \frac{1}{16}(1-4(\alpha+\beta)) & \frac{1}{4} & 0 \\ 0 & \frac{1}{4} & \frac{1}{16}(1-4(\alpha+\beta)) & 0 \\ 0 & 0 & 0 & \frac{1}{16}(1+4(\alpha+\beta)) \end{pmatrix}. \tag{5.45}$$

If we decompose matrix (5.45) into

$$\underbrace{\frac{1}{4}\begin{pmatrix} 0 & 0 & 0 & 0 \\ 0 & 0 & 1 & 0 \\ 0 & 1 & 0 & 0 \\ 0 & 0 & 0 & 0 \end{pmatrix}}_{(i)} + \frac{1}{4}(\alpha+\beta)\underbrace{\begin{pmatrix} 1 & 0 & 0 & 0 \\ 0 & -1 & 0 & 0 \\ 0 & 0 & -1 & 0 \\ 0 & 0 & 0 & 1 \end{pmatrix}}_{(ii)} + \frac{1}{16}\underbrace{\begin{pmatrix} 1 & 0 & 0 & 0 \\ 0 & 1 & 0 & 0 \\ 0 & 0 & 1 & 0 \\ 0 & 0 & 0 & 1 \end{pmatrix}}_{(iii)} \tag{5.46}$$

one can recognise the term (i) as a matrix of an operator

$$|\mathrm{ld}_{1,i}\rangle \otimes |\mathrm{ld}_{2,j}\rangle\langle \mathrm{ld}_{2,i}| \otimes \langle \mathrm{ld}_{1,j}| + |\mathrm{ld}_{2,i}\rangle \otimes |\mathrm{ld}_{1,j}\rangle\langle \mathrm{ld}_{1,i}| \otimes \langle \mathrm{ld}_{2,j}| \tag{5.47}$$

[25] For completeness we add that in this section we utilize the Pauli matrices to represent the operators of spin/pseudospin $\mathrm{S/T} = 1/2$ as well as the operators of pseudospin $\tilde{J} = 1/2$ in the bases for which $|\uparrow\rangle$ and $|+\rangle$ are represented by $\begin{pmatrix} 1 \\ 0 \end{pmatrix}$, while $|\downarrow\rangle$ and $|-\rangle$ are represented by $\begin{pmatrix} 0 \\ 1 \end{pmatrix}$.

which can be furder identified as

$$\tilde{\mathrm{J}}_i^+ \tilde{\mathrm{J}}_j^- + \tilde{\mathrm{J}}_i^- \tilde{\mathrm{J}}_j^+ \tag{5.48}$$

in the effective pseudospins $\tilde{\mathrm{J}} = 1/2$ built from the lower doublet. Similarly, the term $\frac{1}{4}(ii)$ can be recognised as a matrix of the $\tilde{\mathrm{J}}_i^z \tilde{\mathrm{J}}_j^z$ operator:

$$\underbrace{\frac{1}{2}\left(|\mathrm{ld}_{1,i}\rangle\langle \mathrm{ld}_{1,i}| - |\mathrm{ld}_{2,i}\rangle\langle \mathrm{ld}_{2,i}|\right)}_{\tilde{\mathrm{J}}_i^z} \otimes \underbrace{\frac{1}{2}\left(|\mathrm{ld}_{1,j}\rangle\langle \mathrm{ld}_{1,j}| - |\mathrm{ld}_{2,j}\rangle\langle \mathrm{ld}_{2,j}|\right)}_{\tilde{\mathrm{J}}_j^z}. \tag{5.49}$$

Matrix $16(iii)$ represents a constant shift in energy, which can be dropped out. This leads to the effective Hamiltonian in a form

$$\mathcal{H}_{\mathrm{XXZ}} = \frac{J}{2} \sum_i \Big(\tilde{\mathrm{J}}_i^x \tilde{\mathrm{J}}_{i+1}^x + \tilde{\mathrm{J}}_i^y \tilde{\mathrm{J}}_{i+1}^y + 2(\alpha+\beta) \tilde{\mathrm{J}}_i^z \tilde{\mathrm{J}}_{i+1}^z \Big). \tag{5.50}$$

The emerging formula describes the XXZ model [160][26] for the effective pseudospins $\tilde{\mathrm{J}} = 1/2$ with the non-trivial two-parameter dependence of the Ising term.

Correlation functions in $\tilde{\mathbf{J}}$ pseudospins

Similarly to the Hamiltonian case, one can also translate the matrices of the on-site expressions in the spin and/or orbital correlation functions (5.6)-(5.12) to the SOC basis using the unitary transformation (5.42). Below we provide the resulting one-bond expressions, built out of the suitable $\mathcal{O}_i^{\mathrm{SOC}} \otimes \mathcal{O}_j^{\mathrm{SOC}}$, downfolded to the "lower doublet on both sites" part.

In particular, the full Heisenberg correlations S and T reduce to the same Ising form

$$\tilde{S}, \tilde{T} \longrightarrow \left\langle \begin{pmatrix} \frac{1}{4} & 0 & 0 & 0 \\ 0 & -\frac{1}{4} & 0 & 0 \\ 0 & 0 & -\frac{1}{4} & 0 \\ 0 & 0 & 0 & \frac{1}{4} \end{pmatrix} \right\rangle \longrightarrow \langle \tilde{\mathrm{J}}_i^z \tilde{\mathrm{J}}_j^z \rangle. \tag{5.51}$$

Morover, downfolding of the partial correlations $S^{\gamma\gamma}$, $T^{\gamma\gamma}$ reveals that the planar ($\delta = \{x, y\}$) terms disappear

$$\tilde{S}^{\delta\delta}, \tilde{T}^{\delta\delta} \longrightarrow \left\langle \begin{pmatrix} 0 & 0 & 0 & 0 \\ 0 & 0 & 0 & 0 \\ 0 & 0 & 0 & 0 \\ 0 & 0 & 0 & 0 \end{pmatrix} \right\rangle \longrightarrow 0, \tag{5.52}$$

while the zz terms reduce to the Ising form

$$\tilde{S}^{zz}, \tilde{T}^{zz} \longrightarrow \left\langle \begin{pmatrix} \frac{1}{4} & 0 & 0 & 0 \\ 0 & -\frac{1}{4} & 0 & 0 \\ 0 & 0 & -\frac{1}{4} & 0 \\ 0 & 0 & 0 & \frac{1}{4} \end{pmatrix} \right\rangle \longrightarrow \left\langle \tilde{\mathrm{J}}_i^z \tilde{\mathrm{J}}_j^z \right\rangle. \tag{5.53}$$

[26] Exactly solvable by Bethe Ansatz [161].

Another important observation can be made following the downfolding of the nearest-neighbor spin-orbital correlation $\mathcal{C}_{\mathrm{SO}}$.

$$\tilde{\mathcal{C}}_{\mathrm{SO}} \longrightarrow \left\langle \begin{pmatrix} \frac{1}{16} & 0 & 0 & 0 \\ 0 & \frac{1}{16} & \frac{1}{4} & 0 \\ 0 & \frac{1}{4} & \frac{1}{16} & 0 \\ 0 & 0 & 0 & \frac{1}{16} \end{pmatrix} \right\rangle - \left[\left\langle \begin{pmatrix} \frac{1}{4} & 0 & 0 & 0 \\ 0 & -\frac{1}{4} & 0 & 0 \\ 0 & 0 & -\frac{1}{4} & 0 \\ 0 & 0 & 0 & \frac{1}{4} \end{pmatrix} \right\rangle \right]^2 \tag{5.54}$$

$$\longrightarrow \frac{1}{2}\langle \tilde{\mathrm{J}}_i^x \tilde{\mathrm{J}}_j^x + \tilde{\mathrm{J}}_i^y \tilde{\mathrm{J}}_j^y \rangle + \frac{1}{16} - \langle \tilde{\mathrm{J}}_i^z \tilde{\mathrm{J}}_j^z \rangle^2. \tag{5.55}$$

Namely, the first term in the formula (5.6): $(\mathbf{S}_i \cdot \mathbf{S}_{i+1})\,(\mathbf{T}_i \cdot \mathbf{T}_{i+1})$ downfolds to $\frac{1}{2}\left(\tilde{\mathrm{J}}_i^x \tilde{\mathrm{J}}_j^x + \tilde{\mathrm{J}}_i^y \tilde{\mathrm{J}}_j^y\right) + \frac{1}{16}$. We will return to these important observations later, arguing how they explain the spin-orbital entanglement values in the $\lambda \to \infty$ limit.

Lastly, we add a technical note: in order to express the matrix of the on-site spin-orbit correlation function $\mathcal{O}_{\mathrm{SO}}$ in the same convention we multiply it by a 2×2 identity matrix representing the neighboring site:

$$\tilde{\mathcal{O}}_{\mathrm{SO},i} \otimes \mathrm{id}_j \longrightarrow \left\langle \begin{pmatrix} -\frac{1}{4} & 0 & 0 & 0 \\ 0 & -\frac{1}{4} & 0 & 0 \\ 0 & 0 & -\frac{1}{4} & 0 \\ 0 & 0 & 0 & -\frac{1}{4} \end{pmatrix} \right\rangle \longrightarrow -\frac{1}{4}. \tag{5.56}$$

Such a simple constant form of the correlation is easily explainable—we have projected the correlation proportional to the Ising spin-orbit coupling term onto the ground state of the very term, which has antiferro orientation of the spin and pseudospin [cf. formulae (5.38)-(5.39)]. Thus, only the uniform, negative parts corresponding to that ground state were kept after the projection.

Special lines and phase diagram

Now it is time to recall the three white dashed $\alpha + \beta = const.$ lines in Fig. 5.2. As can be seen in Fig. 5.2, the maximally spin-orbitally entangled part of the "quantum stripe"[27] fits rather well within those lines, improving with increasing system size [cf. Fig. B.1(c)]. It turns out that along these lines the effective Hamiltonian (5.50) simplifies even more.

Namely, along the diagonal $\alpha + \beta = 0$ line XXZ model (5.50) simplifies to the AF XY model

$$\mathcal{H}_{\mathrm{XY}} = \frac{J}{2} \sum_i \left(\tilde{\mathrm{J}}_i^x \tilde{\mathrm{J}}_{i+1}^x + \tilde{\mathrm{J}}_i^y \tilde{\mathrm{J}}_{i+1}^y \right). \tag{5.57}$$

Along the parallel $\alpha + \beta = +1/2$ line the $(\alpha + \beta)$ factor before $\tilde{\mathrm{J}}_i^z \tilde{\mathrm{J}}_j^z$ simplifies model (5.50) to the AF Heisenberg model[28]

$$\mathcal{H}_{\mathrm{AFH}} = \frac{J}{2} \sum_i \tilde{\mathbf{J}}_i \tilde{\mathbf{J}}_{i+1}, \tag{5.58}$$

[27] Cf. Sec. 5.4 for the definition.

[28] For completeness we add that in the $\{\alpha, \beta, \lambda\}$ parameter space the AF H line runs above [in λ] the SU(4) point at $(\alpha = \beta = +1/4, \lambda = 0)$.

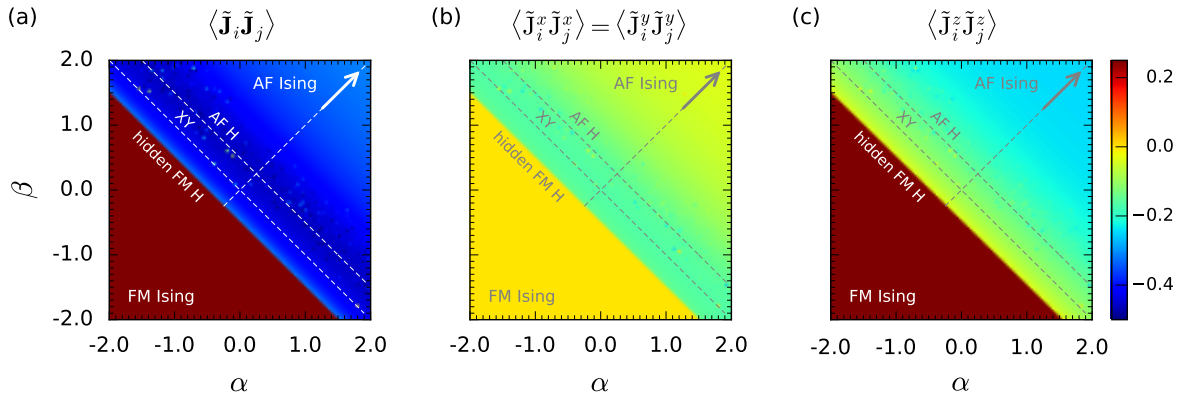

FIGURE 5.11: Ground state-based phase diagram of the effective XXZ model (5.50) emerging from $\langle \tilde{\mathbf{J}}_i \tilde{\mathbf{J}}_j \rangle$, $\langle \tilde{\mathrm{J}}_i^\gamma \tilde{\mathrm{J}}_j^\gamma \rangle$ maps in $\{\alpha, \beta\}$ for the 10-site chain. The diagonal and parallel dashed lines denote simpler models the XXZ models reduces into. The AF Ising label marks both the AF Ising model and the ground state the system converges into for $\alpha, \beta \to +\infty$. In contrast, the FM Ising label relates to the doubly degenerate, polarized FM ground state appearing immediately below the hidden FM Heisenberg line. Naturally, the system is described by FM Ising model for $\alpha, \beta \to -\infty$. Figure has been published in Ref. [144].

while on the $\alpha + \beta = -1/2$ line one obtains

$$\mathcal{H}_{\text{eff}} = \frac{J}{2} \sum_i \Big(\tilde{\mathrm{J}}_i^x \tilde{\mathrm{J}}_{i+1}^x + \tilde{\mathrm{J}}_i^y \tilde{\mathrm{J}}_{i+1}^y - \tilde{\mathrm{J}}_i^z \tilde{\mathrm{J}}_{i+1}^z \Big). \tag{5.59}$$

As observed in Ref. [160], a simple transformation, distinguishing sublattice A for sites i and sublattice B for their nearest neighbors $i \pm 1$

$$\begin{aligned} (\tilde{\mathrm{J}}^x, \tilde{\mathrm{J}}^y, \tilde{\mathrm{J}}^z) &= (-\tilde{\mathrm{J}}^x, -\tilde{\mathrm{J}}^y, \tilde{\mathrm{J}}^z) && \pi\text{-rotation around } z \text{ on sublattice A}, \\ (\tilde{\mathrm{J}}^x, \tilde{\mathrm{J}}^y, \tilde{\mathrm{J}}^z) &= (\tilde{\mathrm{J}}^x, \tilde{\mathrm{J}}^y, \tilde{\mathrm{J}}^z) && \text{identity operation on sublattice B}, \end{aligned} \tag{5.60}$$

reveals the hidden FM Heisenberg nature of model (5.50) along the $\alpha + \beta = -1/2$ line:

$$\mathcal{H}_{\text{FMH}} = \frac{J}{2} \sum_i \Big(-\tilde{\mathrm{J}}_i^x \tilde{\mathrm{J}}_{i+1}^x - \tilde{\mathrm{J}}_i^y \tilde{\mathrm{J}}_{i+1}^y - \tilde{\mathrm{J}}_i^z \tilde{\mathrm{J}}_{i+1}^z \Big) = -\frac{J}{2} \sum_i \tilde{\mathbf{J}}_i \tilde{\mathbf{J}}_{i+1}. \tag{5.61}$$

Besides the entropy maps, the above special lines are also indicated on the $\langle \tilde{\mathbf{J}}_i \tilde{\mathbf{J}}_j \rangle$, $\langle \tilde{\mathrm{J}}_i^\gamma \tilde{\mathrm{J}}_j^\gamma \rangle$ maps in $\{\alpha, \beta\}$ in Fig. 5.11. The maps allow for preparing the ground-state phase diagram of the XXZ model with the unusual $(\alpha + \beta)$-dependent anisotropy (5.50) and compare it to the diagram from the literature [162]. Starting from the left, we report the maximally ferromagnetic $\langle \tilde{\mathbf{J}}_i \tilde{\mathbf{J}}_j \rangle = +0.25$ correlation below the hidden FM Heisenberg line, as indicated in the dark-red color in Fig. 5.11 (a). Figs. 5.11 (b) and (c) reveal vanishing polar correlations and saturated $\langle \tilde{\mathrm{J}}_i^z \tilde{\mathrm{J}}_j^z \rangle = +0.25$. These are all signatures of a classical ferromagnetic pseudospin arrangement, confirmed by the double degeneracy of the ground state level just below the hidden FM Heisenberg line. Naturally, along the hidden FM Heisenberg line the ground state is massively (11-fold for 10 sites) degenerate, due to the large manifold of the maximal total pseudospin $\tilde{\mathrm{J}}_{tot}^{max}$, spanned by $\{|\tilde{\mathrm{J}}_{tot} = \tilde{\mathrm{J}}_{tot}^{max}, \tilde{\mathrm{J}}_{tot}^z = n\rangle\}$, $n \in \{-\tilde{\mathrm{J}}_{tot}^{max}, -(\tilde{\mathrm{J}}_{tot}^{max} - 1), ..., +(\tilde{\mathrm{J}}_{tot}^{max} - 1), +\tilde{\mathrm{J}}_{tot}^{max}\}$ states.[29]

[29] Similarly to the notation of O_{tot}^{max}, introduced in Sec. 4.2.1, here $\tilde{\mathrm{J}}_{tot}^{max}$ is the maximal possible value of the total pseudospin for a given chain.

Along the diagonal XY line we may again utilize the 2-site toy model, this time in $\tilde{\mathrm{J}}$ pseudospins. The ground state of the 2-site AF XY model is the $\frac{1}{\sqrt{2}}(|\uparrow_1\downarrow_2\rangle - |\downarrow_1\uparrow_2\rangle)$ singlet in $\tilde{\mathrm{J}}$ pseudospins, the same as for the AF Heisenberg model, hence, the isotropic negative values of all $\langle\tilde{\mathrm{J}}_i^\gamma\tilde{\mathrm{J}}_j^\gamma\rangle$ are expected. This time however, the 2-site model does not predict the ground-state properties for the longer chains well enough. Already for the 10-site chain the slightly different shades of green color in Fig. 5.11 (b) and (c) indicate a developing anisotropy between the polar and zz correlations. Analytical results[30] confirm this trend: $\langle\tilde{\mathrm{J}}_i^\delta\tilde{\mathrm{J}}_j^\delta\rangle = -1/(2\pi) \approx -0.101$ vs $\langle\tilde{\mathrm{J}}_i^z\tilde{\mathrm{J}}_j^z\rangle = -1/(\pi^2) \approx -0.16$ [163]. Nevertheless, the AF XY ground state still belongs to the spin liquid class. Overall, Fig. 5.11 supports the literature classification of the ground state between the hidden FM Heisenberg and AF Heisenberg lines as the highly fluctuating, spatially entangled quantum 1D antiferromagnet [161, 160, 162].

Above the AF Heisenberg line the system interpolates between the spin-liquid state and the classical Néel state for α, $\beta \to +\infty$. This can be observed in the fairly quickly decreasing polar correlations combined with the increasing zz correlation. Hence, the AF Ising label marks both the AF Ising model and the ground state the system converges to for α, $\beta \to +\infty$.

5.7.2 Origin of the quantum stripe

Recalling once again Fig. 5.2 (a), we see a substantial spin-orbital entanglement confined to the central triangular region of the critical SU(4)-singlet phase in the $\lambda = 0$ limit. This is because the spin-orbital term $J\,(\mathbf{S}_i \cdot \mathbf{S}_{i+1})\,(\mathbf{T}_i \cdot \mathbf{T}_{i+1})$, enabling such amount of the entanglement in the ground state, has to compete with the spin/orbital-only terms, independently multiplied by α and β parameters. Therefore, the right conditions for the substantially spin-orbitally entangled ground state appear only for small enough $|\alpha|$ and $|\beta|$.

In the $\lambda \to \infty$ limit in Fig. 5.2 (c) the white dashed $\alpha + \beta = -1/2$, $\alpha + \beta = 0$ and $\alpha+\beta = +1/2$ lines, corresponding to the hidden FM Heisenberg, XY, and AF Heisenberg models in $\tilde{\mathrm{J}}$ pseudospins, respectively, set the right conditions for the quantum fluctuations and spatial entanglement in $\tilde{\mathrm{J}}$s to appear. Along the $\alpha + \beta = -1/2$ line we have a massively degenerate Heisenberg ferromagnet, represented by both the polarized and the entangled states, slightly above this line however the AF XY term starts to dominate over the Ising part in formula (5.50). Along the $\alpha + \beta = 0$ line the Ising term vanishes completely, "releasing" the AF XY term to fully decide about the ground state — a non-degenerate, spatially entangled, highly fluctuating spin liquid. Along the $\alpha + \beta = +1/2$ the Ising term again matches in strength the XY term, forming the AF Heisenberg model. Thus, for $-1/2 < \alpha + \beta \lesssim 1/2$ the ground state belongs to the the quantum 1D antiferromagnet class. We see that the shape of the quantum stripe follows exactly from the $(\alpha + \beta)$ dependance of the Ising term, with the $\alpha + \beta = x$ constraint forming less competitive conditions than independent α and β in $\lambda = 0$ case. The spacial entanglement in $\tilde{\mathrm{J}}$s is linked to the underlying saturated entanglement between spins and orbitals the $\tilde{\mathrm{J}}$s are made of, even though the link between the two is classical.

The easiest way to see it is by downfolding Hamiltonian (5.2) term by term. Similarly to the correlation functions, the spin-orbital term $J\,(\mathbf{S}_i \cdot \mathbf{S}_{i+1})\,(\mathbf{T}_i \cdot \mathbf{T}_{i+1})$ downfolds to $\frac{J}{2}\left(\tilde{\mathrm{J}}_i^x\tilde{\mathrm{J}}_j^x + \tilde{\mathrm{J}}_i^y\tilde{\mathrm{J}}_j^y\right) + \frac{J}{16}$. Notice, that this term does not carry any α or β dependence even before the downfolding. In contrast, $J\alpha\mathbf{T}_i \cdot \mathbf{T}_{i+1}$ and $J\beta\mathbf{S}_i \cdot \mathbf{S}_{i+1}$ terms both download to $\tilde{\mathrm{J}}_i^z\tilde{\mathrm{J}}_j^z$, multiplied by $J\alpha$ and $J\beta$, respectively. More precisely, while the polar $\mathrm{S}_i^\delta\mathrm{S}_{i+1}^\delta$, $\mathrm{T}_i^\delta\mathrm{T}_{i+1}^\delta$ terms vanish, $\mathrm{S}_i^z\mathrm{S}_{i+1}^z$, $\mathrm{T}_i^z\mathrm{T}_{i+1}^z$ terms both downfold to $\tilde{\mathrm{J}}_i^z\tilde{\mathrm{J}}_j^z$.

The fact that the term generating quantum entanglement in $\tilde{\mathrm{J}}$s at the center of the "quantum stripe", the XY term, originates fully from the $J\,(\mathbf{S}_i \cdot \mathbf{S}_{i+1})\,(\mathbf{T}_i \cdot \mathbf{T}_{i+1})$ term, responsible for the significant spin-orbital entanglement in $\lambda = 0$, while the Ising term, that can both help support

[30] Obtained utilizing the transformation to the fermionic degrees of freedom of the Jordan-Wigner type [163].

the entanglement[31] or suppress it, originates from the terms that were suppressing the spin-orbital entanglement in $\lambda = 0$ limit, is quite remarkable. It allows us to recognise the highly (spin-orbitally) entangled state in the phase diagram 5.9 as the 1D quantum antiferromagnet in $\tilde{\text{J}}$s. Overall, the analysis above brings the analytical justification to the "quantum stripe" and the connection between the saturated spin-orbital entanglement and the high entanglement in $\tilde{\text{J}}$s within the stripe in the $\lambda \to \infty$ limit.

Correlations within the quantum stripe

Here we first compare correlation functions (5.6)-(5.12) along the $\alpha + \beta = 0$ line to their lower doublet-projected forms (5.51)-(5.56), calculated in the ground state of the XY model, and then expand the discussion to the whole "quantum-stripe" region. We start from the $\mathcal{C}_{\text{SO}}$ correlation, denoted by a thick green line in Fig. 5.4. We observe that regardless if we follow cut A or B, above λ_{CRIT} the function converges to its asymptotic value $\tilde{\mathcal{C}}_{\text{SO}}$, denoted by the dark-green dashed line. Along the $\alpha + \beta = 0$ line, above λ_{CRIT}, the $\mathcal{C}_{\text{SO}}$ value is quite uniform, see Fig. 5.3 (b). Moreover, Fig. B.2 (c) reveals the non-zero values of $\mathcal{C}_{\text{SO}}$ for the whole "quantum stripe". Notice, that although $\mathcal{C}_{\text{SO}}$ recognises the same range of the most entangled region in the $\lambda \to \infty$ limit as the entanglement entropy, its absolute value is actually smaller than in the SU(4) singlet for $\lambda = 0$.

On a side note we add that $\mathcal{C}_{\text{SO}}$ has only an infinitesimally small value above the stripe. While we have strong hints that the uniform entanglement entropy above the stripe is a finite-size effect, since it is decreasing with the system size, the difference in behaviour of the entropy and $\mathcal{C}_{\text{SO}}$ above λ_{CRIT} is concerning and suggests that $\mathcal{C}_{\text{SO}}$ can only qualitatively estimate the entanglement. One of the reasons of such shortcomings may be quite straight forward—$\mathcal{C}_{\text{SO}}$ verifies, whether the decoupling of the $(\mathbf{S}_i \cdot \mathbf{S}_{i+1})\,(\mathbf{T}_i \cdot \mathbf{T}_{i+1})$ term to spin-only and orbital-only term is possible, hence, it is restricted to the nearest neighbors.

Returning to Fig. 5.4, one notices that along both cuts A and B, $\mathcal{O}_{\text{SO}}$ correlation also converges to its asymptotic value $\tilde{\mathcal{O}}_{\text{SO}}$, denoted as the dark-red dashed line. Note that the lower-doublet projected $\tilde{\mathcal{O}}_{\text{SO}}$ formula (5.56) is a constant and is valid for the whole $\{\alpha, \beta\}$ parameter plane in the $\lambda \to \infty$ limit. The $-1/4$ antiferro value is a sign that the ground state is built from $|+\downarrow\rangle$, $|-\uparrow\rangle$ on-site Néel arrangements of spins and orbitals. Therefore, the saturated $|\mathcal{O}_{\text{SO}}|$ value is a good indicator of crossing the λ_{CRIT} threshold.[32]

Another good indicator of whether the system is already above λ_{CRIT} is the value of the polar $S^{\delta\delta}$, $T^{\delta\delta}$ correlations (5.9)-(5.10), where $\delta = x, y$. In fact, these functions downfold to zero because the lower-doublet states are of the classical Néel nature in the z direction on each site. Hence, the system is well described by the $\tilde{\text{J}}$ pseudospins as soon as the thick green lines in Fig. 5.6 converge to their zero asymptotes (dark-green dashed lines).

In contrast to the polar correlations, S^{zz} and T^{zz} become negative above λ_{CRIT}, much weaker however than the Ising value -0.25, confirming inter-site quantum fluctuations in the highly entangled state. These values are also well converged to their asymptotes above λ_{CRIT}. What is more, also weakly antiferromagnetic values of the full S and T correlations in Figs. 5.5 (b)-(c) are consistent with the $\langle \tilde{\text{J}}_i^z \tilde{\text{J}}_j^z \rangle$ values, to which they downfold.

All the above tropes suggest that in the $\alpha \in [-1, 1]$ interval of the $\alpha + \beta = 0$ line the system is qualitatively in the highly spin-orbitally entangled state well before $\lambda \to \infty$ and can be already approximately described by $\tilde{\text{J}}$ pseudospins just above λ_{CRIT}. This is also consistent with Fig.

[31] By completing the Hamiltonian into the Heisenberg form.

[32] Another hint that the system is already defined by $\tilde{\text{J}}$ pseudospins built out of the Ising configurations is the possibility of the on-site decoupling in the z components. Namely, $(1/\text{L}) \sum_i (\langle \text{S}_i^z \text{S}_{i+r}^z \text{T}_i^z \text{T}_{i+r}^z \rangle - \langle \text{S}_i^z \text{T}_i^z \rangle \langle \text{S}_{i+r}^z \text{T}_{i+r}^z \rangle) = 0$, $r = 1, 2, ..., \text{L}/2$ while all other spin/orbital combinations do not vanish. We have verified that this happens just above λ_{CRIT}.

5.2, where we see that the saturated spin-orbital entanglement first appears in the center of the maps.

5.7.3 Origin of the classical state

In the $\lambda \to \infty$ limit below the $\alpha + \beta = -1/2$ line there is not only no spin-orbital entanglement [zero entropy values in Fig. 5.2 (c) and zero $\mathcal{C}_{\rm SO}$ values in Fig. B.2 (c)], but any quantum entanglement whatsoever. In Sec. 5.6 we have inspected this classical state along the representative $\alpha + \beta = -1$ line, observing that above $\lambda_{\rm CRIT}$[33] the values of various correlations consistently point to the Ising ferromagnetic patterns along the bonds ($S = T = +1/4$), arranged in such a way, that on each site there is a classical Néel configuration between the S and T degrees of freedom ($\mathcal{O}_{\rm SO} = -1/4$). This means that also in $\tilde{\rm J}$ pseudospins, built out of the above lower-doublet Néel configurations, one should observe the maximally ferromagnetic nearest-neighbor correlations, indicating a polarized state. Indeed, $\langle \tilde{\rm J}_i^z \tilde{\rm J}_i^z \rangle$ reaches uniformly $+1/4$ value in Fig. 5.11 (c) while the planar correlations are zero below the $\alpha + \beta = -1/2$ line. Recalling the downfolded form of the $\mathcal{C}_{\rm SO}$ correlation (5.55), one notices that the FM Ising state in $\tilde{\rm J}$s would return zero value of the average $\langle \tilde{\rm J}_i^x \tilde{\rm J}_j^x + \tilde{\rm J}_i^y \tilde{\rm J}_j^y \rangle$, while the remaining $\langle \tilde{\rm J}_i^z \tilde{\rm J}_i^z \rangle^2 = 1/16$ would be cancelled by the constant term.

Hence, the spin-orbital entanglement disappears completely below the $\alpha + \beta = -1/2$ line because the values of the coupling parameters in both full and effective Hamiltonian support the splitting of the massively degenerate ground-state level immediately below the line. This leaves only the classical FM Ising configurations along the bonds, with the spins and orbitals connected in an antiferromagnetic Ising way on each site.

[33] $\lambda_{\rm CRIT2}$ along cut C and any $\lambda > 0$ along cut D.

5.8 Summary and conclusions

So far the counterintuitive phenomenon of the spin-orbital entanglement was mainly considered for those $3d$ transition-metal oxides (TMOs) for which the orbitals are not fully quenched and partially filled—in particular for the cubic vanadates and titanites. Crucially, for these materials the relativistic on-site spin-orbit coupling is negligible. Somewhat surprisingly, however, this phenomenon has not been systematically explored for the late TMOs with the significant spin-orbit coupling, despite the advanced efforts to describe the honeycomb iridates and ruthenates by the effective Hamiltonian expressed in the low-energy degrees of freedom enforced by the spin-orbit coupling. Interestingly, the phase diagram of the effective Hamiltonian in these degrees of freedom contains finite regions of the strongly spatially entangled phase—the Kitaev spin liquid, cf. Chapters 2-3.

In this chapter we have interpolated between the negligible spin-orbit coupling and the dominant spin-orbit coupling limits in a Mott insulator with spin and orbital degrees of freedom. The primary purpose of this study was to investigate the spin-orbital entanglement and its possible connection to the spatial entanglement in $\tilde{\text{J}}$s. To this end, we have solved a minimal spin-orbital model for the above problem, consisting of the $\text{SU}(2) \otimes \text{SU}(2)$ symmetric Kugel-Khomskii spin-orbital exchange term with the parameters $J = +1$, α and β and the Ising on-site spin-orbit coupling, parametrized by λ. We have utilized the numerical exact diagonalization as a default method for small to moderate-size systems with the expected strongly quantum effects. We have calculated various observables in the ground state of the spin-orbital model on the $\text{L} = 4n$-site chains:

- the entanglement entropy of the von Neumann type $\mathcal{S}_{\text{vN}}$ as well as the spin-orbital correlation $\mathcal{C}_{\text{SO}}$ to examine the spin-orbital entanglement;
- the on-site spin-orbit correlation $\mathcal{O}_{\text{SO}}$ to monitor the response of the system to the spin-orbit coupling;
- the spin and/or orbital correlations to examine the magnetic properties.

When necessary, we performed finite-size scaling.

Last but not least, in the $\lambda \to \infty$ limit we have projected the Kugel-Khomskii Hamiltonian onto the ground state of the Ising spin-orbit coupling, obtaining an effective XXZ Hamiltonian in $\tilde{\text{J}} = 1/2$ pseudospins.

Evolution of the spin-orbital entanglement with increasing spin-orbit coupling

The analysis of the results of the full and effective models allowed us to understand the evolution of the spin-orbital entanglement with increasing λ. Thus, we can now answer the first question posed at the begining of this chapter: *What kind of evolution does the spin-orbital entanglement develop with increasing spin-orbit coupling?* The maps of the entanglement entropy $\mathcal{S}_{\text{vN}}$ and $\mathcal{C}_{\text{SO}}$ revealed that the evolution from the phase diagram of the Kugel-Khomskii model to the phase diagram of the XXZ model is gradual.

To fully understand this complex evolution we selected two representative lines: $\alpha + \beta = 0$ and $\alpha + \beta = -1$. While the former line crosses the most quantum regions both in the $\lambda = 0$ and in the $\lambda \to \infty$ limit, the latter line crosses the completely classical regions in both limits. We have examined in detail the evolution in spin-orbit coupling λ along these lines. It turned out that we could distinguish:

- **The evolution of type A**—from the $\text{FM} \otimes \text{AO}/\text{AF} \otimes \text{FM}$ phases and their perturbed versions for $\lambda/J \lesssim \lambda_{\text{CRIT}}$, through an interval of a rapid spin-orbital entanglement growth λ_{CRIT}, up to the highly entangled state with the saturated spin-orbital entanglement,

recognised as the 1D quantum antiferromagnet in terms of $\tilde{\mathrm{J}}$ pseudospins, cf. Fig. 5.3. While all the observables evolve smoothly in λ, indicating a crossover character of the evolution, the properties of the state below λ_{CRIT} are very different from the ones above it. Below λ_{CRIT} the spin-orbital entanglement and the response to the spin-orbit coupling are at most negligible, while the magnetic features are complementary in the spin and orbital sectors. Above λ_{CRIT} the spin-orbital entanglement and the response to the spin-orbit coupling are saturated while the magnetic features are weakly antiferromagnetic in both spin and orbital sectors.

- **The evolution of type B**, where the system departs from the substantially spin-orbitally entangled, critical SU(4) singlet through n kinks for the $\mathrm{L} = 4n$-site chain, up to a highly entangled state, cf. Fig. 5.3. The finite-size scaling of this discontinuous increase of the spin-orbital entanglement and the response of the system to the spin-orbit coupling suggests that in the thermodynamic limit the SU(4) singlet is unstable for $\lambda > 0$. However, before the spin-orbital entanglement saturates in the highly entangled state, there is an intermediate region of continuously increasing spin-orbital entanglement called an intermediate entangled state (IES). In this case λ_{CRIT} is set by the stabilized position of the final kink, corresponding to the level crossing in the energy spectra. Above λ_{CRIT} the system is in the highly entangled state.

- **The evolution of type C**, starting as a crossover from the FM$\otimes$AO/AF$\otimes$FO phases and their perturbed versions for $\lambda/J \lesssim \lambda_{\mathrm{CRIT1}}$, through an interval of the rapid spin-orbital entanglement growth λ_{CRIT1}, interrupted by a level crossing with a completely classical state at λ_{CRIT2}, cf. Fig. 5.10. Thus, at first the system evolves as in case A, gaining more and more spin-orbital entanglement, but this is abruptly stopped at λ_{CRIT2}. As a result, for $\lambda \to \infty$ the system is in a doubly degenerate state with the classical ferromagnetic spin and orbital correlations on bonds and the classical Néel correlations between spins and orbitals on each site.

- **The evolution of type D**, for which the massive degeneracy of the FM $\otimes$ FO state, containing both the polarized, classical states as well as the states with some "internal" quantum entanglement *within* the spin and orbital sectors but no spin-orbital entanglement, is reduced to the double degeneracy as soon as $\lambda > 0$, cf. Fig. 5.10. As a result, only the fully classical states, consisting of the ferromagnetic configurations on bonds and Néel on-site configurations have the lowest energy.

Moreover, we may summarize the differences between the $\lambda < \lambda_{\mathrm{CRIT}}$ and $\lambda > \lambda_{\mathrm{CRIT}}$ regions as follows:

1. For $\lambda < \lambda_{\mathrm{CRIT}}$:
   - The extent of the significant spin-orbital entanglement in the $\{\alpha, \beta\}$ parameter space is *qualitatively* the same as in the $\lambda = 0$ limit.
   - If the ground state displayed significant amount of the spin-orbital entanglement at $\lambda = 0$, it gains more spin-orbital entanglement with increasing λ (the SU(4)-singlet $\to$ IES case).
   - If the ground state showed no spin-orbital entanglement for $\lambda = 0$, it still shows none or negligible spin-orbital entanglement for $\lambda > 0$ (the FM$\otimes$FO and FM$\otimes$AO/AF$\otimes$FM $\to$ perturbed FM $\otimes$ AO/AF $\otimes$ FM cases, respectively).
2. For $\lambda > \lambda_{\mathrm{CRIT}}$:
   - The significantly spin-orbitally entangled phase occupies larger region of $\{\alpha, \beta\}$ parameter space than in the $\lambda = 0$ case ("quantum stripe" vs SU(4)-singlet, respectively).

- The ground state may become spin-orbitally entangled even if it showed no spin-orbital entanglement in the $\lambda = 0$ case.
- Spin-orbital entanglement may vanish only if the quantum fluctuations vanish in the ground state of the effective model.

Finally, we emphasise the conclusions described in Sec. 5.7.2-5.7.3.

Highlight: spin-orbital entanglement induced by the spin-orbit coupling

Now we may also answer the third question from the beginning of this chapter: *How does the spin-orbital entanglement arise in the limit of strong spin-orbit coupling?* By projecting the full Hamiltonian (to the ground state of the spin-orbit coupling) term by term we determined that the Ising spin-orbit coupling may promote the stronger in value and more robust spin-orbital entanglement. This is due to the quenching of the spin-only and orbital-only terms competing with the $(\mathbf{S}_i \cdot \mathbf{S}_j)(\mathbf{T}_i \cdot \mathbf{T}_j)$ term, enabling significant amount of the spin-orbital entanglement. It turns out that the latter term downfolds to the XY model in $\tilde{\mathrm{J}}$s, while the spin-only and orbital-only terms downfold together to $(\alpha + \beta)\tilde{\mathrm{J}}_i^z \tilde{\mathrm{J}}_j^z$. As a result, the effective model between $-1/2 < (\alpha + \beta) < +1/2$ has a highly entangled spin-liquid ground state, while for $+1/2 < (\alpha + \beta) < +\infty$ the ground state interpolates between the spin liquid and the classical Néel limits of a 1D antiferromagnetic state. The maximal part of the "quantum stripe", seen in the saturated spin-orbital entanglement entropy values is directly connected to the suppression of the Ising term in the XXZ model between the hidden FM Heisenberg and AF Heisenberg lines. In this way the spatial quantum entanglement in $\tilde{\mathrm{J}}$s is connected to the underlying spin-orbital entanglement even for the classical link between these degrees of freedom. In other words, even the classical spin-orbit coupling may promote spin-orbital entanglement if the spin-orbital model in $\lambda = 0$ allowed for the spin-orbital entanglement for certain parameter regime.

Highlight: spin-orbital entanglement suppressed by the spin-orbit coupling

The answer to the remaining, second question from the beginning of the chapter: *Can one always assume that in the limit of strong spin-orbit coupling the spin-orbital entanglement is non-zero?* is negative. In fact, in the $\lambda \to \infty$ limit there is a whole half-plane in $\{\alpha, \beta\}$ parameters, limited by the $\alpha + \beta < -1/2$ line representing the hidden FM Heisenberg model, below which the ground state becomes the Ising ferromagnet in $\tilde{\mathrm{J}}$ pseudospins. In the spin and orbital degrees of freedom this classical, doubly degenerate state is characterized by the ferromagnetic bond and Néel on-site correlations. This classical state may appear for $\lambda \to \infty$ even if below λ_{CRIT2} the values of the entanglement entropy were already substantial and even if at $\lambda = 0$ the independent fluctuations in spin and orbital sectors were allowed [evolution of type C].

Chapter 6

Outlook

Better description of Kitaev materials

The interesting physics of the late transition-metal compounds is still not fully understood. Some of these materials are the spin-orbit assisted Mott insulators, for which substantial value of the on-site spin-orbit coupling enables for opening the charge gap for the realistic values of the on-site Coulomb repulsion U. In this thesis we have considered two examples from this class, Na_2IrO_3 and α-$RuCl_3$—the quasi-2D materials on the honeycomb lattice, and discussed which values of the model parameters could best described the Kitaev-like physics of these compounds.

Below we comment how one can build up on the results presented in this thesis to deepen the understanding of the proximity of the Kitaev-candidate materials to the Kitaev spin-liquid regions.

- **Maps of the ordered moment properties**
  Our multi-method study of the Kitaev-like models (the effective models in the degrees of freedom enforced by the large spin-orbit coupling in the considered materials) resulted in the maps in the models' parameter space of the ordered moment properties such as e.g. length and direction. The maps reveal the general tendencies for fixed values of the selected model parameters and thus allow to understand the evolution of the ordered moment in each parameter separately. Although at this stage they can be quite useful for the experimentalists to understand which term of the effective Hamiltonian can be related to the observed magnetic moment behaviour ultimately *all* the Hamiltonian parameters should be considered together in order to search for the Na_2IrO_3 and α-$RuCl_3$ positions on such maps. In fact, as mentioned in Sec. 3.6, the first study of this kind was recently published for the Na_2IrO_3 case in Ref. [108], with the two candidate locations selected.

- **Usefulness of the CMFT method**
  While the CMFT method is clearly not perfectly suited for the Hamiltonians containing the bond-directional frustration, the imperfect CMFT results can still be used for the qualitative understanding of the evolution of the ordered moment in the long-range ordered phases of the Kitaev-like models. Namely, despite the lower amount of quantum fluctuations in the CMFT ground state, which influences the rate of the evolution of the ordered moment direction and overestimates the ordered moment value in the phases of the antiferromagnetic nature, the results correctly distinguish the quantum vs classical character of each phase.

- **Alternative studies of the ordered moment value**
  Comparison with the experimental magnetic moment values for Na_2IrO_3 and α-$RuCl_3$ suggest that: (a) the ordered moment value may be in general "too flat" in the whole zigzag phase to serve as a mean to narrow down the Hamiltonian parameter range for the considered materials; (b) the CMFT value may be quite overestimated, therefore similar calculations utilizing alternative methods, e.g. higher order perturbation theory [84], would be of great value.

- **Importance of the Na_2IrO_3 and α-$RuCl_3$ positions in the model parameter space**
  In order to realize further plans to utilize the topologically protected excitations (from the gapped version of the KSL state) as stable qubits, one has to first estimate the distance between the positions of the considered materials and the KSL regions existing in the phase diagrams of the Kitaev-like models. In case of Na_2IrO_3 and α-$RuCl_3$ further self-consistent experimental and theoretical effort is necessary to uniquely fix their distance to the hidden AF KSL region, characterized by the FM sign of the K parameter, matching the considered materials. This effort is still in progress, the reader may inspect very interesting recent results published in Ref. [38]. In principle, the hidden FM KSL region may be also interesting in the future, due to its larger size, provided that a material with matching coupling parameters is synthesised.

More realistic studies of spin-orbital entanglement

As explained in Sec. 2.2.1, a typical quantum spin liquid is characterized by the massive spatial quantum entanglement. In the cases discussed in this thesis, this spatial entanglement concerns the $\tilde{J}$ pseudospins—the effective degrees of freedom in the large spin-orbit coupling limit. In fact, both the Kitaev-like models and the effective XXZ model described in Chapter 5 are described in the effective pseudospins $\tilde{J} = 1/2$. As a result, for the latter model in large spin-orbit coupling limit we obtained a region of considerable size with the significant amount of the spatial quantum entanglement in $\tilde{J} = 1/2$ pseudospins—the "quantum stripe". We uncovered the underlying saturated spin-orbital entanglement, mimicking the behaviour of the entanglement in $\tilde{J}$s. Moreover, we found very clear evidence that even the spin-orbit coupling of the Ising type may support the spin-orbital entanglement in the large spin-orbit coupling limit if there is a term in the Kugel-Khomskii part of the Hamiltonian supporting spin-orbitally entangled ground state in the negligible spin-orbit coupling limit.

- **Consequences for real materials**
  Nevertheless, the model considered in Chapter 5 is not a realistic model for the Kitaev-candidate materials. Therefore, a careful study of the spin-orbital entanglement in the large spin-orbit coupling limit for the models consisting of the Kugel-Khomskii and on-site spin-orbit coupling terms derived specifically for iridates and ruthenates would be of great value. In such a quasi-2D case one should carefully consider the bond-directional dependence of the virtual hopping paths in order to obtain the realistic behaviour of the spin-orbital entanglement for the above compounds.

  Here we mention, that even for the simpler geometry of Sr_2IrO_4 with the 180° Ir-O-Ir angles such calculation would have to take into account spin 1/2 and effective orbital 1 local degrees of freedom. This would lead to faster growth rate of the dimension of the Hamiltonian matrix with the system size. Nevertheless, calculations for two square plaquettes [dimension $2^6 \times 3^6 = 46656$] seem easily doable, and even six plaquettes [12 sites, dimension $2^{12} \times 3^{12} = 2176782336$] seem possible with a clever optimization of the ED code, because of the dimension still being lower than for 16 sites in the current case described in Chapter 5.

- **Spin-orbital entanglement evolution with the on-site spin-orbit coupling**
  Furthermore, it would be also interesting to see how the hypothesised spin-orbital entanglement in such more realistic model evolves "down" from the large spin-orbit coupling limit to the negligible spin-orbit coupling limit and verify the universality of the mechanisms described in Chapter 5.

Appendix A

Appendices for Kitaev-like models

A.1 Ground-state energy from the central hexagon

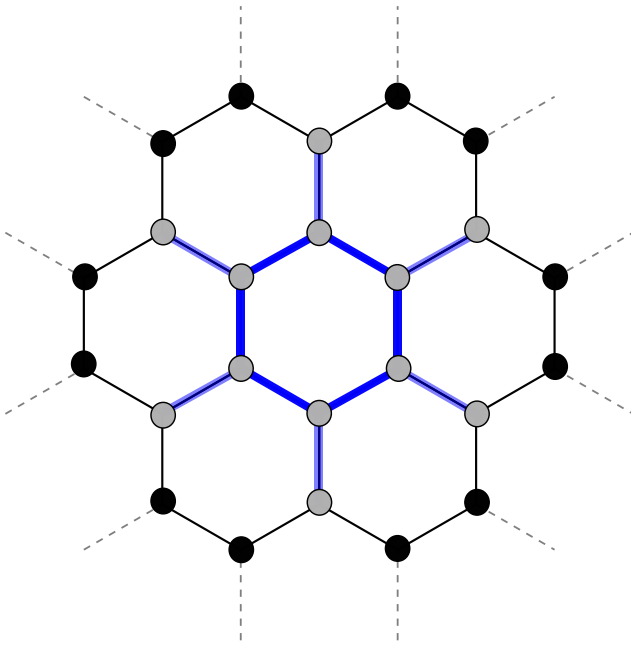

FIGURE A.1: A scheme of retrieving the ground-state energy from the central hexagon of the 24-site cluster with polarized boundary bonds (dashed lines). The bonds marked in solid blue [denoted as *sb* in eq. A.1] are taken into account with a factor 1 while the semi-transparent bonds [*tb* in eq. A.1] are weighted by 1/2 as they only have one site belonging to the central hexagon.

The CMFT procedure is capable of producing the $E_{GS}/site$ value directly by diagonalizing the Hamiltonian. However, the initial polarization of the external sites (black circles in Fig. A.1) deprives the energy from some quantum fluctuations contribution. The way to partially correct this is to obtain the ground-state energy value from the least affected central hexagon of the 24-site cluster, which directly experiences only the fully quantum Hamiltonian. The basic idea is to decompose the estimate of the energy—the average of the internal Hamiltonian (3.22) in the ground state — into the sum of pseudospin correlations. These correlations, calculated in the 24-site CMFT ground state, are then summed over the bonds building the central hexagon (solid blue) with a factor 1 and over the bonds sticking out of the hexagon (semi-transparent blue) with a factor 1/2. At the end we normalize the energy by the 6 sites building the hexagon. As it is commented in Chapter 3, such energy is rather close to the reference ED-based values. The explicit formula for the ground state energy E_{GS} from the central hexagon (*ch*) looks as

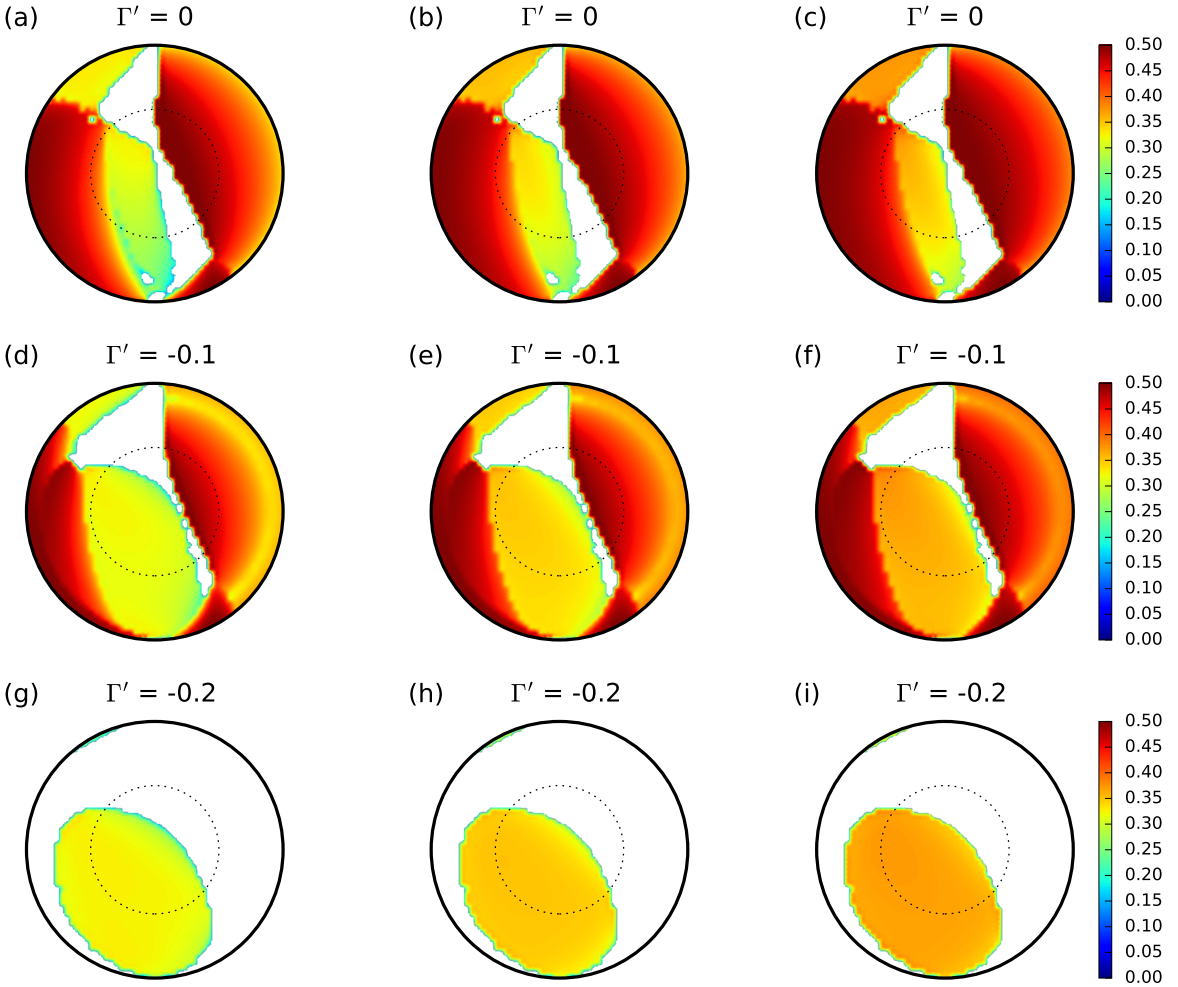

FIGURE A.2: Average of the pseudospin value (CMFT-based) as a function of the distance from the mean-field boundary (MF PBC) bonds: (a), (d), (g)— value averaged over the central hexagon, (b), (e), (h)— value averaged over the whole 24-site cluster, (c), (f), (i)—value taken from the external site.

follows:

$$\mathrm{E}_{\mathrm{GS}ch} = J \sum_{\langle i,j\rangle \in sb} \langle \mathbf{S}_i \cdot \mathbf{S}_j \rangle + K \sum_{\langle i,j\rangle \in sb} \langle \mathrm{S}_i^{\gamma} \mathrm{S}_j^{\gamma} \rangle + \frac{J}{2} \sum_{\langle i,j\rangle \in tb} \langle \mathbf{S}_i \cdot \mathbf{S}_j \rangle + \frac{K}{2} \sum_{\langle i,j\rangle \in tb} \langle \mathrm{S}_i^{\gamma} \mathrm{S}_j^{\gamma} \rangle, \tag{A.1}$$

$$\frac{\mathrm{E}_{\mathrm{GS}ch}}{site} = \frac{\mathrm{E}_{\mathrm{GS}ch}}{6}, \tag{A.2}$$

where *sb* are the solid blue bonds and *tb* are the semi-transparent bonds in Fig. A.1.

A.2 CMFT-based ordered moment

Fig. A.2 presents the CMFT-based results on the 24-site cluster with mean-field (MF) bonds assigned as in the main part of the thesis. Here we present examples of how the ordered moment value changes with the distance from the MF bonds.

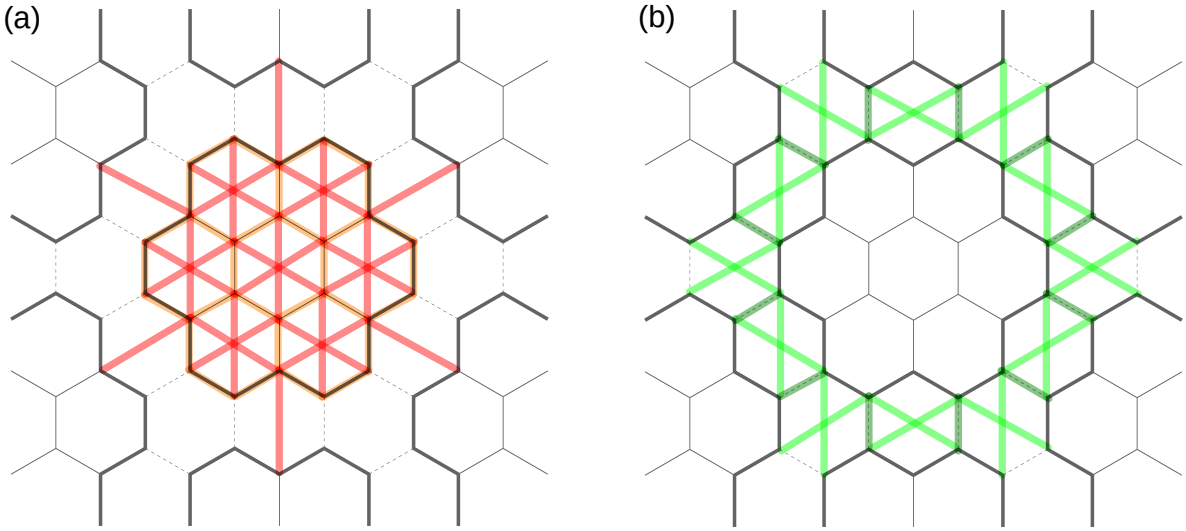

FIGURE A.3: An example of the CMFT bond setup for the nearest and third-neighbor Hamiltonian. The presented scheme maximizes the amount of quantum bonds while minimizing the number of mean-field bonds and restricting them to the original boundary bonds between periodic copies of the 24-site cluster. Panel (a)—nearest-neighbor and third-neighbor operator-operator bonds in orange and red, respectively. Panel (b)—nearest-neighbor and third-neighbor mean-field bonds in dark and light green, correspondingly.

A.3 CMFT setup for J_3

There are multiple ways to introduce further-neighbor interactions into the CMFT Hamiltonian $\mathcal{H} = \mathcal{H}_{\text{IN}} + \mathcal{H}_{\text{MF}}$. In this appendix we present a particular scheme how to supplement the nearest-neighbor (NN) J, K, Γ, Γ' interactions on the honeycomb lattice by the third-neighbor Heisenberg interaction represented by the J_3 coupling parameter. Our approach benefits from the maximal number of quantum operator-operator bonds and the restriction of mean-field bonds to the bonds between original external sites of the 24-site cluster.

Fig. A.3 (a) illustrates the distribution of quantum bonds forming the internal part of the CMFT Hamiltonian ($\mathcal{H}_{\text{IN}}$). Nearest-neighbor (orange) bonds apply to the J, K, Γ and Γ' terms in Hamiltonian (2.22), while third-neighbor (red) bonds concern the J_3 Heisenberg term. We emphasise that the third-neighbor operator-operator connections between the periodic copies of the cluster do not concern the previously defined external sites, marked by the black circles in Fig. 3.2. On the contrary, these new bonds join only the sites previously connected only by the quantum NN bonds.

Fig. A.3 (b) presents the distribution of the mean-field bonds contributing to $\mathcal{H}_{\text{MF}}$. In our proposal not only the NN (dark-green) bonds, but also the third-neighbor (light-green) bonds are restricted to the original external sites form Fig. 3.2.

In this way the structure of the quantum and mean-field parts of the CMFT Hamiltonian is kept consistent. Although the number of connections grows, the boundary of the cluster preserves its "shape", allowing for the comparison of the purely nearest-neighbor and nearest-neighbor + third-neighbor results.

Below we would like to comment on the practical side of the CMFT method. From our experience the CMFT behaviour for the bond-anisotropic Hamiltonian may be initially quite puzzling. Thus, we would like to suggest not taking the results for granted but comparing them with a less biased, more quantum method, e.g. ED-based. Varying convergence time of the CMFT loop is also a disadvantage, because of the high time requirements that only some of the machines in the

computational centers could offer. Keeping this in mind, the calculation proposed above should be feasible.

A.4 Evolution in Γ'

In order to allow the reader to develop some intuition in general Γ' trends below we replot the full maximal-overlap results concerning the evolution of the phases in Γ' parameter when $J_3 = 0$. The results as well as the figure was *prepared by Jiří Chaloupka* and published in Ref. [29].

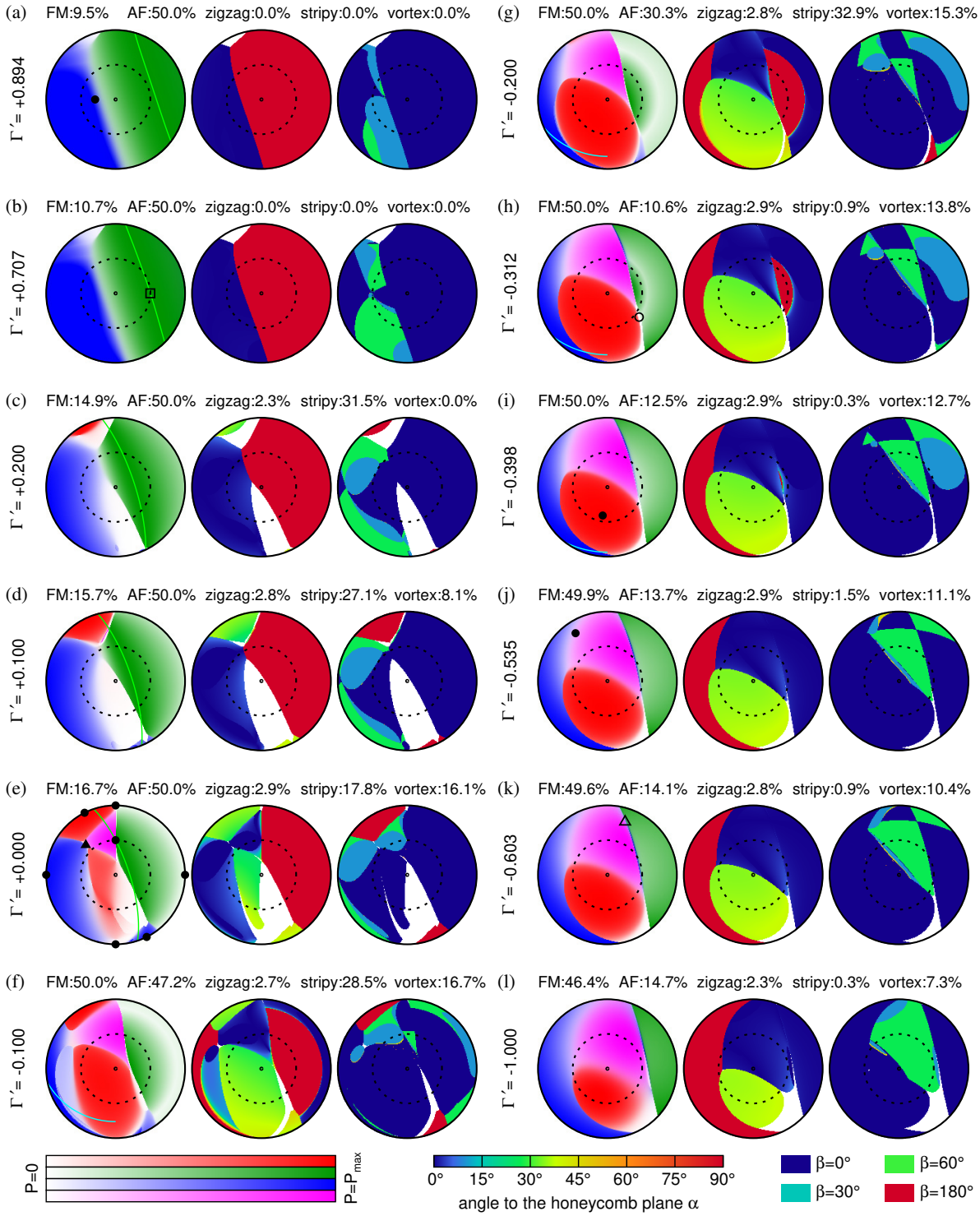

FIGURE A.4: A more dense set of $\Gamma' \neq 0$, $J_3 = 0$ slices of the phase diagram via the maximal-overlap method. The left circle in each row presents the phases with the maximal probability P_{max}. Its change is marked by the color gradient, with the colors: blue marking the FM/stripy, pink—vortex, green — Néel, red—zigzag phases. The middle circle presents the angle α from the honeycomb plane to the pattern while the right cricle illustrates the azimuthal angle ϕ, here denoted by the letter β. The panels have special manifolds indicated: the fluctuation-free lines as well as the special points: hidden and explicit SU(2) points—black circles on panels (a), (e), (i), (j), Kitaev points—black circles on panel (e), empty circle on panel (h), compass points—black triangle on panel (e), empty triangle on panel (k), and Ising point —empty square on panel (b). Figure, published in Ref. [29].

Appendix B

Appendices for spin-orbital entanglement

B.1 Supplementary figures

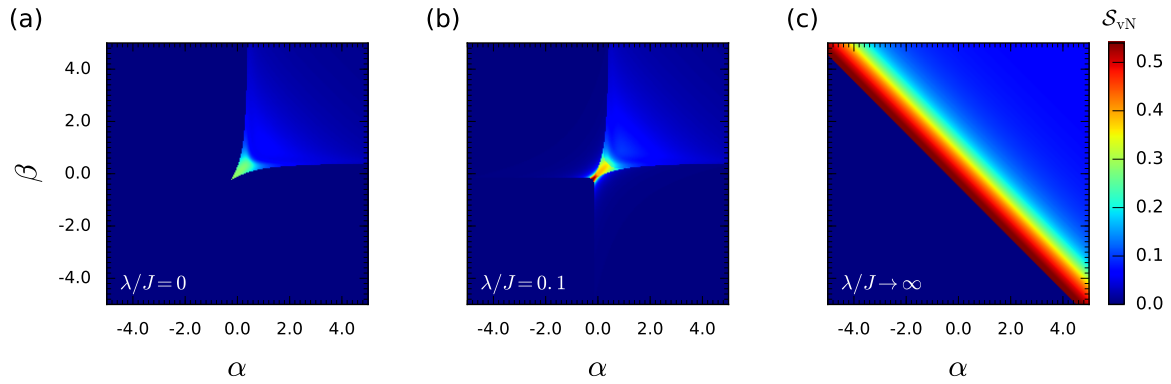

FIGURE B.1: Evolution of the spin-orbital entanglement entropy $\mathcal{S}_{\mathrm{vN}}$ in the on-site spin-orbit coupling parameter λ calculated in the ground state of the 12-site chain. Figure has been published in Ref. [144].

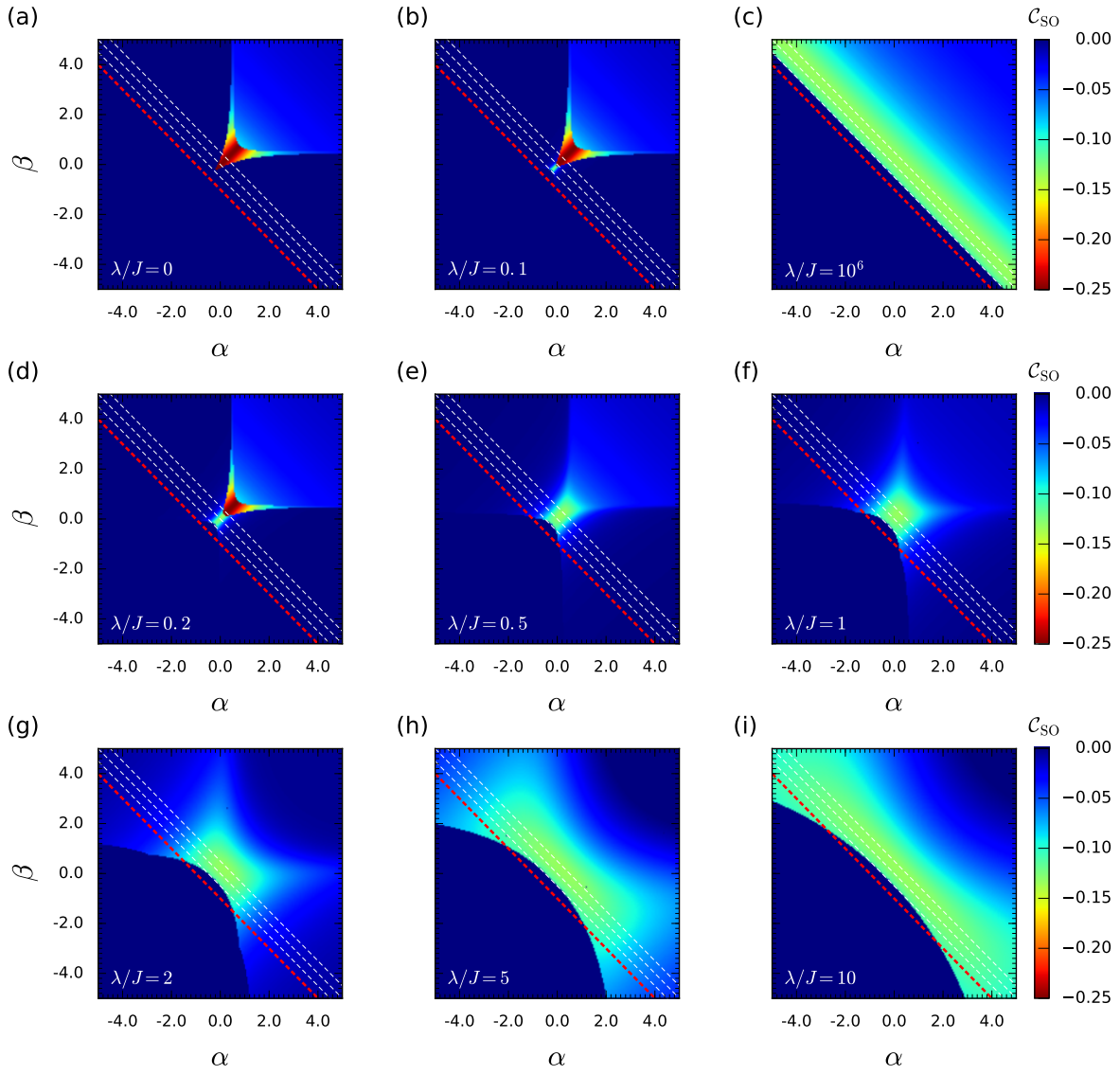

FIGURE B.2: Evolution of the $\mathcal{C}_{\rm SO}$ correlation function in the on-site spin-orbit coupling parameter λ, calculated in the ground state of the 4-site chain. Panels depict $\{\alpha, \beta\}$ slices for the representative values of λ/J. Panels (a) and (b) capture the spin-orbital entanglement for the negligible λ values, in contrast to panel (c), where the dominant λ limit is shown. Panels (d)-(i) show the intermediate stages between (b) and (c). The white dashed lines represent (from the left to the right) the hidden FM Heisenberg, XY, AF Heisenberg models emerging in the dominant λ limit at $\alpha+\beta=-\frac{1}{2}$, $\alpha+\beta=0$ and $\alpha+\beta=\frac{1}{2}$, respectively. The red dashed $\alpha+\beta=-1$ line is representative for the disappearing spin-orbital entanglement in the lower-left part of the slices for the dominant λ parameter.

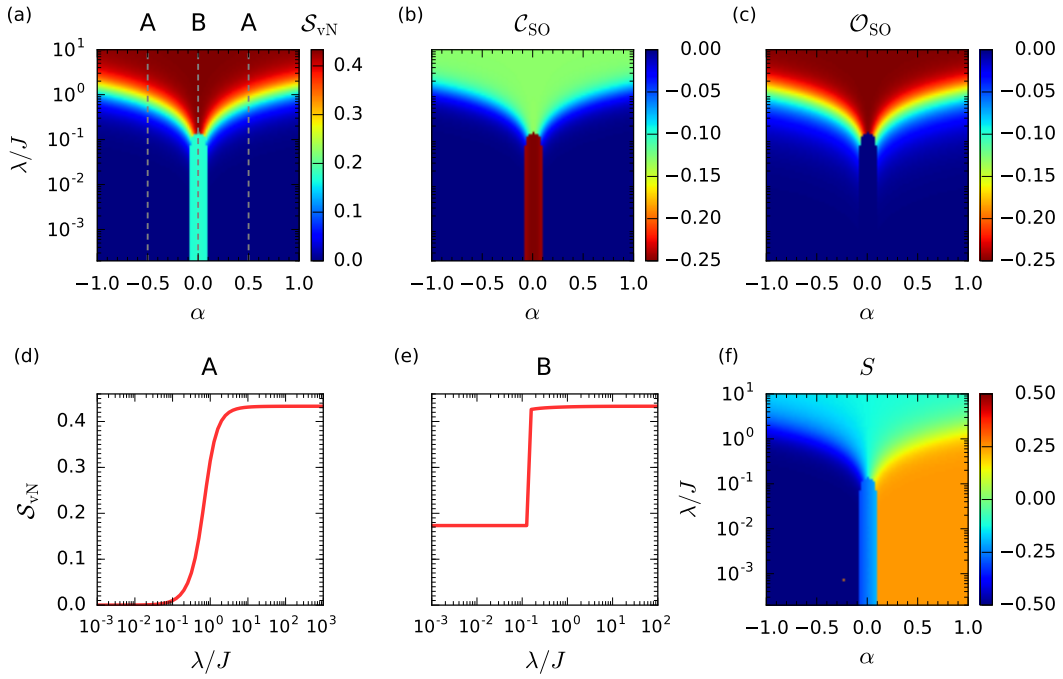

FIGURE B.3: Spin-orbital entanglement evolution in λ along the $\alpha + \beta = 0$ line for the 4-site chain: (a)—entanglement entropy; (b), (c)— $\mathcal{C}_{\mathrm{SO}}$ and $\mathcal{O}_{\mathrm{SO}}$; (d)—entanglement entropy along cut A; (e)—entanglement entropy along cut B; (f)— spin correlation S. Figure published in Ref. [145].

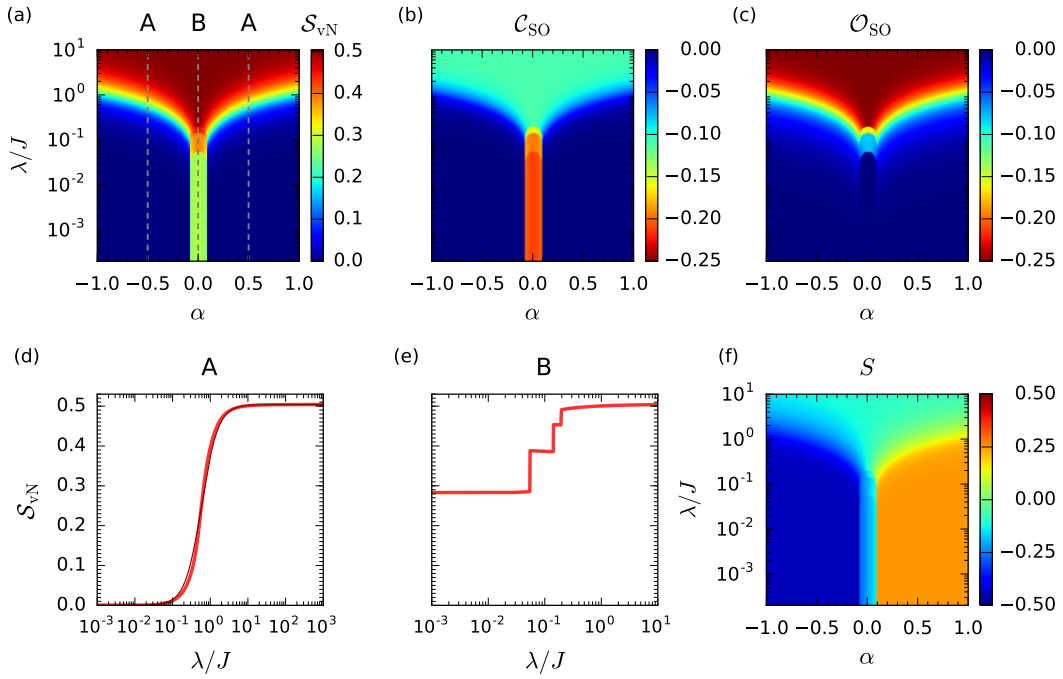

FIGURE B.4: Spin-orbital entanglement evolution in λ along the $\alpha + \beta = 0$ line for the 12-site chain: (a)—entanglement entropy; (b), (c)— $\mathcal{C}_{\mathrm{SO}}$ and $\mathcal{O}_{\mathrm{SO}}$; (d)—entanglement entropy along cut A; (e)—entanglement entropy along cut B; (f)— spin correlation S. Figure has been published in Ref. [144].

B.2 4-site energy spectra

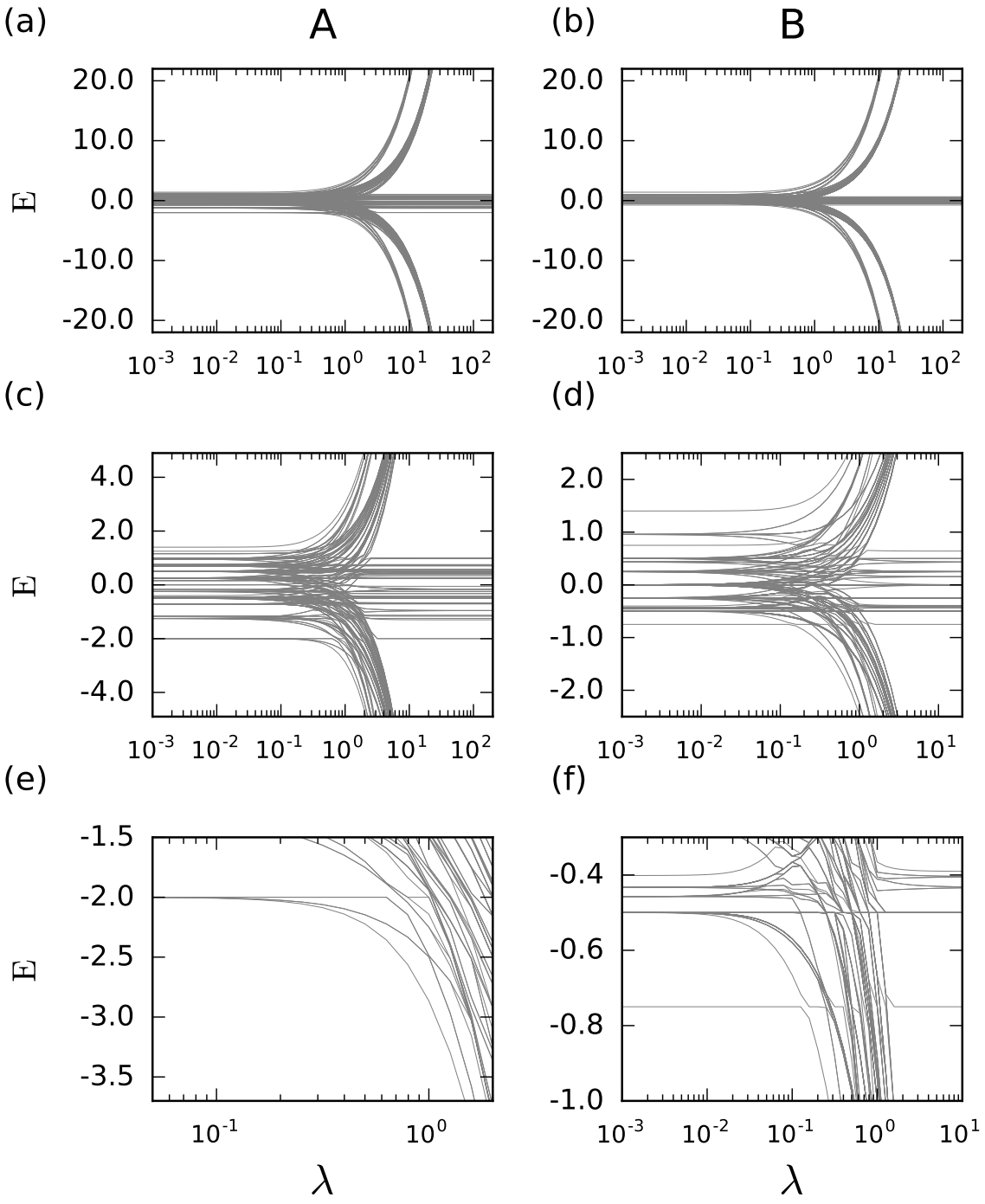

FIGURE B.5: Progressively zoomed in energy spectrum of Hamiltonian (5.1) for the 4-site chain along cuts A and B.

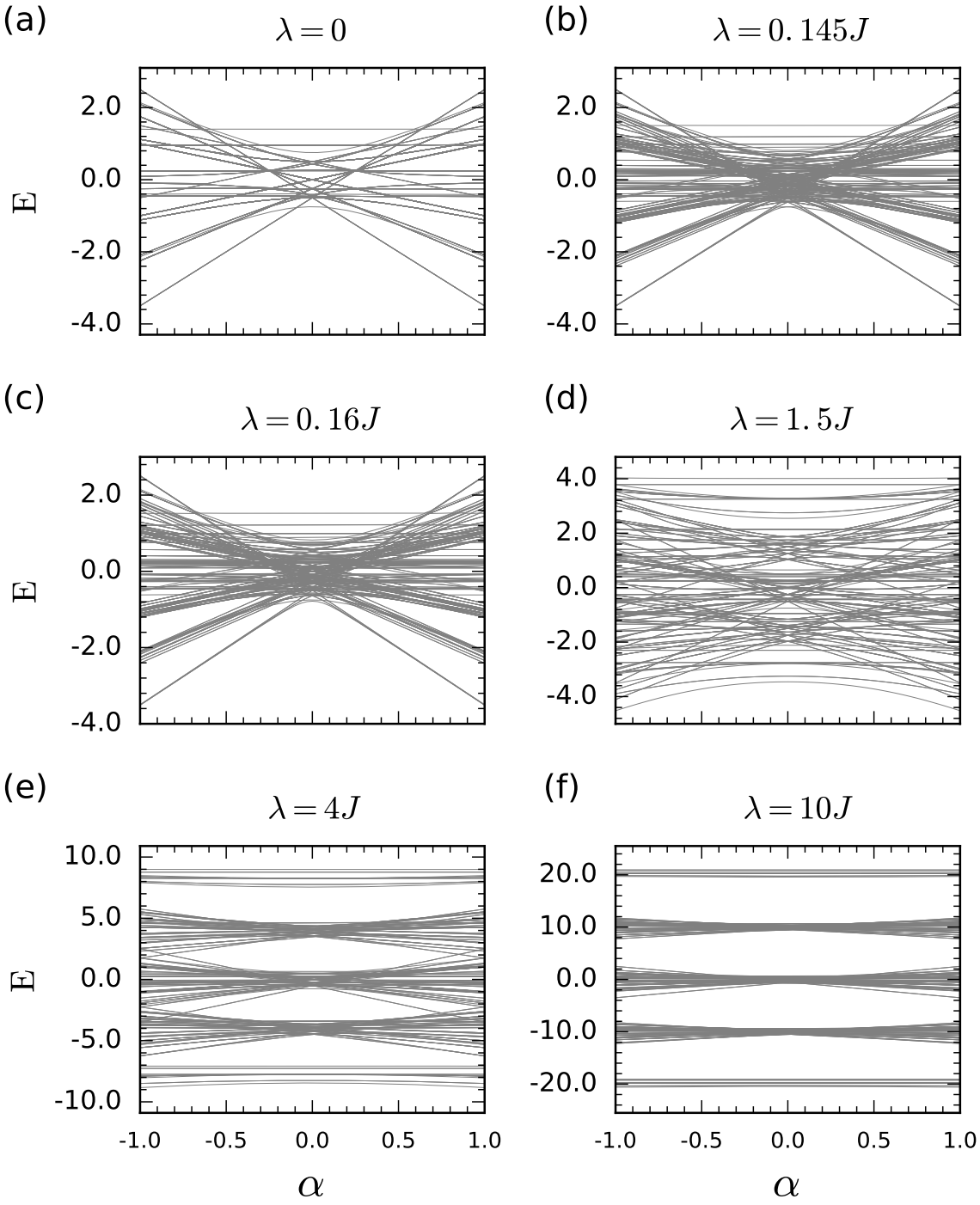

FIGURE B.6: Representative $\lambda = const.$ cuts through the energy spectrum of Hamiltonian (5.1) with the constraint $\alpha + \beta = 0$ for the 4-site chain.

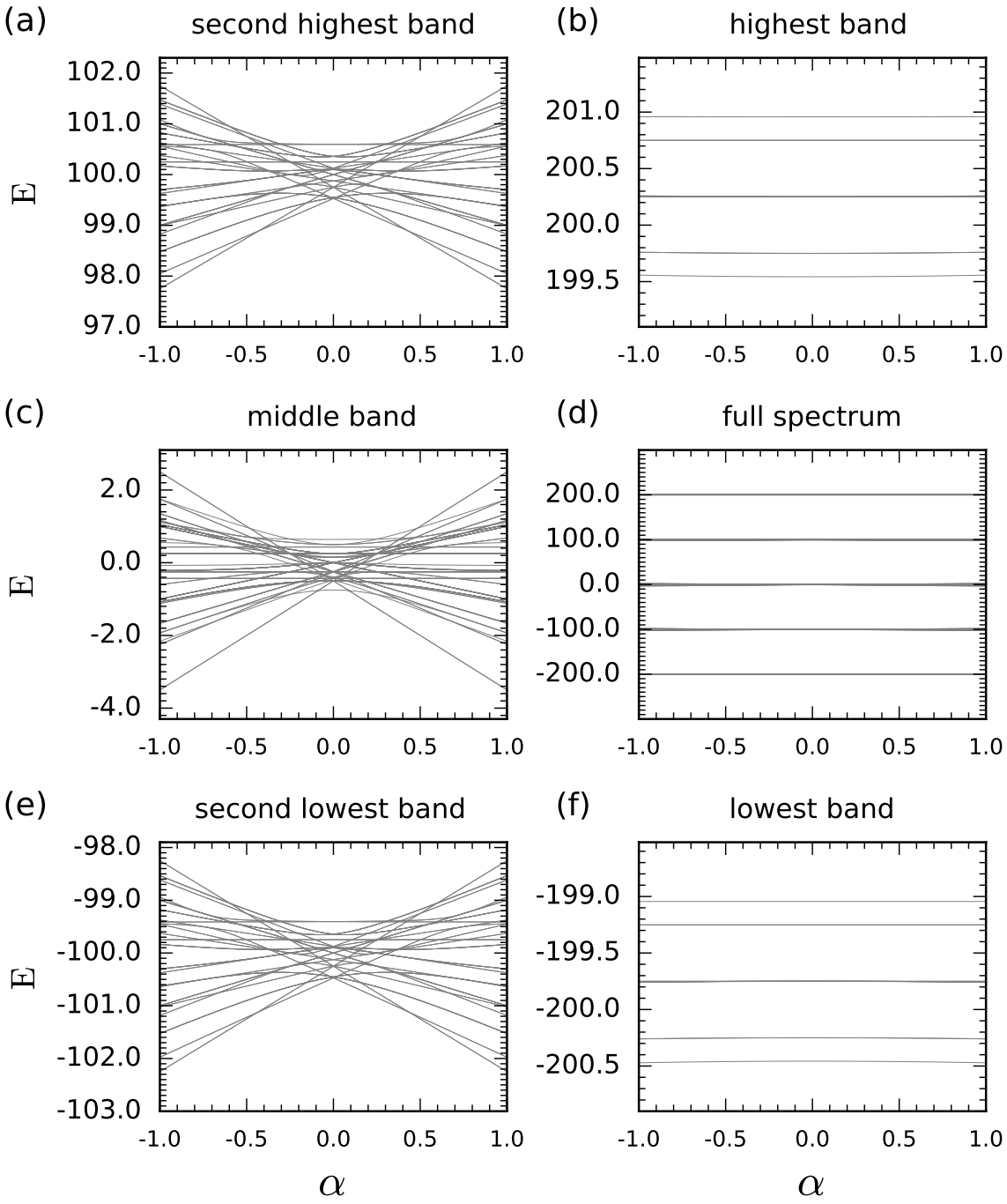

FIGURE B.7: $\lambda/J = 100$ cut through the energy spectrum of Hamiltonian (5.1) with the constraint $\alpha + \beta = 0$.

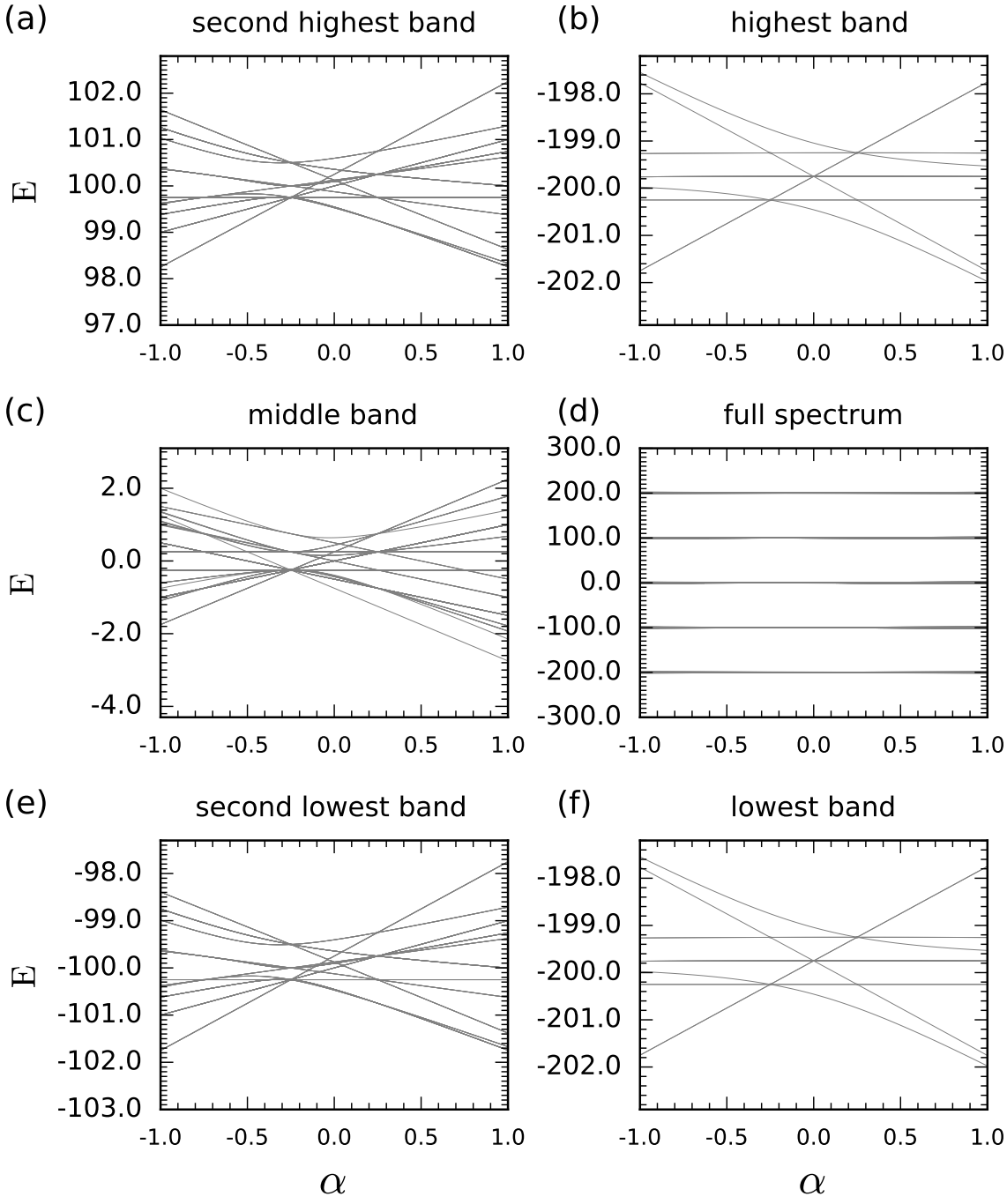

FIGURE B.8: $\lambda/J = 100$ cut through the energy spectrum of Hamiltonian (5.1) with the constraint $\alpha - \beta = 0$.

Bibliography

[1] D. Khomskii. *Basic Aspects of the Quantum Theory of Solids: Order and Elementary Excitations*. Cambridge University Press., 2010. ISBN: 780511788321.

[2] Masatoshi Imada, Atsushi Fujimori, and Yoshinori Tokura. "Metal-insulator transitions". In: *Rev. Mod. Phys.* 70 (1998), pp. 1039–1263.

[3] K. I. Kugel' and D. I. Khomskii. "The Jahn-Teller effect and magnetism: transition metal compounds". In: *Phys. Usp.* 25 (1982), pp. 231–256.

[4] G. Jackeli and G. Khaliullin. "Mott Insulators in the Strong Spin-Orbit Coupling Limit: From Heisenberg to a Quantum Compass and Kitaev Models". In: *Phys. Rev. Lett.* 102 (2009), p. 017205.

[5] Jiří Chaloupka, George Jackeli, and Giniyat Khaliullin. "Kitaev-Heisenberg Model on a Honeycomb Lattice: Possible Exotic Phases in Iridium Oxides A_2IrO_3". In: *Phys. Rev. Lett.* 105 (2010), p. 027204.

[6] Jiří Chaloupka, George Jackeli, and Giniyat Khaliullin. "Zigzag Magnetic Order in the Iridium Oxide Na_2IrO_3". In: *Phys. Rev. Lett.* 110 (2013), p. 097204.

[7] Alexei Kitaev. "Anyons in an exactly solved model and beyond". In: *Annals of Physics* 321 (2006), pp. 2 –111.

[8] Jeffrey G. Rau, Eric Kin-Ho Lee, and Hae-Young Kee. "Generic Spin Model for the Honeycomb Iridates beyond the Kitaev Limit". In: *Phys. Rev. Lett.* 112 (2014), p. 077204.

[9] Jiří Chaloupka and Giniyat Khaliullin. "Hidden symmetries of the extended Kitaev-Heisenberg model: Implications for the honeycomb-lattice iridates A_2IrO_3". In: *Phys. Rev. B* 92 (2015), p. 024413.

[10] Stephen M Winter et al. "Models and materials for generalized Kitaev magnetism". In: *Journal of Physics: Condensed Matter* 29 (2017), p. 493002.

[11] Jiří Chaloupka and Giniyat Khaliullin. "Magnetic anisotropy in the Kitaev model systems Na_2IrO_3 and $RuCl_3$". In: *Phys. Rev. B* 94 (2016), p. 064435.

[12] Hidenori Takagi et al. "Concept and realization of Kitaev quantum spin liquids". In: *Nature Reviews Physics* 1 (2019), 264–280.

[13] Huimei Liu, Jiří Chaloupka, and Giniyat Khaliullin. "Kitaev Spin Liquid in $3d$ Transition Metal Compounds". In: *Phys. Rev. Lett.* 125 (2020), p. 047201.

[14] Yukitoshi Motome et al. "Materials design of Kitaev spin liquids beyond the Jackeli-Khaliullin mechanism". In: *Journal of Physics: Condensed Matter* 32 (2020), p. 404001.

[15] R. Comin et al. "Na_2IrO_3 as a Novel Relativistic Mott Insulator with a 340-meV Gap". In: *Phys. Rev. Lett.* 109 (2012), p. 266406.

[16] C. H. Sohn et al. "Mixing between $J_{\text{eff}} = \frac{1}{2}$ and $\frac{3}{2}$ orbitals in Na_2IrO_3: A spectroscopic and density functional calculation study". In: *Phys. Rev. B* 88 (2013), p. 085125.

[17] Ying Li et al. "Analysis of the optical conductivity for $A_2IrO_3(A = \text{Na}, \text{Li})$ from first principles". In: *Phys. Rev. B* 91 (2015), p. 161101.

[18] Ying Li et al. "Electronic excitations in $\gamma-Li_2IrO_3$". In: *Phys. Rev. B* 95 (2017), p. 045129.

[19] Beom Hyun Kim, Tomonori Shirakawa, and Seiji Yunoki. "From a Quasimolecular Band Insulator to a Relativistic Mott Insulator in t_{2g}^5 Systems with a Honeycomb Lattice Structure". In: *Phys. Rev. Lett.* 117 (2016), p. 187201.

[20] Luke J. Sandilands et al. "Optical probe of Heisenberg-Kitaev magnetism in $\alpha-RuCl_3$". In: *Phys. Rev. B* 94 (2016), p. 195156.

[21] Xiaoqing Zhou et al. "Angle-resolved photoemission study of the Kitaev candidate $\alpha - RuCl_3$". In: *Phys. Rev. B* 94 (2016), p. 161106.

[22] A. Koitzsch et al. "J_{eff} Description of the Honeycomb Mott Insulator $\alpha-RuCl_3$". In: *Phys. Rev. Lett.* 117 (2016), p. 126403.

[23] S. Sinn et al. "Electronic Structure of the Kitaev Material $\alpha-RuCl_3$ Probed by Photoemission and Inverse Photoemission Spectroscopies". In: *Scientific Reports* 6 (2016), p. 39544.

[24] B. J. Kim et al. "Novel $J_{\text{eff}} = 1/2$ Mott State Induced by Relativistic Spin-Orbit Coupling in Sr_2IrO_4". In: *Phys. Rev. Lett.* 101 (2008), p. 076402.

[25] Heung-Sik Kim et al. "Kitaev magnetism in honeycomb $RuCl_3$ with intermediate spin-orbit coupling". In: *Phys. Rev. B* 91 (2015), p. 241110.

[26] Ekaterina M. Pärschke and Rajyavardhan Ray. "Influence of the multiplet structure on the photoemission spectra of spin-orbit driven Mott insulators: Application to Sr_2IrO_4". In: *Phys. Rev. B* 98 (2018), p. 064422.

[27] K. W. Plumb et al. "$\alpha - RuCl_3$: A spin-orbit assisted Mott insulator on a honeycomb lattice". In: *Phys. Rev. B* 90 (2014), p. 041112.

[28] Andrzej M. Oles et al. "Spin-Orbital Entanglement and Violation of the Goodenough-Kanamori Rules". In: *Phys. Rev. Lett.* 96 (2006), p. 147205.

[29] Juraj Rusnačko, Dorota Gotfryd, and Jiří Chaloupka. "Kitaev-like honeycomb magnets: Global phase behavior and emergent effective models". In: *Phys. Rev. B* 99 (2019), p. 064425.

[30] Lucile Savary and Leon Balents. "Quantum spin liquids: a review". In: *Reports on Progress in Physics* 80 (2016), p. 016502.

[31] Leon Balents. "Spin liquids in frustrated magnets". In: *Nature* 464 (2010), p. 199.

[32] Philip Warren Anderson. "Resonating valence bonds: A new kind of insulator?" In: *Matt. Res. Bull.* 8 (1973), pp. 153–160.

[33] J. Knolle et al. "Dynamics of a Two-Dimensional Quantum Spin Liquid: Signatures of Emergent Majorana Fermions and Fluxes". In: *Phys. Rev. Lett.* 112 (2014), p. 207203.

[34] Joji Nasu, Masafumi Udagawa, and Yukitoshi Motome. "Thermal fractionalization of quantum spins in a Kitaev model: Temperature-linear specific heat and coherent transport of Majorana fermions". In: *Phys. Rev. B* 92 (2015), p. 115122.

[35] Junki Yoshitake, Joji Nasu, and Yukitoshi Motome. "Fractional Spin Fluctuations as a Precursor of Quantum Spin Liquids: Majorana Dynamical Mean-Field Study for the Kitaev Model". In: *Phys. Rev. Lett.* 117 (2016), p. 157203.

[36] J. Nasu et al. "Fermionic response from fractionalization in an insulating two-dimensional magnet". In: *Nature Physics* 12 (2016), p. 912.

[37] Stephen Winter et al. "Breakdown of Magnons in a Strongly Spin-Orbital Coupled Magnet". In: *Nature Communications* 8 (2017), p. 1152.

[38] David A. S. Kaib, Stephen M. Winter, and Roser Valentí. "Kitaev honeycomb models in magnetic fields: Dynamical response and dual models". In: *Phys. Rev. B* 100 (2019), p. 144445.

[39] Sae Hwan Chun et al. "- Direct evidence for dominant bond-directional interactions in a honeycomb lattice iridate Na2IrO3". In: *Nature Physics* 11 (2015), p. 462.

[40] Arnab Banerjee et al. "Neutron scattering in the proximate quantum spin liquid α-RuCl3". In: *Science* 356 (2017), pp. 1055–1059.

[41] A Banerjee et al. "Excitations in the field-induced quantum spin liquid state of $\alpha-RuCl_3$". In: *npj Quantum Materials* 1 (2018), p. 8.

[42] Zhe Wang et al. "Magnetic Excitations and Continuum of a Possibly Field-Induced Quantum Spin Liquid in $\alpha - RuCl_3$". In: *Phys. Rev. Lett.* 119 (2017), p. 227202.

[43] A. Sahasrabudhe et al. "High-field quantum disordered state in $\alpha - RuCl_3$: Spin flips, bound states, and multiparticle continuum". In: *Phys. Rev. B* 101 (2020), p. 140410.

[44] Y. Kasahara et al. "Majorana quantization and half-integer thermal quantum Hall effect in a Kitaev spin liquid". In: *Nature* 559 (2018), p. 227.

[45] Kira Riedl et al. "Sawtooth Torque in Anisotropic $j_{\text{eff}} = 1/2$ Magnets: Application to $\alpha-RuCl_3$". In: *Phys. Rev. Lett.* 122 (2019), p. 197202.

[46] L. S. I. Veiga et al. "Pressure tuning of bond-directional exchange interactions and magnetic frustration in the hyperhoneycomb iridate $\beta - Li_2IrO_3$". In: *Phys. Rev. B* 96 (2017), p. 140402.

[47] V. Hermann et al. "Competition between spin-orbit coupling, magnetism, and dimerization in the honeycomb iridates: $\alpha - Li_2IrO_3$ under pressure". In: *Phys. Rev. B* 97 (2018), p. 020104.

[48] J. P. Clancy et al. "Pressure - driven collapse of the relativistic electronic ground state in a honeycomb iridate". In: *npj Quantum Materials* 3 (2018), p. 35.

[49] G. Bastien et al. "Pressure-induced dimerization and valence bond crystal formation in the Kitaev-Heisenberg magnet $\alpha-RuCl_3$". In: *Phys. Rev. B* 97 (2018), p. 241108.

[50] Tobias Biesner et al. "Detuning the honeycomb of $\alpha-RuCl_3$: Pressure-dependent optical studies reveal broken symmetry". In: *Phys. Rev. B* 97 (2018), p. 220401.

[51] K. Kitagawa et al. "A spin–orbital-entangled quantum liquid on a honeycomb lattice". In: *Nature* 554 (2018), pp. 341–345.

[52] Feng Ye et al. "Direct evidence of a zigzag spin-chain structure in the honeycomb lattice: A neutron and x-ray diffraction investigation of single-crystal Na_2IrO_3". In: *Phys. Rev. B* 85 (2012), p. 180403.

[53] S. K. Choi et al. "Spin Waves and Revised Crystal Structure of Honeycomb Iridate Na_2IrO_3". In: *Phys. Rev. Lett.* 108 (2012), p. 127204.

[54] R. D. Johnson et al. "Monoclinic crystal structure of $\alpha - RuCl_3$ and the zigzag antiferromagnetic ground state". In: *Phys. Rev. B* 92 (2015), p. 235119.

[55] J. A. Sears et al. "Magnetic order in $\alpha - RuCl_3$: A honeycomb-lattice quantum magnet with strong spin-orbit coupling". In: *Phys. Rev. B* 91 (2015), p. 144420.

[56] A. Banerjee et al. "Proximate Kitaev quantum spin liquid behaviour in a honeycomb magnet". In: *Nature Materials* 15 (2016), p. 733.

[57] H. B. Cao et al. "Low-temperature crystal and magnetic structure of $\alpha-RuCl_3$". In: *Phys. Rev. B* 93 (2016), p. 134423.

[58] Jennifer A. Sears et al. "Ferromagnetic Kitaev interaction and the origin of large magnetic anisotropy in $\alpha - RuCl_3$". In: *Nature Physics* (2020).

[59] Giniyat Khaliullin. "Orbital Order and Fluctuations in Mott Insulators". In: *Progress of Theoretical Physics Supplement* 160 (2005), pp. 155–202.

[60] Stephen M. Winter et al. "Challenges in design of Kitaev materials: Magnetic interactions from competing energy scales". In: *Phys. Rev. B* 93 (2016), p. 214431.

[61] Stephen M. Winter et al. "Probing $\alpha - RuCl_3$ Beyond Magnetic Order: Effects of Temperature and Magnetic Field". In: *Phys. Rev. Lett.* 120 (2018), p. 077203.

[62] Itamar Kimchi and Yi-Zhuang You. "Kitaev-Heisenberg-J_2-J_3 model for the iridates A_2IrO_3". In: *Phys. Rev. B* 84 (2011), p. 180407.

[63] Yuriy Sizyuk et al. "Importance of anisotropic exchange interactions in honeycomb iridates: Minimal model for zigzag antiferromagnetic order in Na_2IrO_3". In: *Phys. Rev. B* 90 (2014), p. 155126.

[64] Youhei Yamaji et al. "First-Principles Study of the Honeycomb-Lattice Iridates Na_2IrO_3 in the Presence of Strong Spin-Orbit Interaction and Electron Correlations". In: *Phys. Rev. Lett.* 113 (2014), p. 107201.

[65] Vamshi M Katukuri et al. "Kitaev interactions between j= 1/2 moments in honeycomb Na2IrO3 are large and ferromagnetic: insights from ab initio quantum chemistry calculations". In: *New Journal of Physics* 16 (2014), p. 013056.

[66] Ioannis Rousochatzakis et al. "Phase Diagram and Quantum Order by Disorder in the Kitaev $K_1 - K_2$ Honeycomb Magnet". In: *Phys. Rev. X* 5 (2015), p. 041035.

[67] Ravi Yadav et al. "Kitaev exchange and field-induced quantum spin-liquid states in honeycomb α-RuCl3". In: *Scientific Reports* 6 (2016), p. 37925.

[68] H. Suzuki et al. *Quantifying the Exchange Interactions in the Kitaev Model System RuCl3 by Ru L edge Resonant Inelastic X-ray Scattering*. 2020. arXiv: `2008.02037 [cond-mat.str-el]`.

[69] Yuriy Sizyuk, Peter Wölfle, and Natalia B. Perkins. "Selection of direction of the ordered moments in Na_2IrO_3 and $\alpha - RuCl_3$". In: *Phys. Rev. B* 94 (2016), p. 085109.

[70] Jeffrey G. Rau, Lee, and Hae-Young Kee. *Trigonal distortion in the honeycomb iridates: Proximity of zigzag and spiral phases in Na2IrO3*. 2014. arXiv: `1408.4811 [cond-mat.str-el]`.

[71] Lukas Janssen, Eric C. Andrade, and Matthias Vojta. "Magnetization processes of zigzag states on the honeycomb lattice: Identifying spin models for $\alpha-RuCl_3$ and Na_2IrO_3". In: *Phys. Rev. B* 96 (2017), p. 064430.

[72] Katsuhiro Morita, Masanori Kishimoto, and Takami Tohyama. "Ground-state phase diagram of the Kitaev-Heisenberg model on a kagome lattice". In: *Phys. Rev. B* 98 (2018), p. 134437.

[73] Ioannis Rousochatzakis et al. "Kitaev anisotropy induces mesoscopic Z_2 vortex crystals in frustrated hexagonal antiferromagnets". In: *Phys. Rev. B* 93 (2016), p. 104417.

[74] Cliò Efthimia Agrapidis, Jeroen van den Brink, and Satoshi Nishimoto. "Ordered states in the Kitaev-Heisenberg model: From 1D chains to 2D honeycomb". In: *Scientific Reports* 8 (2018), pp. 2045–2322.

[75] Cliò Efthimia Agrapidis, Jeroen van den Brink, and Satoshi Nishimoto. "Ground state and low-energy excitations of the Kitaev-Heisenberg two-leg ladder". In: *Phys. Rev. B* 99 (2019), p. 224418.

[76] Piotr Czarnik, Anna Francuz, and Jacek Dziarmaga. "Tensor network simulation of the Kitaev-Heisenberg model at finite temperature". In: *Phys. Rev. B* 100 (2019), p. 165147.

[77] Maria Laura Baez. "Minimal models of $\alpha-Li_2IrO_3$: Range of interactions, ground state properties, and magnetization processes". In: *Phys. Rev. B* 99 (2019), p. 184436.

[78] Jiří Chaloupka and Giniyat Khaliullin. "Highly frustrated magnetism in relativistic d^4 Mott insulators: Bosonic analog of the Kitaev honeycomb model". In: *Phys. Rev. B* 100 (2019), p. 224413.

[79] M. S. Dresselhaus. *Solid State Physics III. Magnetic Properties of Solids*. URL: `http://web.mit.edu/6.732/www/6.732-pt3.pdf`.

[80] Dorota Gotfryd et al. "Phase diagram and spin correlations of the Kitaev-Heisenberg model: Importance of quantum effects". In: *Phys. Rev. B* 95 (2017), p. 024426.

[81] A Auerbach. *Interacting electrons and quantum magnetism*. Springer Verlag, 1994.

[82] Eva Pavarini, Erik Koch, and Piers Coleman. *Many-Body Physics: From Kondo to Hubbard*. Vol. 5. Modeling and Simulation. Jülich: Forschungszentrum Jülich GmbH Zentralbibliothek, Verlag, 2015. ISBN: 978-3-95806-074-6.

[83] A. F. Albuquerque et al. "Phase diagram of a frustrated quantum antiferromagnet on the honeycomb lattice: Magnetic order versus valence-bond crystal formation". In: *Phys. Rev. B* 84 (2011), p. 024406.

[84] J. Oitmaa. "Phase diagram of the Heisenberg-Kitaev model at $T = 0$". In: *Phys. Rev. B* 92 (2015), p. 020405.

[85] J. Oitmaa. "Erratum: Phase diagram of the Heisenberg-Kitaev model at $T = 0$ [Phys. Rev. B 92, 020405(R) (2015)]". In: *Phys. Rev. B* 94 (2016), p. 179901.

[86] J D Reger, J A Riera, and A P Young. "Monte Carlo simulations of the spin- 1 / 2 Heisenberg antiferromagnet in two dimensions". In: *Journal of Physics: Condensed Matter* 1 (1989), p. 1855.

[87] Eduardo V. Castro et al. "Site dilution of quantum spins in the honeycomb lattice". In: *Phys. Rev. B* 73 (2006), p. 054422.

[88] U Löw. "Properties of the two-dimensional spin-1/2 Heisenberg model on a honeycomb lattice with interlayer coupling". In: *Condens. Matter Phys.* 12 (2009), p. 497.

[89] Zheng Weihong, J. Oitmaa, and C. J. Hamer. "Second-order spin-wave results for the quantum XXZ and XY models with anisotropy". In: *Phys. Rev. B* 44 (1991), pp. 11869–11881.

[90] Juraj Rusnačko. *Magnetic ordering in extended Kitaev-Heisenberg model*. Masaryk University, Brno, 2016.

[91] G. Baskaran, Saptarshi Mandal, and R. Shankar. "Exact Results for Spin Dynamics and Fractionalization in the Kitaev Model". In: *Phys. Rev. Lett.* 98 (2007), p. 247201.

[92] K. S. Tikhonov, M. V. Feigel'man, and A. Yu. Kitaev. "Power-Law Spin Correlations in a Perturbed Spin Model on a Honeycomb Lattice". In: *Phys. Rev. Lett.* 106 (2011), p. 067203.

[93] Matthias Gohlke et al. "Quantum spin liquid signatures in Kitaev-like frustrated magnets". In: *Phys. Rev. B* 97 (2018), p. 075126.

[94] Kazuya Shinjo, Shigetoshi Sota, and Takami Tohyama. "Density-matrix renormalization group study of the extended Kitaev-Heisenberg model". In: *Phys. Rev. B* 91 (2015), p. 054401.

[95] P. Peter Stavropoulos, Andrei Catuneanu, and Hae-Young Kee. "Counter-rotating spiral order in three-dimensional iridates: Signature of hidden symmetry in the Kitaev-Γ model". In: *Phys. Rev. B* 98 (2018), p. 104401.

[96] Eoin Quinn, Subhro Bhattacharjee, and Roderich Moessner. "Phases and phase transitions of a perturbed Kekulé-Kitaev model". In: *Phys. Rev. B* 91 (2015), p. 134419.

[97] Erhai Zhao and W. Vincent Liu. "Orbital Order in Mott Insulators of Spinless p-Band Fermions". In: *Phys. Rev. Lett.* 100 (2008), p. 160403.

[98] Congjun Wu. "Orbital Ordering and Frustration of p-Band Mott Insulators". In: *Phys. Rev. Lett.* 100 (2008), p. 200406.

[99] J. Nasu et al. "Doubly degenerate orbital system in honeycomb lattice: Implication of orbital state in layered iron oxide". In: *Phys. Rev. B* 78 (2008), p. 024416.

[100] Cheng-Chien Chen et al. "Fermionic Symmetry-Protected Topological Phase in a Two-Dimensional Hubbard Model". In: *Phys. Rev. Lett.* 117 (2016), p. 096405.

[101] Jie Lou et al. *Global Phase Diagram of the Extended Kitaev-Heisenberg Model on Honeycomb Lattice*. 2015. arXiv: `1501.06990 [cond-mat.str-el]`.

[102] Haiyuan Zou et al. "A continuum of compass spin models on the honeycomb lattice". In: *New Journal of Physics* 18 (2016), p. 053040.

[103] Juan Osorio Iregui, Philippe Corboz, and Matthias Troyer. "Probing the stability of the spin-liquid phases in the Kitaev-Heisenberg model using tensor network algorithms". In: *Phys. Rev. B* 90 (2014), p. 195102.

[104] B. J. Kim and Giniyat Khaliullin. "Resonant inelastic x-ray scattering operators for t_{2g} orbital systems". In: *Phys. Rev. B* 96 (2017), p. 085108.

[105] Yogesh Singh and P. Gegenwart. "Antiferromagnetic Mott insulating state in single crystals of the honeycomb lattice material Na_2IrO_3". In: *Phys. Rev. B* 82 (2010), p. 064412.

[106] H. Gretarsson et al. "Crystal-Field Splitting and Correlation Effect on the Electronic Structure of A_2IrO_3". In: *Phys. Rev. Lett.* 110 (2013), p. 076402.

[107] Yumi Kubota et al. "Successive magnetic phase transitions in $\alpha - RuCl_3$: XY-like frustrated magnet on the honeycomb lattice". In: *Phys. Rev. B* 91 (2015), p. 094422.

[108] Jungho Kim et al. "Dynamic Spin Correlations in the Honeycomb Lattice Na_2IrO_3 Measured by Resonant Inelastic x-Ray Scattering". In: *Phys. Rev. X* 10 (2020), p. 021034.

[109] Ryszard Horodecki et al. "Quantum entanglement". In: *Rev. Mod. Phys.* 81 (2009), pp. 865–942.

[110] Wojciech Hubert Zurek. "Decoherence, einselection, and the quantum origins of the classical". In: *Rev. Mod. Phys.* 75 (2003), pp. 715–775.

[111] Peter Wittek. "3 - Quantum Mechanics". In: *Quantum Machine Learning*. Ed. by Peter Wittek. Boston: Academic Press, 2014, pp. 25 –39. ISBN: 978-0-12-800953-6.

[112] Tamas Andras Toth. *Quadrupolar Ordering in Two-Dimensional Spin-One Systems*. Lausanne: EPFL, 2011.

[113] W.M. de Muynck. *Foundations of Quantum Mechanics, an Empiricist Approach*. Fundamental Theories of Physics. Springer Netherlands, 2006. ISBN: 9780306480478.

[114] Michael Dickson. "Non-Relativistic Quantum Mechanics". In: *Philosophy of Physics*. Ed. by Jeremy Butterfield and John Earman. Handbook of the Philosophy of Science. Amsterdam: North-Holland, 2007, pp. 275 –415.

[115] T. Scholak et al. "Chapter 1 - Transport and Entanglement". In: *Quantum Efficiency in Complex Systems, Part I: Biomolecular systems*. Ed. by Eicke R. Weber, Michael Thorwart, and Uli Wurfel. Vol. 83. Semiconductors and Semimetals. Elsevier, 2010, pp. 1 – 38.

[116] Walter Greiner, Ludwig Neise, and Horst Stoecker. *Thermodynamics and Statistical Mechanics*. Springer-Verlag New York, 1995. ISBN: 9781461208273.

[117] Erik Anson et al. *Why is there a logarithmic function in the entropy formula.* URL: https://www.quora.com/Why-is-there-a-logarithmic-function-in-the-entropy-formula.

[118] C. E. Shannon. "A mathematical theory of communication". In: *The Bell System Technical Journal* 27 (1948), pp. 379–423.

[119] P.D. Beale. *Statistical Mechanics.* Elsevier Science, 2011. ISBN: 9780123821898.

[120] D. Petz. "Entropy, von Neumann and the von Neumann Entropy". In: *John von Neumann and the Foundations of Quantum Physics. Vienna Circle Institute Yearbook [2000].* Ed. by M. Redei and M. Stoeltzner. Vol. 8. Springer, Dordrecht, 2001.

[121] Wikipedia contributors. *Von Neumann entropy — Wikipedia, The Free Encyclopedia.* https://en.wikipedia.org/w/index.php?title=Von_Neumann_entropy&oldid=967477503. [Online; accessed 11-August-2020]. 2020.

[122] Alexei Kitaev and John Preskill. "Topological Entanglement Entropy". In: *Phys. Rev. Lett.* 96 (2006), p. 110404.

[123] G. Khaliullin and S. Maekawa. "Orbital Liquid in Three-Dimensional Mott Insulator: $LaTiO_3$". In: *Phys. Rev. Lett.* 85 (2000), pp. 3950–3953.

[124] Giniyat Khaliullin, Peter Horsch, and Andrzej M. Oles. "Spin Order due to Orbital Fluctuations: Cubic Vanadates". In: *Phys. Rev. Lett.* 86 (2001), pp. 3879–3882.

[125] S. Nakatsuji et al. "Spin-Orbital Short-Range Order on a Honeycomb-Based Lattice". In: *Science* 336 (2012), pp. 559–563. ISSN: 0036-8075.

[126] Yuki Ishiguro et al. "Dynamical spin–orbital correlation in the frustrated magnet Ba3CuSb2O9". In: *Nature Commun* 4 (2013), p. 2022.

[127] Huiyuan Man et al. "Spin-orbital entangled liquid state in the copper oxide Ba3CuSb2O9". In: *Journal of Physics: Condensed Matter* 30 (2018), p. 443002.

[128] B. Keimer et al. "Spin Dynamics and Orbital State in $LaTiO_3$". In: *Phys. Rev. Lett.* 85 (2000), pp. 3946–3949.

[129] C. Ulrich et al. "Magnetic Order and Dynamics in an Orbitally Degenerate Ferromagnetic Insulator". In: *Phys. Rev. Lett.* 89 (2002), p. 167202.

[130] C. Ulrich et al. "Magnetic Neutron Scattering Study of YVO_3: Evidence for an Orbital Peierls State". In: *Phys. Rev. Lett.* 91 (2003), p. 257202.

[131] Swapan K. Pati, Rajiv R. P. Singh, and Daniel I. Khomskii. "Alternating Spin and Orbital Dimerization and Spin-Gap Formation in Coupled Spin-Orbital Systems". In: *Phys. Rev. Lett.* 81 (1998), pp. 5406–5409.

[132] Yan Chen et al. "Spin-orbital entanglement and quantum phase transitions in a spin-orbital chain with $SU(2) \times SU(2)$ symmetry". In: *Phys. Rev. B* 75 (2007), p. 195113.

[133] Rex Lundgren, Victor Chua, and Gregory A. Fiete. "Entanglement entropy and spectra of the one-dimensional Kugel-Khomskii model". In: *Phys. Rev. B* 86 (2012), p. 224422.

[134] Hans-Jurgen Mikeska and Alexei K. Kolezhuk. *One-dimensional magnetism.* Quantum Magnetism. Lecture Notes in Physics, vol 645, Springer Berlin Heidelberg, 2004, 1–83. ISBN: 9783540400660.

[135] Chigak Itoi, Shaojin Qin, and Ian Affleck. "Phase diagram of a one-dimensional spin-orbital model". In: *Phys. Rev. B* 61 (2000), pp. 6747–6756.

[136] You-Quan Li et al. "Ground state and excitations of a spin chain with orbital degeneracy". In: *Phys. Rev. B* 60 (1999), pp. 12781–12787.

[137] A. K. Kolezhuk and H.-J. Mikeska. "Non-Haldane Spin-Liquid Models with Exact Ground States". In: *Phys. Rev. Lett.* 80 (1998), pp. 2709–2712.

[138] Yasufumi Yamashita, Naokazu Shibata, and Kazuo Ueda. "SU(4) spin-orbit critical state in one dimension". In: *Phys. Rev. B* 58 (1998), pp. 9114–9118.

[139] Bill Sutherland. "Model for a multicomponent quantum system". In: *Phys. Rev. B* 12 (1975), pp. 3795–3805.

[140] Chigak Itoi, Shaojin Qin, and Ian Affleck. "Phase diagram of a one-dimensional spin-orbital model". In: *Phys. Rev. B* 61 (2000), pp. 6747–6756.

[141] P. Azaria et al. "One-Dimensional SU(4) Spin-Orbital Model: A Low-Energy Effective Theory". In: *Phys. Rev. Lett.* 83 (1999), pp. 624–627.

[142] Masahiko G. Yamada, Masaki Oshikawa, and George Jackeli. "Emergent SU(4) Symmetry in $\alpha-ZrCl_3$ and Crystalline Spin-Orbital Liquids". In: *Phys. Rev. Lett.* 121 (2018), p. 097201.

[143] A. A. Nersesyan and A. M. Tsvelik. "One-Dimensional Spin-Liquid without Magnon Excitations". In: *Phys. Rev. Lett.* 78 (1997), pp. 3939–3942.

[144] Dorota Gotfryd et al. "How spin-orbital entanglement depends on the spin-orbit coupling in a Mott insulator". In: *Phys. Rev. Research* 2 (2020), p. 013353.

[145] Dorota Gotfryd et al. "Evolution of Spin-Orbital Entanglement for Increasing Ising Spin-Orbit Coupling". In: *Condens. Matter* 5 (2020), p. 53.

[146] Andrzej M. Oles. "Fingerprints of spin-orbital entanglement in transition metal oxides". In: *Journal of physics. Condensed matter : an Institute of Physics journal* 24 (2012), p. 313201.

[147] Peter Horsch, Giniyat Khaliullin, and Andrzej M. Oles. "Dimerization versus Orbital-Moment Ordering in a Mott Insulator YVO_3". In: *Phys. Rev. Lett.* 91 (2003), p. 257203.

[148] William Witczak-Krempa et al. "Correlated Quantum Phenomena in the Strong Spin-Orbit Regime". In: *Annual Review of Condensed Matter Physics* 5 (2014), pp. 57–82.

[149] M. V. Eremin et al. "Alternating spin-orbital order in tetragonal Sr_2VO_4". In: *Phys. Rev. B* 84 (2011), p. 212407.

[150] J. Choukroun. "Superexchange mechanisms in an ideal $3d^1$ cubic system of the perovskite type". In: *Phys. Rev. B* 84 (2011), p. 014415.

[151] Christopher Svoboda, Mohit Randeria, and Nandini Trivedi. "Effective magnetic interactions in spin-orbit coupled d^4 Mott insulators". In: *Phys. Rev. B* 95 (2017), p. 014409.

[152] Akihisa Koga, Shiryu Nakauchi, and Joji Nasu. "Role of spin-orbit coupling in the Kugel-Khomskii model on the honeycomb lattice". In: *Phys. Rev. B* 97 (2018), p. 094427.

[153] I V Solovyev. "Spin–orbital superexchange physics emerging from interacting oxygen molecules in KO2". In: *New Journal of Physics* 10 (2008), p. 013035.

[154] K. Wohlfeld, M. Daghofer, and A. M. Oles. "Spin-orbital physics for p orbitals in alkali RO2 hyperoxides. Generalization of the Goodenough-Kanamori rules". In: *EPL (Europhysics Letters)* 96 (2011), p. 27001.

[155] Olga Sikora et al. "Origin of the monoclinic distortion and its impact on the electronic properties in KO2". In: *Phys. Rev. B* 102 (2020), p. 085129.

[156] G. Sun et al. "Exploring spin-orbital models with dipolar fermions in zigzag optical lattices". In: *Phys. Rev. B* 86 (2012), p. 155159.

[157] Wen-Long You, Peter Horsch. "Quantum entanglement in the one-dimensional spin-orbital SU(2) $\bigotimes$ XXZ model". In: *Phys. Rev. B* 92 (2015), p. 054423.

[158] Jiří Chaloupka. "Spin-orbital resonating valence bond liquid on a triangular lattice: Evidence from finite-cluster diagonalization". In: *Phys. Rev. B* 83 (2011), p. 094406.

[159] Eva Pavarini et al., eds. *The Physics of Correlated Insulators, Metals, and Superconductors*. Vol. 7. Schriften des Forschungszentrums Jülich Reihe Modeling and Simulation. Jülich: Forschungszentrum Jülich GmbH Zentralbibliothek, Verlag, Sept. 25, 2017, 450 p. ISBN: 978-3-95806-224-5.

[160] Vincenzo Alba, Masudul Haque, and Andreas M Läuchli. "Entanglement spectrum of the Heisenberg XXZ chain near the ferromagnetic point". In: *Journal of Statistical Mechanics: Theory and Experiment* 2012.08 (2012), P08011.

[161] Jacques Des Cloizeaux and Michel Gaudin. "Anisotropic Linear Magnetic Chain". In: *jmph* 7 (1966), pp. 1384–.

[162] Keigo Hijii, Atsuhiro Kitazawa, and Kiyohide Nomura. "Phase diagram of S = $\frac{1}{2}$ two-leg XXZ spin-ladder systems". In: *Phys. Rev. B* 72 (2005), p. 014449.

[163] Max A. Metlitski. *The XY Model in One Dimension*. URL: `https://phas.ubc.ca/~berciu/TEACHING/PHYS503/PROJECTS/XYModel2.pdf`.